

Aerosol, Surface and Cloud retrieval using passive remote sensing over the Arctic

Soheila Jafariserajehlou

Universität Bremen 2021

Aerosol, Surface and Cloud retrieval using passive remote sensing over the Arctic

Vom Fachbereich für Physik und Elektrotechnik
der Universität Bremen

genehmigte Dissertation zur Erladung des akademischen Grades
Doktor der Naturwissenschaften
(Doktor rer. nat.)

von **Soheila Jafariserajehlou**

eingereicht am: 20. September 2021
Tag des mündlichen Kolloquiums: 29. October 2021

1. Gutachter: Prof. Dr. John P. Burrows
2. Gutachter: Prof. Dr. Andreas Macke



Abstract

The lack of knowledge of aerosol optical properties is one of the sources of uncertainty in assessment and projections of the evolution of climate change and the phenomenon of Arctic Amplification. The spatial and temporal change of microphysical, chemical and optical properties of aerosols in the Arctic and the induced effects through direct and indirect radiative forcing of aerosols remain an open question. The cause of this gap in our understanding and therefore in the global aerosol optical thickness (AOT) maps is associated with the difficulty of retrieving aerosol properties over bright surfaces covered with snow and ice. Decoupling a strong surface signal from that of aerosol in the measured top-of-atmosphere reflectance is challenging and still hampered due to remaining unresolved issues in state-of-the-art algorithms. Despite the promising performance of previously-developed methods and ongoing research, there is no published long-term AOT product over polar regions (over land and ocean) to be used for climate studies.

In this work, to extend our knowledge about the open issues and improve the existing algorithms, first we focus on the two major obstacles in the retrieval of AOT over snow/ice surfaces: i) cloud identification, and ii) surface properties; Second, we apply the outcome of studying the two mentioned prerequisites to improve the previously-developed aerosol retrieval algorithm called AEROSNOW (Istomina, 2012; Istomina et al., 2011) and create a long-term data record for aerosol optical thickness over the Arctic circle.

In the framework of this work, a new cloud identification algorithm called the AATSR/SLSTR Cloud Identification Algorithm (ASCIA) has been developed to screen cloudy scenes in observations of Advanced Along-Track Scanning Radiometer (AATSR) on-board ENVISAT as well as its successor Sea and Land Surface Temperature Radiometer (SLSTR) on-board Sentinel-3. The cloud detection results are verified by comparing them with available cloud products over the Arctic. Furthermore, the cloud product from ASCIA is validated using the ground-based measurements SYNOP, resulting in a promising agreement. In general, ASCIA shows an improved performance in comparison with other algorithms applied to AATSR measurements over snow/ice.

For the study of snow surface properties, the reflectance is simulated in a snow-atmosphere system, using the SCIATRAN radiative transfer model, and the results are compared with those of airborne measurements. A sensitivity study is conducted to highlight the importance of having a priori knowledge about snow morphology (size and shape) and atmospheric parameters to minimise the difference between simulated and real world reflectance. The absolute difference between the modelled results and measurements in off-glint regions is generally small and promising.

In the final step, we apply the outcome of previous steps in the AEROSNOW algorithm as far as possible within the scope of this work and retrieve AOT over the Arctic circle for the 2002-2012 period with the spatial resolution of $1 \times 1 \text{ km}^2$. The retrieved AOT is validated using ground-based measurements AEROSOL ROBOTIC NETWORK (AERONET). The results of validation are promising and show the suc-

cessful performance of the algorithm especially during haze episodes. However, in some cases large differences exist between the retrieved AOT and AERONET measurements for which more statistical and physical analysis are necessary to better understand the cause. Nevertheless, the long-term data record and validation produced hold significant value as are the first attempt to better understand the role of aerosols in the Arctic Amplification over land and ocean on the full Arctic scale.

List of peer-reviewed publications

As first author:

- **Jafariserajehlou, S.**, Mei, L., Vountas, M., Rozanov, V., Burrows, J. P., Hollmann, R., A., A cloud identification algorithm over the Arctic for use with AATSR/SLSTR measurements, *Atmos. Meas. Tech.*, 12, 1059-1076, 2019.
- **Jafariserajehlou, S.**, Rozanov, V. V., Vountas, M., Gatebe, C. K., Burrows, J. P., Simulated reflectance above snow constrained by airborne measurements of solar radiation: implications for the snow grain morphology in the Arctic, *Atmos. Meas. Tech.*, 14, 369–389, 2021.

As co-author:

- Vountas, M., Belinska, K., Rozanov, V. V., Lelli, L., Mei, L., **Jafariserajehlou, S.**, Burrows, J. P., Retrieval of aerosol optical thickness and surface parameters based on multi-spectral and multi-viewing space-borne measurements, *Journal of Quantitative Spectroscopy and Radiative Transfer*, 56, 107311, 2020.
- Wendisch, M., Macke, A., Ehrlich, A., [...] **Jafariserajehlou, S.**, et al. The arctic cloud puzzle: using ACLOUD/PASCAL multiplatform observations to unravel the role of clouds and aerosol particles in Arctic Amplification, *Bulletin of the American Meteorological*, 100 (15), 841-871, 2019.

Conferences contributions

- Swain, B., Vountas, M., Mei, L., **Jafariserajehlou, S.**, Burrows FRS, J. P., Remote sensing of aerosol properties and surface reflectance in the Arctic from satellite observations, (AC)³ Science Conference on Arctic Amplification, Potsdam, Germany, 25 - 27 October 2021.
- **Jafariserajehlou, S.**, Rozanov, V. V., Pohl, C., Mei, L., Vountas, M., Burrows, J. P., Bidirectional reflectance of snow: measurements from ARCTAS Campaign and modeling using SCIATRAN radiative transfer model, ESA living planet symposium, Milan, Italy, May 2019.
- **Jafariserajehlou, S.**, Mei, L., Vountas, M., Rozanov, V. V., Burrows, J. P., Studies to Aerosol retrieval over the Arctic: prerequisites and case studies, EGU conference, 7 - 12 April 2019, Vienna, Austria.
- **Jafariserajehlou, S.**, Mei, L., Vountas, M., Rozanov, V. V., Burrows, J. P., A new algorithm for cloud identification over the Arctic using AATSR/SLSTR and its application for ACLOUD/PASCAL campaigns, 15th International Circumpolar Remote Sensing Symposium (ICRSS), Potsdam, Germany, 10 - 14 September 2018.
- **Jafariserajehlou, S.**, Mei, L., Vountas, M., Rozanov, V. V., Burrows, J. P., Cloud masking for aerosol retrieval over the Arctic using AATSR/SLSTR time-series measurements, poster presentation, EGU conference, 8 - 13 April 2018, Vienna, Austria.
- **Jafariserajehlou, S.**, Rozanov, V. V., Pohl, C., Mei, L., Vountas, M., Burrows, J. P., Comparison of snow reflectance measured during ARCTAS campaign with model results using SCIATRAN RTM, (AC)³ conference, 12 - 14 November, 2018, Bremerhaven, Germany.
- **Jafariserajehlou, S.**, Mei, L., Vountas, M., Rozanov, V. V., Burrows, J. P., Detection of biomass burning plume for aerosol remote sensing: potential application to the Arctic regions, Joint Assembly 2017 (IAPSO-IAMAS-IAGA assembly hosted by IUGG), Cape town, South Africa, 27 August - 1 September, 2017.
- Mei, L., **Jafariserajehlou, S.**, Rozanov, V., Lelli, L., Vountas, M., Burrows, J., Recent progress of aerosol remote sensing over the Arctic in the AC3 project, AeroCom2017, 9 - 13 October, 2017, Finland.
- Mei, L., Rozanov, V., **Jafariserajehlou, S.**, Vountas, M., Burrows, J. P., Arctic air pollution seen from space, PACES 2017, 27 - 29, June 2017, Victoria, Canada.
- **Jafariserajehlou, S.**, Mei, L., Vountas, M., Rozanov, V. V., Burrows, J. P., Cloud masking for aerosol retrieval over the Arctic using AATSR time-series measurements, poster presentation at (AC)³ conference, March 2016.

Contents

1	Introduction	20
1.1	Aerosol remote sensing and the challenge over the Arctic	23
1.2	Aims of this work	26
1.3	Thesis outline	27
2	Scientific background	29
2.1	Atmosphere	29
2.1.1	Vertical structure of atmosphere	30
2.2	Atmospheric general circulation	33
2.3	Environmental issues relevant to the atmosphere	35
2.3.1	Global warming and Arctic amplification	35
2.4	Atmospheric aerosol	41
2.4.1	Aerosols in the Arctic	42
2.4.2	Physical and chemical properties	44
2.4.3	Aerosol radiative properties	50
2.4.4	Climatic effects of Aerosol	56
2.5	Theoretical background for space-based aerosol retrieval	60
2.5.1	Radiative transfer in the atmosphere	60
2.5.2	Reflectance in the atmosphere-surface system	63
3	Data	69
3.1	Satellite data	69
3.1.1	Advanced Along-Track Scanning Radiometer	69
3.1.2	Sea and Land Surface Temperature Radiometer	72
3.1.3	Moderate Resolution Imaging Spectroradiometer	74
3.2	Airborne data	74
3.2.1	Cloud absorption radiometer	74
3.3	Ground-based measurements	76
3.3.1	Synoptic surface measurements	76
3.3.2	Aerosol Robotic Network	77
4	Improved Cloud detection for Aerosol Optical Thickness retrieval	80
4.1	Overview of cloud detection methods	80
4.2	AATSR standard cloud product	81
4.3	Cloud detection over the Arctic	82
4.4	Developing a new cloud detection algorithm	83
4.4.1	Theoretical background	84
4.4.2	Methodology	88
4.4.3	Results and comparison to space-borne cloud products	92
4.4.4	Comparison to ground-based measurements	98
4.4.5	Supporting ACLOUD/PASCAL campaign with ASCIA	101

5	Improved assessment of BRF and snow surface reflectance for Aerosol Optical Thickness retrieval	106
5.1	Introduction	106
5.2	Theoretical background	108
5.3	Reflectance modelling	110
5.3.1	Snow physical parameters (shape and size)	112
5.3.2	Atmospheric effect	120
5.4	Comparison of results: CAR measurements vs. SCIATRAN modelling	122
6	Retrieval of Aerosol Optical Thickness in the Arctic using satellite measurements	128
6.1	Theoretical background	129
6.2	AOT retrieval algorithm: AEROSNOW	131
6.3	Look-up table calculation	133
6.3.1	Rayleigh scattering	134
6.3.2	Aerosol scattering and absorption	134
6.4	Application limits of the algorithm	135
6.5	Brief highlights of anomaly fixes and improvements in the updated version of AEROSNOW	136
6.6	Processing of a long-term AOT data record	143
6.7	Validation vs. AERONET	145
7	Summary and outlook	153
8	Bibliography	158

List of Figures

1	Mean temperatures (unit Kelvins) shown per location and year as variations from 1951–1980 mean temperatures (Wendisch et al., 2017). The data are provided by the NASA Goddard Institute for Space Studies.	20
2	Time series of monthly averaged particulate sulphate and nitrate concentrations for (a) Barrow, Alaska (Quinn et al., 2007), Data made available for Barrow by NOAA PMEL (http://saga.pmel.noaa.gov/data/).	21
3	Aerosol and cloud above the Cryosphere and ocean: the MODIS true color RGB image, smoke over Svalbard, 11 th July 2002, adapted from the NASA website (https://visibleearth.nasa.gov/images/).	22
4	Arctic maps for the seasonal average of level-3 AOT at 0.55 μm derived from MODIS/Aqua (upper panel) and MODIS/Terra data (bottom panel) recorded from 2005 to 2012 during the spring (left column) and summer (right column) periods (Tomasi et al., 2015).	25
5	The temperature variation in the atmosphere as a function of altitude (http://unilaggeography2012.blogspot.com/p/gry-101-introduction-to-physical.html).	31
6	The pressure variation in the atmosphere as a function of altitude (http://www.atmo.arizona.edu/)	32
7	Schematic representation of the atmospheric circulation patterns (Wallace and Hobbs, 2006).	34
8	Upper panel: Land-ocean temperature anomaly, 1880 to present, with base period 1951-1980. The solid black line is the global annual mean and the solid red line is the five-year LOWESS smooth (locally weighted scatterplot smoothing). The gray shading represents the total (LSAT and SST) annual uncertainty at a 95% confidence interval. Bottom panel shows how much warmer each month is than the annual global mean (http://data.giss.nasa.gov/gistemp).	36
9	Upper panel: Linear trends in annual mean surface air temperature for the period 1960–2019, based on the National Aeronautics and Space Administration Goddard Institute for Space Sciences (NASA GISS) temperature analysis (http://data.giss.nasa.gov/gistemp). Bottom panel: Linear trends over the 60-year analysis period averaged by latitude.	37
10	Anomalies in winter (a, December–February), spring (b, March–May), summer (c, June–August) and autumn (d, October–November) temperature for the 1960–2019 computed with respect to the reference period 1960–2019. Results are based on the NASA GISS temperature analysis, (http://data.giss.nasa.gov/gistemp).	38

11	Warming contributions of individual feedback mechanisms, a) Arctic versus tropical warming from a TOA perspective, b) Arctic winter versus summer warming, c) Arctic versus tropical warming from a surface perspective. For a, b and c, feedbacks above the 1:1 line contribute to Arctic amplification, whereas feedbacks below the line oppose Arctic amplification. Grey is the residual error of the decomposition. ‘Ocean’ includes the effect of ocean transport changes and ocean heat uptake (Pithan and Mauritsen, 2014).	40
12	Desert dust, volatile organic compounds from vegetation, smoke from forest fires, and volcanic ash (credit (left to right): Western Sahara Project, Jonathan Jessup, Vox, and Ludie Cochrane).	41
13	An aerosol model shows swirls of sea salt caught in cyclones (blue), black and organic carbon particles emitted by fires (green), sulfate (white) and desert dust (red). Credit: NASA Global modeling and assimilation office.	42
14	Scanning electron microscope images of aerosols: volcanic ash, pollen, sea salt, and soot. Micrographs courtesy USGS, UMBC (Chere Petty), and Arizona State University (Peter Buseck).	44
15	Typical bimodal atmospheric aerosol volume size distribution (Covert et al., 1980).	46
16	Monthly median number size distributions (20–500 nm), measured with a scanning mobility particle sizer at Alert, Nunavut, for 2011–2013 and with a differential mobility particle sizer at Zeppelin, Svalbard, for 2011–2013. Error bars are 20th–80th percentiles (Croft et al., 2016).	46
17	Ground-level particulate matter sampled at Ny-Ålesund for different seasonal periods March-May in Spring 2011-2015 and June-September in summer 2011-2015: (a) and (b) PM10 in spring and summer respectively, (c) and (d) sub-micrometric particles in spring and summer, (e) and (f) super micrometric (1-10 micrometer) particles in spring and summer. Colors indicate different constituents: sea-salt, non sea-salt sulfate and nitrate, methanesulfonic acid (MSA), mineral dust, black carbon (BC) and organic carbon (OC) (Udisti et al., 2020).	49
18	Sub-micrometric particles samples in the Central Arctic Ocean during the ASCOS experiment from 5 th August to 8 th September 2008, (a) to (f) panels show measurements at different stations. Colors indicate different constituents: sea-salt, non sea-salt sulfate and nitrate, methanesulfonic acid (MSA), mineral dust, black carbon (BC) and organic matter (OM) (Udisti et al., 2020).	50
19	Size parameter depending on the particle radius and wavelength showing different scattering regimes (Wallace and Hobbs, 2006).	51
20	Rayleigh phase function for aerosol particle with different radii (Sinnhuber, 2015).	52
21	Mie phase function for aerosol particle with different radii (Sinnhuber, 2015).	54

22	The extinction, scattering and absorption cross section of aerosol particles per unit volume as a function of size, calculated from Mie theory (Covert et al., 1980).	57
23	The relationship between absorption-to-backscattering ratio (a/b) and the critical surface albedo α (lower scale), and between a/b and the imaginary index of refraction (n_{im} , upper scale) for a given radius of particle (dashed line). Calculations are for real part of index of refraction equal to 1.5, and for a solar zenith angle of 65° (an average value taking the globe as a whole). Shaded area indicates locus of some critical values when infrared radiation was taken into account along with solar radiation (Kellogg, 1980).	58
24	Schematic illustration of aerosol radiative effects on climate including the different direct and indirect effects (Haywood and Boucher, 2000).	60
25	Successive orders of radiation interactions in the surface and atmosphere system, Tanre et al. (1979).	63
26	Sun-Earth-satellite remote sensing geometry. This schematic of observation geometry is from Kokhanovsky and de Leeuw (2009).	64
27	Successive orders of radiation interactions in the surface-atmosphere system (Tanre et al., 1979).	66
28	Typical AATSR viewing geometries (image credit: ESA).	70
29	Upper left: the RGB image of AATSR over Svalbard, 10 th May 2006, upper right: 1.6 μm reflectance, lower left: 3.7 μm reflectance, lower right: 11 μm brightness temperature.	71
30	Upper left: the RGB image of SLSTR over Svalbard, 18 th April 2017, upper right: 1.37 μm reflectance, lower left: 1.6 μm reflectance, lower right: 3.7 μm reflectance.	73
31	SYNOP network coverage over the Arctic, the dark blue points indicate the location of SYNOP stations.	76
32	AERONET global network coverage, credit: NASA.	77
33	The schematic flowchart of ASCIA.	89
34	Examples of the results of ASCIA on AATSR observations, first row: over the scenes over Greenland, between (75°N , 48°W), (75°N , 75°W), (81°N , 48°W), (81°N , 75°W), taken on 18 th May 2008 and second row: over Svalbard, within (75°N , 4°E), (75°N , 32°E), (81°N , 4°E), (81°N , 32°E) on 1 st March 2008. Left panels: RGB false-colour images (using 0.67, 0.87 and 0.55 μm channels), middle panels: cloud detection at block level ($25 \times 25 \text{ km}^2$), right panels: cloud detection at scene level ($1 \times 1 \text{ km}^2$).	91
35	(a) The RGB false-colour image (using 0.67, 0.87 and 0.55 μm channels) of AATSR over northern Greenland, 24 th May 2008; (b) nadir cloud flag from the AATSR L2 product; (c) cloud detection based on the spectral shape of clear snow; (d) cloud detection of ASCIA and (e) the difference between ISTO and ASCIA.	94

36	(a) The RGB false-colour image (using 0.67, 0.87 and 0.55 μm channels) of AATSR over Svalbard, 10 th May 2006; (b) nadir cloud flag from the AATSR L2 product, (c) cloud detection based on the spectral shape of clear snow, (d) cloud detection of ASCIA and (e) the difference between ISTO and ASCIA.	94
37	(a) The RGB false-colour image (using 0.67, 0.87 and 0.55 μm channels) of AATSR over Svalbard, 18 th March 2008; (b) nadir cloud flag from the AATSR L2 product; (c) cloud detection based on the spectral shape of clear snow; (d) cloud detection of ASCIA and (e) the difference between ISTO and ASCIA.	95
38	(a) The RGB false-colour image (using 0.67, 0.87 and 0.55 μm channels) of AATSR over Svalbard, 6 th July 2008; (b) nadir cloud flag from the AATSR L2 product; (c) cloud detection based on the spectral shape of clear snow; (d) cloud detection of ASCIA and (e) the difference between ISTO and ASCIA.	95
39	(a) The RGB false-colour image (using 0.67, 0.87 and 0.55 μm channels) of AATSR over Svalbard, 3 rd May 2006; (b) nadir cloud flag from the AATSR L2 product; (c) cloud detection based on the spectral shape of clear snow; (d) cloud detection of ASCIA and (e) the difference between ISTO and ASCIA.	96
40	(a) The RGB false-colour image (using 0.67, 0.87 and 0.55 μm channels) of AATSR over Svalbard, 14 th July 2008, 16 h 40 min 45 s, (b) The MODIS cloud mask algorithm retrieved data: 1 is cloudy, 2 is probably cloudy, 3 is probably clear, 4 is clear (red rectangle shows the coverage of AATSR) for 16 h 25 min, (c) the results for the cloud detection of ASCIA.	96
41	(a) The RGB false-colour image (using 0.67, 0.87 and 0.55 μm channels) of AATSR over Greenland, 18 th May 2008, 23 h 13 min 38 s, (b) The MODIS cloud mask: 1 is cloudy, 2 is probably cloudy, 3 is probably clear, 4 is clear (red rectangle shows the coverage of AATSR) for 23 h 5 min, (c) cloud detection of ASCIA.	97
42	(a) The RGB false-colour image (using 0.67, 0.87 and 0.55 μm channels) of SLSTR over Svalbard, 18 th April 2017, 10 h 15 min 6 s, (b) The MODIS cloud mask: 1 is cloudy, 2 is probably cloudy, 3 is probably clear, 4 is clear (red rectangle shows the coverage of AATSR) for 11 h 30 min, (c) cloud detection of ASCIA.	97
43	Density plot of occurrences of the CFC by ASCIA as a function of SYNOP.	99
44	Histogram of CFC differences (blue is ASCIA minus SYNOP; red is ESA cloud product minus SYNOP).	100
45	CFC in percentage by ASCIA (red), SYNOP (blue) and ESA Cloud Product (green) for 100 scenarios in March, May and July 2008 over Svalbard and Greenland. Light-blue error bars show the range of percentage values for each okta from SYNOP measurements.	100

46	Multiplatform measurement setup during the ACLOUD/PASCAL campaigns, for details see Wendisch et al. (2019).	101
47	Flight paths (light blue for Polar 5 aircraft, pink for Polar 6 aircraft) and R/V Polarstern ship track (black and white line) during the ACLOUD/PASCAL campaigns. For details see Wendisch et al. (2019).	102
48	Cloud fraction calculated by ASCIA using SLSTR measurements over Svalbard, on 23 rd May 2017 for 6 orbits with corresponding measurements from 1.6 μm channel. Cloud fraction is derived for the area of the airborne operation (77.5° – 80°N , 0° – 10.5°E and 80° – 82.5°N , 0° – 20°E), excluding the Svalbard archipelago.	103
49	Cloud fraction calculated by ASCIA using SLSTR measurements over Svalbard, on 10 th June 2017 for 6 orbits with corresponding measurements from 1.6 μm channel. Cloud fraction is derived for the area of the airborne operation (77.5° – 80°N , 0° – 10.5°E and 80° – 82.5°N , 0° – 20°E), excluding the Svalbard archipelago.	103
50	Time series of daily means of cloud fraction of different cloud types as derived from MODIS cloud product (Collection 6.1). The daily mean values of the top height of low-level clouds and cloud fraction were derived for the area of the airborne operation (77.5° – 80°N , 0° – 10.5°E and 80° – 82.5°N , 0° – 20°E), excluding the Svalbard archipelago. Daily mean cloud fraction, derived from ASCIA using the SLSTR data, is shown by triangles. For details see Wendisch et al. (2019)	104
51	Similar to Fig. 50 but showing minimum and maximum cloud fraction per day.	104
52	Angular distribution of a reflectance in the snow–atmosphere system derived from CAR measurements on 7 th April 2008 at Elson Lagoon (71.3°N , 156.4°W), showing reflectance in the spectral range between 0.339 μm and 1.032 μm , and three flight altitudes of 206, 647, and 1700 m. The principal plane is the horizontal line ($\Phi = 0^{\circ}$ and $\Phi = 180^{\circ}$), and the viewing zenith angle is shown as the radius of the polar plots from 0° (nadir) to 70° . The solar zenith angle is 70.23, 69.11, and 67.78° for flight altitudes of 206, 647, and 1700 m, respectively.	107
53	Reflectance factor in the snow–atmosphere system derived from CAR measurements in principal plane (left) ($\Phi = 0^{\circ}$ and $\Phi = 180^{\circ}$) and cross plane (right) ($\Phi = 90^{\circ}$ and $\Phi = 270^{\circ}$), on 15 th April 2008 at Elson Lagoon (71.3°N , 156.4°W), showing reflectance at the spectral range between 0.67 μm and 1.649 μm , flight altitude 180m. The shadow of aircraft can be seen as a reduction of reflectance in the left panel.	108
54	The change in reflectance factor in the principal plane ($\Phi = 0^{\circ}$ and $\Phi = 180^{\circ}$) with the size and shape of ice crystals at the wavelength of 1.649 μm . The left column of the legend in each panel shows the maximum length of the ice crystal, and the right column is its equivalent effective radius.	113

55	Comparison of measured and simulated reflectance factors. Measurements were performed by the CAR instrument over old snow at 647 m flight altitude on 7 th April 2008 at 1.649 μm . The uncertainty in CAR measurements is indicated by the envelope (shading). SCI-ATRAN simulations in the principal and cross plane given by the dashed-dotted and dotted lines, respectively, and by different colors (green, blue, and red) present smooth, moderately roughened, and severely roughened crystal surfaces. Positive and negative VZA (viewing zenith angles) correspond to azimuthal angles $\Phi = 0^\circ$ and $\Phi = 180^\circ$ for the principal plane and $\Phi = 90^\circ$ and $\Phi = 270^\circ$ for the perpendicular plane, respectively.	116
56	The same as Fig. 55 but the measurements by the CAR instrument were performed on 15 th April at 181 m flight altitude over fresh snow.	118
57	Comparison of snow grain size retrieval and best fit of reflectance at three wavelengths of 0.677, 0.873, and 1.649 μm . Old snow case. Effective radius is retrieved at 1.649 μm	119
58	Comparison of snow grain size retrieval and best fit of reflectance at three wavelengths of 0.677, 0.873, and 1.649 μm . for fresh snow case. Effective radius is retrieved at 1.649 μm	120
59	Measured and simulated reflectance factor at (0.67 μm) versus the viewing zenith angle (VZA) in the principal plane ($\Phi=0^\circ$ and 180°) at three different flight altitudes. Panels represent results at 206, 647, and 1700 m flight altitudes, respectively. The green lines indicate simulated reflectance assuming Rayleigh scattering (case i). The blue line shows reflectance for case ii (as in case i, including absorption of O_3 and NO_2). The orange lines show the reflectance for case iii (as in case ii but adding aerosol with an aerosol optical thickness (AOT) of 0.11 for three types of aerosol, namely (i) weakly absorbing, (ii) moderately absorbing, and (iii) strongly absorbing)	121
60	Left column: the reflectance factor at three wavelengths, namely 0.677, 0.873, and 1.649 μm , from the CAR measurements acquired on 7 th April 2008 at Barrow, Alaska, at an altitude of 647 m. middle column: the absolute difference between reflectance of simulation(RSCIATRAN) and that of measurement (RCAR): (RSCIATRAN – RCAR); right column depicts the relative difference in percent (%).	123
61	The same as Fig. 60 but the measurements by the CAR instrument were performed on 15 th April 2008 at 181 m flight altitude over fresh snow.	124
62	The scatterplot with corresponding Pearson correlation coefficient of reflectance factor measured by CAR and simulated by SCIATRAN. Left column: the results for old snow and right column: fresh snow. Here the color bar represents the number density of the pixels.	125
63	Measured aerosol phase function of Arctic haze, on 23 rd March 2000, and Spitsbergen, Ny Ålesund, Svalbard (Istomina, 2012).	135

64	Haze event, 3 rd May 2006, Svalbard, left panel: output of AEROSNOW with the incorrect formulation of the scattering angle, right panel: the output of AEROSNOW after solving the issue.	137
65	Time series of AOT maps before and during the Haze event, May 2006, Svalbard.	138
66	The impact of creating artificial glint conditions using the AEROSNOW algorithm, shown for May 2006 over the Arctic circle, upper panel: the average AOT for the whole of May, bottom panel: one selected day to highlight the stripe pattern in the AOT records for all of orbits.	140
67	Zoom into one region where the pattern could be detected to study all parameters related to AOT on the sample pixels: reflectance, AOT and corresponding VZA, SZA and RAA.	141
68	The impact of solving the artificial glint condition, for one day selected in May 2006, over the Arctic circle.	142
69	The effect of improving cloud detection in AEROSNOW AOT retrieval algorithm for two days. Left column: AEROSNOW with original cloud detection method (see details in Istomina et al. (2010)). Right column: AOT after improving cloud detection in AEROSNOW algorithm using ASCIA (see Sect. 4). Upper row: 29 th March 2006, bottom panel: During Haze event, 3 rd May 2006, Svalbard.	143
70	Monthly mean AOT over the Arctic circle in 2006, reprocessed using the new version of AEROSNOW algorithm.	144
71	AERONET stations in the Arctic region.	145
72	Top panel: Hornsund station, the red star shows the location of station at Svalbard, bottom panel: Monthly mean AOT in 2006-2011. AATSR data are shown with blue lines and symbols, AERONET measurements are shown in orange.	146
73	Monthly mean AOT at Kangerlussuaq station, Greenland, 2008-2011. AATSR data are shown with blue lines and symbols, AERONET measurements are shown in orange.	147
74	Daily AOT at Hornsund station, Svalbard, 2006-2011. AATSR data are shown with blue line and symbols, AERONET measurements are shown in orange.	148
75	Daily AOT at Kangerlussuaq station, Greenland, 2008-2011. AATSR data are shown with blue line and symbols, AERONET measurements are shown in orange.	148
76	Daily AOT at Hornsund station, Svalbard, 2008-2009. AATSR data are shown with blue line and symbols, AERONET measurements are shown in orange.	149
77	Daily AOT at Kangerlussuaq station, Greenland, 2008-2011. AATSR data are shown with blue line and symbols, AERONET measurements are shown in orange.	149

78	Daily AOT at Hornsund station, Svalbard, 2006. AATSR data are shown with blue line and symbols, AERONET measurements are shown in orange.	150
79	Daily AOT at OPAL station, Ellesmere Island, Nunavut, Canada, 2008. AATSR data are shown with blue line and symbols, AERONET measurements are shown in orange, upper panel shows daily AOT, bottom panel: zoom in upper panel, the green ellipse highlights the 4 different AOT value in one day.	151

List of Tables

1	AATSR spectral channels (Huot et al., 2001).	70
2	SLSTR radiometric bands (https://sentinels.copernicus.eu/web/sentinel/user-guides/).	72
3	Spectral specification of the CAR instrument (https://airbornescience.nasa.gov/instrument/CAR).	75
4	Calculation of cloudiness in percentage for corresponding okta value (Boers et al., 2010).	77
5	Simulated and observed reflectance values at $3.7 \mu\text{m}$ (Allen et al., 1990a).	87
6	Land classification criteria for cloud-free scenes.	91
7	Retrieval of the physical characteristics of ice crystals with different shapes in the case of most roughened habits. Numbers in italics indicate minimum root mean square error (RMSE).	117
8	Available AERONET stations and corresponding coordinates and temporal coverage.	146

1 Introduction

Over the past 25 years, scientists have observed that the average rate of temperature increase in the Arctic is about twice that of the global average temperature (Fig. 1). The strong trends in warming accompanied by the change in other climate variables such as dramatic loss of sea ice and decrease of snow cover over the Arctic have received strong attention from the climate change research community. A number of studies using global and regional observations and climate models have confirmed this phenomenon called Arctic Amplification (AA) and provided evidence that its impact extends beyond the Arctic, e.g. a large number of extreme heat and rainfall events (Wendisch et al., 2017; Cohen et al., 2014; Kim et al., 2017; Cohen et al., 2020).

The attribution of the origins of this phenomenon is controversially discussed and

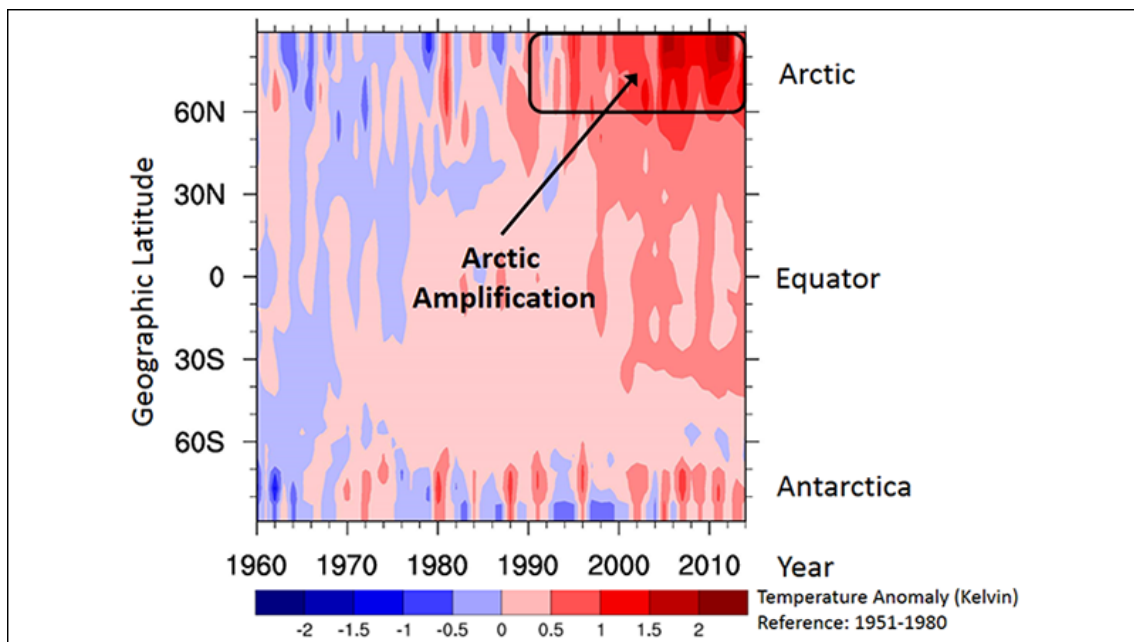


Figure 1: Mean temperatures (unit Kelvins) shown per location and year as variations from 1951–1980 mean temperatures (Wendisch et al., 2017). The data are provided by the NASA Goddard Institute for Space Studies.

has emerged as a major debate among scientists (Serreze and Barry, 2011; Pithan and Mauritsen, 2014). Several processes are mentioned to be involved in AA including local radiative effects from increased greenhouse gas forcing, changes in the snow and ice-albedo feedback induced by a diminishing cryosphere, aerosol concentration changes and deposits of black carbon on snow and ice surfaces, changes in Arctic cloud cover and water vapour content, and a relatively smaller increase in emissions of longwave radiation to space in the Arctic compared with the tropics for the same temperature (Cohen et al., 2014, and references therein). We need to identify, investigate, and evaluate the key processes involved in AA to improve our understanding of the major feedback mechanisms and quantify the relative importance of these mechanisms (Wendisch et al., 2017). The focus of this work is to study aerosol as one of the known key parameters in AA.

In general, the spatial and temporal variation of microphysical, chemical and optical properties of aerosol as well as their concentration introduce direct radiative forcing effects on the surface-atmosphere system. Additionally, the indirect impact of aerosols on the climate is connected to the complex of aerosol-cloud interactions, which results in a change in cloud microphysical, radiative properties, amount and lifetime. Scattering and absorption of aerosols are enhanced if the surface is highly reflecting due to multiple scattering of solar radiation between the surface and aerosol particles, which leads to warming at the surface. For this reason, the Arctic is more sensitive to changes in aerosol properties compared to lower latitudes (Randles et al., 2004; Quinn et al., 2007, and references therein). To better understand and quantify the impact of aerosol and its changes on AA, we need to extend our knowledge about the source of Arctic aerosol, their spatial and temporal distribution and optical, chemical and microphysical properties. One of the most famous aerosol events in the polar regions is the regularly occurring "Arctic haze", which is a remarkable increase in concentrations of several key particulate pollutants, e.g. sulphate (Mitchell, 1956; Shaw, 1995; Quinn et al., 2007).

The long range transport of pollutants from mid-latitudes contributes to the formation of haze in late winter and early spring, leaving the seasonal mark of haze

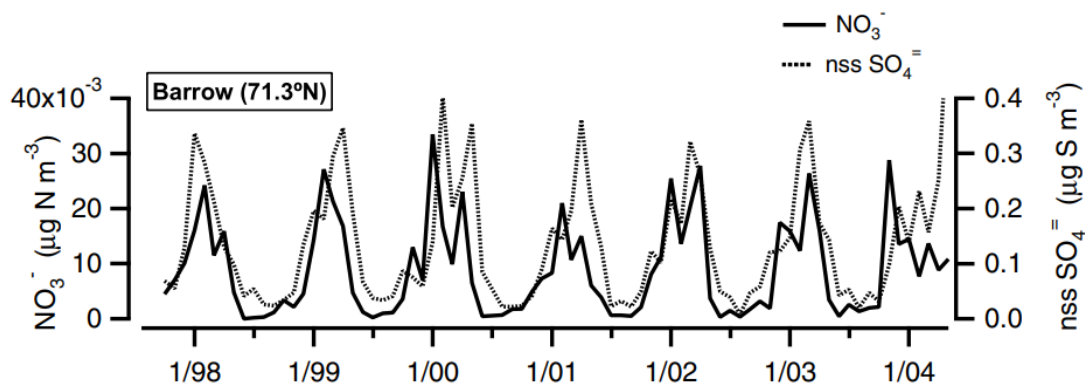


Figure 2: Time series of monthly averaged particulate sulphate and nitrate concentrations for (a) Barrow, Alaska (Quinn et al., 2007), Data made available for Barrow by NOAA PMEL (<http://saga.pmel.noaa.gov/data/>).

in time series of measurements (see Fig. 2). Several studies have been conducted across decades to determine the chemical and physical fingerprints of haze, besides its origin and radiative fluxes. Despite a large number of studies, the severe conditions and remoteness of the polar region significantly limit the availability of ground-based sun photometers, e.g. AErosol ROBotic NETwork (AERONET), ship-borne (e.g. MAN or campaign measurements) and airborne (sun photometer) data. This limitation prevents us from having a big picture of Arctic aerosol that meets the necessary temporal and spatial resolution and coverage for climate change studies. For this reason, the analysis of the growing number of long-term records of the data products (e.g. the amount of trace gases, aerosol, and cloud parameters) retrieved from passive and active satellite observations provides potentially invaluable information for identifying and quantifying the evolution and consequences of AA and the role of aerosol in this phenomenon (Wendisch et al., 2017). Retrieving aerosol over highly reflecting snow/ice surface using space-borne data is challenging and state-of-the-art algorithms are not optimised for this purpose. Figure 3 is one example of aerosol load (smoke) in the Arctic region and it displays the challenge of aerosol remote sensing in the Arctic region.

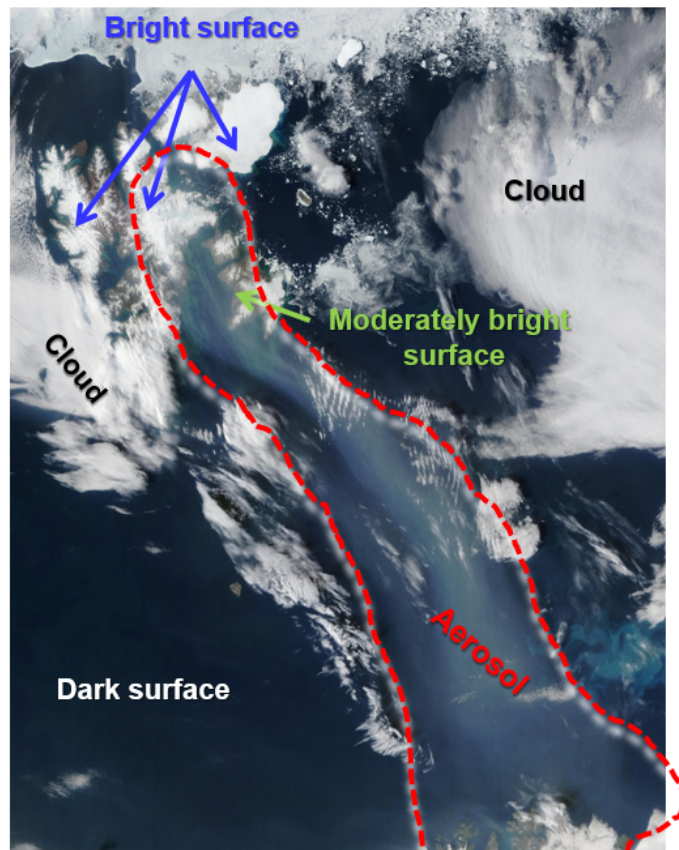


Figure 3: Aerosol and cloud above the Cryosphere and ocean: the MODIS true color RGB image, smoke over Svalbard, 11th July 2002, adapted from the NASA website (<https://visibleearth.nasa.gov/images/>).

The greyish smoke highlighted with a dashed red line originates from wildfires in

Saskatchewan, Canada, and has crossed the Atlantic Ocean, passing over Svalbard (top centre) and arriving over the shores of Norway (bottom centre) on 11th July 2002, which was out of the classical haze period. This case shows the major obstacle in retrieving aerosol over snow/ice in Polar Regions, namely a lack of adequate contrast between aerosol, cloud and underlying surface, a criterion based on which most aerosol retrieval algorithms are designed.

1.1 Aerosol remote sensing and the challenge over the Arctic

Satellite remote sensing has been used for the retrieval of aerosol properties since 40 years ago (Kokhanovsky and de Leeuw, 2009; Lee et al., 2009). Many aerosol retrieval algorithms have been developed for use with various satellite measurements, exploiting the unique feature of the sensors such as having single or multiple wavelengths, nadir view and multi-angle views, with or without polarisation, and being low Earth or with geostationary orbits. Some of the widely-known and commonly-used retrieval algorithms and relevant publications are as follows:

- Geostationary satellite algorithms (Knapp et al., 2005);
- Single-channel algorithm for Advanced Very High Resolution Radiometer (AVHRR) (Rao et al., 1989; Stowe, 1991);
- Dual-Channel AVHRR algorithm (Stowe et al., 1997; Mishchenko et al., 1999b);
- Multi-channel algorithms for Sea-viewing Wide Field-of-view Sensor (SeaWiFS) (von Hoyningen-Huene et al., 2003);
- Multi-channel algorithms for Moderate Resolution Imaging Spectroradiometer (MODIS) (Kaufman et al., 1997; Tanre et al., 1997, 1999; Remer et al., 2005b; Levy et al., 2007b; Remer et al., 2006; Hsu et al., 2004);
- Multi-channel algorithms for MEdium Resolution Imaging Spectrometer (MERIS) (von Hoyningen-Huene et al., 2006);
- Multi-angle, multi-channel algorithm for Multi-angle Imaging SpectroRadiometer (MISR) (Martonchik and Diner, 1992; Martonchik and Gordon, 1998);
- Polarization based algorithms for POLARization and Directionality of the Earth Reflectance (POLDER) (Herman et al., 1997; Deuze et al., 1999; Dubovik et al., 2011; Vountas et al., 2020); and
- Algorithms for Advanced Along-Track Scanning Radiometer (AATSR) (Xue et al., 2009; Sayer et al., 2010; North, 2002; Veefkind and de Leeuw, 1998; Veefkind et al., 1999).

Despite the successful performance of the mentioned algorithms, there remains a large gap over the Arctic on snow/ice-covered surface especially over land (see Fig. 4). Although, algorithms differ based on characteristics of the relevant sensor, there are generic processes and common steps applied in many of them. Many satellite instruments measure the top-of-atmosphere (TOA) reflectance in a specific geometry

that varies with sensors and the time of the day/year. The measured reflectance can be used to retrieve several surface and atmospheric parameters, all of which interact with electromagnetic radiation scattered and/or absorbed by the atmospheric constituents and the surface. To retrieve aerosol properties, we need to decompose the elements mixed in the measured signal by satellite: atmospheric gases, clouds, aerosols, and the surface (Lee et al., 2009).

To obtain aerosol properties from satellite measurements based on inverse modelling, there are three steps common in many retrieval algorithms:

- Cloud detection: Clouds are highly reflective and they overwhelm the TOA reflectance in the observed scene by satellite. The first step is to identify and mask cloudy scenes out;
- Decoupling surface reflection from the atmospheric path in the measured TOA signal in cloud-free scenes;
- Accounting for molecular scattering due to atmospheric molecules and gas absorption in the atmospheric path. The Rayleigh path radiance can be determined using the spectral dependence of the well-known Rayleigh optical depth (ROD) and the Rayleigh phase function.

The first two steps can be implemented in different ways. Depending on the underlying surface type, reflectance range and wavelengths used, we may face unique challenges. For example, many cloud detection algorithms over land and ocean exploit the coldness and brightness tests in visible or thermal channels with the assumption that clouds are colder and brighter than the underlying surface. However, this assumption does not necessarily hold over snow/ice surface. This means that the common threshold-based methods for cloud detection are often inadequate over snow/ice surface (Rossow and Garder, 1993; Curry et al., 1996).

Over ocean surfaces, AOT retrieval can be achieved with comparatively simple methods because the surface is dark in the visible and near IR wavelengths range and therefore TOA reflectance is mostly determined by scattering in the atmosphere (in the absence of gaseous absorption). Over land, aerosol retrieval is more complicated compared to the ocean case due to the relatively strong contribution of surface reflectance to TOA signal, directional properties of surface and larger inhomogeneities. The level of contribution of the surface reflectance to TOA signal depends on the surface type and selected wavelength. For example, the contamination caused by a dark surface covered with vegetation in TOA reflectance at a visible channel is weak in comparison to that of a bright desert surface in the same spectral range. Using the wavelengths in UV or near UV can solve this issue for bright desert surface because most of the surfaces appear dark in these wavelengths. The retrieval routine becomes more complicated and difficult if the underlying surface is covered with snow/ice, because surface reflectance dominates the aerosol signal in TOA reflectance. Additionally, snow surface has specific directional signatures, e.g. a strong increase with viewing angle, which makes the task of aerosol retrieval in polar regions difficult.

In general, there are several ways to account for surface reflectance: i) using an

external surface database, ii) simultaneous retrieval of surface and atmospheric parameters, and iii) removal of surface in the algorithm. The latter solution has been used with sensors using multiple viewing (e.g. multi-angle imaging spectroradiometer (MISR)) or dual view (e.g. AATSR) capabilities, since, observing the target from several different viewing angles enables gathering additional information about the target. This method has been initially proposed by Leroy et al. (1997).

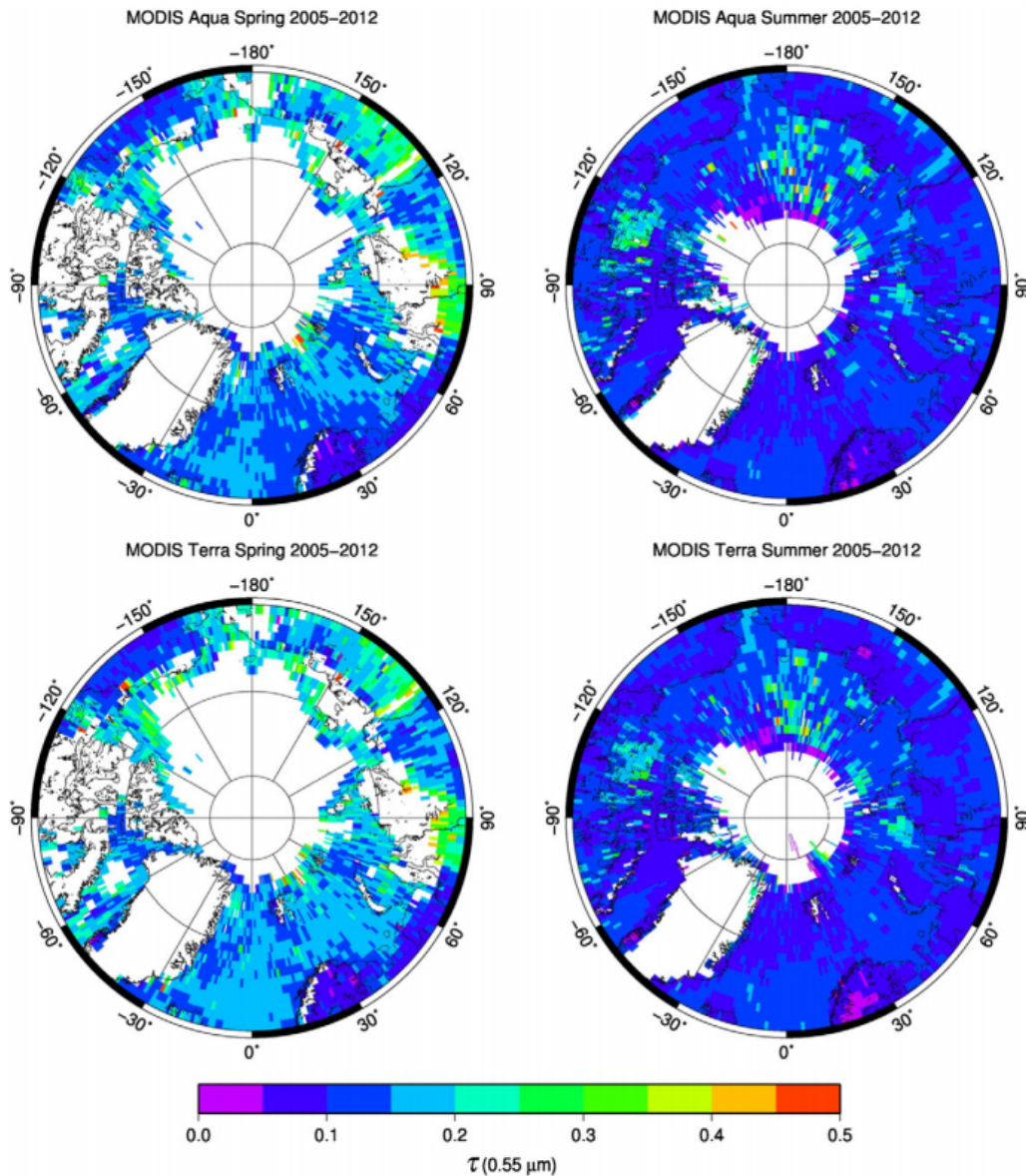


Figure 4: Arctic maps for the seasonal average of level-3 AOT at $0.55 \mu\text{m}$ derived from MODIS/Aqua (upper panel) and MODIS/Terra data (bottom panel) recorded from 2005 to 2012 during the spring (left column) and summer (right column) periods (Tomasi et al., 2015).

Istomina (2012) applied the same concept of dual-viewing to retrieve AOT over

snow/ice-covered surface. In this work, we apply the same method to retrieve AOT in the Arctic region. Despite the promising performance reported in Istomina (2012), we have attempted to address several technical and scientific issues in this work. In addition, the mentioned major obstacles for the retrieval of aerosol over snow highlight the importance of studying the prerequisites to better address unresolved issues. For this reason, this work starts with prerequisites including cloud identification and surface properties. Using the outcome of these two studies, the existing retrieval algorithm has been improved. The new version of the aerosol retrieval algorithm is applied on the full data set delivered by AATSR in 2002 to 2012 to create a long-term data record of AOT.

The outcome of this research will also be used for the investigations of the trans-regional ArctiC Amplification: Climate relevant Atmospheric and surfaCe processes and feedback mechanisms (AC)³ project (Wendisch et al., 2017). This project aims to identify and quantify the different parameters involved in the rapidly changing climate in the Arctic. In this respect, the analysis of this study will be used to improve the assumptions made for snow/ice surface, cloud and aerosol in different studies above polar regions.

1.2 Aims of this work

The main scientific objectives of this work are as follows:

- to study the prerequisites for aerosol retrieval in the Arctic, i.e. cloud detection and surface properties;
- to improve the previously-developed aerosol retrieval algorithm using the outcome of studying the prerequisites; and
- to apply the new improved version of aerosol retrieval algorithm on long-term data of AATSR and validate it.

To achieve the mentioned objectives, the following key points have been considered and implemented:

- developing a new cloud identification algorithm to overcome the known limitation and unresolved issues with respect to thin cloud detection in previously-developed cloud screening algorithms (Istomina et al., 2010);
- simulation of reflectance in a snow-atmosphere system and comparing the results with airborne measurement, evaluating the accuracy of SCIATRAN radiative transfer modelling in simulation of reflectance in a snow-atmosphere system;
- retrieval of snow surface properties (morphology) using airborne measurements;
- conducting a sensitivity study to indicate the importance of a priori information about the surface and atmosphere to achieve an accurate reflectance

simulation;

- identifying and solving some of the scientific and technical issues in the previously-developed aerosol retrieval algorithm;
- application of the improved version of aerosol retrieval algorithm to a long dataset of AATSR measurements from 2002 to 2012 and creating a long data record of AOT;
- validation of AOT retrieved using ground-based measurements and producing first long-term validation results.

1.3 Thesis outline

In the next chapter, the scientific background of this work is presented, which includes the necessary points about atmosphere, environmental issues related to the atmosphere, global warming and AA. In the second half of chapter 2, the necessary theoretical background about atmospheric aerosol, the radiative transfer and light scattering in the atmosphere is presented.

Chapter 3 is dedicated to introducing the data utilised in this study, including satellite data, airborne data and ground-based measurements.

Chapter 4 describes the study for the first prerequisite for aerosol retrieval, namely cloud detection. Here, the newly-developed cloud identification algorithm ASCIA for use with AATSR and SLSTR data is explained, as well as the theoretical background, methodology, cloud detection results, validation and verification of the cloud product.

In chapter 5, we present the study on the second prerequisites for aerosol retrieval, namely surface reflectance. We use SCIATRAN RTM to simulate reflectance in a snow-atmosphere system, conduct a sensitivity study, retrieve surface properties, and evaluate the accuracy of SCIATRAN in simulating the reflectance in a snow-atmosphere system.

In chapter 6, the AOT retrieval over snow in the visible spectral range using the AATSR dual viewing observations is described. Several scientific and technical issues are discussed and solved. The algorithm is applied on a long data set, and a long-term data record of AOT has been produced. The second half of chapter 6 is dedicated to the validation of the retrieved AOT.

The summary and conclusions are drawn in chapter 7, followed by an outlook and recommendations.

2 Scientific background

2.1 Atmosphere

The atmosphere of the Earth is the thin layers of gases expanded up to 120 km above the mean sea level, surrounding the Earth and retained by its gravitation (Burrows et al., 2011). The mixture of these gases is called "air".

Air is primarily composed of the gases N₂ (78.09%), O₂ (20.95%) and Ar (0.93%), CO₂ (0.04%), and small amounts of other gases called "trace gases" including greenhouse gases (e.g. CO₂, CH₄, N₂O, O₃) and gaseous pollutants with a relative short life-time (e.g. NO₂, SO₂, CO etc.). The composition of today's atmosphere is of little resemblance to the early form, which was rich in H₂ and He.

Approximately 4 billion years ago, after the dissipation of cosmic gases, the primordial atmosphere was produced. Several gaseous materials were liberated from solid Earth (volcanic eruptions, disruption and chemical reactions) and formed secondary constituents. With the increase of secondary substances e.g. CO₂, and H₂O, which absorb the infrared radiation emitted by the Earth's surface, atmosphere started playing a role in controlling the temperature. The Earth's temperature raised from -15° to 0°.

A turning point in the history of the dramatically evolving atmosphere was approximately 2.4 billion years ago, during the Great Oxidation Event (GOE). In this period, the biologically-produced molecular oxygen (O₂) started to accumulate in Earth's atmosphere. There is considerable documentation in the literature to show that the major part of the increase in the oxygen level during geological time was due to the photosynthetic activity of the biosphere (Mészáros, 1981).

To explain the state of an air parcel - a mixture of gases - in the atmosphere, we use the equation of state. In terrestrial conditions, many atmospheric gases behave as ideal gases and obey the gas laws. Therefore, using ideal gas laws we can see how the condition, state and volume of an air parcel depends on its temperature and pressure (Hobgood, 1993). For one mole of gas, we can write:

$$PV = R \cdot T \tag{2.1}$$

where P is pressure, V is the volume of the gas, T is temperature and R is the gas

constant. We can replace the volume of gas with its density ρ as follows:

$$P = \rho R \cdot T \quad (2.2)$$

where R is the specific gas constant. To obtain the similar equation for an air parcel, we can sum up the state equations written for each individual gas in air. The state equation is used in meteorology to determine one of the three variables of density, temperature and pressure when the other two are known. In this section, we briefly explain the vertical profile of temperature, pressure and density in the atmosphere to better understand the state of the air.

2.1.1 Vertical structure of atmosphere

2.1.1.1 Vertical profile of temperature

The dependency of atmosphere on temperature leads to dividing it into four regions either with positive or negative temperature gradients as shown in Fig. 5 (Hobgood, 1993):

i) Troposphere (Greek: well-mixed region) below ~ 12 to ~ 20 km:

As the lowest layer of Earth's atmosphere structure, the troposphere extends from the Earth's surface to an average height of about 12 km above sea level at mid-latitudes. This altitude varies from about 6-8 km at the geographic poles to 18 km in the tropics. In this layer, the temperature declines fairly with increasing altitude. The temperature lapse rate is closely linked to frequently occurring convection in this layer, in particular vertical movement of air. Although the value of lapse rate changes with time and geographical location, it is generally close to $6 \text{ }^\circ\text{C km}^{-1}$.

ii) Stratosphere (Greek: stratified region) ~ 20 to ~ 50 km:

The lapse rate of temperature ends at the tropopause, above which the stratosphere starts as the second-lowest layer of the Earth's atmosphere. The atmospheric behaviour is significantly different in the stratosphere compared with that of the troposphere. This layer extends from the top of the troposphere at roughly 12 km above the Earth's surface to the stratopause at an altitude of about 50 to 55 km. This layer of the Earth's atmosphere contains relatively high concentrations of ozone. In the absence of vertical motion, the stratosphere defines a layer in which temperatures changes non-adiabatically and rises with increasing altitude. The increase of temperature in this layer is caused by the absorption of ultraviolet (UV) radiation from the Sun by the ozone layer, which restricts turbulence and mixing. Although the temperature may be $-60 \text{ }^\circ\text{C}$ at the tropopause, the top of the stratosphere is much warmer, and may be close to 0° .

iii) Mesosphere (Greek: middle) ~ 50 to ~ 90 km:

The mesosphere is the third highest layer of the Earth's atmosphere, occupying the region above the stratosphere. It extends from the stratopause at an altitude of about 50 km to the mesopause at 80–85 km above sea level.

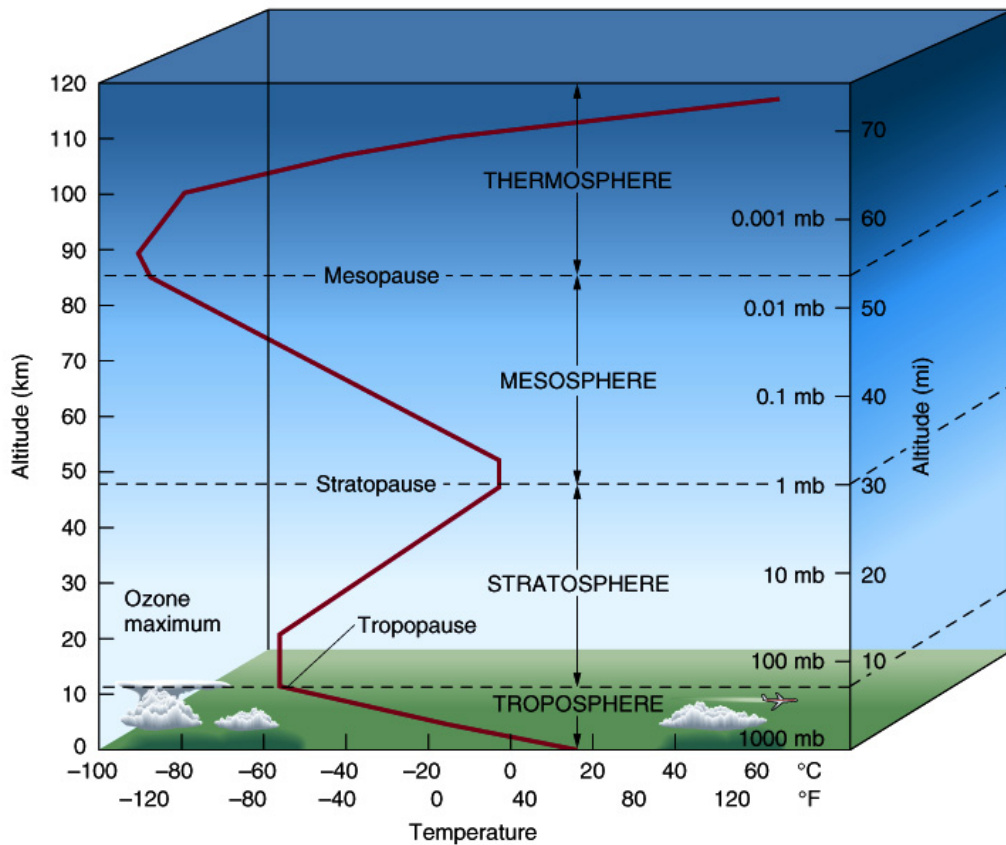


Figure 5: The temperature variation in the atmosphere as a function of altitude (<http://unilaggeography2012.blogspot.com/p/gry-101-introduction-to-physical.html>).

Temperature drops with increasing altitude to the mesopause, which marks the top of this middle layer of the atmosphere. It is the coldest place on Earth and has an average temperature of around $-100\text{ }^{\circ}\text{C}$.

iv) Thermosphere (Greek: heated region) above $\sim 90\text{ km}$:

The thermosphere is the second-highest layer of the Earth's atmosphere. It extends from the mesopause (which separates it from the mesosphere) at an altitude of about 80 km up to 120 km . Within this layer of the atmosphere, ultraviolet radiation causes photoionisation/photodissociation of molecules, creating ions. The temperature sharply increases with height due to the absorption of highly energetic solar radiation and it can reach values up to $1500\text{ }^{\circ}\text{C}$.

2.1.1.2 Vertical profile of pressure

Air pressure at any height in the atmosphere is due to the force per unit area exerted by the weight of all of the air located above that height. An air parcel experiences the gravitational attraction (between the parcel and the Earth), as a downward force, which by definition is the weight of the parcel. The change of pressure with

altitude within the atmosphere is huge, decreasing by a factor of about of one million between surface and tropopause. However, unlike the vertical profile of temperature, this huge change is distributed evenly within the atmosphere and pressure changes smoothly with altitude (Hobgood, 1993).

We can explain the upward lapse of pressure with altitude by describing the balance of forces on air parcels in the atmosphere. In a static atmosphere, the upward and downward forces on any air parcel must balance. If we assume an air parcel in an unbalanced state, the air will move towards another altitude, to the point where the net upward pressure force on the parcel exactly balances its weight. This balance is known as hydrostatic equilibrium and it can explain the observed upward lapse of pressure. In hydrostatic equilibrium, the atmospheric pressure obeys the barometric equation and exponentially decreases with altitude by about a factor of ten every 17 km.

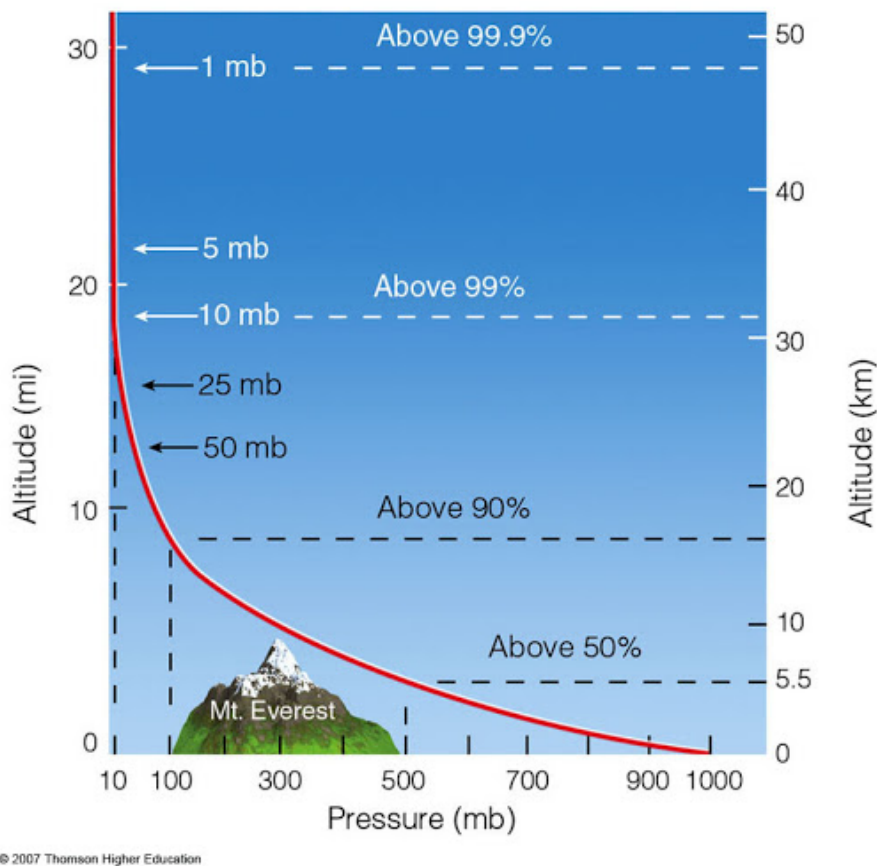


Figure 6: The pressure variation in the atmosphere as a function of altitude (<http://www.atmo.arizona.edu/>)

2.1.1.3 Vertical profile of air density

Following the vertical distribution of temperature and pressure, we can explain the vertical profile of air density using the equation of state Eq. 2.2. The pres-

sure strongly varies with altitude but the change of temperature is small compared to that of pressure. Therefore, the vertical profile of air density is quite similar to that of pressure and density decreases exponentially with altitude.

In addition to the distribution of mass, vertical profiles of air density can explain density-related phenomena such as chemical reactions or the interaction of solar radiation with air molecules. One example is blue sky that turns to black with increasing altitude and therefore the decreasing density of molecules that scatter the light (Hobgood, 1993).

2.2 Atmospheric general circulation

The horizontal gradients of pressure and temperature are much smaller compared to vertical changes in atmosphere, yet they have important impacts on the state of atmosphere. The most pronounced horizontal gradients are in meridional directions. These gradients are associated with the strong variation and uneven distribution of solar radiation along a meridian due to the axial tilt of the Earth for 23.44° . The downward gradient leads to circulation of air masses in the north-south direction as shown in Fig. 7.

Here, a brief explanation of the fundamentals of the atmospheric general circulation is provided. Moving from the subtropics toward the pole, temperature decreases. In response, tropics warm and polar regions cool, leading to a heating gradient in the atmosphere as shown in Fig. 7a. Thermal expansion in the tropics develops an upward move of pressure surfaces, while the opposite effect in the polar regions forces the pressure surfaces to bend downward. Latitudinal redistribution of mass causes the pressure to drop in the tropics and rise in high latitudes. The equator-to-pole pressure gradient leads to equator-ward flow and circulation cells depicted in Fig. 7b as the first response to the heating gradient.

This meridional circulation is modified by Coriolis force created by the Earth's rotation as shown in Fig. 7c. The equator-ward flow in the lower troposphere deviates to the west and pole-ward flow in the upper part of the troposphere deviates to the east. The flows become more zonal until the pressure gradient and Coriolis forces balance each other and result in geostrophic flow or balance. The difference between geostrophic wind at upper and lower altitudes is known as thermal wind, which is the hypothetical vertical wind shear (or wind gradient) and it increases with a strengthening equator-to-pole temperature gradient. The vertical component of wind is created by Coriolis force because winds originating from the west are amplified by Coriolis force while winds from the east are weakened due to the friction.

The final pattern of general atmospheric circulation indicated in Fig. 7d originates from baroclinic instability (baro: pressure, cline: slope; barocline), i.e. instability arising from sloped pressure contours. In baroclinic atmosphere, the density depends on both the temperature and the pressure, unlike barotropic atmosphere in which the density depends only on the pressure. When the meridional temperature gradient reaches a critical value, baroclinic instability emerges in the mid-latitude

lower troposphere and adds a wave-like character to the flow. In these waves, warm, humid subtropical air masses flow pole-ward, while cold, dry polar air masses flow equator-ward through the cyclones (rotating large-scale air mass around a low pressure centre in the atmosphere). Baroclinic waves develop weak northern and southern hemisphere circulation cells called Ferrel cells at 45° . Hadley cells appear at subtropical latitudes 30° where we also have anticyclones (rotating large scale air mass around a high pressure center in the atmosphere). In the Hadley cell, the winds that flow from the east to the west (easterly wind) at the ground level are called trade winds.

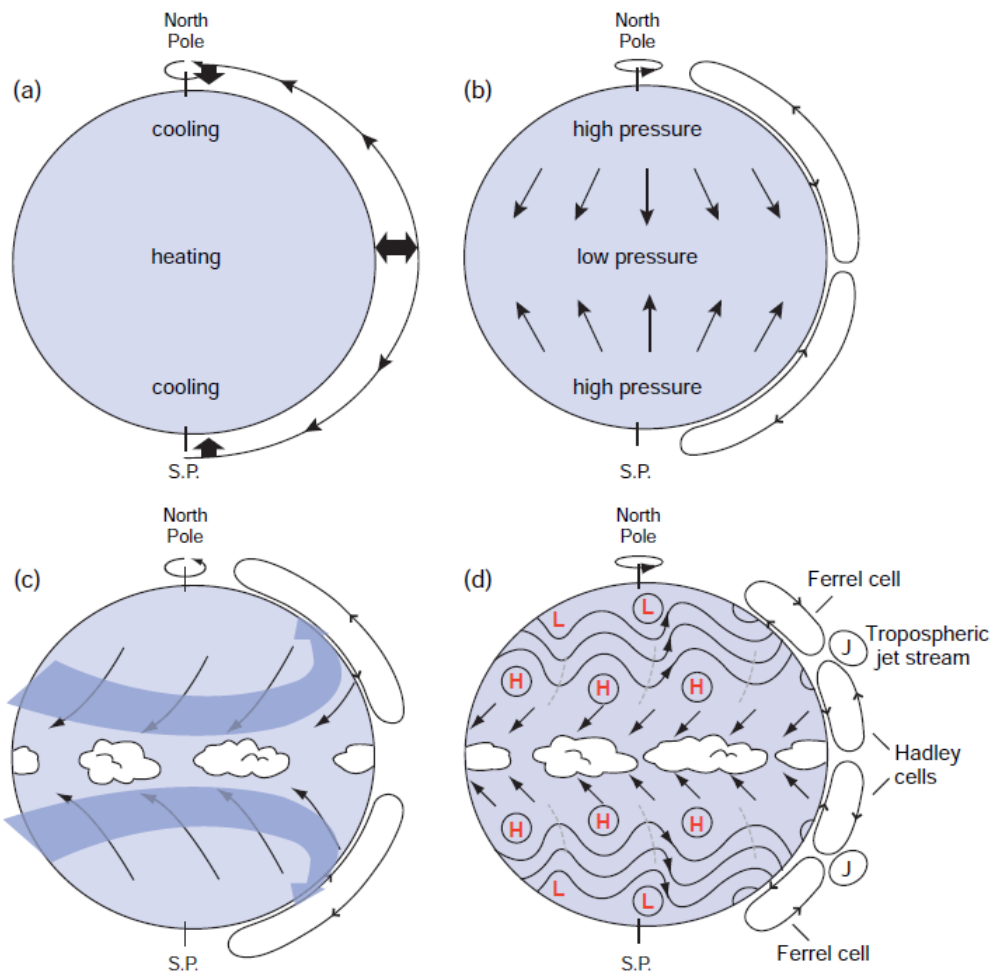


Figure 7: Schematic representation of the atmospheric circulation patterns (Wallace and Hobbs, 2006).

Part of the air rising at 60° latitude diverges at high altitude towards the poles and creates the polar cell, which is not shown in Fig. 7. Although the air masses at the poles are cold and dry relative to the equator, they are still sufficiently warm and moist to undergo convection and drive a thermal loop. In addition to Hadley, Ferrel, and polar cells that are oriented along the latitudes and have a synoptic scale

(thousands of kilometres), there are more circulation cells whose axes of circulation are longitudinally oriented and occur at the mesoscale (a horizontal range of 5 to several hundred kilometres). Longitudinal circulation occurs due to the heat capacity of water, its absorptivity, and mixing. Water absorbs more heat than land, but its temperature does not rise as strongly as the land. As a result, temperature variations on land are greater than on water. The Pacific Ocean cell is an entirely ocean-based cell originating from a remarkable difference in the surface temperatures of the western and eastern Pacific. This circulation plays a key role in the El Niño and La Niña phenomena.

2.3 Environmental issues relevant to the atmosphere

2.3.1 Global warming and Arctic amplification

In the recent centuries, one of the most important environmental issues relevant to the atmosphere, and more specifically troposphere is global warming. Global warming means that the temperature is increased (Fig. 8) and the increased concentration of greenhouse gases (infrared absorbing gases) is widely believed to be part of the reason (Serreze and Francis, 2006).

Although greenhouse gases are fairly uniformly distributed around the world, the warming is accelerated in the Arctic region and upward trends of near-surface air temperature accompanied by a reduction in sea ice have been observed in polar areas in recent decades (Serreze and Francis, 2006; Serreze and Barry, 2011). The rate of temperature increase in the Arctic has been significantly larger compared to the global average warming, almost twice as large as the global average (Serreze and Francis, 2006). This phenomenon is called Arctic Amplification (AA). Fig 8 and 9 indicates that AA is prominent in the annual surface air temperature trend in recent decades (Serreze and Barry, 2011).

AA was first investigated by Arrhenius (1896) over one hundred years ago. Budyko (1969) and Sellers (1969) are well known for their contribution to understanding of climate change and the first publications about the concept. AA was later confirmed by a number of studies using observations and climate models, and whereby now it is well established as an inherent feature of the global climate system (Stroeve et al., 2012; Cohen et al., 2014; Pithan and Mauritsen, 2014; Wendisch et al., 2017).

AA and therefore the consequent profound changes in the Arctic environment have resulted in huge impacts within the Arctic on the local ecosystem (Hinzman et al., 2013), greening of coastal tundra (Bhatt et al., 2010), altering wind patterns (Overland and Wang, 2010) and on the global scale impacts beyond the Arctic region in extreme weather conditions at mid-latitudes (Cohen et al., 2014; Kim et al., 2017; Cohen et al., 2020). For this reason, AA has received strong attention from the climate change research community in recent years.

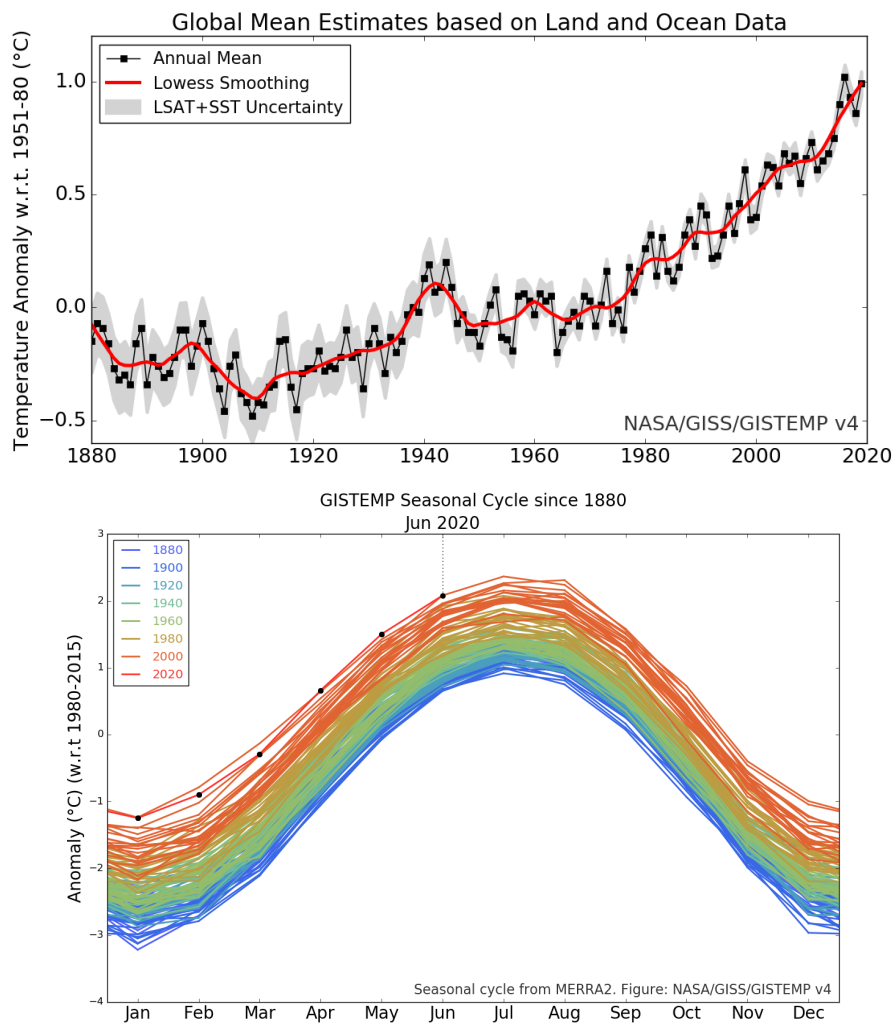


Figure 8: Upper panel: Land-ocean temperature anomaly, 1880 to present, with base period 1951-1980. The solid black line is the global annual mean and the solid red line is the five-year LOWESS smooth (locally weighted scatterplot smoothing). The gray shading represents the total (LSAT and SST) annual uncertainty at a 95% confidence interval. Bottom panel shows how much warmer each month is than the annual global mean (<http://data.giss.nasa.gov/gistemp>).

AA is best expressed during the autumn and winter and it is much weaker in spring and summer, as shown in Fig. 10. The most striking evidence of AA is declining sea ice coverage in summer and early autumn over recent decades (Stroeve et al., 2012). The long-term satellite data record starting from 1978 monitoring the sea ice concentration and extent indicates a decline of -12.9% per decade in summer sea ice (Pithan and Mauritsen, 2014) in which several amplifying/reinforcing feedbacks originating from changes in Arctic atmosphere and ocean play a role (Stroeve et al., 2012; Pithan and Mauritsen, 2014; Cohen et al., 2020).

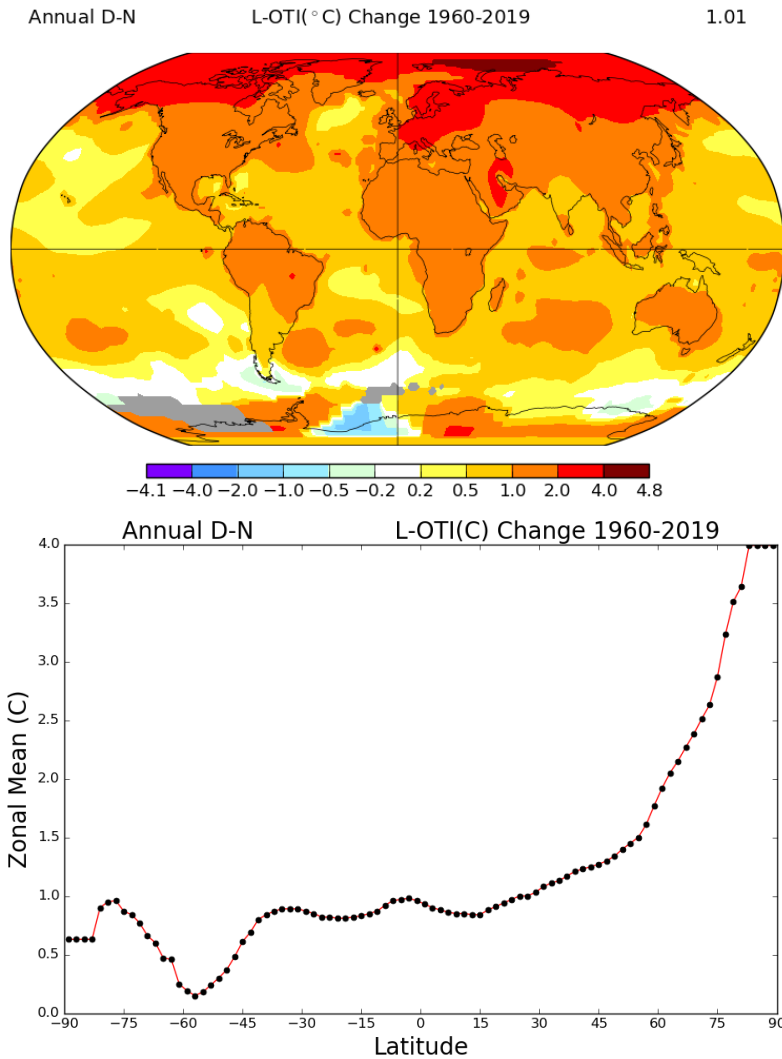


Figure 9: Upper panel: Linear trends in annual mean surface air temperature for the period 1960–2019, based on the National Aeronautics and Space Administration Goddard Institute for Space Sciences (NASA GISS) temperature analysis (<http://data.giss.nasa.gov/gistemp>). Bottom panel: Linear trends over the 60-year analysis period averaged by latitude.

A quantitative understanding of the physical mechanisms underlying AA has considerably evolved in recent decades (Cohen et al., 2020). The most important contributions to AA are associated with feedbacks of: i) temperature, ii) water vapour, iii) clouds, iv) surface albedo, v) aerosol particles and vi) changes in atmospheric and oceanic heat transport (Pithan and Mauritsen, 2014). In a simple sense, these feedbacks can be explained as follows:

Temperature feedback

The increasing temperature of the surface or atmosphere leads to an increase in longwave radiation at TOA by the fourth power of the temperature. Temperature

feedback can be decomposed into two different contributions (Pithan and Mauritsen, 2014; Döscher et al., 2014):

- Planck feedback: associated with the vertically homogeneous warming of the surface and troposphere. Assuming Stephan-Boltzman law, the longwave thermal-infrared radiation emitted from the surface increases with temperature, and therefore thermal energy transforms to radiative energy and surface cools and results in a negative feedback.
- Lapse rate feedback: associated with the tropospheric warming and its vertical structure that deviates from vertically uniform warming as a result of the interaction between thermal radiation and natural convection. In the tropics, this mechanism leads to greater warming in the upper troposphere compared to that at the surface, and results in a negative feedback there. However, in the Arctic the stably stratified atmosphere, prevents transferring heat to higher altitudes, and therefore warming resides close to the surface and additional warming leads to further warming of surface, and results in a positive feedback.

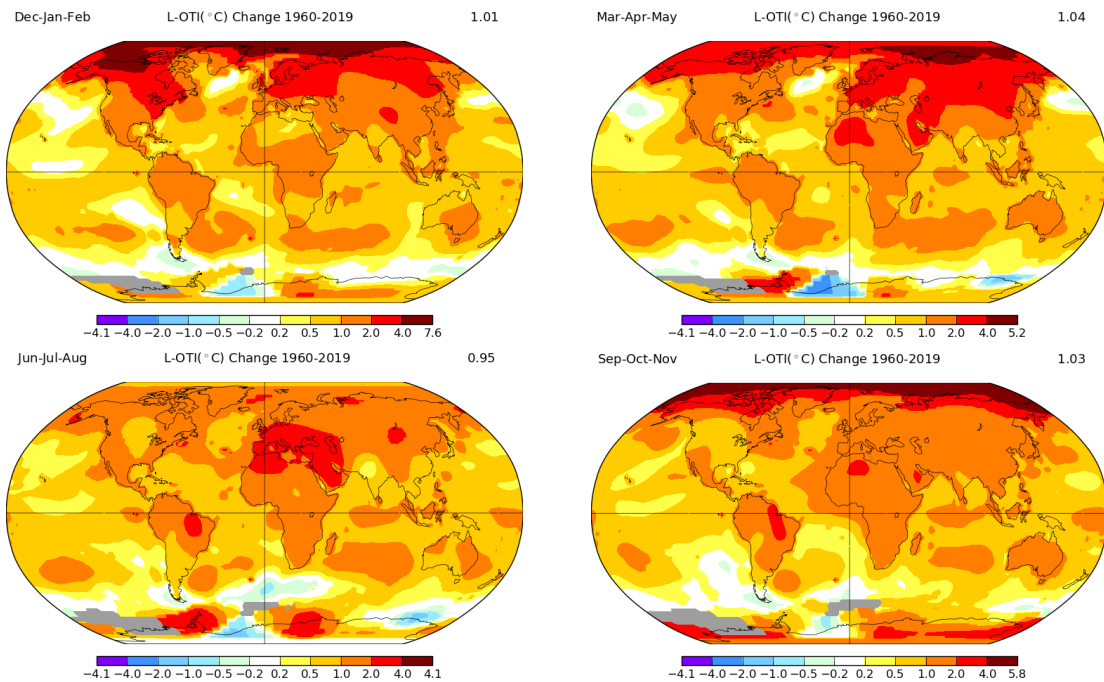


Figure 10: Anomalies in winter (a, December–February), spring (b, March–May), summer (c, June–August) and autumn (d, October–November) temperature for the 1960–2019 computed with respect to the reference period 1960–2019. Results are based on the NASA GISS temperature analysis, (<http://data.giss.nasa.gov/gistemp>).

Cloud feedback and water vapour feedback

Cloud and water vapour play a key role in unbalancing the radiative budget in Arctic in different ways (Serreze and Barry, 2011; Pithan and Mauritsen, 2014):

-
- decreasing solar radiation due to high albedo of cloud and the consequent cooling effect at the surface;
 - warming temperature leads to an increased amount of water vapour in the atmosphere as a greenhouse gas and to amplify other positive feedbacks such as ice-albedo feedback (Döscher et al., 2014);
 - increasing the downward longwave flux and therefore warming surface, accelerating sea-ice loss and extending ice-free state (Serreze and Barry, 2011). The net effect of cloud and water vapour is found to have a warming impact in the Arctic region, unlike lower latitude clouds, which have a net cooling effect (Serreze and Barry, 2011).

Surface albedo feedback

The positive feedback of surface albedo initiates with the increase of temperature due to different forcings, namely natural or anthropogenic. Consequent warming leads to melting of snow/ice cover in the Arctic and therefore replacing a highly reflecting surface with a darker one with lower albedo, which absorbs more solar energy and results in further warming and reduction of the snow/ice extent (Serreze and Barry, 2011).

The surface albedo feedback is known as the most significant contributor to AA (Taylor et al., 2013). However, Graverson and Wang (2009) showed that the difference between the amplification signal with varying albedo and that of fixed albedo is only 15%. Model studies indicated that we can explain the AA with a fixed surface albedo, thus accounting for the leading contribution from cloud feedback (Döscher et al., 2014; Langen and Alexeev, 2007). A similar conclusion was drawn by Winton (2006) based on twelve climate models used in the IPCC Fourth Assessment Report.

Changes in atmospheric and oceanic heat transport

Common to all of aforementioned feedbacks is the notion that we expect to see their peak impact close to the surface in the lowest part of the atmosphere due to the strong atmospheric stratification in the Arctic (Serreze and Barry, 2011; Graverson et al., 2008). However, Graverson et al. (2008) found that this pattern with a near-surface maximum was observed only in spring.

In summer time, they found an amplification signal throughout most of the troposphere with a peak between 800 and 600 hPa. This evidence was indicative of the impact from atmospheric heat transport into the Arctic and the sensitivity of the Arctic temperature to changes in the mid-latitude circulation (Graverson et al., 2008; Graverson, 2006).

Aerosol feedback

Although the contribution of key parameters and mechanisms to AA is discussed controversially (Serreze and Barry, 2011; Pithan and Mauritsen, 2014), aerosol is one of the well-known parameters that plays a role in the Arctic climate and there-

fore changes on a global scale (Abbatt et al., 2019; Tomasi et al., 2015). For this reason, aerosol in the Arctic has received strong attention from the climate change research community in recent years and our understanding of the Arctic aerosol has been strongly advanced from the time that the Arctic was thought to be a pristine environment.

Ten years ago, the first pieces of evidence to highlight the aerosol influence on AA was provided by Shindell and Faluvegi (2009). They indicated that decreasing concentrations of sulphate aerosols and increasing concentrations of black carbon have substantially contributed to rapid Arctic warming during the past three decades (Shindell and Faluvegi, 2009). More details on aerosols in the Arctic are presented in the following section.

Comparison of feedback contribution to Arctic Amplification:

Pithan and Mauritsen (2014) used TOA fluxes to decompose feedbacks and determine their relative contribution to AA. As can be seen in Fig. 11, the largest contribution belongs to lapse rate feedback. In absolute terms, albedo feedback is the largest contributor but lapse rate feedback reduces tropical warming, which leads to further AA. On the contrary, CO₂ and water vapour feedback amplify tropical warming and therefore weaken AA.

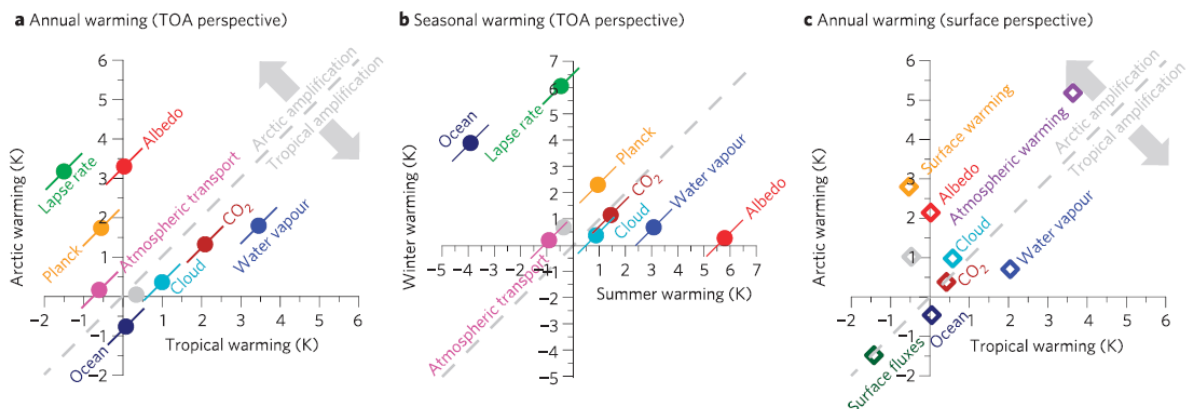


Figure 11: Warming contributions of individual feedback mechanisms, a) Arctic versus tropical warming from a TOA perspective, b) Arctic winter versus summer warming, c) Arctic versus tropical warming from a surface perspective. For a, b and c, feedbacks above the 1:1 line contribute to Arctic amplification, whereas feedbacks below the line oppose Arctic amplification. Grey is the residual error of the decomposition. ‘Ocean’ includes the effect of ocean transport changes and ocean heat uptake (Pithan and Mauritsen, 2014).

From a seasonal perspective, Arctic warming is stronger in winter (December-February) compared to summer (June-August), as shown in Fig. 11. The largest contributor to seasonal warming is lapse rate feedback in winter, which dominates the

warming effect from water vapour and albedo feedbacks in summer (Pithan and Mauritsen, 2014).

In non-Arctic regions where we have well-mixed troposphere, the surface temperature behaviour can be estimated from TOA fluxes. However, this is not the case in the Arctic where a positive lapse rate feedback decouples the surface and troposphere. To compare the effect of different feedbacks at the surface, we can break temperature feedback into two surface (emitted longwave) and atmospheric (down-welling longwave radiation received by surface) feedbacks. The efficiency of each feedback in increasing surface temperature is shown in Fig. 11. Surface temperature feedback is the largest contributor (for further information, see Pithan and Mauritsen (2014)).

In the next section, we will continue discussing aerosol in the Arctic, as the main focus of this study.

2.4 Atmospheric aerosol

Aerosol is defined as the mixture of suspended solid or liquid particles in a gas (Seinfeld and Pandis, 1998). The radii of aerosol particles vary from nanometers to more than a hundred micrometers and they have a different shape, size and composition (Seinfeld and Pandis, 1998). Atmospheric aerosol - in other words, particulate matter - can be directly injected into the atmosphere from different sources (e.g. sea spray aerosol, dust, biomass burning aerosol, volcanic ash, primary organic aerosol) or produced from precursor gases (e.g. sulphates, nitrates, ammonium salts, secondary organic aerosol). These particles are found in the lowest layers of the atmosphere, namely the troposphere and stratosphere (having a scale height of about 2–3 km), and they can be classified in two different categories:

- primary aerosol: from anthropogenic and natural sources, e.g. industry, traffic, households, biomass burning, agriculture, sea spray, mineral dust, volcanic ash, plant and animal debris.
- secondary aerosol: produced from chemical processes in the atmosphere such as gas-to-particle conversion based on precursor gases such as SO_2 , NO_2 , and volatile organic compounds (VOC).



Figure 12: Desert dust, volatile organic compounds from vegetation, smoke from forest fires, and volcanic ash (credit (left to right): Western Sahara Project, Jonathan Jessup, Vox, and Ludie Cochrane).

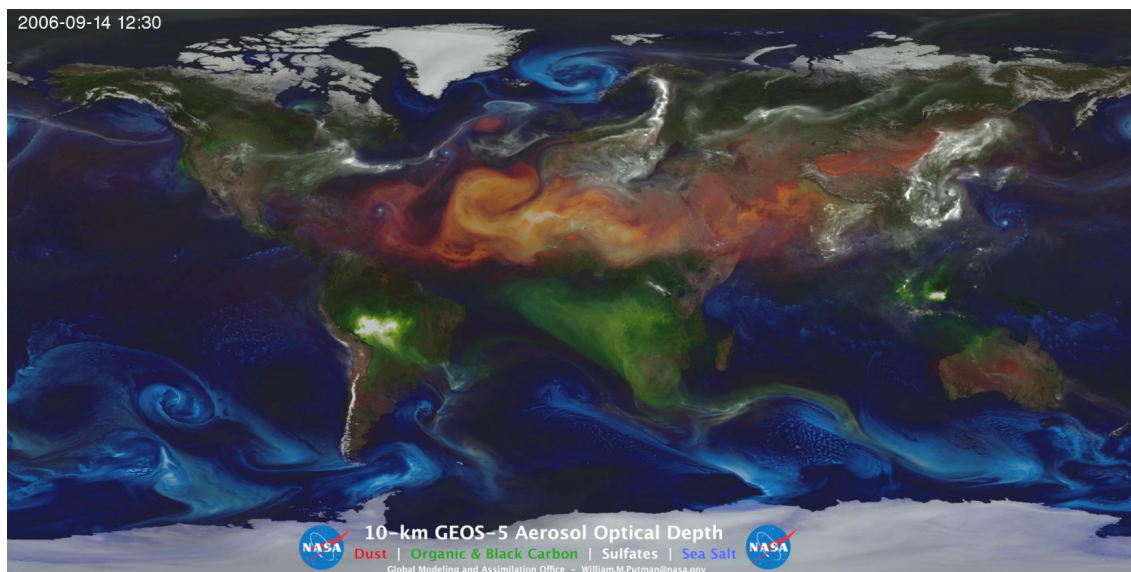


Figure 13: An aerosol model shows swirls of sea salt caught in cyclones (blue), black and organic carbon particles emitted by fires (green), sulfate (white) and desert dust (red). Credit: NASA Global modeling and assimilation office.

Once suspended in the atmosphere from natural or anthropogenic sources, aerosols can be transported over long distances that may stay a few hours to several weeks and experience different chemical and physical processes by which the size, shape, composition and therefore physical and chemical properties of aerosols change. The removal of aerosol from the atmosphere occurs by going through dry and wet depositions (Seinfeld and Pandis, 1998). Dry deposition includes all mechanisms involved in the direct transport of particles onto surfaces (e.g. gravitation, collisions with obstacles). In case of wet deposition or precipitation scavenging, a particle is intercepted by cloud or fog drops, rain or snow. Due to the time scales characterising these processes, the residence time of aerosols in the atmosphere is relatively short compared to those of most greenhouse gases. Their relatively short lifetime together with the heterogeneity of the sources render aerosol concentrations and composition over the globe highly variable in both space and time.

2.4.1 Aerosols in the Arctic

The history and first signs of Arctic aerosol (haze) started with the documentation from Nordenskiöld (1883) and Nansen (1924) about pollutants and their deposition on the surface as dark stains in the Arctic. Later on, pilots flying over Canadian and Alaskan Arctic (Greenaway, 1950; Mitchell, 1956) reported reduced visibility due to a so-called "Arctic haze". In the beginning, the source of the haze was unknown and debated to be the ice crystals from open leads (Ottar et al., 1986). However, twenty years later, observations made in the 1970s raised new questions and led to a better understanding of the chemical composition, morphology of the Arctic haze, its structure and source. It was suggested that Arctic haze - observed as thick layers

of 1-3 km, being hundreds to thousands of kilometres wide, with grey-blue colour in anti-solar direction and reddish-brown in solar direction - are truly aerosols (Rahn et al., 1977). Arctic haze occurs in vertically and spatially inhomogeneous layers located at the lowest 5 km of the Arctic atmosphere, with the highest concentration in the lowest 2 km. The haze is mainly composed of non-sea salt (NSS) sulphate and particulate organic matter (POM). It also contains ammonium, nitrate, black carbon (BC), dust aerosols, Ozone precursors (nitrogen oxides NO_x) and VOCs (Law and Stohl, 2007; Quinn et al., 2007).

Through rough trajectory analysis and experiments of chemical fingerprints showing urban-industrial pollutants, crustal aerosols and sea salt, the origin of haze was attributed to anthropogenic emissions and natural aerosols transported from mid-latitudes (Rahn et al., 1977; Ottar et al., 1986).

To explain this long range transport over more than 1000 km, it is necessary to consider several mechanisms (Ottar et al., 1986; Quinn et al., 2007). The haze event is regularly observed in late winter and early spring (December through April). At this time, surface temperature is low and therefore strong surface-based temperature inversions and consequently a stable atmosphere form and reduce wet/dry deposition or any removal processes (Bradley et al., 1992). In addition, the formation of constant potential temperature surfaces and a closed dome over the Arctic isolates the Arctic lower troposphere from the rest of the atmosphere by a seasonally shifting transport barrier referred to as the Arctic front (Klonecki et al., 2003). Under these circumstances, the pollution transport is only possible from regions with the same low potential temperature such as northern Eurasia on time scales of a few days to weeks (Carlson, 1981; Iversen, 1984; Barrie, 1986; Rahn et al., 1977). Iversen (1986) confirmed the linkage between the episodic occurrence of Arctic haze and indices of meridional air exchange.

In summer time, when areas at lower latitude warm, the Arctic front recedes northward and prevents the direct transport of pollution into the Arctic. Instead, long range transport mechanisms lead to an accumulation of aerosol into the middle and upper troposphere rather than near the surface, which is the case in winter time. Therefore, Arctic haze is characterised with strong seasonality, with the maximum concentration in late winter and early spring. This is linked to (Willis et al., 2018):

- the pattern and seasonality of mean circulation of the atmosphere;
- Arctic front; and
- wet removal processes during long range transport in summer.

In addition to long range transport, the regional Arctic processes associated with solar radiation (its changes from dark polar night to polar sunrise), temperature and sea ice also lead to change of aerosol load and its properties in the Arctic (Willis et al., 2018):

- photochemical oxidation of organic species (from biological production, atmospheric deposition, or in-situ chemical formation) within snow and ice, which produces VOCs (Fu et al., 2009; Kawamura et al., 2010);

- primary salt-containing aerosol from snow and ice processes (frost flowers at ice surfaces, blowing snow which contains salt from different sources e.g. deposition of sea salt) (Abram et al., 2013; Rhodes et al., 2018);
- release of primary marine aerosol in marginal ice zone and open leads (Kirpes et al., 2018; Gilgen et al., 2018; Browse et al., 2014; May et al., 2016; Deshpande and Kamra, 2014; Leck and Svensson, 2015);
- planktonic organisms within and below the sea ice that produce dimethylsulphide (DMS) and organic matter (Galindo et al., 2014; Lévassieur, 2013);
- accumulation of surface emissions due to persistent temperature inversions induced by sea ice (Pavelsky and Hall);
- control of removal processes of aerosols by sea ice via controlling moisture transport to atmosphere and cloud formation;
- formation of new particles by oxidation products of DMS, ammonia, amines, iodine oxides, and condensable organic species (Asmi et al., 2016; Dall’Osto et al., 2017; Leaitch et al., 2013).

2.4.2 Physical and chemical properties

To explain aerosol properties, multiple parameters need to be taken into account including particle size, particle number distribution (aerosol concentration as a function of size), shape and chemical composition (which determines complex refractive index). Optical properties of aerosols are identified by the latter two parameters.

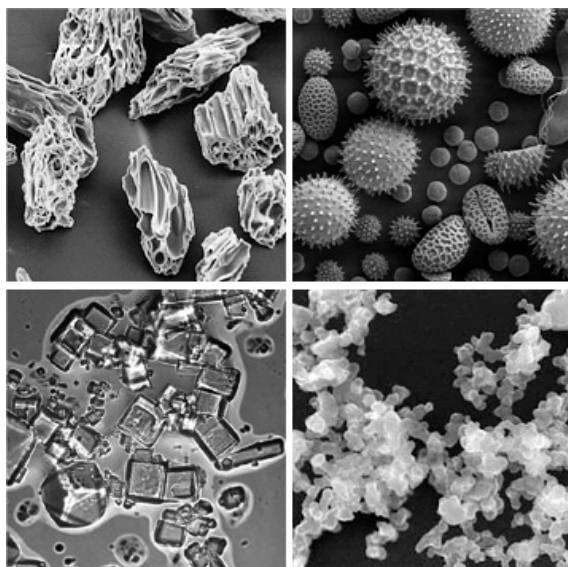


Figure 14: Scanning electron microscope images of aerosols: volcanic ash, pollen, sea salt, and soot. Micrographs courtesy USGS, UMBC (Chere Petty), and Arizona State University (Peter Buseck).

In this section, the terms: volume or area distribution, the number density of the log normal mode, an n-mode log-normal distribution, some of the relevant moments of a log normal distribution and the effective radius are explained. The definitions and the derivation of the terms aerosol, size, size distribution, relevant moments, effective radius are well described by Grainger (2015) and Levy (2009).

Aerosol size, size distribution and effective radius

Aerosols can be classified based on their size or mode. The term size refer to the diameter as defined by in-situ measurements community, or radius, used in remote-sensing terminology. Particles with a radius larger than $1.0 \mu\text{m}$ are referred to as coarse aerosols. Two main sources of coarse particles are mineral dust and sea salt. Particles with a size below $1.0 \mu\text{m}$ are known as fine aerosols and include two sub-modes: the accumulation mode (with size 0.1 to $1 \mu\text{m}$) and nuclei or the Aitken mode with a typical size below $0.1 \mu\text{m}$. The primary source of the accumulation mode is incomplete combustion (from biomass burning or coal power plants) and coagulation of very fine particles categorised in the Aitken nuclei mode. These particles are usually secondary aerosols that are produced by nucleation or condensation of atmospheric gas compounds, but primary sea salt particles have also been observed in this mode.

Aerosol size distribution describes the number of aerosols as a function of size. For any size distribution of aerosol, the number concentration of aerosols as a function of radius is related to volume or area distribution as follows:

$$\frac{dN}{dlnr} = \frac{3}{4\pi r^3} \frac{dV}{dlnr} = \frac{1}{\pi r^2} \frac{dA}{dlnr}. \quad (2.3)$$

Aerosols in the atmosphere are found to have approximately lognormal distribution and therefore in theoretical studies they are modelled as a lognormal distribution defined by the effective mean radius and standard deviation. For a single lognormal mode, the number size distribution can be written as:

$$\frac{dN}{dlnr} = \frac{N_0}{\sigma\sqrt{2\pi}} \exp\left(-\frac{[\ln(r/r_g)]^2}{2\sigma^2}\right), \quad (2.4)$$

where N is the number distribution of aerosols with radius of r , N_0 is the total number, r_g is the geometric mean radius and σ is the geometric standard deviation of the lognormal mode. Bimodal size distributions are often assumed. An n-mode lognormal distribution can be written as:

$$\frac{dN}{dlnr} = \sum_{i=1}^n \frac{N_i}{\sigma_i\sqrt{2\pi}} \exp\left(-\frac{[\ln(r_i/r_{gi})]^2}{2\sigma_i^2}\right), \quad (2.5)$$

Figure 15 indicates the typical size distribution of atmospheric aerosols. It is well known that particles of an intermediate size in the range of $0.1 - 1 \mu\text{m}$ remain for the longest times in atmosphere due to two main mechanisms (Shaw, 1987): coarse particles with diameters above $1.0 \mu\text{m}$ (e.g. grains of windblown sand) are

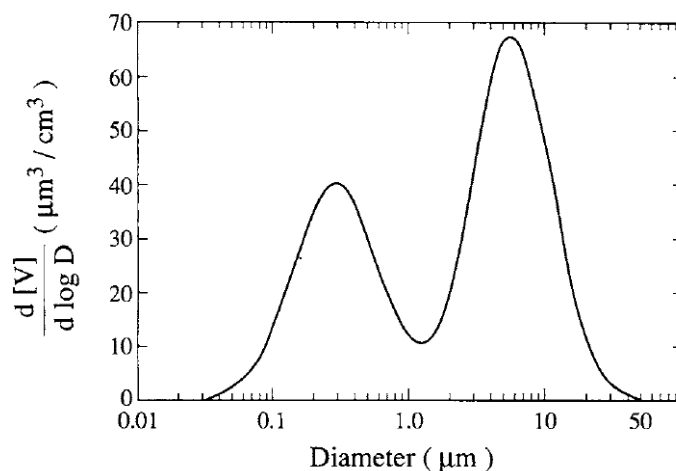


Figure 15: Typical bimodal atmospheric aerosol volume size distribution (Covert et al., 1980).

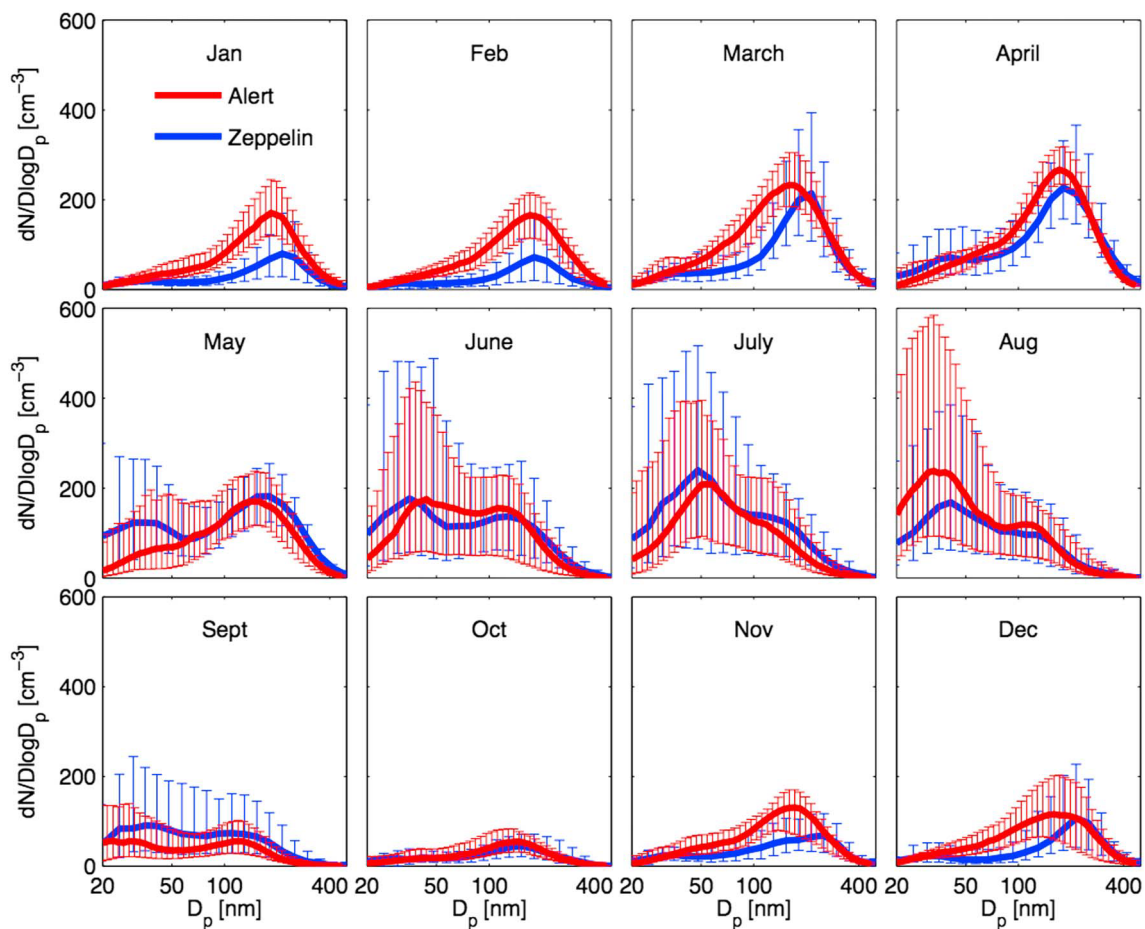


Figure 16: Monthly median number size distributions (20–500 nm), measured with a scanning mobility particle sizer at Alert, Nunavut, for 2011–2013 and with a differential mobility particle sizer at Zeppelin, Svalbard, for 2011–2013. Error bars are 20th–80th percentiles (Croft et al., 2016).

rapidly removed, e.g. by precipitation. Fine particles with a diameter below $0.1 \mu\text{m}$ are quickly removed by diffusion and coagulation.

The moments of a size distribution are simple metrics to express the shape of the distribution. For a lognormal, the moments of order k , M^k are:

$$M^k = \int_0^\infty r^k \frac{dN}{d\ln r} d\ln r = (r_g)^k \exp(0.5k^2\sigma^2) \quad (2.6)$$

For example, the mean is the first raw moment of a size distribution. The effective radius of aerosols is defined as the ratio of the third moment of the particle size distribution to the second moment. The usefulness of effective radius, r_e , comes from the fact that energy removed from a light beam by a particle is proportional to the particle's area (provided the radius of the particle is similar to or larger than the wavelength of the incident light), which is why the effective radius is sometimes called the area weighted mean radius. The effective radius of aerosols is calculated as follows:

$$r_{eff} = \frac{M^3}{M^2} = \frac{\int_0^\infty r^3 \frac{dN}{d\ln r} d\ln r}{\int_0^\infty r^2 \frac{dN}{d\ln r} d\ln r} = \frac{3 V_0}{4 A_0} = r_g \exp\left(\frac{5}{2}\sigma^2\right) \quad (2.7)$$

The number size distribution of Arctic haze pictured via measurements can be explained by well-aged particles with a median size of 0.2 micron (Leitch et al., 1984; Heintzenberg, 1980; Shaw, 1984), a range in which particles are efficient scatters of visible solar radiation.

Chemical properties

To compute optical properties of aerosol particles, first the chemical composition and microphysics of particles should be discussed, which tacitly expresses the amount of water in the particle (Burrows et al., 2011). Hygroscopicity means the ability of an aerosol particle to absorb water. Most atmospheric aerosols are hygroscopic if the relative humidity is above the deliquescence point, the threshold at which the aerosol goes from a solid dry phase to an aqueous or mixed solid-aqueous phase (Tang et al., 1997). For common atmospheric aerosol particles, the deliquescence point occurs at a very low RH (Seinfeld and Pandis, 1998). Therefore, most aerosols can be assumed as spherical particles.

Tropospheric aerosols contain sulphate, ammonium, nitrate, sodium, chloride, trace metals, carbonaceous material (both elemental - BC or soot - and organic carbon), crustal element and water (Seinfeld and Pandis, 1998). Aerosols can be divided into six major categories according to their chemical composition:

- sulfate based: produced from the oxidation of sulphur dioxide (SO_2) of anthropogenic (e.g. fossil fuel combustion) or natural origin (e.g. volcanic eruptions and dimethyl sulphide (DMS) from phytoplankton);
- nitrate based: formed by oxidation processes applying to nitrate dioxide (NO_2) from anthropogenic (e.g. combustion of fossil fuels, biomass burning) or natural

sources (e.g. microbial activity in soils, marine emissions);

- sea salt: produced by ocean-wave activity that propels salt particles into the air, and by spume drops generated from surface tearing at the wave crests, with a radius of $0.8 - 4 \mu\text{m}$ primarily comprising sodium chloride (NaCl). These particles are hygroscopic and known to be the major source of cloud condensation nuclei (CCN) (Monahan et al., 1986; Tang et al., 1997);
- ammonium salts: produced either by the reaction of gas phase ammonia NH_3 with acidic species or the dissolution of NH_3 in water (e.g. cloud or rain droplets). Ammonium salts are emitted into the atmosphere from anthropogenic (e.g. fertiliser application in agriculture, combustion, fossil fuels from traffic, ships, domestic and industrial heating, etc.) and natural sources (excreta of wild animals, emission from soil vegetation and ocean) (Bouwman et al., 1997);
- mineral dust: emitted to the atmosphere during storms over arid/semiarid areas and deserts or dried agricultural lands (Ginoux et al., 2010). Dust particles are composed of minerals such as aluminium, silicon, iron oxide and carbonates;
- carbonaceous aerosols are composed of organic carbon and BC. OC is emitted from both anthropogenic sources (e.g. vehicular exhaust, biomass burning, cooking, agriculture, industry practices emitting VOC, etc.) and natural ones (biogenic emissions in the marine atmospheric boundary layer and sea spray, forest emissions, natural forest fires and biological metabolic processes) (Kawamura and Bikkina, 2016; Rinaldi et al., 2011; Steinberg and Bada, 1984).

Arctic aerosols originate from both primary and secondary processes including natural and anthropogenic aerosols. Therefore, the chemical composition of Arctic aerosols can significantly vary over space and time (Kokhanovsky and Tomasi, 2020). The multimodal aerosol size distribution over the Arctic indicates three modes:

- nucleation mode with a mean geometric diameter of $0.02 \mu\text{m}$ and a geometric standard deviation of 1.8 mainly containing small sulphuric acid droplets or combustion matter;
- accumulation mode with a mean diameter of $0.15 \mu\text{m}$ and standard deviation of 1.4;
- coarse particle mode containing particles mainly in the size range of 5 to more than $8 \mu\text{m}$ from mineral dust and sea salt.

The chemical composition of Arctic haze particles has been measured and understood well: Arctic haze mainly contains a mixture of sulphate, organic particulate matter, ammonium, nitrate, dust, BC and heavy metals (Law and Stohl, 2007; Quinn et al., 2007). Figure 17 shows one example from measurements of aerosol chemical composition at Ny-Ålesund (N $78^\circ 56'$ E $11^\circ 55'$) on the island of Spitsbergen (Svalbard, Norway) during March-September campaigns from 2010 to 2015 and the comparison with the central Arctic ocean.

In Svalbard, the main source of sea salt is open ocean, and it is mainly present in the super-micrometric fraction $1 - 10 \mu\text{m}$ (Huang and Jaeglé, 2017). Its concentration is higher in spring compared to summer. Anthropogenic sulfate together with ammonium is known to be the major source of Arctic haze. Since sulphate is a secondary aerosol, it is mainly present in the sub-micrometre fraction as methanesulphonic acid (MSA). In Fig. 17, strong seasonality of sulphate is observed with the maximum concentration in spring because the dominant source of these particles in the Arctic is anthropogenic and transported by Arctic haze. Nitrate plays a minor role in Arctic haze, while OC is a major component in PM₁₀ (coarse particulate matter, particles in the order of 10 micrometres or less) measurements. As can be seen from Fig. 17, mineral dust is the second most important component observed at Ny-Ålesund.

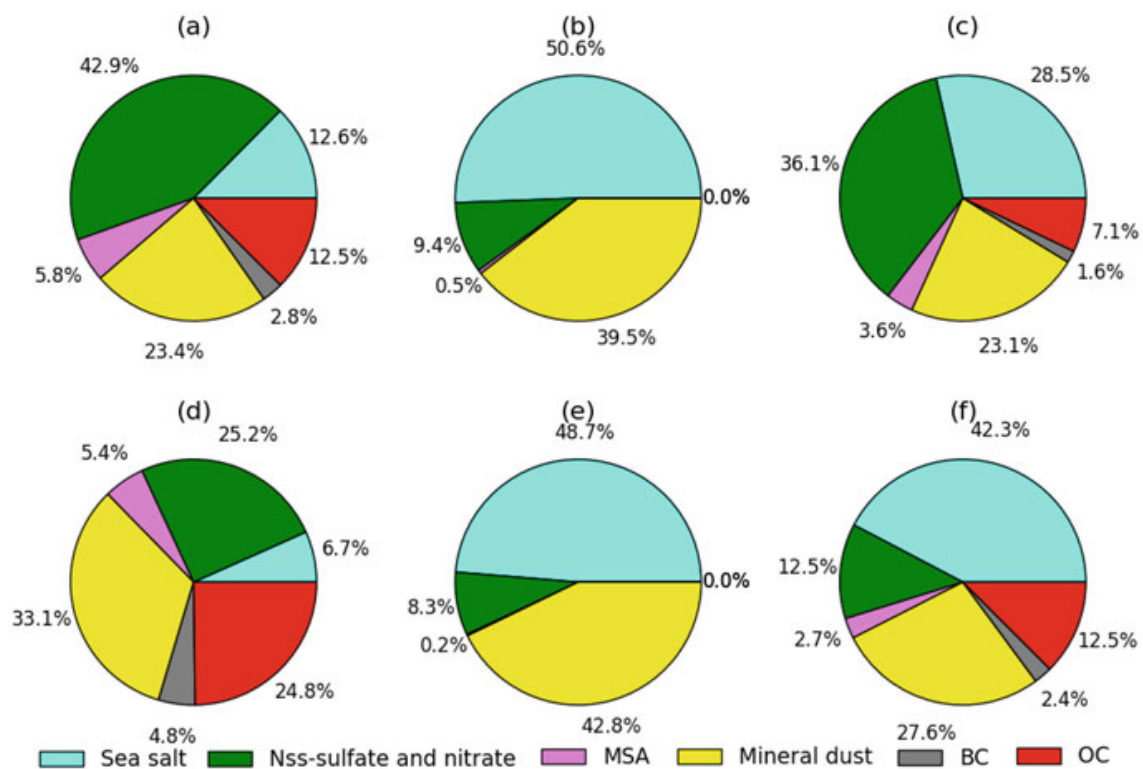


Figure 17: Ground-level particulate matter sampled at Ny-Ålesund for different seasonal periods March-May in Spring 2011-2015 and June-September in summer 2011-2015: (a) and (b) PM₁₀ in spring and summer respectively, (c) and (d) sub-micrometric particles in spring and summer, (e) and (f) super micrometric (1-10 micrometer) particles in spring and summer. Colors indicate different constituents: sea-salt, non sea-salt sulfate and nitrate, methanesulfonic acid (MSA), mineral dust, black carbon (BC) and organic carbon (OC) (Udisti et al., 2020).

Since mineral dust originates from primary sources, these particles should mainly be observed in the super-micrometric mode. However, considering the long-range transport of mineral dust from southern latitudes and the deposition of large parti-

cles during and before the transport, the mineral dust in the Arctic contains many small particles, as can be seen in the sub-micrometric as well as super-micrometric components of Fig. 17.

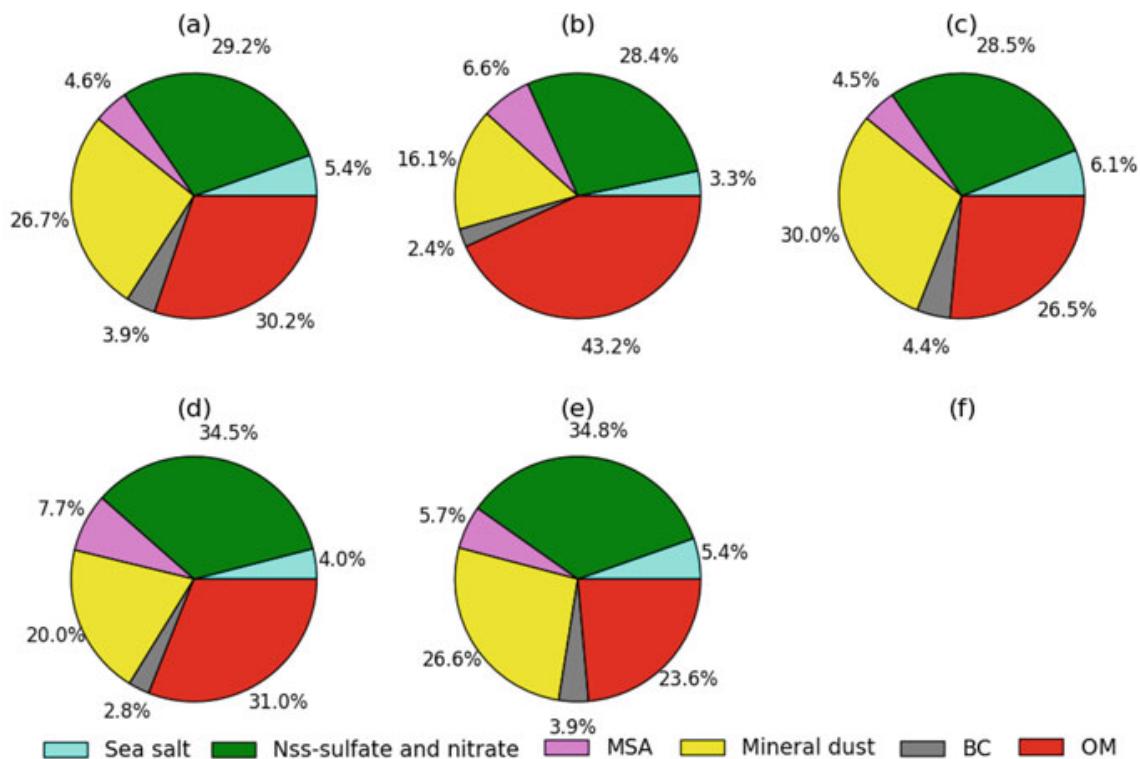


Figure 18: Sub-micrometric particles samples in the Central Arctic Ocean during the ASCOS experiment from 5th August to 8th September 2008, (a) to (f) panels show measurements at different stations. Colors indicate different constituents: sea-salt, non sea-salt sulfate and nitrate, methanesulfonic acid (MSA), mineral dust, black carbon (BC) and organic matter (OM) (Udisti et al., 2020).

As mentioned above, the chemical composition of aerosols can significantly differ with respect to time and location, as can be seen in Fig. 18 for the remote Arctic ocean.

2.4.3 Aerosol radiative properties

Molecules and particles in the atmosphere attenuate incident solar radiation. Aerosols may absorb or scatter radiation depending on their chemical composition, size, orientation of particles and the wavelength of electromagnetic radiation. For a single spherical aerosol, the two wavelength-dependent parameters of the complex refractive index (determined by chemical composition) and size parameter are used to describe scattering and absorbing properties of aerosol particles and they are de-

defined as follows, respectively:

$$m(\lambda) = n(\lambda) + i \cdot k(\lambda) \quad (2.8)$$

$$X = \frac{2\pi r}{\lambda} \quad (2.9)$$

where the real part (n) of the complex refractive index (m) represents scattering and the imaginary part (k) the absorption of an aerosol particle.

Scattering

Depending on the value of the size parameter, we have different scattering regimes in the atmosphere, as shown in Fig. 19. In this section, we explain two scattering regimes in which aerosol particles are involved: Mie theory, which is applied to many aerosols, and Rayleigh scattering theory, which is relevant only for very small particles compared to the wavelength of the radiation.

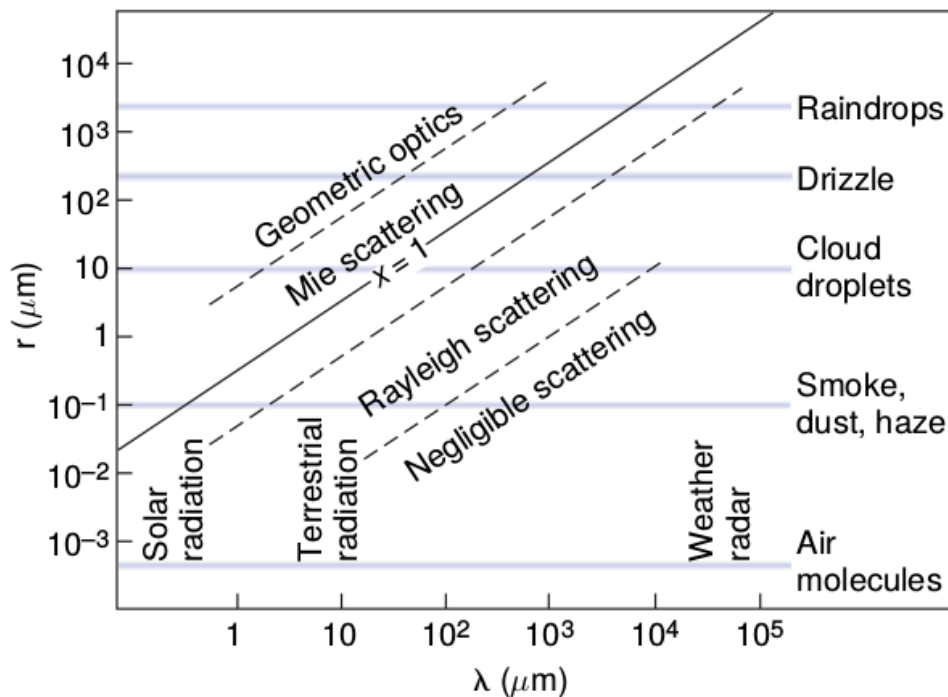


Figure 19: Size parameter depending on the particle radius and wavelength showing different scattering regimes (Wallace and Hobbs, 2006).

Rayleigh scattering

If the size parameter is much smaller than the wavelength of the incident radiation ($X \ll \lambda$), the scattering process by molecules and small aerosol particles in the atmosphere is called Rayleigh or molecular scattering (Wallace and Hobbs, 2006). In this case, the interaction of light with particles creates a dipole moment inside of

the particle, which is proportional to the power of incident light and oscillates with its frequency. The scattered intensity can be formulated as follows (Liou, 1992):

$$I(\Theta, r) = \frac{I_0}{r^2} \alpha^2 \left(\frac{2\pi}{\lambda} \right)^4 \frac{1 + \cos^2 \Theta}{2}. \quad (2.10)$$

where I is the scattered intensity with an angle of Θ to the incident intensity I_0 , in a medium containing molecules or particles, and r is the distance from scattering particle. α represents the polarizability of small particles, which can be calculated by:

$$\alpha = \frac{3}{4\pi N_s} \left(\frac{m^2 - 1}{m^2 + 2} \right). \quad (2.11)$$

N_s is the number of molecules in a unit volume and m is the refractive index of the molecules (Liou, 1992).

As can be seen from the equation, some characteristics of Rayleigh scattering are as follows:

- being symmetrical in backward and forward direction: $I(\Theta, r) = I(\pi - \Theta, r)$
- being inversely proportional to λ^4 , meaning that Rayleigh scattering is stronger for shortwave radiation and therefore longwave radiation is weakly scattered in this regime.

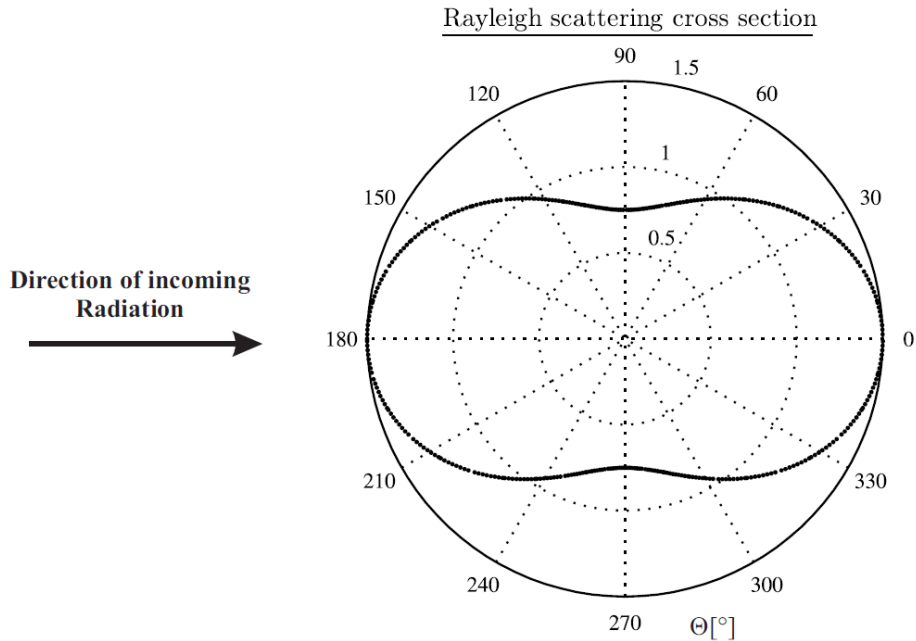


Figure 20: Rayleigh phase function for aerosol particle with different radii (Sinnhuber, 2015).

-
- being proportional to the particle size (diameter) and thus having a stronger effect from larger particles.
 - being inversely proportional to the r , meaning that the effect becomes smaller if the distance from particle increases.

The angular distribution of scattered light (phase function) integrated over all solid angles is as follows:

$$P(\Theta) = \frac{3}{16\pi}(1 + \cos^2 \Theta) \quad (2.12)$$

The phase function for Rayleigh scattering is shown in Fig. 20. The degree of asymmetry of scattering is indicated by the asymmetry factor (the average or statistically expected value of the cosine of the scattering angle for the scattered radiation):

$$g = \frac{1}{2} \int_0^\pi P(\Theta) \cos \Theta \sin \Theta \quad (2.13)$$

Values of g range from -1 for entirely back-scattered light to +1 for entirely forward scattering. In Rayleigh scattering, g is equal to zero.

Mie scattering

If the particle size is comparable to the wavelength of the incident electromagnetic radiation, the assumption of a single dipole moment no longer applies and a three-dimensional charge distribution is induced. The Mie theory provides an exact solution of the Maxwell's equations for scattering at spherical particles, e.g. many aerosols (Mie, 1908). The scattered intensity can be written as:

$$I(\Theta) = I_0 \Omega_{\text{eff}} \frac{P(\Theta)}{4\pi} = I_0 \left(\frac{\sigma_s}{r^2} \right) \frac{P(\Theta)}{4\pi} \quad (2.14)$$

where I is the scattered intensity with a scattering angle of Θ to the initial intensity I_0 , P is the phase function, Ω_{eff} is the effective solid angle and r is the distance between the particle and the observer, σ_s is Mie scattering cross-section, the scattering efficiency Q_s is given as:

$$\sigma_s / \pi r^2 = Q_s = c_1 X^4 (1 + c_2 X^2 + c_3 X^4 + \dots) \quad (2.15)$$

where X is the size parameter and the coefficients can be written for non-absorbing particles as:

$$c_1 = \frac{8}{3} \left(\frac{m^2 - 1}{m^2 + 2} \right)^2, \quad c_2 = \frac{6}{5} \left(\frac{m^2 - 1}{m^2 + 2} \right),$$

$$c_3 = \frac{3}{175} \frac{m^6 + 41m^4 - 28m^2 + 284}{(m^2 + 2)^2} + \frac{1}{900} \left(\frac{m^2 + 2}{2m^2 + 2} \right)^2 [15 + (2m^2 + 3)^2].$$

with m being the refractive index (Liou, 1992). The phase function for Mie scattering

is shown in Fig. 21.

The asymmetry factor is given by:

$$g = \frac{4}{X^2 Q_s} \sum_{n=1}^{\infty} \left(\frac{n(n+2)}{n+1} \operatorname{Re}(a_n a_{n+1} + b_n b_{n+1}) + \frac{2n+1}{n(n+1)} \operatorname{Re}(a_n b_n) \right) \quad (2.16)$$

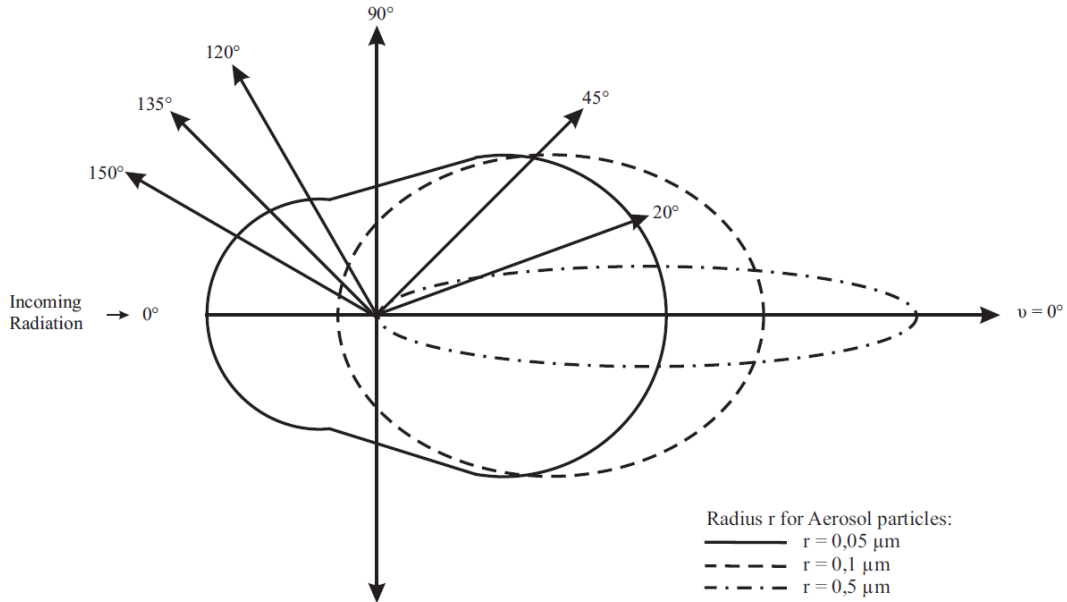


Figure 21: Mie phase function for aerosol particle with different radii (Sinnhuber, 2015).

Mie scattering has a strong forward peak and - as can be seen from the equation above - the asymmetry increases with the decrease of size parameter. For aerosol, g typically ranges between 0.6 and 0.7 (mostly forward scattering) (Andrews et al., 2006).

The Mie theory is only applicable if we assume spherical particles. For non-spherical particles, Mishchenko (1993) showed the significant sensitivity of phase function to the shape of particle and the importance of taking non-sphericity into account.

Extinction

For a single spherical particle, extinction is defined as the sum of wavelength-dependent absorption and scattering coefficient or cross-section:

$$\sigma_{ext}(\lambda) = \sigma_{sca}(\lambda) + \sigma_{abs}(\lambda) \quad (2.17)$$

To calculate the extinction for a distribution of aerosol particles, one can assume that the distance between particles is much larger compared to particle radius, and therefore particles can be supposed to be independent of each other. For a media

(unit volume) containing N particles with radii of r , the integrated extinction cross-section/coefficient, is given by:

$$\beta_{ext} = \int \sigma_{ext}(r)N(r)dr \quad (2.18)$$

Extinction represents the amount of electromagnetic radiation lost through its interaction with particles. Following the Beer-Lambert-Bouguer law, the attenuation of light over an infinitesimal path of length dz is given by:

$$dI(z, \mu, \phi) = -\frac{\beta_{ext}(z)}{\mu}I(z, \mu, \phi)dz \quad (2.19)$$

where the direction of incident light is identified by the zenith angle θ (with $\mu = \cos\theta$) and the solar azimuth angle ϕ , z is the altitude, and $\sigma_{ext}(z)$ is the volume extinction coefficient.

Aerosol optical thickness

The AOT is the integration of the aerosol extinction coefficient over the vertical path from the surface to the TOA:

$$\tau_{aer}(\lambda) = \int_0^{TOA} \beta_{ext}(\lambda, z)dz. \quad (2.20)$$

Considering the contribution from other atmospheric particles, the optical thickness can be re-written as:

$$\tau(\lambda) = \tau_{aer}(\lambda) + \tau_{Ray}(\lambda) + \tau_{Gas}(\lambda) \quad (2.21)$$

where $\tau_{aer}(\lambda)$, $\tau_{Ray}(\lambda)$ and $\tau_{Gas}(\lambda)$ stand for aerosol, Rayleigh and atmospheric gases optical thickness. Subsequently, the Beer-Lambert-Bouguer law (Eq. 2.19) can be re-written as:

$$I(z, \mu, \phi) = I_0(\tau, \mu, \phi)e^{-\frac{\tau\lambda}{\mu}} \quad (2.22)$$

Single scattering albedo

Single scattering albedo ω_0 is defined as the ratio of the total scattering to the total extinction:

$$\omega_0 = \frac{\beta_{scat}}{\beta_{ext}} \quad (2.23)$$

Hence, ω_0 is 0 for a solely absorbing particles and 1 for a solely scattering ones. Most aerosols are weakly absorbing in mid-visible wavelengths (such as sea-salt and water-soluble aerosols) and extinction is mainly by scattering, leading to a larger single scattering albedo (SSA), > 0.9 at $0.55 \mu\text{m}$ wavelength. Black or elemental

carbon have a SSA < 0.5. Mineral dust has spectral-dependent absorption and it strongly absorbs in short visible in UV ($\lambda < 0.47 \mu\text{m}$) (Bond and Bergstrom, 2006).

Angstrom exponent

The Angstrom exponent α describes how AOT depends on the wavelength of electromagnetic radiation (Angstrom, 1929):

$$\frac{\tau_\lambda}{\tau_{\lambda_0}} = \left(\frac{\lambda}{\lambda_0} \right)^{-\alpha} \quad (2.24)$$

where λ is the wavelength. Calculating the Angstrom exponent provides information about the aerosol size and the slope of aerosol size distribution. If the size distribution is dominated by large particles (e.g. sea salt and dust), α decreases and it is closer to zero, but it increases up to 3 if the size distribution mainly contains small particles (e.g. small sulphate and nitrate). In case of very large particles such as freshly-injected sea salt or desert dust, the Angstrom parameter may also have negative values.

2.4.4 Climatic effects of Aerosol

The sun is the primary source of energy for the Earth's surface and atmosphere. The sun's energy in the blue, visible and near-infrared (shortwave) spectrum reaches to the Earth. A portion of this energy is reflected back to space, while another portion is absorbed and scattered by the atmosphere (aerosol, clouds and greenhouse gases). In turn, land and ocean surfaces emit energy back as longwave radiation. The amount of emitted longwave energy is balanced by the shortwave solar energy and the Earth system reaches a thermal equilibrium. The Earth's radiative forcing (RF) can be defined as the difference between incoming and outgoing radiative energy (Wm^{-2}) at the tropopause after stratospheric temperatures re-adjust to radiative equilibrium. Climate forcing factor is expressed as the imposed change of energy (Wm^{-2}) that affects the planetary radiation balance and changes the climate system. In the presence of climate forcing, the climate system evolves towards a new equilibrium. A net negative radiative budget is associated with a cooling effect, while a positive net leads to warming the atmosphere.

Aerosol particles interact with short and longwave radiation and therefore have a significant impact on the Arctic climate system (Najafi et al., 2015; Navarro et al., 2016). There is strong uncertainty in our understanding of the climatic effect of aerosols due to their short lifetime and highly uneven distribution in space and time, which make them difficult to detect in the whole Arctic. Aerosols influence the climate system in two different ways, namely through direct and indirect effects.

Direct radiative effects

The interaction of aerosol particles with light is strongest when the particle size is

comparable to the wavelength of radiation. Figure 22 shows that the efficiency of scattering and absorption of light by aerosol particles is dependent on the particle diameter. Here for light with a wavelength of 550 nm and a particle complex refractive index, $m = (1.5-0.02i)$, i.e. a moderately scattering and fairly weakly absorbing aerosol (Covert et al., 1980). One can see that the maximum efficiency of scattering and absorption occurs around particle diameters of $0.4 - 0.5 \mu\text{m}$ at which atmospheric aerosols also have the largest number size distribution. This coincidence means atmospheric turbidity is mostly affected by aerosols in the size range of $0.1 - 1 \mu\text{m}$ (Shaw, 1987).

The sum of scattering and absorption of shortwave (solar energy) and longwave radiation (emitted from surface, cloud and atmosphere) is known as the direct radiative effect of aerosol particles. Therefore, absorption is relatively minor compared to the scattering effect of aerosols because most outgoing radiation has the wavelength of $7 \mu\text{m}$ at which only sea salts and some desert dust have the potential to absorb radiation. Scattering of solar radiation is connected to a cooling effect while absorption is associated with a trapping energy.

To assess the relative importance of scattering and absorption and the resulting cooling or warming effect more precisely, one needs to consider SSA of aerosols and surface albedo. The basic idea is that aerosols lead to cooling if they have a SSA larger than the underlying surface, and to warming if they are darker. Figure 23 represents the combinations of aerosol SSA and surface albedo that reflects the cooling or warming effect of aerosol particles (Kellogg, 1980). It is evident from this figure that only some very dark aerosols can lead to warming. Anthropogenic aerosols remote from their sources with typical SSA values in the range of 0.85-0.95 will have a cooling effect unless they are over clouds, snow or ice.

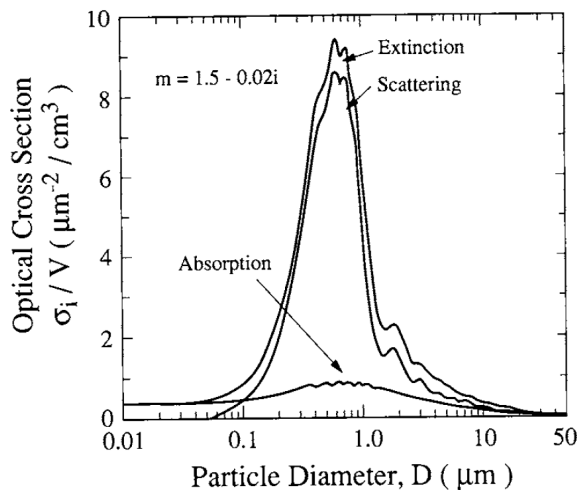


Figure 22: The extinction, scattering and absorption cross section of aerosol particles per unit volume as a function of size, calculated from Mie theory (Covert et al., 1980).

In general, aerosols are known to cause a net negative direct RF (cooling) over darker surfaces (e.g. oceans or dark forest areas) and a positive RF (warming) over brighter surfaces (e.g. desert, snow, ice or cloud cover). Soil dust aerosols typically have a higher SSA of 0.97-0.99, although very low values of 0.86 have been reported for the highly absorbing red Saharan dust. Thus, most mineral dust aerosols will also result in cooling, especially if they are blown over the oceans or vegetated areas. One can see that dust aerosols over desert regions are near the division line between warming and cooling. In such cases, more information with respect to aerosol size distribution and size-dependent optical properties is necessary to determine the warming or cooling effect.

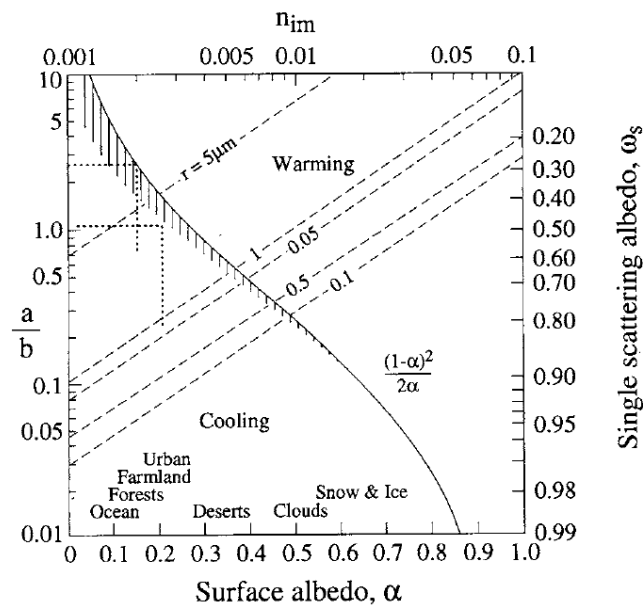


Figure 23: The relationship between absorption-to-backscattering ratio (a/b) and the critical surface albedo α (lower scale), and between a/b and the imaginary index of refraction (n_{im} , upper scale) for a given radius of particle (dashed line). Calculations are for real part of index of refraction equal to 1.5, and for a solar zenith angle of 65° (an average value taking the globe as a whole). Shaded area indicates locus of some critical values when infrared radiation was taken into account along with solar radiation (Kellogg, 1980).

In the Arctic, the dominant radiative effect of aerosols is known to be cooling and decrease of pollution in the Arctic circle, leading to a warming effect (Najafi et al., 2015; Navarro et al., 2016). Absorbing aerosols such as BC contributes to further Arctic warming in three different ways (Willis et al., 2018):

- trapping the incoming solar radiation, warming the lower troposphere and cooling the surface, enhancing the atmospheric stratification and thus inducing changes in local circulation (Engvall et al., 2009; Shindell and Faluvegi, 2009; Rinke et al., 2004);

-
- absorbing aerosols at lower latitudes, which enhances latitudinal temperature gradients and also leads to increased pole-ward heat transport (Sand et al., 2013a,b); and
 - absorbing aerosol deposits at snow/ice-covered surface reducing the surface albedo (Flanner, 2013).

Indirect radiative effects

Cloud-aerosol interactions affect cloud microphysical and radiative properties besides the amount and lifetime of clouds and lead to indirect climate forcing by aerosols.

Water-soluble aerosol particles with a sufficiently large size can serve as a nucleus for the growth of water droplets (Kohler, 1921). These particles are called CCN on which water vapour condenses when relative humidity increases until a level after which the nucleus reaches a critical diameter and becomes activated CCN and grows rapidly into a cloud droplet. The presence of CCN in the rapid formation of cloud droplets is critical since the formation of cloud droplets from gas molecules requires a large amount of energy (Wallace and Hobbs, 2006). The fraction of particles that contribute to the formation of cloud droplets depends on the particle size, the chemical composition (solubility) of the particles, the rising rate of the air mass, and the total number of CCN present.

Although, there is no linear relationship between the CCN concentration in a given air mass and the number of cloud droplets, an increase in the concentration of CCN leads to a higher number of cloud droplets in a cloud. The cloud optical depth is a function of the number of droplets besides the size of droplets, cloud geometric thickness and the extinction efficiency of cloud droplets. The cloud albedo is a function of cloud optical thickness, liquid water content (LWC), droplet number concentration, size distribution, and solar elevation. Therefore, CCN can affect the cloud albedo. In other words, an increase in the number of CCN present in a specific amount of water vapour leads to a lesser amount of water vapour condensation on each CCN, and as a result cloud droplets become smaller. Droplets with smaller size scatter light more efficiently and lead to a higher albedo of cloud, whereby this effect is called cloud albedo or the Twomey effect (Twomey et al., 1984).

In addition, the probability that raindrops can form from smaller cloud droplets is low, which leads to a longer cloud lifetime and consequently a larger fraction of the Earth that is covered by cloud (Albrecht, 1989). This effect is known as the cloud lifetime effect or Albrecht effect (Albrecht, 1989).

Clouds cover on average 60% of the globe and therefore the increase in CCN number may have a significant cooling impact on the Earth. However, clouds interact not only with the incident shortwave radiation, but also with the infrared radiation emitted by the Earth. For this reason, they also have a greenhouse function and absorbing aerosol enhances the ability of clouds to absorb longwave radiation. Therefore, an increase in cloud density or fractional cloud cover should in principle also have a warming component in addition to their cooling effect (Ackerman

et al., 2000). The overall outcome of aerosol and cloud interaction remains subject to strong uncertainty. In the Arctic, different studies have indicated that clouds only contribute to a cooling effect only in the summer and a warming effect in the rest of the year (Doscher et al., 2014). Therefore, the increase of CCN may have either warming or cooling effect (Willis et al., 2018). Figure 24 presents a schematic of the above-mentioned different direct and indirect effects induced by cloud-aerosol interactions.

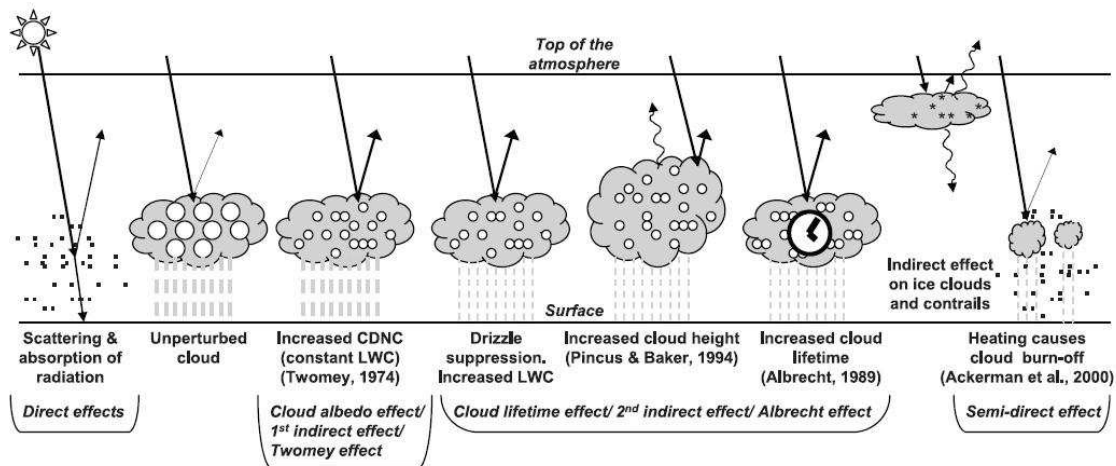


Figure 24: Schematic illustration of aerosol radiative effects on climate including the different direct and indirect effects (Haywood and Boucher, 2000).

2.5 Theoretical background for space-based aerosol retrieval

2.5.1 Radiative transfer in the atmosphere

Radiative transfer in the atmosphere describes light propagation through a medium and the processes of scattering, absorption and emission by which electromagnetic radiation is affected. The radiative transfer equation includes all of these processes in a mathematical form and can be written under two different assumptions: i) plane parallel atmosphere, and ii) spherical atmosphere. In each case, we may assume Lambertian or non-Lambertian surface assumptions. Regardless of these assumptions, there are three main sources of loss and gain of radiance I_λ along the path ds :

i) loss of radiation due to extinction (sum of scattering and absorption):

$$dI_\lambda = -\sigma_{ext,\lambda} I_\lambda ds \quad (2.25)$$

where $\sigma_{ext,\lambda}$ is the volume extinction coefficient as the sum of absorption and scattering coefficients.

ii) gain due to multiple scattering, whereby the scattered intensity from the direction

Θ' in direction Θ can be written as follows:

$$dI_\lambda = \frac{1}{4\pi} ds \int_{4\pi} P(\Theta, \Theta') I_\nu(\Theta') d\Theta'. \quad (2.26)$$

where P is the phase function.

iii) gain through emission by molecules, whereby following Planck law, we can write the emitted intensity for a black-body as follows:

$$B_\lambda(T) = \frac{2hc^2}{\lambda^5 (e^{\frac{hc}{k\lambda T}} - 1)}; \quad (2.27)$$

where k is the Boltzmann constant, λ stands for the wavelength and h is the Planck's constant (Salby, 1996).

Accordingly, we can write the radiative transfer equation as follows:

$$\frac{dI_\lambda}{ds} = -\sigma_{ext,\lambda} I_\lambda + \frac{2hc^2}{\lambda^5 (e^{\frac{hc}{k\lambda T}} - 1)} + \frac{1}{4\pi} \int_{4\pi} P(\Theta, \Theta') I_\nu(\Theta') d\Theta' \quad (2.28)$$

If we ignore multi-scattering components, the basic form of the radiative transfer equation can be written as the Schwartzschild equation:

$$\frac{dI_\lambda}{\sigma_{ext,\lambda} \rho ds} = -I_\lambda + J_\lambda \quad (2.29)$$

where J_λ is the source function, which comprises the emitted radiation into the beam.

The basic RTE with the assumption of a plane parallel and spherical plane will be re-written as follows:

Plane parallel atmosphere

Atmospheric stratification results from vertical variations of temperature, air pressure and density. For example, temperature has a complicated profile with altitude, and it may increase or decrease with altitude in some regions as discussed in the beginning of this chapter. In radiation models, to simplify the solutions and reduce the number of computations with respect to vertical stratification of the atmosphere, one can assume the plane parallel or flat atmosphere. In this assumption, the atmosphere is composed of layers that are horizontally homogeneous, and the only variation occurs in the vertical direction. Each layer is identified by its bottom and top. Assuming a light beam that travels in a plane parallel atmosphere, we can write $ds = \frac{dz}{\cos\theta}$, and thus RTE will be as follows:

$$\cos\theta \frac{dI_\lambda}{\sigma_{ext,\lambda} \rho dz} = -I_\lambda + J_\lambda \quad (2.30)$$

where θ is the angle from zenith. Additionally, the optical thickness τ is defined by:

$$\tau = \int_z^\infty \sigma_\lambda \rho dz. \quad (2.31)$$

This can be inserted in Eq. 2.30, giving:

$$\mu \frac{dI_\lambda}{d\tau} = -I_\lambda + J_\lambda. \quad (2.32)$$

We can apply the plane parallel assumption for cases in which the solar zenith angle is below 60° .

If we multiply both sides by $\exp(-\frac{\tau}{\mu})$ and integrate the equation from τ to τ_1 , the up-welling radiation ($\mu \geq 0$) is formulated as follows:

$$I \uparrow (\tau, \mu_v, \phi_r) = I \uparrow (\tau_1, \mu_v, \phi_r) \exp(-\frac{\tau_1 - \tau}{\mu}) + \frac{1}{\mu} \int_\tau^{\tau_1} \exp(-\frac{\tau' - \tau}{\mu}) J \uparrow (\tau', \mu_v, \phi_r) d\tau' \quad (2.33)$$

The down-welling radiation ($\mu < 0$) is written as follows:

$$I \downarrow (\tau, \mu_v, \phi_r) = I \downarrow (0, \mu_v, \phi_r) \exp(-\frac{\tau}{|\mu|}) + \frac{1}{|\mu|} \int_\tau^{\tau_1} \exp(-\frac{\tau - \tau'}{|\mu|}) J \downarrow (\tau', \mu_v, \phi_r) d\tau' \quad (2.34)$$

Using Eq. 2.33 and 2.34, the radiant flux at TOA ($\tau=0$) and surface level ($\tau = \tau_1$) are calculated as follows:

$$I \uparrow (\tau, \mu_v, \phi_r) = I \uparrow (\tau_1, \mu_v, \phi_r) \exp(-\frac{\tau_1}{\mu}) + \frac{1}{\mu} \int_0^{\tau_1} \exp(-\frac{\tau'}{\mu}) J \uparrow (\tau', \mu_v, \phi_r) d\tau' \quad (2.35)$$

$$I \downarrow (\tau_1, \mu_v, \phi_r) = I \downarrow (0, \mu_v, \phi_r) \exp(-\frac{\tau_1}{|\mu|}) + \frac{1}{|\mu|} \int_0^{\tau_1} \exp(-\frac{\tau_1 - \tau'}{|\mu|}) J \downarrow (\tau', \mu_v, \phi_r) d\tau' \quad (2.36)$$

In Eq. 2.35 and 2.36, the first term on the right side is the radiation at TOA and surface, respectively. The second term is the atmospheric part of up-welling and down-welling radiation in Eq. 2.35 and 2.36 respectively.

Solving these equations to obtain the radiant flux at TOA and the Earth's surface is a challenging task due to multiple interactions over the full range of solid angles. Several numerical approaches (Stamnes et al., 1988; C.E., 2000; Min and Duan, 2004) have provided solutions - mostly assuming a plane parallel atmosphere - for

this challenging task.

Spherical atmosphere

If the sun is low and the sun zenith angle is larger than 60° , we need to take the curvature of the atmosphere into account. Fig. 25 shows how the path of light beam changes from a plane parallel atmosphere to spherical one. To bring a spherical atmosphere into RTE, we need to add air mass $M(z)$ (Kasten and Young, 1989):

$$\frac{dI_\lambda}{M(z)\sigma_{ext,\lambda}\rho ds} = -I_\lambda + J_\lambda \quad (2.37)$$

where $M(z)$ is given by Kasten and Young (1989):

$$M(z) = \frac{1}{\cos(z) + a(b - c)^{-c}} \quad (2.38)$$

where $a=0.50572$, $b=6.07995$ and $c=1.6364$.

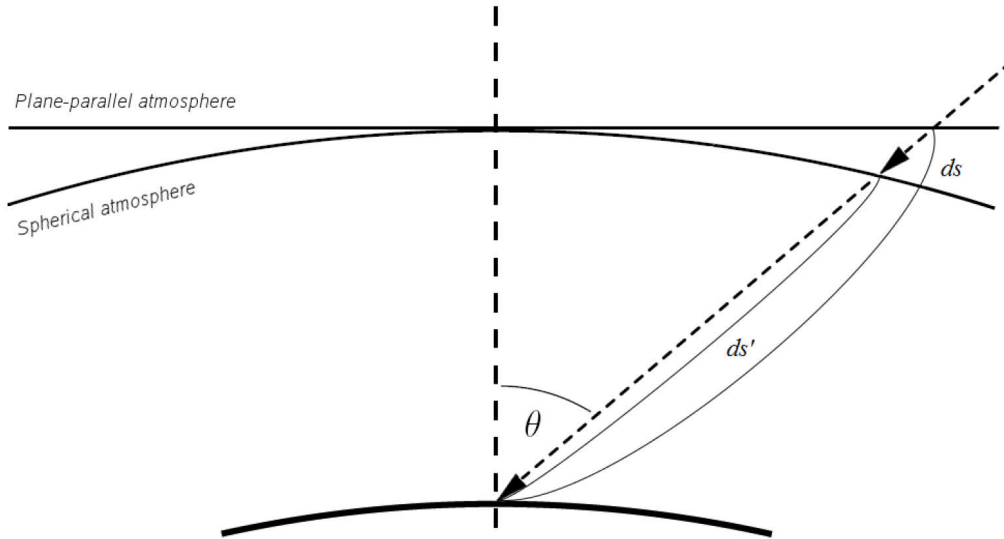


Figure 25: Successive orders of radiation interactions in the surface and atmosphere system, Tanre et al. (1979).

2.5.2 Reflectance in the atmosphere-surface system

To retrieve aerosol properties from space-based data, we apply the retrieval methods to TOA reflectance measurements from satellites. The geometry of sun-Earth-satellite for TOA measurements is shown in Fig. 26: θ_s ; θ_0 and Φ are the solar zenith, target view zenith and relative solar/target relative azimuth angles, respectively.

The scattering angle (angle between incident and reflected radiation), Θ is:

$$\Theta = \arccos(-\cos\theta_0\cos\theta_s + \sin\theta_0\sin\theta_s\cos\Phi) \quad (2.39)$$

TOA reflectance is a dimensionless parameter formulated as below:

$$\rho(\lambda, \mu_s, \mu_v, \phi_r) = \frac{\pi \cdot L(\lambda, \mu_s, \mu_v, \phi_r)}{\cos(\theta_0) \cdot F_0(\lambda)} \quad (2.40)$$

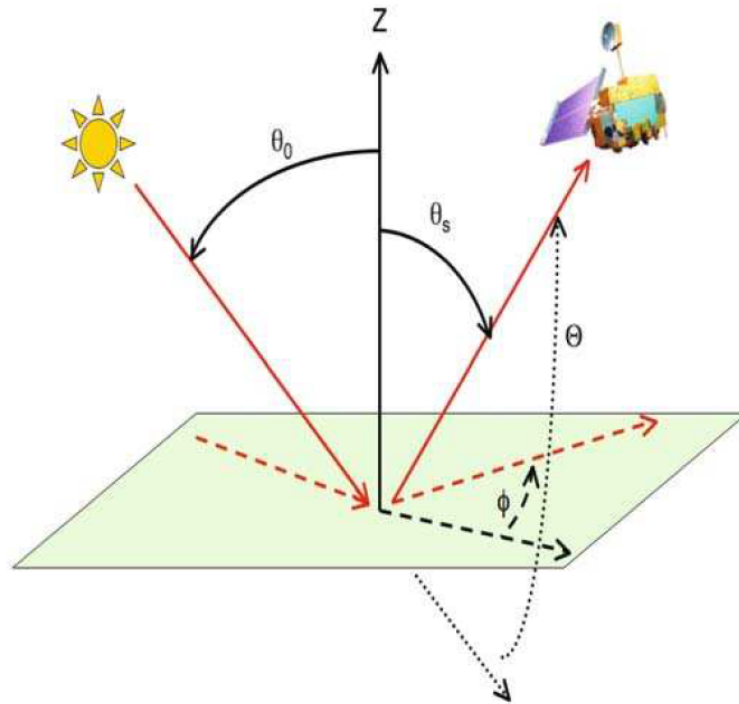


Figure 26: Sun-Earth-satellite remote sensing geometry. This schematic of observation geometry is from Kokhanovsky and de Leeuw (2009).

where L is the measured radiance ($W \cdot m^{-2} \cdot s^{-1}$), and $F_0(W \cdot m^{-2} \cdot s^{-1})$ is the extra-terrestrial solar irradiance at the wavelength λ .

The bidirectional reflectance measured at TOA includes different contributions from the underlying surface and atmosphere containing gas molecules, aerosols and clouds.

To decouple surface and atmosphere contribution and isolate the aerosol impact, the measured signal is expressed as the sum of different radiation interactions in the coupled atmosphere-surface system, and then in the next section the radiative transfer theory is applied to this model.

To start, the two following assumptions are considered:

- When the light passes through the entire atmosphere from the sun to surface (downward) and surface to satellite (upward) directions, its attenuation (by scattering and absorption) is expressed by transmission coefficients.
- Each of the downward and upward transmissions is a combination of direct (T) and a diffuse (t) component. The direct transmission is attenuation of light in its way (upward or downward), and the diffuse component is to account for

multiple scattering of photons in downward/upward direction.

Tanre et al. (1979) formulated TOA reflectance as the sum of five contributions from the atmosphere and surface as shown in Fig. 27. The TOA reflectance can be decomposed as follows:

$$\rho(\lambda, \mu_s, \mu_v, \phi_r) = \rho_{atm} + T \downarrow \rho_{sfc_{dir}} T \uparrow + t \downarrow \rho_{sfc_{dif}} T \uparrow + T \downarrow \rho'_{sfc} t \uparrow + t \downarrow \rho_{sfc_{iso}} t \uparrow \quad (2.41)$$

where

- ρ_{atm} is the intrinsic atmospheric contribution (from atmospheric gases and aerosol particles) in terms of reflectance. This term is also called path reflectance;

- ρ_{sfc} is ground reflectance and terms 2,3,4 and 5 are the interaction of photons with surface reflectance:

- term 2 stands for the direct solar radiation reflected by the surface and represents bidirectional reflectance distribution function (BRDF);
- term 3 contains the diffuse part of solar radiation reflected by the surface, and thus the average of the surface BRDF weighted by the contribution of the downward diffuse;
- term 4 represents target background of target; and
- term 5 represents radiation interaction for n times with the ground.

As can be seen from Eq. 2.41, we have different terms related to the surface reflectance:

- $\rho_{sfc_{dir}}$: the specular component of surface reflectance;

- $\rho_{sfc_{dif}}$: the diffuse component of surface reflectance or the fraction of diffuse incident radiation with solar zenith angle of θ_0 scattered by the surface at θ_v and a relative azimuth angle of Φ , which can be formulated as the average of BRDF weighted by the ratio of downward diffuse radiation to the total downward radiation integrated over all incident angles (Tanre et al., 1979):

$$\rho_{sfc_{dif}} = \bar{\rho}(\lambda, \mu_s, \mu_v, \phi_r) = \frac{\int_0^{2\pi} \int_0^1 \mu L \downarrow(\mu_s, \mu, \phi') \cdot \rho_{sfc_{dir}}(\mu_s, \mu, \phi' - \phi_r) d\mu d\phi'}{\int_0^{2\pi} \int_0^{\pi/2} \mu L \downarrow(\mu_s, \mu, \Phi') \cdot d\mu d\phi'} \quad (2.42)$$

- ρ'_{sfc} : the average reflectance of the environment, which is not easy to formulate (for further details, see (Tanre et al., 1979)). We can assume a simplified form as $\rho_{sfc_{dif}}$ but at a target point of M' :

$$\rho'_{sfc}(M', \mu_s, \mu_v, \phi_r) = \rho_{sfc_{dif}}(M', \mu_s, \mu_v, \phi_r) \quad (2.43)$$

- $\rho_{sfc_{iso}}$: the isotropic component of surface reflectance, which can be approximated

by the hemispherical albedo:

$$\rho_{sf_{c_{iso}}} = \bar{\rho}_{dir}(\lambda) = \int_0^1 \mu \int_0^{2\pi} \int_0^1 \mu' \rho_{sf_{c_{dir}}}(\mu, \mu', \phi' - \phi_r) d\mu' d\phi' d\mu \quad (2.44)$$

The radiative transfer solution for surface-atmosphere is expressed as follows (Tanre et al., 1979):

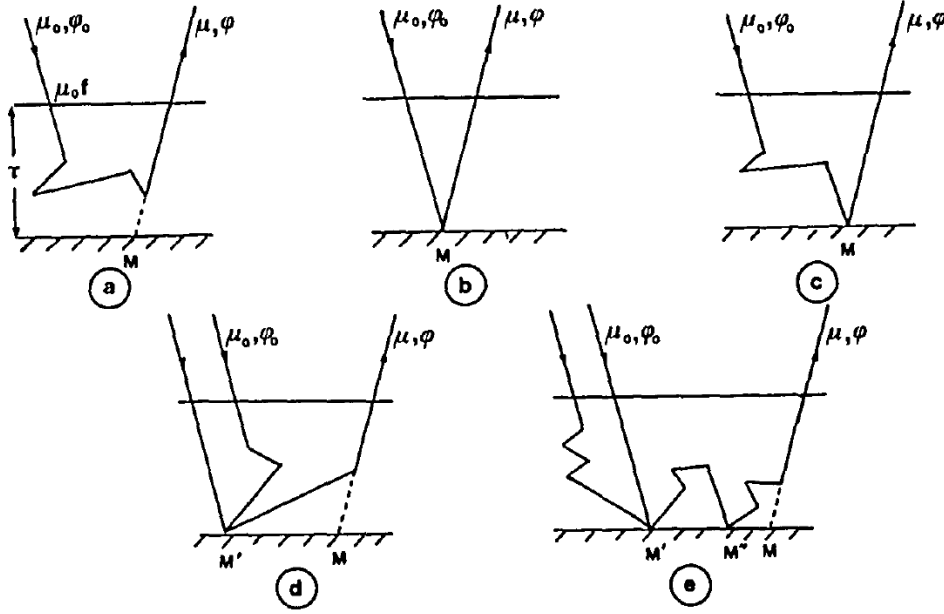


Figure 27: Successive orders of radiation interactions in the surface-atmosphere system (Tanre et al., 1979).

$$\begin{aligned} \rho(M, \mu_0, \mu, \phi) = & \rho_a(\mu_0, \mu, \phi) + \exp\left(-\frac{\tau}{\mu_0}\right) \rho \exp\left(-\frac{\tau}{\mu}\right) + \\ & E(\mu_0) \rho \exp\left(-\frac{\tau}{\mu}\right) + \left[\exp\left(-\frac{\tau}{\mu_0}\right) + E(\mu_0)\right] \rho E'(\mu) + \\ & \sum_{n=1}^{\infty} \left[\exp\left(-\frac{\tau}{\mu_0}\right) + E(\mu_0)\right] (\rho r)^n \end{aligned} \quad (2.45)$$

where τ is the optical thickness of the atmosphere, $\theta = \arccos \mu$ is the zenith viewing angle, and ϕ is the relative azimuth angle. $\rho_a(\mu_0, \mu, \phi)$ is the intrinsic atmospheric contribution in terms of reflectance, $\exp\left(-\frac{\tau}{\mu_0}\right) \rho \exp\left(-\frac{\tau}{\mu}\right)$ is the term that contains the information from direct solar radiation reflected by the target, $E(\mu_0) \rho \exp\left(-\frac{\tau}{\mu}\right)$ is the contribution from diffuse downward solar radiation at the ground at point M, and $\left[\exp\left(-\frac{\tau}{\mu_0}\right) + E(\mu_0)\right] \rho E'(\mu)$ represents the first-order contribution of the target background. The geometric series in Eq. 2.45 corresponds to higher orders of interaction with the ground, and the term $\left[\exp\left(-\frac{\tau}{\mu_0}\right) + E(\mu_0)\right] (\rho r)^n$ corresponds

to radiation having interacted n times with the ground. $E(\mu_0)$ and $E'(\mu)$ are diffuse transmittances from TOA to the surface and from the surface to the receiver, respectively, and are given by:

$$E(\mu_0) = \frac{1}{\mu_0 f} \int_0^{2\pi} \int_0^1 I \downarrow (\tau, \mu_0, \mu, \phi) \mu d\mu d\phi \quad (2.46)$$

If we assume that the surface is Lambertian - which means that it reflects the incident radiation equally in all directions - we can write a simple approximation of Eq. 2.40 suggested by Chandrasekhar (1960):

$$\rho = \rho_{atm} + \frac{\rho_{sfc}}{1 - s_\lambda \rho_{sfc}} T_{total} \quad (2.47)$$

where s_λ is the spherical albedo of the atmosphere (atmospheric backscattering ratio: diffuse reflectance of the atmosphere for isotropic light leaving the surface) and T_{total} is the upward and downward transmission for both direct and diffuse components. The second term in this simplified form accounts for multiple orders of interaction between the ground and atmosphere. In fact, all terms in this equation except that of the surface are a function of aerosol type, chemical composition, size and optical depth. If the surface contribution is small (e.g. land in the UV range of the spectrum), this approximation is sufficiently good because it is less sensitive to the errors induced by neglecting surface BRDF effects. If the surface is black, the entire second term on the right side is 0 (Torres et al., 2002), and therefore aerosols can be retrieved easily. If the surface becomes brighter, larger errors are possible when calculating surface-atmosphere interactions. In numerous aerosol and surface property retrieval works, Eq. 2.47 is used extensively (Veefkind and de Leeuw, 1998; Vermote et al., 1977; von Hoyningen-Huene et al., 2006).

In the following section, we will apply radiative transfer theory to the TOA reflectance defined above and its components.

3 Data

In this work, several space-borne, airborne and ground-based measurements are used for different purposes, e.g. retrieval of atmospheric and surface parameters, validation and verification of the retrieved parameters. In the following section, all of the data and relevant instruments are introduced in detail and the motivation behind selecting them for this work is described:

- space-borne data for cloud identification and AOT retrieval: AATSR, SLSTR, and for verification of cloud detection: MODIS;
- airborne data to study surface properties: Cloud absorption radiometer (CAR);
- ground-based measurements to validate cloud fraction and retrieved AOT: SYNOP and AERONET.

3.1 Satellite data

3.1.1 Advanced Along-Track Scanning Radiometer

The Advanced Along-Track Scanning Radiometer (AATSR) was on-board European Space Agency (ESA)'s ENVISAT satellite, an advanced polar-orbiting Earth observation satellite. This imaging radiometer was the third in the series of instruments designed to collect data of sea surface temperature (SST) after ATSR-1 and ATSR-2 on European Remote Sensing-1, ERS-1 and ERS-2, AATSR. AATSR was operational from the launch of ENIVSAT in March 2002 until its failure in 2012. The primary scientific objective behind the design of AATSR was the continuity of previous missions for SST measurement with high accuracy (higher than 0.3 K) needed for climate research (0.5 K or better). The secondary objective was the observation of environmental parameters such as aerosols, clouds, fires, gas flares, vegetation moisture, biomass, and vegetation health and growth.

To meet the high accuracy of surface temperature measurement, in addition to an exceptionally precise and stable on-board calibration system, an optimal and accurate atmospheric correction is needed. For this purpose, the conical imaging geometry was used in AATSR to have dual-viewing capability as shown in Fig. 28. Each scene was imaged twice sequentially to have two different atmospheric path lengths. The

first measurement of the ground scenes is along the track of satellite but in the forward direction at a viewing angle of 55° . The second occurs 150 sec later at a close to nadir angle. The two views theoretically yield independent information about atmosphere and the surface to be retrieved, which makes AATSR an ideal radiometer to be used in a range of atmospheric conditions and for the study of surfaces with complex reflectance characteristics, such as snow and ice (Istomina et al., 2010).

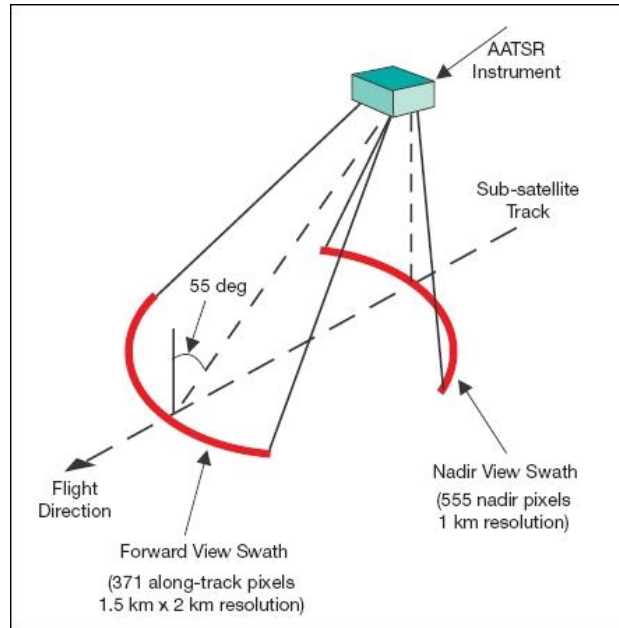


Figure 28: Typical AATSR viewing geometries (image credit: ESA).

To derive the surface temperature, AATSR had three channels in thermal infrared ($3.7 \mu\text{m}$, $10.85 \mu\text{m}$, $12.00 \mu\text{m}$). In addition, AATSR had four more channels in visible and near-infrared spectrum: ($0.55 \mu\text{m}$, $0.66 \mu\text{m}$), NIR ($0.87 \mu\text{m}$, $1.6 \mu\text{m}$) to identify cloudy areas and measure solar radiation scattered and reflected from the Earth's surface and atmosphere (see Table 1). The spatial resolution of the instrument is $1 \times 1 \text{ km}^2$ at nadir view and the swath width is 512 km.

Central wavelength in μm	Bandwidth in nm	Retrieval parameter
0.555	20	Chlorophyll
0.659	20	Vegetation index
0.865	20	Vegetation index
1.61	300	Cloud clearing
3.7	300	SST
10.85	1000	SST
12.00	1000	SST

Table 1: AATSR spectral channels (Huot et al., 2001).

The unique design of AATSR offers the opportunity to extract different information from the wide spectral coverage of this instrument, as shown in the example of the AATSR image over Svalbard in Fig. 29. One can see the notable contrast between the cloud and the underlying surface in the upper right panel in Fig. 29. At this channel ($1.6 \mu\text{m}$), the reflectance over snow/ice-covered surface significantly decline. A similar separation of snow/ice and cloud is observed in the reflectance at $3.7 \mu\text{m}$ shown in the lower left panel in Fig. 29. At the longer wavelength of $11 \mu\text{m}$, temperature information helps to detect thin clouds, as can be seen in the bottom right panel. Here, thin cloud patterns appear in the south-western scenes close to and above Svalbard, which have small signatures in the shorter wavelength.

Having a broad spectral range holds strong importance over complicated scenes measured from satellite in which there is insufficient contrast between cloud and the underlying surface in visible wavelengths. Combining the information from the different channels in an appropriate way enables identifying cloud over such scenes.

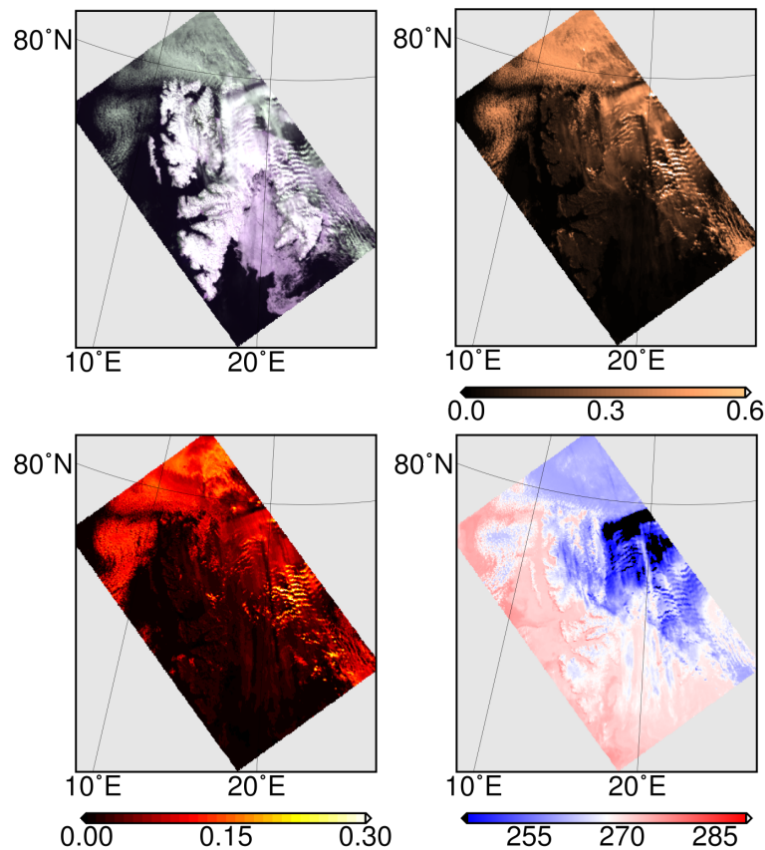


Figure 29: Upper left: the RGB image of AATSR over Svalbard, 10th May 2006, upper right: $1.6 \mu\text{m}$ reflectance, lower left: $3.7 \mu\text{m}$ reflectance, lower right: $11 \mu\text{m}$ brightness temperature.

Examples of AOT algorithms applied to AATSR data including the AATSR Dual-View algorithm (ADV) which was initially proposed by Veefkind et al. (1999) and AATSR single-view algorithm (ASV) by Veefkind and de Leeuw (1998), the Swansea

University (SU) algorithm (North et al., 1999) and Oxford RAL Aerosol and Cloud retrieval (ORAC) algorithm (Thomas et al., 2009). These algorithms typically are not optimised for the retrieval of AOT at high latitudes, which is the focus of this study.

3.1.2 Sea and Land Surface Temperature Radiometer

The SLSTR is on-board Sentinel-3A, which was launched on 16th February 2016 as part of the Copernicus programme. Sentinel-3B is the second satellite in the orbit launched on 25th April 2018. The primary mission objective was to continue the long-term sea surface temperature data with a high level of accuracy (better than 0.3 K for SST) provided by the previous series ATSR-1 and -2, and their successor AATSR. The secondary objective was being used for aerosol retrieval and fire radiative power products. The design of the SLSTR instrument follows its predecessors with respect to conical imaging and the capability of dual-viewing to enable a robust atmospheric correction. In addition, SLSTR has some significant improvements compared to A(A)TSR (Coppo et al., 2010b). For instance, the swath width is increased from 500 km in AATSR to 1420 km (in single view) and 750 km (in dual view) in SLSTR. The wider swath coverage enables the instrument to provide global revisit times of 1.9 days at the equator for the dual view and 1 day for the single view.

Table 2 indicates the wavelengths at which SLSTR delivers data. As can be seen, the channels are similar to that of AATSR in Table 1, but with two more channels in the SWIR, one at the wavelength of 1.37 μm and the other at 2.25 μm . The two new extra channels are used extensively to provide more accurate cloud, cirrus and aerosol information and also are used to correct for atmospheric radiative transfer effects in the determination of surface reflectance (Coppo et al., 2010b). The 2.25 μm channel is also dedicated to fire detection (Coppo et al., 2010b).

Central wavelength in μm	Bandwidth in nm	Primary application
0.554	19.26	Cloud, vegetation, aerosol
0.659	19.25	NDVI, vegetation, aerosol
0.868	20.60	NDVI, cloud, co-registration
1.374	20.80	Cirrus detection over land
1.613	60.68	Cloud, ice, snow, vegetation
2.255	50.15	Vegetation state, cloud
3.742	398	SST, LST, Active fire
10.854	776	SST, LST, Active fire
12.022	905	SST, LST
3.742	398	Active fire
10.854	776	Active fire

Table 2: SLSTR radiometric bands (<https://sentinels.copernicus.eu/web/sentinel/user-guides/>).

One example of the SLSTR data over Svalbard is shown in Fig. 30. The upper

left panel shows the RGB image and the upper right panel depicts the new $1.37 \mu\text{m}$ measurements. As we see from the figure, thin cirrus clouds are highlighted at $1.37 \mu\text{m}$ while they are only weakly identified in reflectance at $3.7 \mu\text{m}$ shown in Fig. 30. Despite the strong opportunity that this wavelength offers to improve the cloud detection methods, it is not used in this study because the developed retrieval algorithm is designed to be applied to both SLSTR and AATSR, while the latter did not measure the radiance and TOA reflectance at the $1.37 \mu\text{m}$ wavelength. In addition, to incorporate $1.37 \mu\text{m}$ in any cloud detection algorithm, e.g. cirrus detection, one should consider the high amount of water vapour absorption above and within clouds (Meyer and Platnick, 2010).

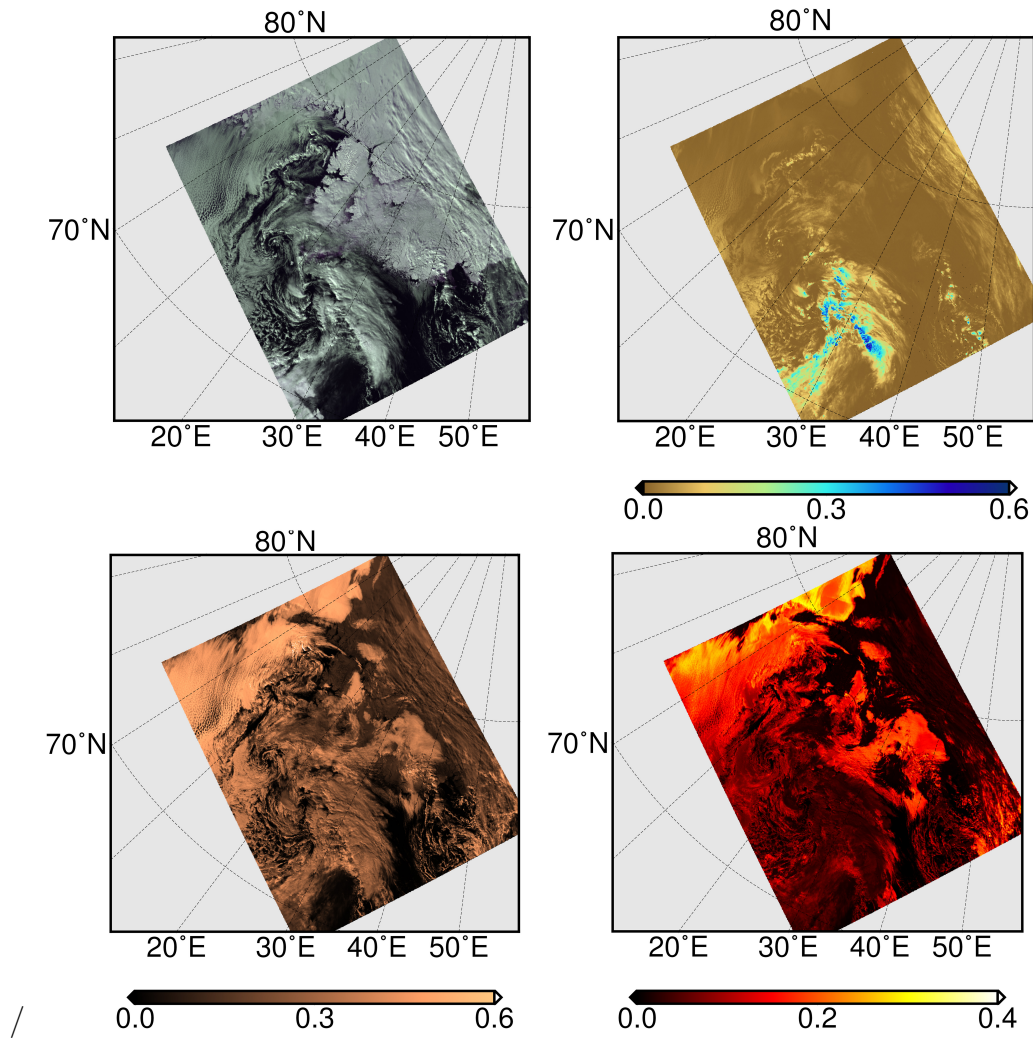


Figure 30: Upper left: the RGB image of SLSTR over Svalbard, 18th April 2017, upper right: $1.37 \mu\text{m}$ reflectance, lower left: $1.6 \mu\text{m}$ reflectance, lower right: $3.7 \mu\text{m}$ reflectance.

In addition to the more advanced spectral coverage, SLSTR has a higher spatial resolution ($0.5 \times 0.5 \text{ km}^2$ in the VIS and SWIR measurements) compared to AATSR. As mentioned above, there are differences between AATSR and SLSTR, which means

that any algorithm developed for common use should incorporate these differences. However, the use of the observations from SLSTR and AATSR together enables a long-term time series of clouds and aerosol parameter retrieval, which was the motivation behind including SLSTR in this study besides AATSR. Nevertheless, there is a gap of 4 years between the end of the ENVISAT mission and the start of SLSTR.

3.1.3 Moderate Resolution Imaging Spectroradiometer

The Moderate Resolution Imaging Spectroradiometer (MODIS) from National Aeronautics and Space Administration (NASA) flies on-board the Terra and Aqua satellite launched in 1999 and 2002, respectively, as part of the Earth Observing System (EOS) programme of NASA, and it has delivered data up to present. Terra flies on a descending orbit (equatorial crossing time at 10:30 am), while Aqua operates in an ascending mode and crosses the equator at 1:30 pm. The MODIS instruments were developed for various land, ocean and atmospheric applications.

MODIS measures radiances at 36 wavelengths between 0.41 and 14 μ m. Depending on the channel, the spatial resolution of the measurements lies between 250, 500 and 1000 m. Furthermore, MODIS has a short revisit time and provides nearly every day global coverage. Global coverage, multi-spatial resolution and multi-spectral images make MODIS a powerful instrument to meet atmospheric, oceanographic, and terrestrial needs. In this work, we use the MODIS cloud product for verifying the developed cloud identification algorithm.

3.2 Airborne data

3.2.1 Cloud absorption radiometer

The CAR is an airborne multi-spectral and multi-angular scanning radiometer developed at NASA's Goddard Space Flight Center. CAR has been mounted and operated on several aircraft from 1984 up to present within the framework of different field campaigns around the world. The main objective of developing CAR was to measure the SSA of clouds, the bidirectional reflectance of various surface types and acquiring images of cloud and Earth surface features.

CAR measures both up-welling and down-welling radiances at fourteen narrow spectral bands located in the atmospheric block regions of UV, visible and near-infrared from 0.34 μ m to 2.3 μ m. As can be seen from Table 3, the spectral coverage of CAR comprises important wavelengths relevant for remote sensing applications such as aerosol retrievals. Therefore, CAR has been used in many remote sensing studies besides satellite data to address the need for information about the surface reflectance.

In addition to the wide spectral coverage, the geometry of data acquisition in CAR makes this instrument suitable for surface BRDF calculation and studies. The measurement is conducted by a rotating scan mirror, which measures the full hemisphere

and covers a wide range of zenith and azimuth angles. CAR acquires data by rotating 360° in a plane perpendicular to the direction of flight with a 190° aperture that allows collecting data from local zenith to nadir or horizon to horizon - viewing zenith angle (VZA) $[-90^\circ, 90^\circ]$ - with an angular resolution of 1° . Besides, the aircraft flies in full circles, which results in having all angles for a full BRDF in 2-3 minutes. Depending on the flight altitude, the spatial resolution of CAR can be different, e.g. 10 m^2 and 18 m^2 at nadir for 600 m and 1000 m flight altitude, respectively, which increases with the VZA, e.g. 580 m^2 at 80° VZA for 1000 m flight altitude.

Central wavelength in μm	Bandwidth in nm
0.480	21
0.687	26
0.340	9
0.381	6
0.870	10
1.028	4
0.609	9
1.275	24
1.554	33
1.644	46
1.713	46
2.116	43
2.203	43
2.324	48

Table 3: Spectral specification of the CAR instrument (<https://airbornescience.nasa.gov/instrument/CAR>).

In addition to the special measurement geometry and wide spectral range, CAR data are acquired at different altitudes (200, 600 and 1700 m), which provides the opportunity to evaluate the sensitivity of reflectance with respect to atmospheric effects in the radiative transfer simulation. Having measurements close to the surface (e.g. 200 m) minimises the effect of atmosphere and makes the measurement very close to surface reflectance. Depending on the altitude, no further atmospheric correction is necessary and measurements can be used as surface reflectance in remote sensing applications.

For this study, we used CAR data from the Arctic Research of the Composition of the Troposphere from the Aircraft and Satellites (ARCTAS) campaign conducted at Elson Lagoon, near Barrow/Utqiagvik, Alaska, in April 2008 (Lyapustin et al., 2010; Gatebe and King, 2016). The goal of this campaign was to study physical and chemical processes in the Arctic atmosphere and surface.

3.3 Ground-based measurements

3.3.1 Synoptic surface measurements

The surface synoptic observations (SYNOP) are ground-based measurement conducted at manual and automated weather stations. The data are provided as numerical code (called FM-12) by World Meteorological Organization (WMO). The main objective of the product is mapping large-scale weather information around the world. SYNOP reports a variety of meteorological parameters such as temperature, barometric pressure, visibility, etc., as well as cloud amount, which are observed at standard synoptic hours (every 3 or 6 hours, sometimes 1 hour) simultaneously throughout the globe. Although, SYNOP data cover the whole globe, its coverage is limited in the Arctic circle, especially in central Arctic where data is almost entirely absent, as can be seen in Fig. 31.

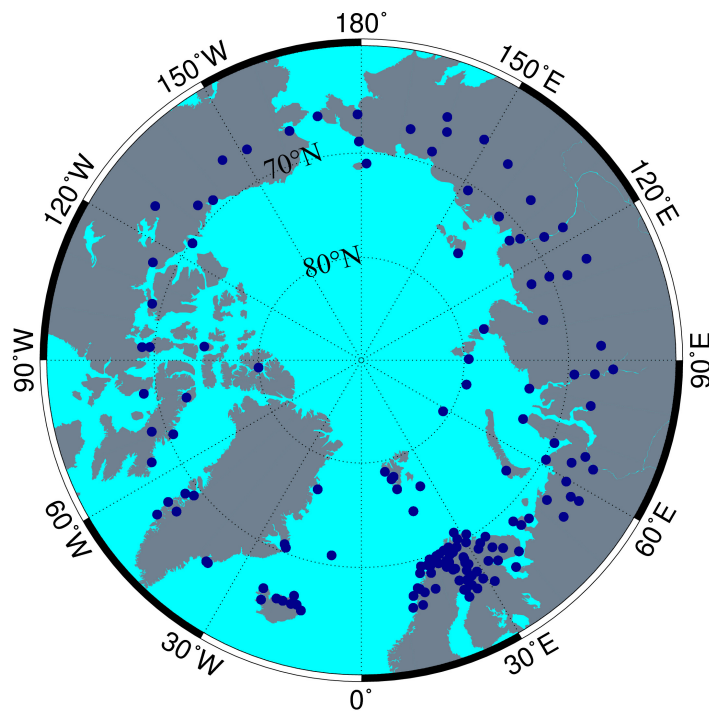


Figure 31: SYNOP network coverage over the Arctic, the dark blue points indicate the location of SYNOP stations.

The SYNOP measurements are extensively used to validate cloud screening algorithms or forecast models. In such comparison and validation studies, it is necessary to take into account the fact that the SYNOP cloud fraction is reported in okta scale, and proper conversion is necessary. Okta scale ranges from 0 (completely clear sky) to 8 (completely obscured by clouds). Converting discrete okta values to continuous percentage can be achieved in different ways. A common assumption made by climatologists is that 1 okta is equal to 12.5% of cloud coverage (Boers

et al., 2010; Kotarba, 2009). In addition to okta conversion, one needs to make an estimate of the error or uncertainty contained in the measurements. It is assumed that the man-made cloudiness estimation introduces an error of ± 1 okta and even larger values of ± 2 okta in the non-zero or non-eight okta situations (Boers et al., 2010; Werkmeister et al., 2015). Boers et al. (2010) suggested defining a larger range of 18.75% for 1 okta instead of the commonly-used value of 12.5%. Following this idea, Table 4 can be used for the SYNOP data application.

Percentage of cloud	okta
0	0
$0 < \% < 18.75$	1
$18.75 \leq \% < 31.25$	2
$31.25 \leq \% < 43.75$	3
$43.75 \leq \% < 56.25$	4
$56.25 \leq \% < 68.75$	5
$68.75 \leq \% < 81.25$	6
$81.25 \leq \% < 100$	7
100	8

Table 4: Calculation of cloudiness in percentage for corresponding okta value (Boers et al., 2010).

3.3.2 Aerosol Robotic Network

The Aerosol RObotic NETwork (AERONET) is a network of ground-based sun photometers which measure aerosol properties under cloud-free conditions continuously with passive remote sensing technique. NASA and the University of Lille (PHOTom-

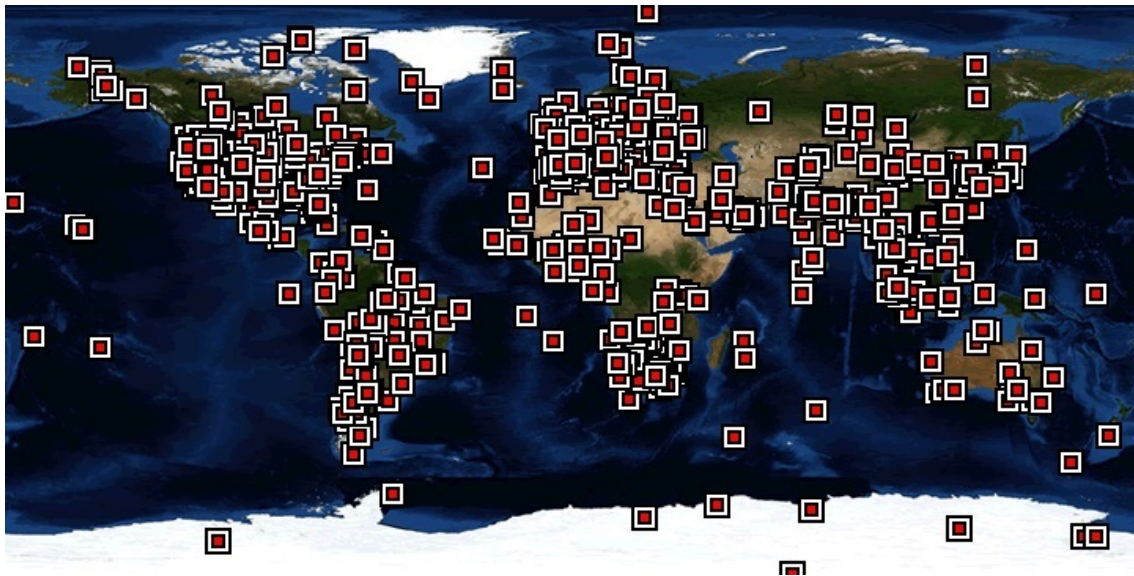


Figure 32: AERONET global network coverage, credit: NASA.

étrie pour le Traitement Opérationnel de Normalisation Satellitaire (PHOTONS) established AERONET which, comprises about 700 stations around the globe (see Fig. 32) and provided data for 25 years. The primary scientific objective behind the AERONET was to create a database for validation of AOT retrieval within the EOS programme of NASA.

AERONET data provide AOT, inversion products such as aerosol volume size distribution, complex index of refraction, single scattering albedo, phase functions and perceptible water in diverse aerosol regimes (Holben et al., 1998).

AERONET data are extensively used in aerosol validation studies (Vountas et al., 2020) due to the high temporal resolution (15 minutes), being accurate (within 0.01 to 0.021) as well as freely available.

AERONET data are categorised and available in three levels: level 1.0 (unscreened), level 1.5 (cloud screened and quality controlled) and level 2.0 (quality assured). Data are available via NASA website (<https://aeronet.gsfc.nasa.gov/>).

4 Improved Cloud detection for Aerosol Optical Thickness retrieval

AOT retrieval algorithms include different steps, and cloud screening is one of the essential ones because clouds are much brighter (depending on the cloud type and microphysics) compared to aerosols. The strong contribution of cloud to the TOA reflectance overwhelms the magnitude of change in reflectance due to aerosols. Therefore, for accurate aerosol retrieval, the area of interest must be cloud-free.

In a cloud-free scene, the TOA reflectance can be decomposed into three main contributions:

- reflection by the surface;
- molecular scattering; and
- aerosol scattering.

All three components are affected by scattering and absorption within the atmosphere. After cloud screening, any aerosol retrieval algorithm needs to decouple the three components or use radiative transfer models to create look-up tables and account for cross-terms.

In the following sub-sections, cloud identification and its theoretical background, state-of-the-art algorithms, the new identification algorithm, results, validation and verification will be discussed. A large part of the research conducted in this section has been published by Jafariserajehlou et al. (2019).

4.1 Overview of cloud detection methods

The accuracy of cloud filtering significantly affects the accuracy of aerosol retrieval. An inadequate cloud screening and the resulting cloud residual in the retrieval scene leads to an over-estimation of the retrieved AOT. This is a well-known issue in aerosol retrieval methods that use passive remote sensing (Shi et al., 2014b; Várnai and Marshak, 2015; Christensen et al., 2017; Arola et al., 2017).

In addition, cloud contamination in aerosol retrieval limits the accuracy of further analysis and aerosol products based on the preliminary retrieval, e.g. estimation of

the aerosol indirect and direct effect in climate change. To minimise the uncertainty originating from cloud contamination, the development of an adequate cloud screening method is a prerequisite to any AOT retrieval algorithm (Martins et al., 2002; Remer et al., 2012; Wind et al., 2016; Christensen et al., 2017).

The key concept of cloud detection methods is the variation of radiance whether in wavelength, space, time or spectral domain (Rossow, 1998). One can classify them in four general scenarios:

- Algorithms employing time series of satellite measurements, which rely on the fact that a clear surface exhibits unchanged or a little changed pattern within the time series of data within a suitable time interval, whereas the radiative properties measured at cloudy pixels show high variability in space and time. Therefore, the clear surface is reproducible from a time series of data and cloud patterns would be detectable by computing covariance values between various images. Since cloudy pixels exhibit a low covariance, a clear surface can be discriminated with a high covariance value among images (Reynolds and Vonder Haar, 1977; Minnis and Harrison, 1984; Key and Barry, 1989; Lyapustin et al., 2008; Lyapustin and Wang, 2009; Lyapustin et al., 2012).
- Algorithms applying single or a group of thresholds, whereby some empirically-determined thresholds are applied to each pixel. These thresholds can be applied to spectral features or other properties of objects, such as cloud height. In other words, the thresholds enable classifying images in different groups, which may include cloud, snow, etc. (Rossow, 1998; Rossow et al., 1985; Allen et al., 1990b; Breon and Colzy, 1999; Minnis et al., 2001; Trepte et al., 2001; Spangenberg et al., 2001; Lotz et al., 2009; Kokhanovsky et al., 2009; Schlundt et al., 2011; von Hoyningen-Huene et al., 2011; Thompson et al., 2015; Werner et al., 2016).
- Algorithms following the spatial variability of reflectance in a scene, whereby such approaches consider the high spatial variability of clouds in comparison with aerosols and other surface types (Koffler et al., 1973; Coakley et al., 1982; Gutman et al., 1987; SÈZE and Rossow, 1991; Martins et al., 2002).
- Algorithms introducing the spectral signature of an object (from surface or cloud) as the principle parameter for picking out cloud-free pixels or classifying clouds. In these methods, a spectral shape criterion for cloud-free surface (for example snow) is used to screen out cloudy or other type of surface pixels (Shenk and Holub, 1976; Inoue, 1987; Raschke et al., 1987; Istomina et al., 2010).

4.2 AATSR standard cloud product

The standard cloud product of AATSR has been developed by ESA. This product covers the Arctic circle, although it is not optimised for the Arctic environment. The operational cloud mask called Synthesis of ATSR Data Into Sea-surface Temperature

(SADIST) was initially developed to be used over the ocean surface (Zavody et al., 2000).

The AATSR standard cloud product is developed using a threshold-based method by applying the latitudinal thresholds for various cloud types, and it was subsequently modified by Birks (2007) to be applicable over land (Ghent et al., 2017).

Despite the extensive successful application of the global cloud product by the remote-sensing community, there are reported problems. For example, Kolmonen et al. (2013a) studied the uncertainty of the AATSR cloud product and indicated that the cloud flags in this product are noticeably restricted. In other words, using the AATSR cloud product for aerosol retrieval led to aerosol episodes not being observed. Additionally, SADIST is known to misclassify ice, cloud and open ocean in polar regions. To resolve this problem, Bulgin et al. (2015) developed a Bayesian approach within ESA's Climate Change Initiative (CCI) project (Hollmann et al., 2013).

Sobrino et al. (2016) reviewed different cloud-clearing methods including the AATSR operational cloud mask in the framework of the Synergistic Use of the Sentinel Missions for Estimating and Monitoring Land Surface Temperature (SEN4LST) project. They highlighted the potential uncertainty in different versions of this product, which results in these errors being propagated in subsequent data products. For example, the AATSR operational cloud mask falsely detects cloud in 16% of the observations. This is attributed to the flagging of land features (such as rivers) incorrectly as cloud (see Sobrino et al. (2016)).

4.3 Cloud detection over the Arctic

Cloud screening using space-borne data over the Arctic region is a challenging task compared to masking clouds over lower latitudes. This is based on the unique atmospheric and environmental conditions in the Arctic, e.g. the minimal contrast between cloud and the underlying surface covered by snow and ice in commonly-used optical, thermal and microwave channels in cloud identification methods (Rossow and Garder, 1993; Curry et al., 1996). Figure 3 is one example of a MODIS RGB to illustrate the challenge of separating cloud, cloud-free and aerosol scenes in the cryosphere. In addition, the Arctic atmosphere exhibits hazes and fogs due to temperature and humidity inversions, which have only a small signature in satellite observations. Furthermore, strong variability of clouds and limitations of satellite performance in the Arctic regions due to the poor solar illumination amplify the difficulty of cloud detection over the Arctic (Curry et al., 1996).

One method to detect cloud-free snow and ice over high latitudes using AATSR data was developed by Istomina et al. (2010). In this approach - here called ISTO -, the spectral shape of clear snow is used to identify cloud-free surface covered with snow and ice within the ground scene (Istomina et al., 2010). The ISTO method was designed to be used as a prerequisite for aerosol retrieval over snow and ice. Therefore, in the result, cloud-free land and ocean is also masked out in addition to

clouds.

To detect cloud-free snow scenes which also contain air masses over snow and ice to retrieve aerosols, a series of empirically-determined thresholds has been applied to reflectance ratios calculated from measurements at different spectral wavelengths selected from seven AATSR channels in the range of VIS to thermal infrared (TIR). Although a validation study indicates that this method screens out cloudy scenes over snow and ice in most cases, the similarity of spectral signature of snow/ice and cloud lead to under-/over-estimation of clouds. In fact, this problem is an inherent limitation of many threshold-based techniques, because defining a reliable threshold to guarantee a successful identification of cloud under different atmospheric conditions over various snow/ice surface types remains a challenging task.

To avoid the error arising from similarity of snow/ice spectral shape to that of thin clouds and minimise the amount of residual thin clouds in the scene for further aerosol retrieval, a new cloud detection method has been developed within the framework of this doctoral work, which is explained in the following sub-sections.

4.4 Developing a new cloud detection algorithm

In this work, a new cloud identification algorithm has been developed based on time series of space-borne measurements. Identification of clouds using a time series of observations has a long history in remote-sensing studies (Leese et al., 1970; Lyapustin et al., 2008). The key idea behind this approach is that cloud reflectance significantly varies in the time series of TOA reflectance, while the surface reflectance remains unchanged or exhibits only small variation (Lyapustin et al., 2008; Gómez-Chova et al., 2017). To measure the temporal variation of reflectance within a scene, an indicator such as covariance is needed. The textural pattern at the surface such as topography features, lakes, man-made buildings and structures, etc. remains almost entirely unchanged during a specific time interval and the coherency of data over these features separates them from highly variable clouds (Lyapustin et al., 2008). In this work, the Pearson correlation coefficient (PCC) is used, which is a function of covariance.

The use of the knowledge of geometrical structures in the method minimises the error and uncertainties arising from illumination conditions and might lead to a successful performance of the algorithm under different conditions. However, the lack of surface features makes the standalone use of the covariance inadequate because the value of covariance decreases while there is no change in the reflectance within the scene. In addition, thin clouds do not considerably alter the reflectance of a scene, causing under-estimation of clouds within pixels (Lyapustin et al., 2008). For this reason, the use of PCC analysis is combined with a threshold on the reflectance of solar radiation at $3.7 \mu\text{m}$ in which a large contrast between cloud and snow/ice-covered surface exists. The use of this channel is described in the next sub-section.

Another argument that makes the use of time series method over the Arctic favourable is the availability of multiple data delivered by the AATSR and SLSTR sensors over

the polar regions. The larger the number of observations over a scene, the more information that is available about the surface as well as more reliable statistics and a better separation of cloud and cloud-free scene. The revisit time of AATSR is 3-4 days over the mid-latitudes (Kolmonen et al., 2013b). At high latitudes, the number of measured scenes increase and due to orbital convergence and therefore, the revisit time decreases to two days over the Arctic circle (Soliman et al., 2012). For the two SLSTR-A/B, the revisit time is less than one day at the equator (Coppo et al., 2010a), which decreases at higher latitudes.

The newly-developed ASCIA is designed to be used as a prerequisite for AOT retrieval and producing a long-term data record. Therefore, it is important to account for distinguishing cloud and heavy aerosol load adequately.

In the following sections, the theoretical background behind the algorithm design and its application to AATSR and SLSTR is described in detail. The result of cloud detection is validated and verified using ground-based and space-borne measurement, the ESA standard cloud product for AATSR and SLSTR, MODIS cloud product and previously-developed ISTO method.

4.4.1 Theoretical background

4.4.1.1 Pearson correlation coefficient

To analyse and have a measure of the correlation between features in the sequence of satellite images in the given time period, the PCC (Pearson, 1896) is used. PCC has been used in many studies as a standard statistical parameter to indicate the strength and direction of correlation between two variables (Benesty et al., 2009).

Assuming x and y as two random variables, PCC is formulated as follows:

$$PCC = \frac{COV(x, y)}{\sigma_x \sigma_y} \quad (4.1)$$

where $COV(x, y)$ is the covariance of two variables and σ is the root mean square variation of each random variable. PCC is a function of covariance, as can be seen in Eq. 4.1. In PCC, the covariance of two variables is normalised by their standard deviations (Rodgers and Nicewander, 1988; Benesty et al., 2009).

The covariance of two variables x and y is calculated as follows (Rodgers and Nicewander, 1988; Benesty et al., 2009):

$$COV(x, y) = \frac{1}{N^2} \sum_{i=1}^N \sum_{i=1}^N (x_i - \bar{x})(y_i - \bar{y}) \quad (4.2)$$

and

$$\sigma_x^2 = \frac{1}{N^2} \sum_{i=1}^N (x_i - \bar{x})^2 \quad (4.3)$$

$$\sigma_y^2 = \frac{1}{N^2} \sum_{i=1}^N (y_i - \bar{y})^2 \quad (4.4)$$

where \bar{x} and \bar{y} are the mean value of x and y variables respectively. If we combine all equations, PCC can be formulated as follows:

$$PCC = \frac{\sum_{i=1}^N (x_i - \bar{x})(y_i - \bar{y})}{(\sum_{i=1}^N (x_i - \bar{x})^2 \sum_{i=1}^N (y_i - \bar{y})^2)^{\frac{1}{2}}} \quad (4.5)$$

In ASCIA, x and y refer to the reflectance of one pixel (pointing to the same target) in two images, \bar{x} and \bar{y} correspond to the mean reflectance values in the selected block (in our case 10×10 pixels), and N is equal to the number of images used in PCC analysis. We assume that under cloud-free conditions the selected blocks are stable in a short period and the resultant PCC is high. Under cloudy conditions - at which two blocks include pixels with more variable reflectance - the PCC value decreases.

From statistical perspective, PCC values range from -1 to $+1$. The larger the PCC, the stronger the correlation (Rodgers and Nicewander, 1988). A value of $+1$ implies a total positive linear correlation between the two variables x and y , which means that a linear equation can perfectly describe the relation between x and y , whereby both variables increase or decrease. The 0 value indicates that there is no linear correlation, and -1 refers to a total negative linear correlation between x and y , meaning that the increase in one variable corresponds to the decrease of another (Benesty et al., 2009).

Prior to the implementation of the PCC analysis, two questions should be answered:

- What is the best wavelength to use for the PPC calculation?
- What is the best block size for the PCC calculation?

To answer the first question, the use of all seven channels of AATSR is tested, including $0.55 \mu\text{m}$, $0.66 \mu\text{m}$, $0.87 \mu\text{m}$, $1.6 \mu\text{m}$, $3.7 \mu\text{m}$, $11 \mu\text{m}$, $12 \mu\text{m}$. The outcome of the analysis indicates that the visible channels ($0.55 \mu\text{m}$, $0.66 \mu\text{m}$) are not optimal for cloud detection over snow and ice especially in case of thin cloud, because the contrast between cloud and surface is very small. However, the channels in SWIR and TIR such as $1.6 \mu\text{m}$ and beyond are very suitable for PCC analysis because the reflectance of snow and ice significantly declines at these wavelengths due to strong absorption of liquid water and ice. The large reduction of reflectance between clear snow/ice as compared to liquid clouds between $0.87 \mu\text{m}$ and $1.6 \mu\text{m}$ provides a noticeable contrast between cloud and cloud-free scene, which is favourable for PCC analysis (Kokhanovsky, 2006).

In addition to placing the PCC analysis at wavelengths where we have sufficient contrast between cloud and the underlying surface, we need to take into account the capability of the selected wavelengths in classifying heavy aerosol loads and clouds correctly, because the disentangling of cloud and heavy aerosol load is a challenging

and known issue in cloud and aerosol studies (Remer et al., 2005a; Shi et al., 2014a; Grandey et al., 2013; Sogacheva et al., 2017). The use of the 1.6 μm reflectance partly addresses this need because it is less affected by aerosols than visible wavelengths (Lyapustin et al., 2008).

To answer the second question about the block size in PCC analysis, initially it was defined as 10 by 10 pixels because ASCIA is developed to be used for aerosol retrieval, which will be carried out with the resolution of 10×10 pixels. However, our tests and previous studies show that $10 \times 10 \text{ km}^2$ is not sufficient to capture surface patterns. Thus, blocks of $25 \times 25 \text{ km}^2$ area as proposed in previous studies (Lyapustin et al., 2008) were used. More details about the implementation of PCC analysis are described in the next sub-sections.

4.4.1.2 Reflectance of 3.7 μm wavelength

Cloud detection algorithms often take the advantage of contrast between cloud and the underlying surface. In visible wavelengths, this contrast is manifested through the measured reflectance, but in infrared channels the difference is expressed by brightness temperature (BT), which is comprised of emission and solar reflection. In other words, the observed signal (radiance or BT) at the top of atmosphere during day-time in the infrared spectrum, 3 – 4 μm is a combination of thermal (emission) and reflected part of radiation (Musial et al., 2014). To use reflectance or emission for quantitative applications, one needs to separate them by applying some assumptions explained in the following section. Indeed, different studies have used the extracted information from the reflectance part of 3.7 μm or 3.9 μm to retrieve cloud properties (e.g. effective radius, thermodynamic phase of cloud) or separating cloud and snow/ice-covered surfaces. (Meirink and van Zadelhoff, 2016; Klüser et al., 2015; Musial et al., 2014; Kokhanovsky, 2006; Pavolonis et al., 2005; Rosenfeld et al., 2004; Spangenberg et al., 2001; Allen et al., 1990a).

There are two main reasons behind the extensive application of this wavelength range in cloud identification and retrieval algorithms:

- First, the SSA of cloud at this band compared to shorter VIS and NIR wavelengths is different. SSA is highly sensitive to the thermodynamic phase and particle size of clouds (Platnick and Fontenla, 2008). For example, the scattering of liquid clouds having small droplets is relatively larger than the absorption and the ratio of NIR/VIS reflectance approaches one, while in the case of large liquid droplets or ice particles the absorption increases and this ratio is closer to zero (Platnick and Fontenla, 2008).
- Second, the reflectance of surfaces covered with snow and ice is relatively small compared to that of clouds at 3.7 μm channel, leading to a considerable contrast (Derrien et al., 1993; Platnick and Fontenla, 2008).

To use the reflectance of 3.7 μm wavelength in ASCIA that detects cloud during daytime, we need to remove the emission part from the up-welling radiation. For this purpose, we follow the method and applied assumptions in previous studies.

To have an estimate of emission, the independent temperature data from 11 μm channel is used, because most phenomena behave as black-bodies and the impact from water vapour and other gases for this channel is small (Istomina et al., 2010; Musial et al., 2014).

To extract the reflectance of 3.7 μm , Eq. 4.6 (Meirink and van Zadelhoff, 2016; Musial et al., 2014) is used:

$$R_{3.7} = \frac{L_{3.7} - B_{3.7}(T_{11})}{\mu_0 F_{0,3.7} - B_{3.7}(T_{11})} \quad (4.6)$$

where $R_{3.7}$ is the reflectance, i.e. the ratio of scattered radiance to incident solar radiance, whereby $L_{3.7}$ is measured radiance at 3.7 μm . The contribution from thermal emission at 3.7 μm is expressed by the Planck function radiance $B_{3.7}(T_{11})$ estimated from the temperature value obtained from the measurements at 11 μm , whereby $F_{0,3.7}$ is the solar constant at 3.7 μm , which is weighted by μ_0 as the cosine of the solar zenith angle.

Allen et al. (1990a) calculated the reflectance at 3.7 μm channel using Advanced Very High Resolution Radiometer (AVHRR) measurements and compared it to that of simulations. In this work, the results of the investigation by Allen et al. (1990a) are used to define thresholds for discriminating cloud and cloud-free snow and ice. Table 5 shows a summary of the study by Allen et al. (1990a):

Surface/cloud type	simulated $R_{3.7}$	observed $R_{3.7}$
Ice cloud	0.01–0.3	0.02–0.27
Liquid cloud	0.1–0.45	0.08–0.36
Clear land	0.15	0.03–0.1
Snow cover	0.005–0.025	0.02–0.04

Table 5: Simulated and observed reflectance values at 3.7 μm (Allen et al., 1990a).

Allen et al. (1990a) investigated the dependency of reflectance at 3.7 μm to different parameters:

- for liquid clouds, $R_{3.7}$ of TOA observation ranges between 0.08–0.36 and it mainly varies by the change in cloud droplet size and solar zenith angle;
- for ice clouds, $R_{3.7}$ of TOA observation is between 0.02–0.27 and it primarily depends on the ice particle shape, size distribution, cloud optical thickness (COT), and sun-satellite geometry.

Another study conducted by Arking and Childs (1985) indicated that calculated 3.7 μm reflectance for ice clouds varies between 0.01 to 0.30 for the COT of 0.1 to 100 and ice crystal effective radius of 2 μm to 32 μm , solar zenith angle of 60°. Spangenberg et al. (2001) reported a typical value of 0.04 to 0.4 for clouds.

The reflectance of snow/ice-covered surfaces depends on the snow grain size, solar zenith angle, LWC, snow impurities, etc. Allen et al. (1990a) reported that the $R_{3.7}$

ranges between 0.005 and 0.025, assuming the snow grain size is in the range of $50 \mu\text{m}$ to $200 \mu\text{m}$, with a solar zenith angle of 40° to 80° , while the simulated values for snow reflectance vary between 0.005 and 0.025. From satellite TOA observation, snow reflectance varies between 0.02 to 0.04 and the difference with simulated values can be due to several parameters such as snow impurities.

As can be seen from Table 5, $R_{3.7}$ for clear land is about 0.15. Allen et al. (1990a) indicated that this value changes with soil type, vegetation type, coverage and moisture content.

In ASCIA, the advantage of existing contrast between cloud-free snow/ice and cloudy scenes at the reflectance of $3.7 \mu\text{m}$ is exploited. Nevertheless, the following issues need to be taken into account:

- the reflectance of snow is close to that of ice cloud: to solve this issue we combine the information extracted from $3.7 \mu\text{m}$ with the PCC analysis;
- the reflectance of cloud is close to land (not covered with snow/ice): for this, we extract more information from visible channels at which land is much darker than cloud.

In the next section, the methodology and the design of ASCIA are explained in detail.

4.4.2 Methodology

4.4.2.1 Time series data preparation

In any algorithm developed based on time-series, the first step is the preparation of the data series. In ASCIA, we defined the temporal interval as one month. Hagolle et al. (2015) indicated that in a series of Sentinel-2 measurements with a revisit time of five days, each ground scene appears cloud-free at least once a month. This means that for AATSR and SLSTR, with a shorter revisit time, this possibility is higher and one month is sufficiently long to capture cloud-free scene at least once.

For AATSR, the amount of data over a scene varies for different latitudes between 10 to 50 per month. The number of data increases at higher latitudes. In summer and spring - longer polar days - the number of measurements over the Arctic circle increases.

ESA provides the geolocated and calibrated AATSR L1b data at a spatial resolution of $1 \times 1 \text{ km}^2$. The second step is to geo-reference all data acquired within one month. The geo-location information is already provided with AATSR L1b data. This information is created from the interpolation of the tie points distributed across a single AATSR image. The geo-referencing and re-gridding step in time-series methods, leads to altering the original intensity of each pixel. However, in AATSR, there is no need for this step as the geo-location for each pixel is already provided in the L1b data.

It is necessary to take into account the fact that the time series data are acquired by

the satellite from different viewing geometries. Therefore, to calculate PCC values over the same areas from data acquired on different days, the approach looks for the closest similar scenes using geo-location information. The closest distance is often found to be within 0.006 degree and increases to 0.01 degree in the worst case, and thus it is of negligible significance.

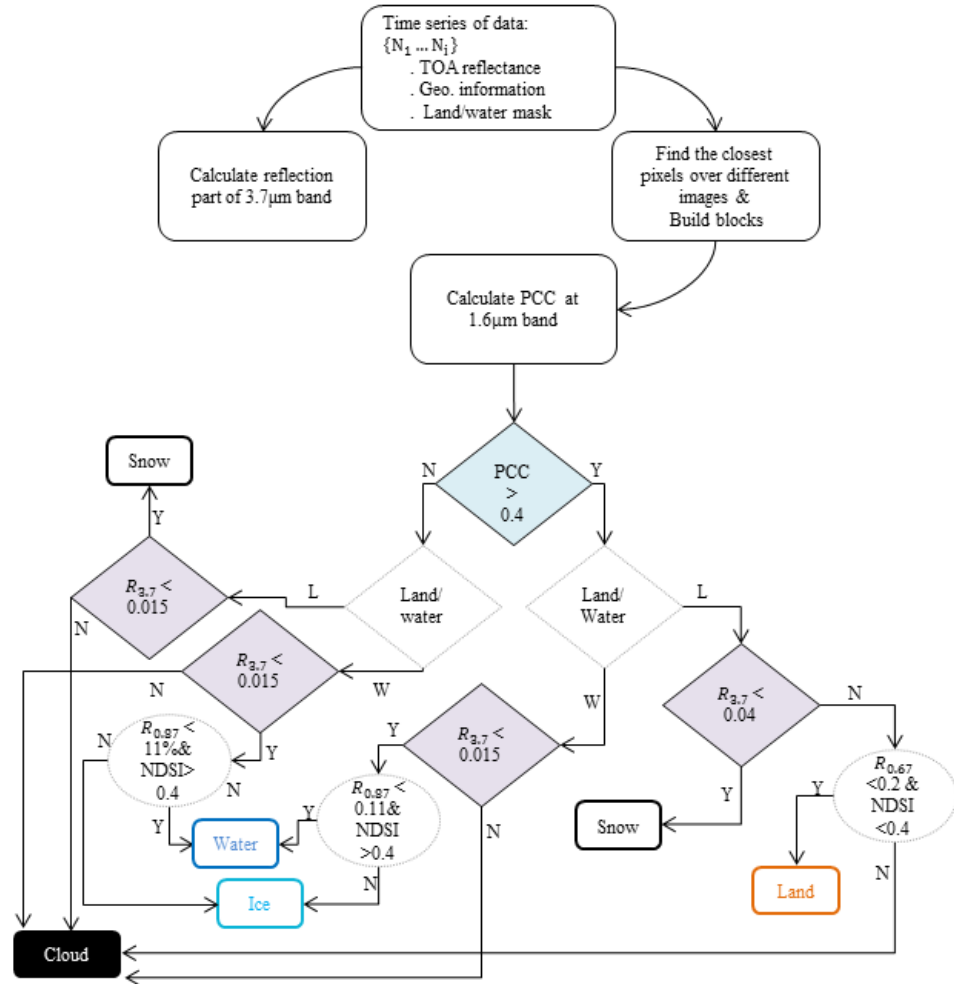


Figure 33: The schematic flowchart of ASCIA.

4.4.2.2 Cloudy and cloud-free scene identification

After finding the same targets and blocks over different dates within a month, ASCIA comprises two main parts:

- PCC analysis at 1.6 μm ;
- applying thresholds to the reflectance of 3.7 μm channel.

In the first step, we calculate the PCC value between two images using blocks of $25 \times 25 \text{ km}^2$. If the PCC value is high, the block is assumed to be cloud-free. In case of low values for PCC, the block is considered cloudy. The output of this step is a binary value at the block level.

In the second step, ASCIA uses the information extracted from $3.7 \mu\text{m}$ channel to produce a binary flag at the pixel level. For AATSR, pixel-level output has a resolution of $1 \times 1 \text{ km}^2$, while for SLSTR the resolution is $0.5 \times 0.5 \text{ km}^2$.

The key idea in the design of ASCIA is to combine the above-mentioned two steps to avoid the shortcomings of each standalone step. For example, a high PCC value cannot guarantee the accurate identification of cloudiness, especially in the case of thin clouds or broken clouds in which the number of cloudy pixels is not sufficiently high within a block to significantly reduce the PCC. Another argument regarding the shortcomings of the usage of the PCC is that the value is low if the surface does not include sufficient textural patterns or a sudden change in the short time interval. Again, in this case the reflectance of $3.7 \mu\text{m}$ channel provides important information.

Lyapustin et al. (2008) suggested a PCC of 0.63 as the suitable threshold to identify cloudy and cloud-free blocks at mid-latitudes where we have sufficient textural patterns. Considering the decrease of surface topography and man-made structures in the Arctic circle, we defined a lower value of 0.4 for ASCIA in the polar regions. Based on the statistics in this work, 0.6 is appropriate over lower latitudes.

First, two images (the last and previous one) are compared and the first binary flag at the block level is produced. ASCIA keeps the result in memory and repeats the PCC calculation between the last image and second previous data. Based on the new outcome, the binary flag is updated. This procedure continuous until the last data of month is involved in the PCC calculation.

The output of the first step enters the second step to convert the block-level cloud to pixel-level one. We emphasise that the threshold of reflection at $3.7 \mu\text{m}$ channel is defined differently for cloudy (with low PCC) and cloud-free blocks (with high PCC). Because the snow/ice reflectance at $3.7 \mu\text{m}$ channel (0.005-0.025) has interference with those of ice clouds (0.01-0.3) at this wavelength, the PCC analysis is defined as a decision point of ASCIA for further steps as follows:

- For a high $\text{PCC} \geq 0.4$, the whole block is considered to be cloud-free and then the algorithm starts looking for remaining small cloud scenes within a block, with scenes with $R_{3.7}$ larger than the maximum value observed over snow at $3.7 \mu\text{m}$: $R_{3.7} > 0.04$, (Allen et al., 1990a).
- For $\text{PCC} < 0.4$, the block is assumed to be cloudy, whereby ASCIA removes all scenes within the block and only keeps scenes that satisfy the $R_{3.7}$ test when < 0.015 . This threshold is equal to or smaller than the lowest observation of ice cloud reflectance at $3.7 \mu\text{m}$ (Allen et al., 1990a).

In summary, in the ASCIA, PCC analysis controls the procedure and the conservative decision is only made within blocks with a low PCC value. The loss of some

cloud-free scenes in blocks with a small PCC is an unavoidable side effect of using strict criteria in particular over land if it has small PCC and large $3.7 \mu\text{m}$ reflectance values. However, the ASCIA detects the presence of thin cirrus cases with a relatively high accuracy. A schematic flowchart of the approach is shown in Fig. 33, with the use of the two main constraints being highlighted.

Surface type	Test	Description
Water	$R_{0.87} < 11\%$ and $\text{NDSI} \geq 0.4$	MODIS ATBD
Sea ice	$R_{0.87} > 11\%$ and $\text{NDSI} \geq 0.4$	Hall et al. (2001)
Land	$R_{3.7} > 0.04$ and $R_{0.66} < 0.2$ or $\text{NDSI} < 0.4$	Allen et al. (1990a)
Snow	$R_{3.7} \leq 0.04$	Allen et al. (1990a)

Table 6: Land classification criteria for cloud-free scenes.

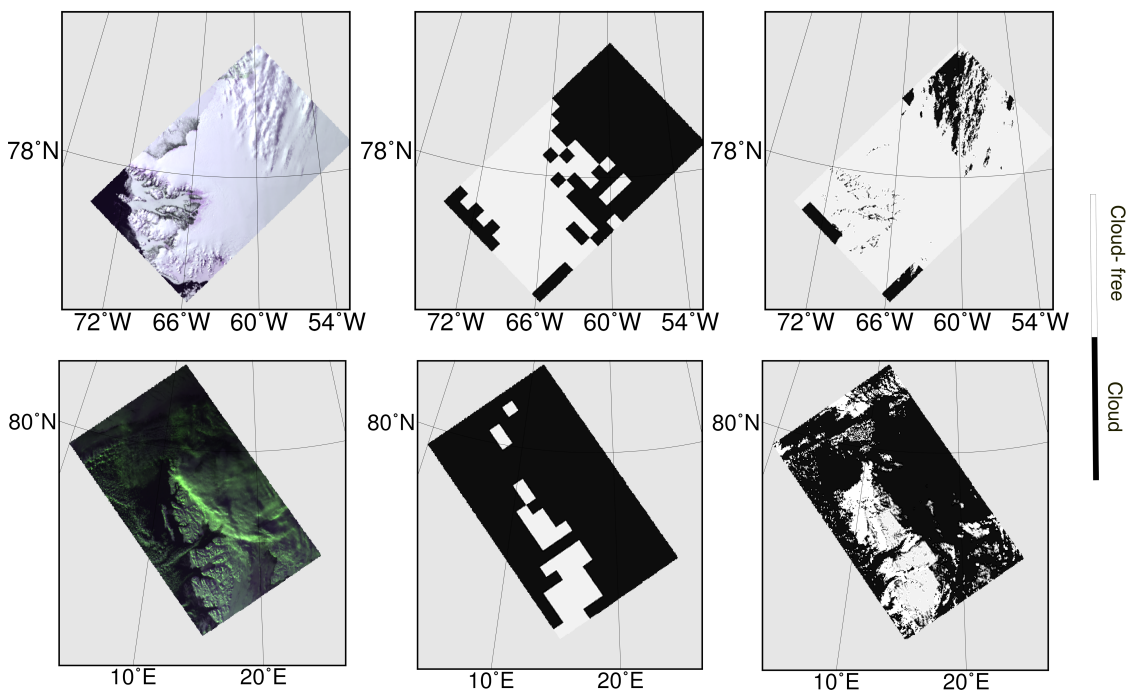


Figure 34: Examples of the results of ASCIA on AATSR observations, first row: over the scenes over Greenland, between $(75^\circ\text{N}, 48^\circ\text{W})$, $(75^\circ\text{N}, 75^\circ\text{W})$, $(81^\circ\text{N}, 48^\circ\text{W})$, $(81^\circ\text{N}, 75^\circ\text{W})$, taken on 18th May 2008 and second row: over Svalbard, within $(75^\circ\text{N}, 4^\circ\text{E})$, $(75^\circ\text{N}, 32^\circ\text{E})$, $(81^\circ\text{N}, 4^\circ\text{E})$, $(81^\circ\text{N}, 32^\circ\text{E})$ on 1st March 2008. Left panels: RGB false-colour images (using 0.67 , 0.87 and $0.55 \mu\text{m}$ channels), middle panels: cloud detection at block level ($25 \times 25 \text{ km}^2$), right panels: cloud detection at scene level ($1 \times 1 \text{ km}^2$).

In addition to picking out cloudy scenes, a simple land classification procedure is undertaken in this step of the ASCIA. Snow/ice scenes are identified with low $3.7 \mu\text{m}$

reflection, whereas land scenes with high reflection are classified with the aid of the darkness test over visible channels. The corresponding thresholds for the land classification scheme are listed in Table 6.

In ASCIA, a land scene may refer to soil, different types of vegetation cover or even melting snow. If the latter is mixed with soil, it becomes sufficiently dark to be filtered out from the snow class. Sea ice is distinguished from water based on its higher brightness: one scene might be sufficiently white to be considered as ice, whereas melting or broken ice would not be labelled as ice. Snow over sea ice is not distinguished from pure sea ice and both of them are labelled as sea ice. This also means that ice over land is also marked as snow as well as pure snow.

Figure 34 shows representative examples of the ACIA performance and the resultant cloud flag at the block level $25 \times 25 \text{ km}^2$ in the middle panel and converted to the pixel level of $1 \times 1 \text{ km}^2$. The scene depicts the region over northwest Greenland in spring-time enclosed in the coordinates for four corners (75°N , 48°W), (75°N , 75°W), (81°N , 48°W), (81°N , 75°W) taken on 18th May 2008. In this example, we can see the performance of ASCIA over a combination of fairly homogeneous snow cover, land, ocean, sea ice and cloud. As we discussed earlier, the ambiguity of the PCC analysis over homogeneous surfaces on the right side of AATSR scene in Fig. 34 is entirely compensated by using additional information from the $3.7 \mu\text{m}$ channel. Another example in Fig. 34 is taken over a surface with highly variable topography at Svalbard in March with a relatively high solar zenith angle ($>80^\circ$), enclosed in the coordinates for four corners (75°N , 4°E), (75°N , 32°E), (81°N , 4°E), (81°N , 32°E) acquired on 1st March 2008.

4.4.3 Results and comparison to space-borne cloud products

In this section, the developed ASCIA algorithm is applied to AATSR and SLSTR L1b (TOA reflectance) gridded data with a nominal spatial resolution of 1 km at nadir view and a swath width of 512 km. The input file to the process chain is one scene of the AATSR L1b product with the whole month data of the date of interest. The output comprises five classes of surface types including snow/ice, sea ice, ocean, cloud and land. The location and time of selected case studies are considered to match with our main purpose, which is cloud detection for aerosol retrieval over the Arctic.

For this aim, the data are selected from:

- 2006, when a strong Arctic haze was reported with an origin in agricultural fires burning in Eastern Europe (Law and Stohl, 2007); and
- 2008, when validation data is available from SYNOP stations.

One month of data from each season of these years is selected from AATSR measurements over Greenland and Svalbard to assess the performance of the algorithm under a wide range of conditions. In order to take into account various surface types in the Arctic, case studies including highly variable topography (e.g. Svalbard) and

very homogeneous snow cover (e.g. Greenland), coast lines, land and ocean along snow- and ice-covered surfaces are defined. Therefore, the design of algorithm is adjusted to make the algorithm sufficiently flexible to perform adequately over various parts of the Arctic under different solar illumination conditions, except for polar winter-time, when only thermal measurements are available.

The results obtained in this study are compared with AATSR L2 nadir cloud flag and those of a previously-suggested method using the spectral shape of cloud-free snow. Further details about this approach can be found in Istomina et al. (2010).

In summary, three different satellite cloud products have been used in this work to qualitatively validate and verify ASCIA: (i) the AATSR L2 nadir cloud flag; (ii) results obtained with ISTO (Istomina et al., 2010); and (iii) the MODIS cloud product. For a quantitative validation, the results of ASCIA are compared with ground-based measurements described in the next section.

Figure 35 shows the AATSR scene over northwest Greenland where a combination of very homogeneous snow cover, land, ocean, sea ice and cloud was found. As discussed before, the lack of performance of the PCC analysis over a very homogeneous surface due to less surface patterns like on the right side of the AATSR scene in Fig. 35 is entirely compensated by additional information from the $3.7 \mu\text{m}$ channel. Thin and broken clouds are well detected over smooth snow cover as well as clouds over the southern part of the scene, which is covered with snow and ocean. However, the ESA standard nadir cloud flag and the ISTO method based on spectral shape of snow were unable to detect these thin and broken clouds. Misclassification of thin cirrus cloud and clear snow is reported to be an unresolved problem of the ISTO approach.

The difference between the results of ASCIA and ISTO is described in the right panel of Fig. 35, in which the dark-blue regions show clouds not detected by ISTO but identified by ASCIA. The reddish regions show cloud-free cases that ISTO fails to detect but are correctly labelled by ASCIA as cloud-free. In addition to the edge of clouds - which are difficult to detect over snow and ice - there is a significant number of undetected cloud scenes in the ISTO results, which are identified successfully by ASCIA. However, for the rest of these two scenes, the two algorithms show good agreement. The ESA cloud product from L2 data over-estimates cloud, which leads to a loss of clear snow and ice scenes. The tendency of this product to flag clear scenes as cloud is also visible in the next examples.

Figure 36 is another example of cloud detection over Svalbard on 10th May 2006. The AATSR scene includes ocean, cloud over the ocean, the snow/ice-covered surface of Svalbard with highly variable topography and sea ice with a thin cloud over it. In addition to a clear signature of thin cloud over sea ice in the $1.6 \mu\text{m}$ channel that is distinguishable based on visual inspection, the extracted reflection part of the $3.7 \mu\text{m}$ channel confirmed the presence of a thin cloud over the south-west part of Svalbard. Nevertheless, both the ESA standard cloud detection method and the previous approach failed to detect this thin cloud, which is mostly detected by ASCIA.

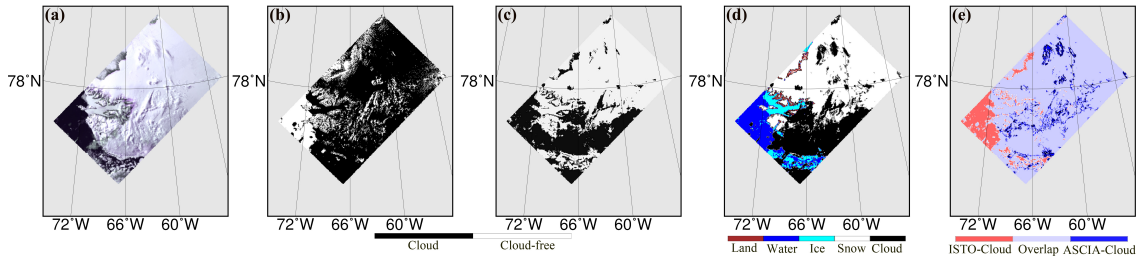


Figure 35: (a) The RGB false-colour image (using 0.67, 0.87 and 0.55 μm channels) of AATSR over northern Greenland, 24th May 2008; (b) nadir cloud flag from the AATSR L2 product; (c) cloud detection based on the spectral shape of clear snow; (d) cloud detection of ASCIA and (e) the difference between ISTO and ASCIA.

In addition to the problem with thin cloud, the lack of good performance in winter-time over the Arctic with high solar zenith is observed in all of the results of the ISTO method and AATSR standard cloud product. In winter time, the problems of cloud detection over highly reflecting surface are amplified with a very large solar zenith angle (larger than 80°), which leads to false detection of clouds in the mentioned methods. Figures 36 and 37 are two examples over Svalbard that reveal the potential deficiency of these methods, which is considered and mitigated in our algorithm. The time series algorithm is adjusted to this problem by considering a wide range of solar zenith angle ($40^\circ - 80^\circ$), which leads to defining the reflectance of snow/ice between 0.02 and 0.04 at the 3.7 μm channel.

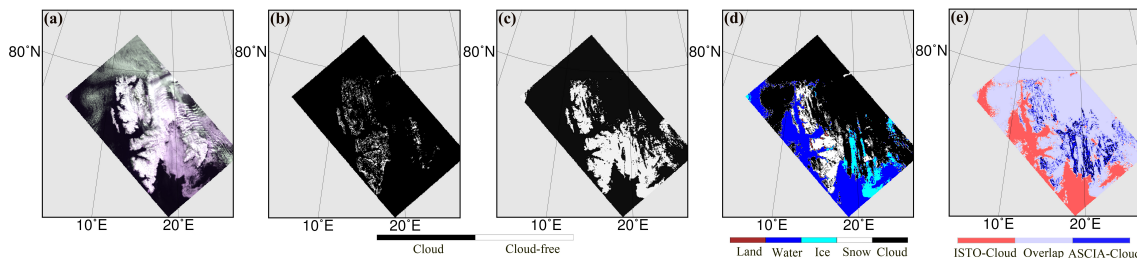


Figure 36: (a) The RGB false-colour image (using 0.67, 0.87 and 0.55 μm channels) of AATSR over Svalbard, 10th May 2006; (b) nadir cloud flag from the AATSR L2 product, (c) cloud detection based on the spectral shape of clear snow, (d) cloud detection of ASCIA and (e) the difference between ISTO and ASCIA.

The results in Fig. 37 show undetected clouds as another problem of the AATSR level 2 cloud product, which happens frequently at large solar zenith angles. Over a highly variable surface type such as Svalbard, the reflection at 3.7 μm can have large values such as 0.035, which is similar to that from cloud reflection. In this case, the PCC analysis holds strong importance for keeping cloud-free snow scenes from the strict criteria of the second step, in particular in cases with larger solar zenith angles.

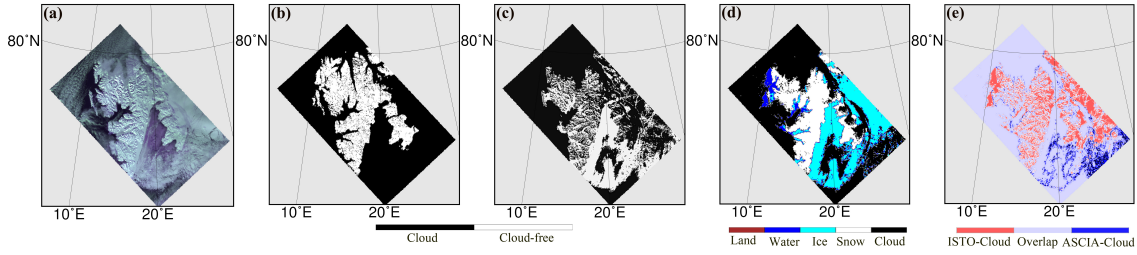


Figure 37: (a) The RGB false-colour image (using 0.67 , 0.87 and $0.55 \mu\text{m}$ channels) of AATSR over Svalbard, 18th March 2008; (b) nadir cloud flag from the AATSR L2 product; (c) cloud detection based on the spectral shape of clear snow; (d) cloud detection of ASCIA and (e) the difference between ISTO and ASCIA.

Figure 39 shows an example of a haze event over Svalbard on 3rd May 2006. As discussed in Section 4, computing the PCC using $1.6 \mu\text{m}$ channel provides the algorithm with the capability of cloud detection without misclassifying it with heavy aerosol plumes over the Arctic. Both the ESA cloud product and ISTO method showed good performance in this case, except the undetected thin cloud pixels that are falsely detected as clear snow in case of the ISTO. The appropriate design and application of PCC analysis enables clouds to be discriminated from heavy aerosol loads. However, aerosol loads above clouds could not be separated from cloudy scenes. The only season in which all three approaches detected clouds with similar efficiency was in July, as shown in Fig. 38.

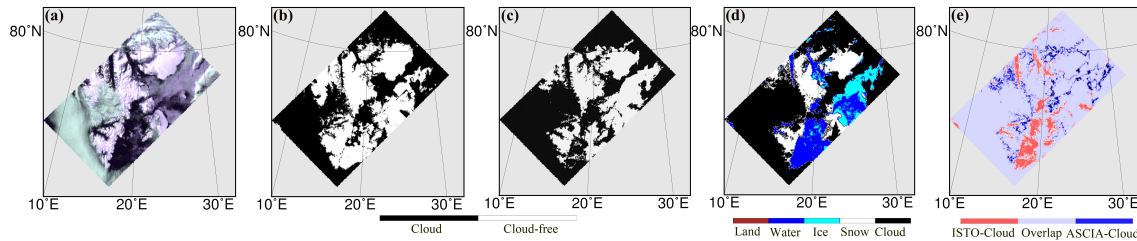


Figure 38: (a) The RGB false-colour image (using 0.67 , 0.87 and $0.55 \mu\text{m}$ channels) of AATSR over Svalbard, 6th July 2008; (b) nadir cloud flag from the AATSR L2 product; (c) cloud detection based on the spectral shape of clear snow; (d) cloud detection of ASCIA and (e) the difference between ISTO and ASCIA.

ASCIA has an overall better performance compared to the standard AATSR cloud mask and the ISTO approach, in particular for thin clouds. However, the required computational time for cloud detection and surface classification is larger than for the two other methods.

In addition, the results of ASICA are compared with the MODIS cloud product. As an example, Fig. 40 shows the AATSR scene over Svalbard on 14th July 2008 where

a large part of sea ice is covered with thin clouds which have a negligible signature in visible channels. The middle panel shows the MODIS cloud mask for the same area. In spite of a small time difference of 15 minutes between MODIS and AATSR data acquisition time, we can see cloudy scenes of ASCIA highly correspond to those of MODIS.

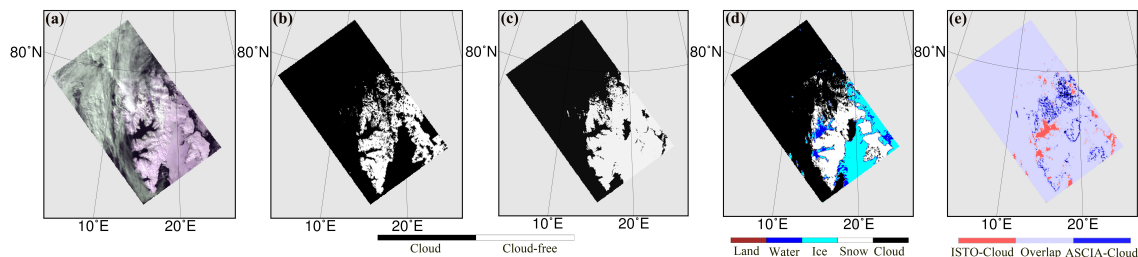


Figure 39: (a) The RGB false-colour image (using 0.67, 0.87 and 0.55 μm channels) of AATSR over Svalbard, 3rd May 2006; (b) nadir cloud flag from the AATSR L2 product; (c) cloud detection based on the spectral shape of clear snow; (d) cloud detection of ASCIA and (e) the difference between ISTO and ASCIA.

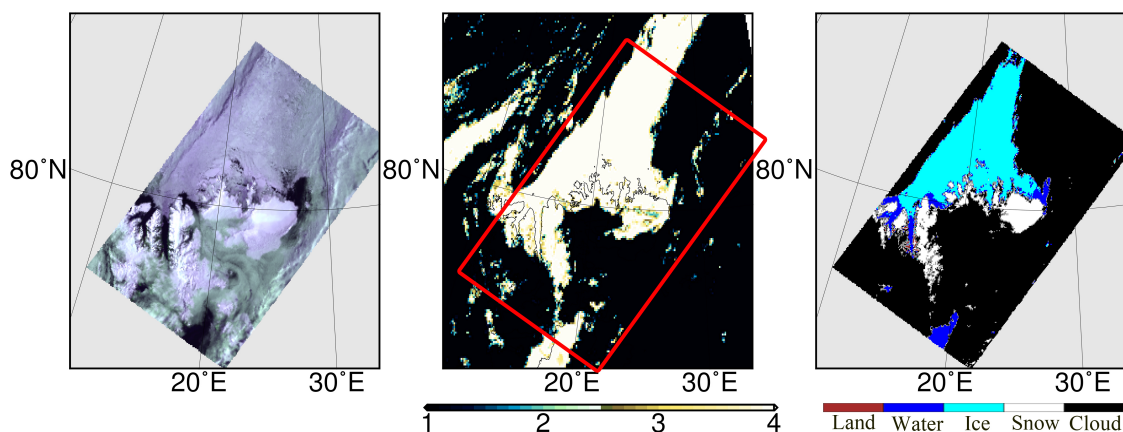


Figure 40: (a) The RGB false-colour image (using 0.67, 0.87 and 0.55 μm channels) of AATSR over Svalbard, 14th July 2008, 16 h 40 min 45 s, (b) The MODIS cloud mask algorithm retrieved data: 1 is cloudy, 2 is probably cloudy, 3 is probably clear, 4 is clear (red rectangle shows the coverage of AATSR) for 16 h 25 min, (c) the results for the cloud detection of ASCIA.

Figure 41 shows another example over the north-west of Greenland on 18th May 2008. The thin and broken clouds are well detected over the snow cover by ASCIA, as well as the clouds over the southern part of the scene, which is covered with snow and ocean. As we can see from the comparison between ASCIA and MODIS cloud identification, cloudy scenes in the northern part of scene are not captured by the

MODIS product, but the presence of clouds is seen in the RGB image in the left panel.

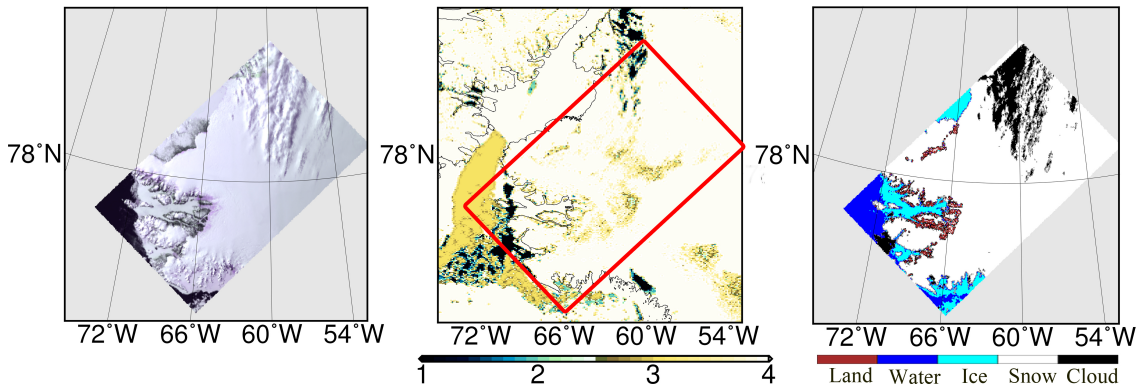


Figure 41: (a) The RGB false-colour image (using 0.67, 0.87 and 0.55 μm channels) of AATSR over Greenland, 18th May 2008, 23 h 13 min 38 s, (b) The MODIS cloud mask: 1 is cloudy, 2 is probably cloudy, 3 is probably clear, 4 is clear (red rectangle shows the coverage of AATSR) for 23 h 5 min, (c) cloud detection of ASCIA.

Other cases with similar differences have been found, especially for thin and broken clouds. There are two potential sources of these differences: (1) time differences, which are 10 minutes in this case; or (2) an inadequate performance of the MODIS cloud mask over bright surfaces covered by snow and ice.

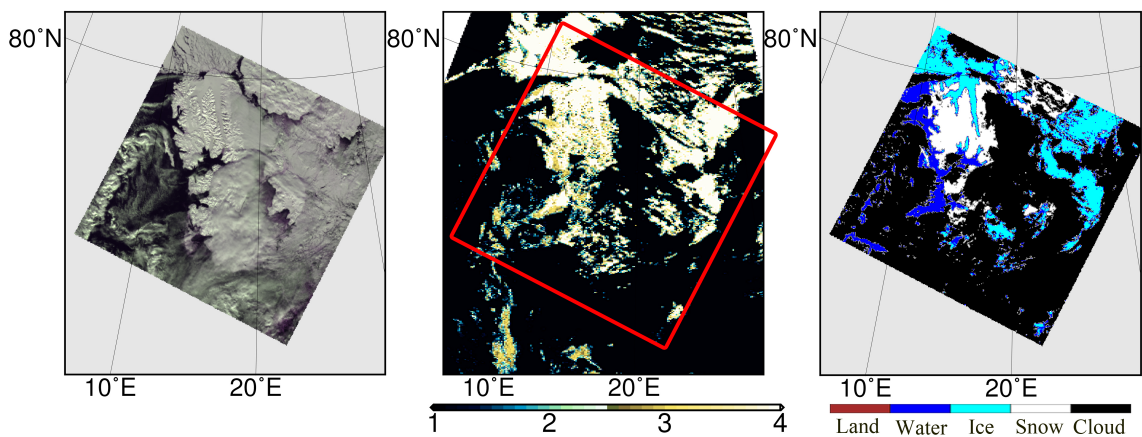


Figure 42: (a) The RGB false-colour image (using 0.67, 0.87 and 0.55 μm channels) of SLSTR over Svalbard, 18th April 2017, 10 h 15 min 6 s, (b) The MODIS cloud mask: 1 is cloudy, 2 is probably cloudy, 3 is probably clear, 4 is clear (red rectangle shows the coverage of AATSR) for 11 h 30 min, (c) cloud detection of ASCIA.

Due to the loss of ENVISAT and thus AATSR data in 2012 and the need for long time series of consistent data, we also tested ASCIA with data of the AATSR successor SLSTR. Figure 42 shows results over Svalbard from 18th April 2017. Due to the smaller swath width of AATSR compared to SLSTR, ASCIA is not applied to the full coverage of SLSTR and the selected scene is cropped to have a similar coverage of $500 \times 500 \text{ km}^2$. Despite, of some unresolved calibration issues in this sensor, the higher spatial resolution in SLSTR clearly helps to improve cloud identification in the first step, because the PCC analysis is more sensitive to smaller changes in $0.5 \times 0.5 \text{ km}^2$ scenes compared to $1 \times 1 \text{ km}^2$. Moreover, the shorter revisit time of the Sentinel-3 satellite provides more acquired images over the same scene. This results in a larger number of reference images compared to those from ENVISAT. Overall, these effects result in an expected improved performance of ASCIA when applied to SLSTR data compared to when it is applied to AATSR. The comparison of MODIS and ASCIA results indicates that ASCIA detected more cloudy scenes than the MODIS algorithm in agreement with the above.

4.4.4 Comparison to ground-based measurements

In this section, a quantitative validation of ASCIA results against SYNOP and AERONET measurements is presented. The ESA standard cloud product is also compared with the mentioned validation data sets.

In addition to the discussed details for recalculating continuous percentage values using discrete okta ones, one might take into account the difference in spatial and temporal resolution of two products to increase the reliability of validation.

To define the optimal maximum temporal difference between SYNOP and satellite data, other validation activities used different temporal intervals such as 10 min (Werkmeister et al., 2015), 15 min (Musial et al., 2014), 1 h (Dybbroe et al., 2005) and 4 h (Meerkötter et al., 2004).

The investigation and results in the previous publications indicate that temporal differences in the validation of satellite retrievals against SYNOP depend on meteorological conditions. Allowing only a small temporal difference between measurement data sets (here, SYNOP and ASCIA) ensures an optimal temporal overall but can introduce a significant sampling error due to the small number of scenes suitable for validation (Bojanowski et al., 2014). According to Bojanowski et al. (2014), temporal difference of 90 min between measurement datasets (SYNOP measurements at a temporal resolution of 3 hand satellite retrievals) minimises the sampling error. However, a potentially longer temporal difference will introduce an error, which should be considered among other sources of uncertainty (different viewing perspective, different spatial footprint, etc.).

Here, we considered only the AATSR measurements with suitable acquisition time, which means that the difference between the recording time of satellite data and SYNOP is minimal. In most cases, this time difference is below ± 20 minutes and generally does not exceed ± 45 minutes. Moreover, to compare surface measurement

from the SYNOP hemispheric view with the cloud mask (with $1 \times 1 \text{ km}^2$ resolution) achieved from satellite measurement, the cloudiness is calculated as the percentage of cloudy pixels within a block of $20 \times 20 \text{ km}^2$ around each SYNOP station over the cloud mask, since, similar distance is considered in previous studies to validate satellite-based cloud masks against surface measurements (Kotarba, 2017; Werkmeister et al., 2015; Minnis et al., 2003).

The cloud detection data product was then compared to the three selected months (March, May and July) of SYNOP observations. These result in 100 measurements over Svalbard and Greenland. In Fig. 43, the relation between the calculated cloud fractional cover (CFC) from ASCIA and SYNOP measurements, is presented as well as the density plot of occurrences of the CFC by ASCIA as a function of SYNOP, following the idea of Werkmeister et al. (2015).

The two data sets have a correlation coefficient of $R=0.92$. In 31% of the scenarios, ASCIA estimates one okta more than SYNOP, while in 14% of match-ups SYNOP shows a higher CFC of one okta. Figure 43 also reveals that most of the ± 1 okta differences occur when either SYNOP or ASCIA estimate seven or eight oktas, which could be due to the definition of eight oktas (100% CFC) and the conversion of a continuous percentage to okta (Werkmeister et al., 2015). For instance, CFC of 99.9% is considered as seven oktas by using Table 4, but the CFC difference is only 0.1% with eight oktas.

The under-estimation of CFC by SYNOP is also indicated in the histogram of the difference between ASCIA and SYNOP in Fig. 44. This under-estimation has also been confirmed by previous studies (Kotarba, 2009; Werkmeister et al., 2015).

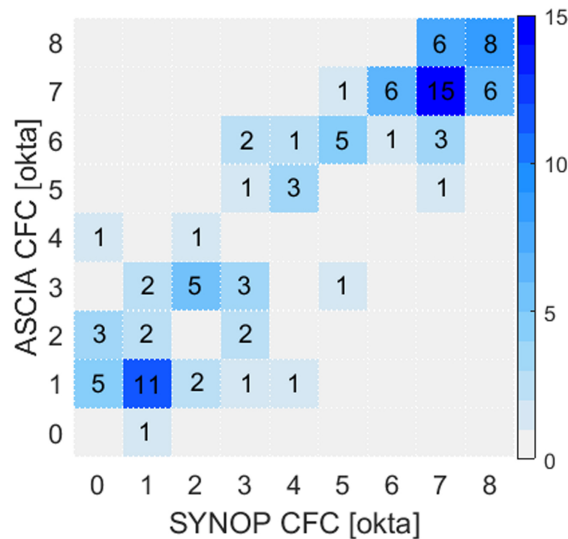


Figure 43: Density plot of occurrences of the CFC by ASCIA as a function of SYNOP.

The accuracy of ASCIA for cloud detection is better compared to the ESA cloud product. The cloud cover reported from SYNOP agrees in 96% (within ± 2 okta)

and 83% (within ± 1 okta) of the observations with the cloud identification data from ASCIA. As discussed earlier, an error of ± 1 to ± 2 okta would be expected as the accepted accuracy range from SYNOP cloud cover values due to the man-made nature of the observation and viewing conditions (Boers et al., 2010; Werkmeister et al., 2015).

In comparison, the ESA cloud product agrees 68% (within ± 2 okta) and 50% (within ± 1 okta) with SYNOP CFCs.

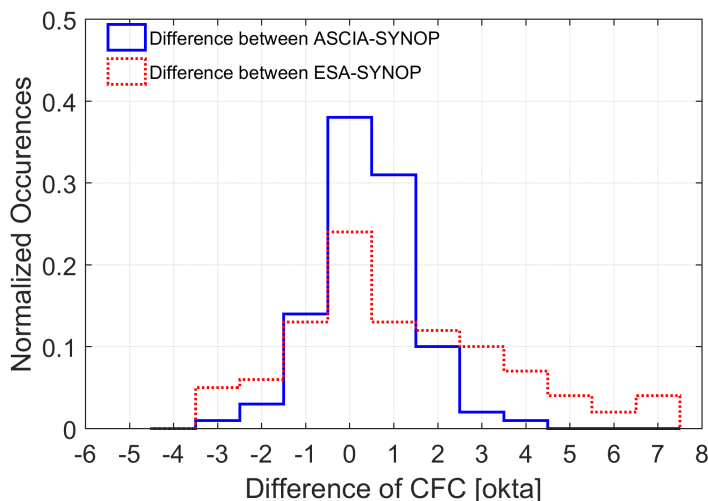


Figure 44: Histogram of CFC differences (blue is ASCIA minus SYNOP; red is ESA cloud product minus SYNOP).

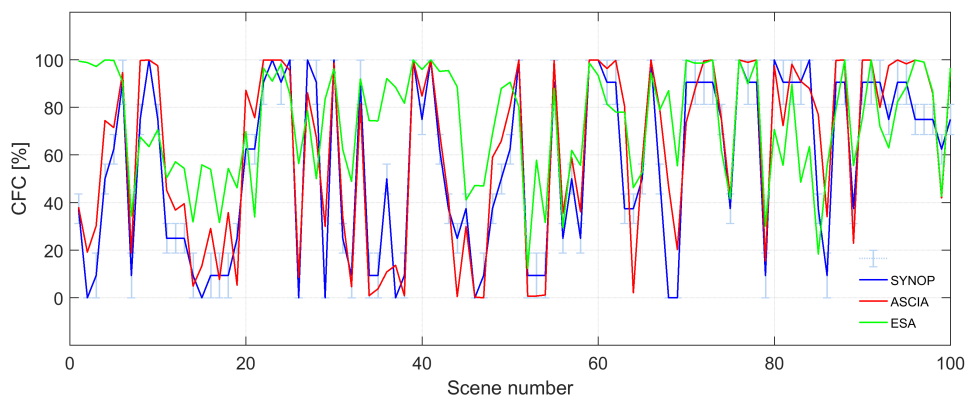


Figure 45: CFC in percentage by ASCIA (red), SYNOP (blue) and ESA Cloud Product (green) for 100 scenarios in March, May and July 2008 over Svalbard and Greenland. Light-blue error bars show the range of percentage values for each okta from SYNOP measurements.

The larger differences between the SYNOP and ESA cloud products are also indicated in Fig. 45, where the CFC values are shown as percentages for ASCIA, ESA

and SYNOP for the validation scenarios. The blue error bars indicate the range of okta values for each SYNOP as explained in Table 4. The ASCIA cloud identification results have been validated against AERONET level 1.5 measurements, which are cloud screened. The procedure for this validation takes place in two steps: (1) converting AERONET-observed AOT to a cloud flag (AOT is provided in AERONET only under cloud-free conditions); and (2) validation of ASCIA with AERONET cloud flag. In 86.1% of 36 studied scenes over Svalbard, both ASCIA and AERONET confirm the presence of clouds.

4.4.5 Supporting ACLOUD/PASCAL campaign with ASCIA

In the framework of (AC)³ project, two comprehensive field studies were conducted: the Arctic Cloud Observations Using Airborne Measurements during Polar Day (ACLOUD) aircraft campaign and the Physical Feedbacks of Arctic Boundary Layer, Sea Ice, Cloud and Aerosol (PASCAL). The aim of these campaigns was to study cloud properties, aerosol impact on clouds, atmospheric radiation, and turbulent dynamical processes. The location of both campaigns was in the vicinity of Svalbard, Norway, in May and June 2017.

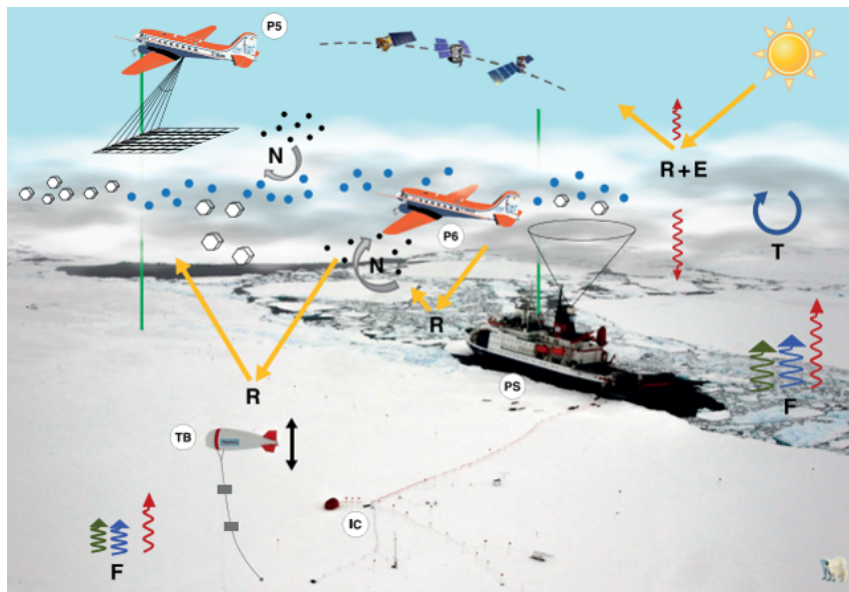


Figure 46: Multiplatform measurement setup during the ACLOUD/PASCAL campaigns, for details see Wendisch et al. (2019).

Figure 46 is a schematic presentation of different platforms involved in ACLOUD and PASCAL campaigns. For instance, one aircraft (Polar 5) observed cloud from top while another aircraft (Polar 6) conducted measurements into and below the clouds. Ground-based observations provided measurements of vertical column of cloud. The aerosol particles were measured using remote-sensing techniques with instruments carried by the R/V Polarstern (ship and ice floe camp) and at Ny-Ålesund. Satellite observations are also part of these multiplatform campaigns. More details about

ACLOUD and PASCAL campaigns can be found in Wendisch et al. (2019). Figure 47 shows the flight paths and ship tracks during ACLOUD/PASCAL campaigns.

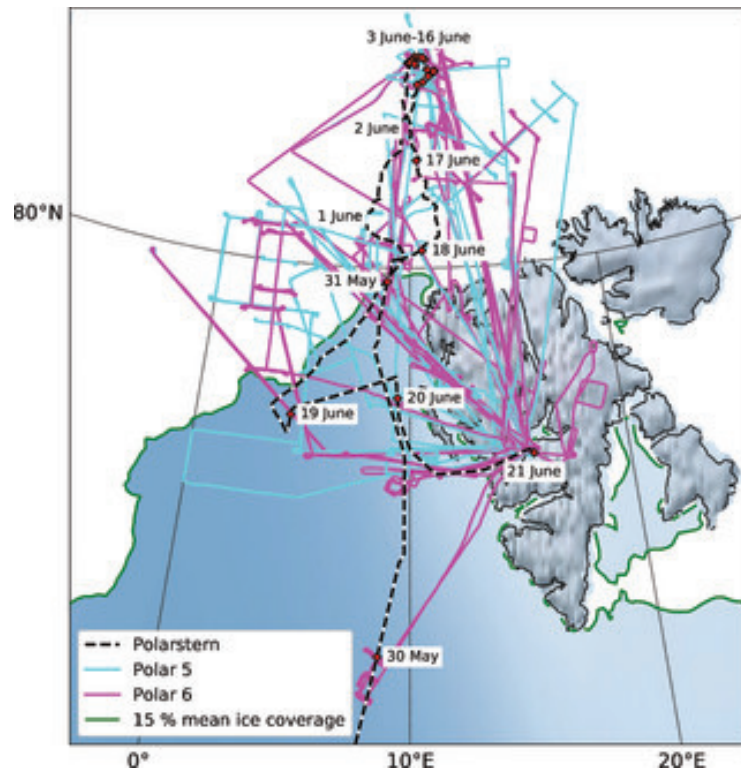


Figure 47: Flight paths (light blue for Polar 5 aircraft, pink for Polar 6 aircraft) and R/V Polarstern ship track (black and white line) during the ACLOUD/PASCAL campaigns. For details see Wendisch et al. (2019).

ASCIA was involved in the ACLOUD/PASCAL campaign, and it provided daily cloud fraction in the region of interest using SLSTR measurements. Figures 48 and 49 show two examples of cloud detection results and calculated cloud fraction per orbit pass. In each day, there are at least six satellite overpasses for this area. To calculate the daily average cloud fraction, we selected only morning orbits by which the region of interest is fully covered. Note that the Svalbard archipelago is excluded from the cloud fraction calculation.

In Fig. 48 and 49, the measurements at $1.6 \mu\text{m}$ beside the result of cloud detection from ACIA are depicted, because the contrast between cloud and snow/ice surface at $1.6 \mu\text{m}$ helps to estimate cloudiness visually and compare it with the results of ASCIA. Figure 50 shows the calculated cloud fraction for the whole time series of ACLOUD/PASCAL campaign from 23rd May to 26th June 2017. In addition to ASCIA, the cloud fraction from MODIS is presented as well as the cloud type. The general agreement between ASCIA and MODIS is promising. Nevertheless, as can be seen, ASCIA indicates higher cloud fraction especially in the presence of high ice cloud. The comparison studies shown thus far in this work indicated that ASCIA shows better performance compared to MODIS, but the difference between ASCIA

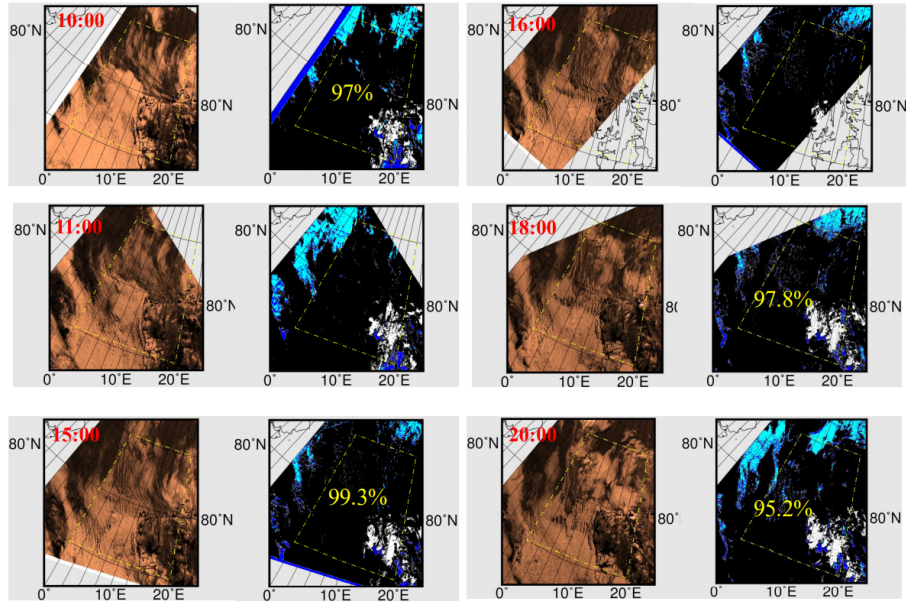


Figure 48: Cloud fraction calculated by ASCIA using SLSTR measurements over Svalbard, on 23rd May 2017 for 6 orbits with corresponding measurements from 1.6 μm channel. Cloud fraction is derived for the area of the airborne operation (77.5° – 80° N, 0° – 10.5° E and 80° – 82.5° N, 0° – 20° E), excluding the Svalbard archipelago.

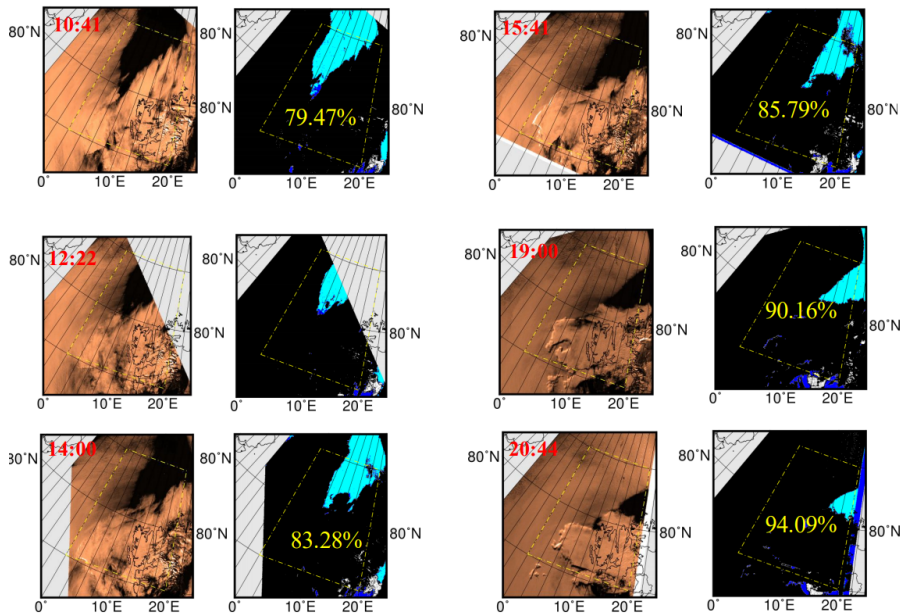


Figure 49: Cloud fraction calculated by ASCIA using SLSTR measurements over Svalbard, on 10th June 2017 for 6 orbits with corresponding measurements from 1.6 μm channel. Cloud fraction is derived for the area of the airborne operation (77.5° – 80° N, 0° – 10.5° E and 80° – 82.5° N, 0° – 20° E), excluding the Svalbard archipelago.

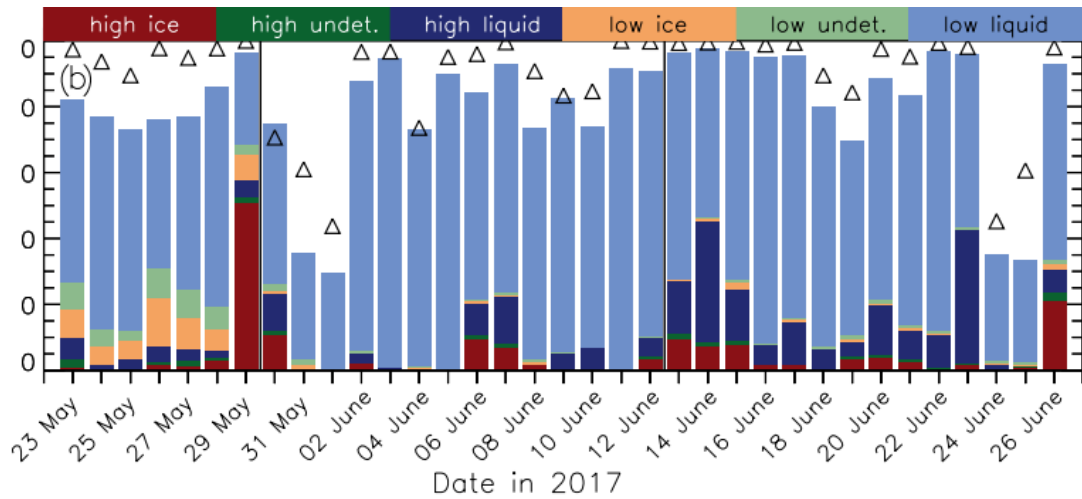


Figure 50: Time series of daily means of cloud fraction of different cloud types as derived from MODIS cloud product (Collection 6.1). The daily mean values of the top height of low-level clouds and cloud fraction were derived for the area of the airborne operation (77.5° – 80° N, 0° – 10.5° E and 80° – 82.5° N, 0° – 20° E), excluding the Svalbard archipelago. Daily mean cloud fraction, derived from ASCIA using the SLSTR data, is shown by triangles. For details see Wendisch et al. (2019)

and MODIS could also originate from the difference in the orbit overpass time of satellites. The minimum and maximum cloud fraction of the day is shown in Fig. 51. Interestingly, in some of cases, e.g. 1st June, the results of ASCIA (minimum cloud) are closer to that of MODIS. This can partly explain the origin of differences: time difference between the acquisition of measurements.

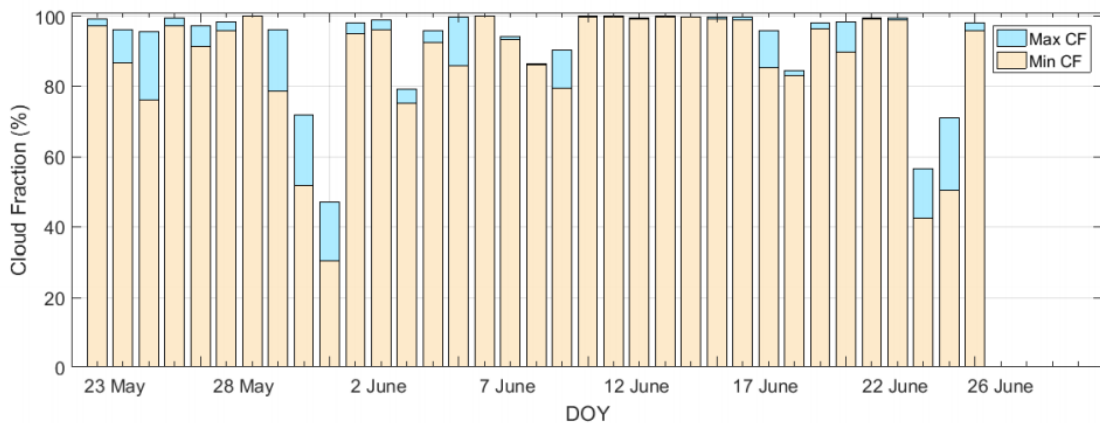


Figure 51: Similar to Fig. 50 but showing minimum and maximum cloud fraction per day.

5 Improved assessment of BRF and snow surface reflectance for Aerosol Optical Thickness retrieval

5.1 Introduction

For aerosol retrievals over the Arctic area, accurate knowledge about the surface is needed. In fact, retrieving atmospheric variables, e.g. aerosol, trace gases, etc. over polar regions using space-borne data requires accurate modelling of directional signature of the snow reflectance to decouple the measured TOA reflectance from highly reflecting snow/ice-covered surface (Istomina et al., 2010; Jafariserajehlou et al., 2019). In this section, the properties of snow covered surface and the reflectance in a snow-atmosphere system are presented. To better understand the effect of surface properties and different parameters in the overlaying atmosphere that contributes to the reflected radiance from a snow-atmosphere system, a sensitivity study is conducted. Furthermore, the accuracy of the radiative transfer model - used in this work - for modelling the reflectance of snow surface for aerosol retrieval is estimated. A large part of the research conducted in this section has been published by Jafariserajehlou et al. (2021).

In addition to the importance of surface properties for aerosol retrieval - which is the main motivation behind the study - the key role of snow extent and type in climate change, highlights the importance of developing methods for better modelling of snow. Snow/ice-covered surface has the highest reflectivity among different surface types on Earth. The changes of snow extent and therefore albedo - especially over the polar regions - influence the climate of the globe and play an important role in AA (Schneider and Dickinson, 1974; Curry et al., 1995; Cohen et al., 2014; Kim et al., 2017). An accurate knowledge of optical properties of snow, angular distribution of reflected light from the snow surface and the subsequent derivation of albedo hold fundamental importance for assessing snow/ice-related climate feedbacks.

In the past, a large number of experimental and theoretical studies have been conducted to measure and model the reflectance properties of snow. The beginning of these studies started with the analysis of transmittance and reflectance of a layer comprising snow (Middleton and Mungal, 1952; Dunkle and Bevans, 1956). The scattering of snow surface was explained by a radiative transfer model for the first time

by Barkstrom (1972). These studies continued with substantial progress in understanding the angular distribution of snow reflectance that have been made through applying RT models and experimental efforts (Wiscombe and Warren, 1980; Warren et al., 1998; Arnold et al., 2002; Painter et al., 2003; Kokhanovsky and Zege, 2004; Li and Zhou, 2004; Hudson et al., 2006; Hudson and Warren, 2007; Lyapustin et al., 2010; Kokhanovsky and Breon, 2012).

The main scattering patterns of a snow/ice-covered surface have been revealed throughout these studies. Snow surface has an anisotropic nature and is not a Lambertian reflector (Warren, 1982; Lyapustin et al., 2010), e.g. it has a pronounced forward peak, the larger anisotropy in the principal plane (i.e. observations that lie in the same plane as the local vertical and the incoming direct solar radiation are referred to as reflectance in the principal plane) compared to perpendicular plane (orthogonal to principal plane). These features can be seen in measurement examples in Fig. 52 and 53.

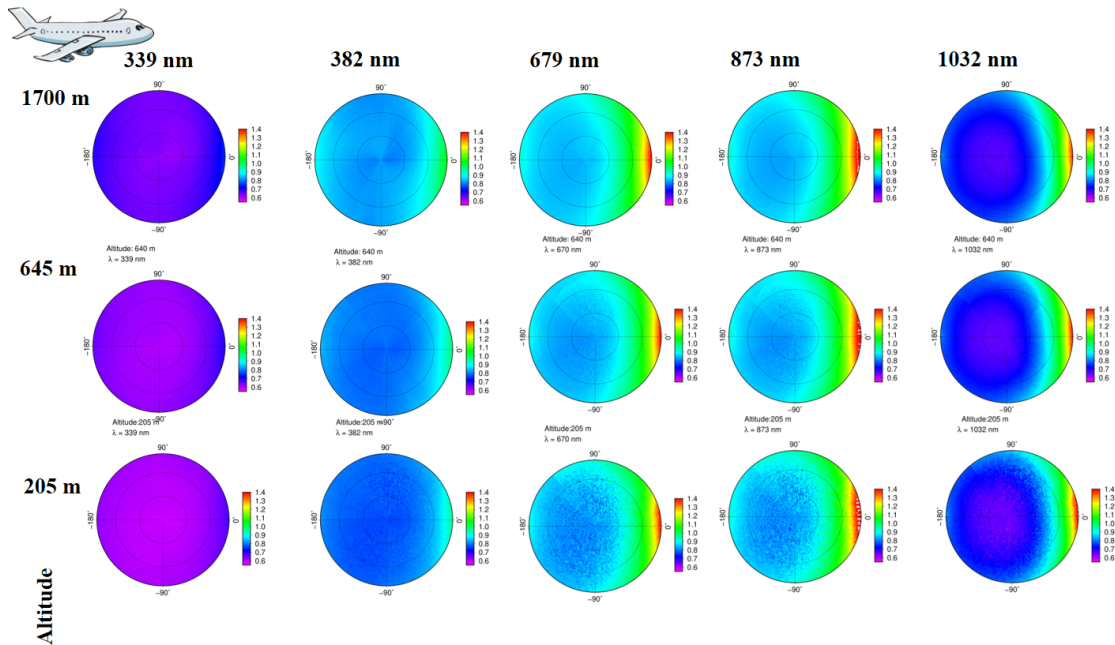


Figure 52: Angular distribution of a reflectance in the snow-atmosphere system derived from CAR measurements on 7th April 2008 at Elson Lagoon (71.3°N, 156.4°W), showing reflectance in the spectral range between 0.339 μm and 1.032 μm , and three flight altitudes of 206, 647, and 1700 m. The principal plane is the horizontal line ($\Phi = 0^\circ$ and $\Phi = 180^\circ$), and the viewing zenith angle is shown as the radius of the polar plots from 0° (nadir) to 70° . The solar zenith angle is 70.23, 69.11, and 67.78° for flight altitudes of 206, 647, and 1700 m, respectively.

Despite the incredible progress in our understanding about reflectance above a snow-covered surface, remaining discrepancies were found between the simulated results and field measurements which led to further investigations in single scattering prop-

erties of snow grains (Mishchenko et al., 1999a; Jin et al., 2008; Yang and Liou, 1998; Yang et al., 2013), surface roughness (Warren et al., 1998; Hudson et al., 2006; Hudson and Warren, 2007; Lyapustin et al., 2010; Zhuravleva and Kokhanovsky, 2011) and atmospheric correction methods (Lyapustin et al., 2010). Although, substantial improvements have been made, radiative transfer models still predict more anisotropic behaviour for snow, e.g. in glint region than observed in reality (Zhuravleva and Kokhanovsky, 2011; Lyapustin et al., 2010; Hudson and Warren, 2007; Warren et al., 1998).

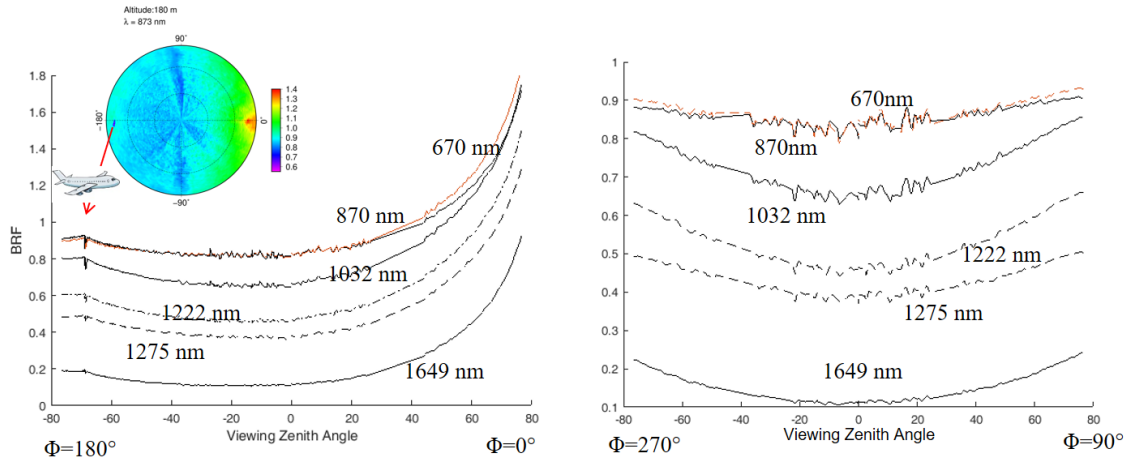


Figure 53: Reflectance factor in the snow-atmosphere system derived from CAR measurements in principal plane (left) ($\Phi = 0^\circ$ and $\Phi = 180^\circ$) and cross plane (right) ($\Phi = 90^\circ$ and $\Phi = 270^\circ$), on 15th April 2008 at Elson Lagoon (71.3°N , 156.4°W), showing reflectance at the spectral range between $0.67 \mu\text{m}$ and $1.649 \mu\text{m}$, flight altitude 180m. The shadow of aircraft can be seen as a reduction of reflectance in the left panel.

5.2 Theoretical background

The reflectance of a surface element is defined as the ratio of the reflected radiance in the direction (θ_1, ϕ_1) and the incident irradiance from the direction (θ_2, ϕ_2) . By integrating this quantity over the solid angle of a hemisphere, the directional reflectance (θ_i, ϕ_i) will be achieved, which is the fraction of the radiant power incident on the direction (θ_i, ϕ_i) that is reflected in all directions into a hemisphere. This quantity can be used for describing the directional signature of a surface reflectance.

Nicodemus (1965) defined the mathematical form of BRDF below (Schaeppman-Strub et al., 2006):

$$RRDF_\lambda = \frac{dL_r(\theta_i, \phi_i, \theta_r, \phi_r; \lambda)}{dE_i(\theta_i, \phi_i; \lambda)} \quad (5.1)$$

where L_r is the reflected radiance, θ and ϕ are the zenith and azimuth angles respectively, i corresponds to the incident and r to the reflected solar beams. E is the incident flux density (Irradiance) and λ is the wavelength.

Nevertheless, BRDF is not a measurable quantity due to being formulated as a ratio of infinitesimal elements (Nicodemus et al., 1977; Schaepman-Strub et al., 2006). Nicodemus (1965) gave an extensive description of reflectance terminologies and measurable quantities in practice, e.g. bidirectional reflectance factor (BRF), hemispherical directional reflectance factor (HDRF), directional hemispherical reflectance (DHR), etc. According to Nicodemus et al. (1977) and Schaepman-Strub et al. (2006), each of the above-mentioned terms is defined to resemble the specific illumination and reflectance geometries in which the reflectance properties are measured, e.g. satellite, airborne or laboratory measurement conditions. Following the method of Gatebe and King (2016), in this study the effective BRDF at a horizontal reference plane is used, which is as an average of BRDF over an appropriate area, angle and solid angle for a specific source-target-sensor geometry (Gatebe and King, 2016):

$$BRDF_{\lambda}^e = \frac{\Delta L_r(\theta_i, \phi_i, \theta_r, \phi_r; \lambda)}{\Delta E_i(\theta_i, \phi_i; \lambda)} \quad (5.2)$$

$$= \frac{\Delta L_r(\theta_i, \phi_i, \theta_r, \phi_r; \lambda)}{\Delta L_i(\theta_i, \phi_i; \lambda) \cos \theta_i \Delta \omega_i} \quad (5.3)$$

where $\Delta \omega_i$ is a finite solid angle element. However, the validity of this approximation depends on experimental evidence that BRDF is not significantly influenced by the effect of finite intervals of area, angle, solid angle and the distribution function, the effect of sub-surface scattering, the effect of other radiation parameters such as wavelength and polarisation, fluorescence, etc. (Nicodemus et al., 1977; Gatebe and King, 2016). Following the above-mentioned definition, $BRDF_{\lambda}^e$ of measurements and simulations in this study calculated by:

$$BRDF_{\lambda}^e = \frac{L_r^e(\theta_i, \phi_i, \theta_r, \phi_r; \lambda)}{F_{0,\lambda} \cos \theta_i} \quad (5.4)$$

where L_r^e is the measured radiance, $F_{0,\lambda}$ is the solar irradiance incident on the TOA. To have a better description of the difference between measured surface and a Lambertian reflector, equivalent BRF, which is $BRDF_{\lambda}^e$ times π , is more representative. However, to calculate precise BRF values, the application of atmospheric correction methods, e.g. by using radiative transfer schemes, is necessary. In fact, the measured radiance includes four diffuse components due to atmosphere (Schaepman-Strub et al., 2006): i) atmospheric path radiance, ii) scattering by the atmosphere before reaching the surface, iii) scattering by the atmosphere after being reflected by the surface, and iv) scattering by the atmosphere before and after reaching the surface. For measurements close to the surface, the diffuse components of i, iii and iv are almost zero, although without correcting for the second diffuse component, measurements should be reported as HDRF. Schaepman-Strub et al. (2006) statistically analysed the difference between HDRF (includes diffuse component coming from

atmosphere) and BRF (without diffuse component). They indicated that the effect due to the atmospheric diffuse component of measured radiance is largest at blue wavelengths (because of atmospheric Rayleigh scattering dominance at these wavelengths). However, HDRF and BRF are strongly correlated ($r^2 > 0.98$) throughout the spectral bands considered (Schaepman-Strub et al., 2006). Therefore, in this study, to avoid uncertainties arising from different assumptions included in atmospheric correction methods and evaluate the ability of the radiative transfer model used in this work for simulating atmospheric conditions, no atmospheric correction is applied to measured radiances yet. However, independent information of atmospheric parameters at the time and location of measurements are acquired and applied to simulation routine. Therefore, we calculate and use the reflectance at flight altitude with the following equation:

$$R = \frac{\pi L_{r,h}(\theta_i, \phi_i, \theta_r, \phi_r; \lambda)}{F_{0,\lambda} \cos \theta_i} \quad (5.5)$$

where $L_{r,h}$ is the measured radiance at flight altitude.

5.3 Reflectance modelling

The reflectance in a snow-atmosphere system can be defined by multiple scattering by snow grains, and the radiative interaction between the snow layer and atmosphere (Aoki et al., 1999). The reflectance varies with the snow physical parameters and the external parameters (e.g. atmospheric conditions and measurement geometry). For modelling purposes, the physical parameters are categorised in two groups, which affect:

- single scattering (snow grain size, morphology and impurities); and
- multiple scattering (snow depth, layer structure, density, water contents, surface condition and impurities).

Although, all of the mentioned parameters play a key role in defining the reflectance, it is not always possible to take into account all of them in the simulation due to the lack of knowledge (e.g. about snow impurities in the area of interest) or the limited capabilities of the software used for simulation (e.g. the possibility to simulate snow/ice surface roughness).

The external parameters refer to the atmospheric effects and conditions such as cloud cover, aerosols, air pressure, atmospheric gases and solar zenith angle.

To simulate the reflectance in the solar wavelength range over snow surface or in a coupled snow-atmosphere system, radiative transfer models have been used in different studies (Perovich, 1990; Grenfell et al., 1994; Leroux et al., 1998; Aoki et al., 2000; Green et al., 2002; Xie et al., 2006; Kokhanovsky et al., 2018). In all of these RT models, first the single scattering properties of snow has to be defined: extinction and scattering coefficients, SSA, phase function and asymmetry parameter. All of these parameters depend on wavelength, the size and shape and the refractive index

of snow particle.

The accurate calculation of the single scattering properties of a snow grain is challenging due to the complexity of particle shapes. For this reason, in most previous modelling efforts, the “equivalent spheres” with same volume-to-surface ratio as the actual snow grains are commonly assumed to represent snow grains. Therefore, the Mie theory could be used to compute single scattering parameters. The scattering phase function for an ice crystal is linked to particle shape, whereby the phase function of non-spherical particles may differ dramatically from those of spheres. However, directional quantities such as bidirectional reflectance and radiance are more sensitive to scattering phase function and hence to the particle shape. Therefore, models that take the particle shape into account advance the retrieval of snow properties (e.g. snow grain size) using space-borne measurements (Jin et al., 2008).

In this work, the SCIATRAN RTM is used to simulate the reflectance in the snow-atmosphere system. SCIATRAN is a software package developed at the Institute of Environmental Physics (IUP) at the university of Bremen (Roazanov et al., 2002, 2014). The SCIATRAN RTM is applied in a variety of studies to simulate transmittance, scattering, reflection, thermal emission and surface reflection processes in the spectral range from the ultraviolet to the thermal infrared ($0.18 \mu\text{m} - 40 \mu\text{m}$) assuming either a plane parallel or a spherical atmosphere (Roazanov et al., 2014).

The BRDF of a snow-covered surface in SCIATRAN is implemented based on an extended Rahman Pinty Verstraete (RPV) model (Degünther and Meerkötter, 2000). Instead of using the RPV model, a more accurate treatment of the snow surface reflectance is performed, and the radiative transfer within the snow layer is calculated (Roazanov et al., 2014).

For this purpose, a vertically and horizontally homogeneous ice cloud layer composed of monodisperse snow grains is added. This layer is optically thick but geometrically thin, below the atmospheric layers (Roazanov et al., 2014; Kokhanovsky et al., 2011). The optical characteristics of ice clouds are approximated by the ray tracing Monte-Carlo technique in the framework of the geometrical optics (Macke et al., 1996). For the ice refractive index, the data tabulated by Warren and Brandt (2008) is used. The ice particles are assumed to be randomly oriented and represented by different shapes (see Section 5.3.1). The assumption is a snow layer comprising equal size ice particles. The impact of snow impurities on absorption and scattering of electromagnetic waves is neglected. The calculations are performed at a source-target-sensor geometry extracted from airborne measurements with solar zenith angles of 70.23° , 69.11° and 67.68° , VZA $0^\circ - 70^\circ$ and relative azimuth angles $0 - 360^\circ$ with angular resolution of 1° and three different altitudes of 206 m, 647 m and 1700 m. More detailed information of atmospheric and surface parameters in modelling snow BRDF is given and discussed separately in the following sub-sections.

Since the measured reflectance over a snow field is governed by light scattering from snow grains (determined by snow physical parameters) and atmospheric transmittance, in this section the results are presented in two steps discussing the dependence of snow BRDF on:

- snow physical parameters such as snow grain size and morphology; and
- external parameters such as atmospheric gases and aerosols.

Because the effect of external parameters varies with snow physical parameters, the snow surface has to be known before introducing the atmospheric conditions (Aoki et al., 1999; Leroux et al., 1998). Therefore, we start our investigation with snow physical parameters.

5.3.1 Snow physical parameters (shape and size)

To simulate snow surface with RTMs, the single scattering properties of ice particles including extinction and scattering efficiencies, SSA, phase function and asymmetry parameter need to be defined. All of these parameters are dependent on the wavelength, size and shape of the particle (Leroux et al., 1998).

In SCIATRAN RTM, the fractal particle model introduced by Macke et al. (1996) has been used as the representative shape to account for non-sphericity and irregularity of ice particles. This model is constructed of an initial regular tetrahedron that grows and results in first and second generation of the triadic Koch-fractal (Macke et al., 1996; Rozanov et al., 2014). A new database of basic single scattering properties of ice particles from Yang et al. (2013) has recently been incorporated in SCIATRAN. In this newly-expanded database, eleven ice crystal habits, droxtals, solid and hollow columns, compact aggregates composed of eight solid columns, prolate spheroids, oblate spheroids, hexagonal plates, small spatial aggregates composed of five plates, large spatial aggregates composed of ten plates, and solid and hollow bullet rosettes are considered for calculating single scattering properties at the wavelengths from UV to far IR. To study the influence of ice particle morphology on BRF values of snow surface, the simulation is performed at the wavelength of $1.649 \mu\text{m}$ for three main reasons (Leroux et al., 1998):

- The absorption of ice particles is very small in the visible domain of the spectrum and therefore the effect of ice particle shape and size on snow BRF is negligible. However, in the near-infrared range, the snow reflectance is significantly affected by the snow grain size, due to the large absorption of ice particles at these wavelengths;
- The BRF properties at $1.649 \mu\text{m}$ are closer to single scattering behaviour and linked to the phase matrix, which strongly depends on the shape of ice particles;
- The diffuse incident irradiance (originating from atmosphere) is very small and negligible.

To illustrate the sensitivity of BRF values to the varying size of ice particles, at $1.649 \mu\text{m}$, snow reflectance is simulated assuming the above-mentioned ice crystal habits with varying size. For each particle shape, the range of size in terms of maximum dimension and the equivalent effective radius are presented besides the results in Figure 54. For example, in the model, the maximum dimension of ice

particles changes from 60 μm 10000 μm for the aggregate of eight column shape, 60 μm to 10000 μm for droxtal and 50 μm to 300 μm for Koch fractals. The maximum dimension and effective radius are represented for each ice crystal habit.

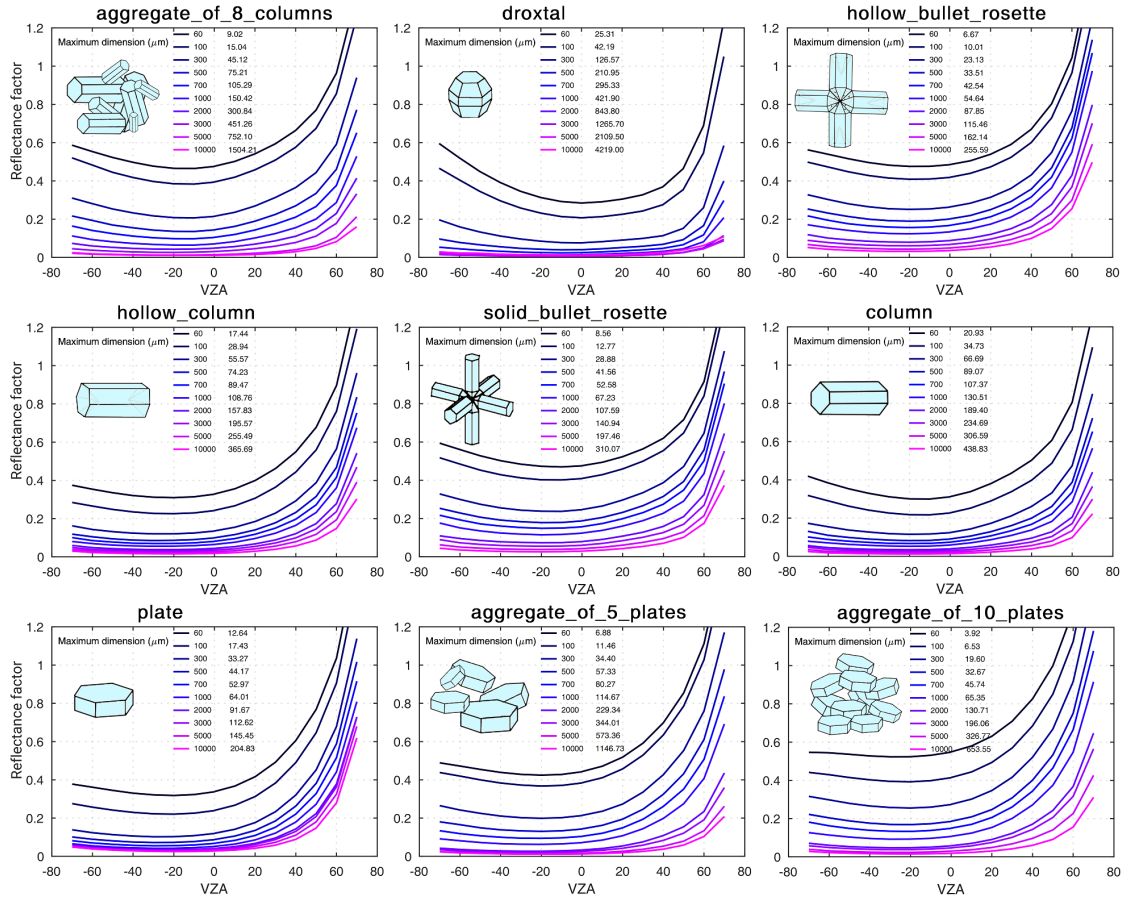


Figure 54: The change in reflectance factor in the principal plane ($\Phi = 0^\circ$ and $\Phi = 180^\circ$) with the size and shape of ice crystals at the wavelength of 1.649 μm . The left column of the legend in each panel shows the maximum length of the ice crystal, and the right column is its equivalent effective radius.

The simulated values are calculated in the principal plane at which the relative azimuth angle between the sun and observing instrument is 0° or 180° . The results indicate that the effect of changing size of particles is more important and larger than the impact of differentiating between various shapes of ice particles. Fig. 54 shows the effect of changing ice particle size and shape for nine ice crystal habits according to modelling the reflectance factor using SCIATRAN. Each panel in this figure shows the change of BRF in principal plane as a function of VZA over a snow layer composed of the specified ice crystal habit. The aggregate of eight columns ice particles exhibits BRF changes ranging from 40% at the nadir to 70% in the forward scattering direction due to the changing dimension of particles from 60 μm to 10000 μm , which is considerably large.

5.3.1.1 Snow grain size and shape retrieval

The large impact of snow grain size and shape on the reflectance in a snow-atmosphere system shows the importance of having a priori information about snow morphology for an accurate simulation and further analysis. The a priori information about ice crystal size (here size refers to the effective radius of ice crystal) and shape can be obtained from field measurements, which were not available for our case study. In order to estimate the optimal ice crystal morphology, a snow grain size and shape retrieval algorithm is used.

For the selected snow models using different ice crystal morphologies, the variation in the snow reflectance $R(\lambda, \Omega)$ at wavelength λ and direction Ω with respect to the variation $\delta r_e(z)$ in the effective radius profile $r_e(z)$ along the vertical coordinate z within snow layer can be presented - neglecting non-linear terms - by the following equation:

$$R(\lambda, \Omega) = R_0(\lambda, \Omega) + \int_0^{Z_t} W_r(z, \lambda, \Omega) \delta r_e(z) dz \quad (5.6)$$

where $R_0(\lambda, \Omega)$ and $R(\lambda, \Omega)$ are the reflection functions calculated, assuming an effective radius profile of $r_e(z)$ and $r_e(z) + \delta r_e(z)$, respectively. For the angular variables, θ_0 is the solar zenith angle, θ and ϕ are the zenith and relative azimuthal angles of observation direction Z_t is the top altitude of snow layer and in the following

$$W_r(Z, \lambda, \Omega) = \frac{\delta R(\lambda, \Omega)}{\delta r_e(z)} \quad (5.7)$$

is the functional derivative of the function $R(\lambda, \Omega)$ with respect to the function $r_e(z)$, which is also called the weighting function (Rozanov et al., 2007). The weighting function was calculated using a numerically efficient forward–adjoint approach (Rozanov and Rozanov, 2007; Rozanov, 2006) implemented in the SCIATRAN model. Here, it is assumed that properties of snow do not change in the horizontal plane, and within the snow layer there is no additional absorber such as soot, dust, or other pollutants. We note that the weighting function includes the contribution of variations not only by the scattering and extinction coefficients but also by the phase function. The linear relationship given by Eq. 5.6 can be used to retrieve the vertical profile of the effective radius within the snow layer in a way similar to that used for the morphology of water droplets Kokhanovsky and Rozanov (2012). By introducing the weighting function for the absolute variation of the effective radius as follows:

$$W_r(Z_t, \lambda, \Omega) = \int_0^{Z_t} W_r(z, \lambda, \Omega) dz \quad (5.8)$$

we have the following:

$$R(\lambda, \Omega) = R_0(\lambda, \Omega) + W_r(z, \lambda, \Omega)\delta r_e. \quad (5.9)$$

The resultant linear relationship is a basic equation used to formulate the inverse problem with respect to the parameter r_e , using measurements of spectral reflectance.

For practical applications, Eq. 5.9 should be re-written in the vector–matrix form as follows:

$$Y - Y_0 = K(X - X_0) \quad (5.10)$$

The components of vectors Y and Y_0 are the measured and simulated reflectance at a discrete number of observation direction j and wavelengths λ_i , the elements of matrix K are weighting functions $W_r(\lambda_i, \Omega_j)$, $X = [r_e]$ is the state vector, and $X_0 = [r'_e]$ is the a priori state vector. We note that in the case under consideration, the matrix K and state vector X are represented by the column vector and scalar, respectively. Assuming that the number of discrete observation directions and wavelengths λ_i is larger than the dimensions of the state vector, the solution of Eq. 5.10 is obtained by minimising the following cost function:

$$\Delta = \|Y - Y_0 - K(X - X_0)\|^2 \quad (5.11)$$

which describes the root mean square deviation between measured and simulated snow reflectance. Owing to the linear relationship given by Eq. 5.10, the minimisation problem formulated above can be solved analytically as follows:

$$X = X_0 + (K^T K)^{-1} K^T (Y - Y_0) \quad (5.12)$$

when deriving Eq. 5.12, we have neglected the linearisation error, which can be significant if X_0 is far from X . To mitigate the impact of the linearisation error, we solve the minimisation problem given by Eq. 5.11 iteratively. In particular, instead of Eq. 5.12, the following is used:

$$X_n = X_{n-1} + (K_{n-1}^T K_{n-1})^{-1} K_{n-1}^T (Y - Y_{n-1}) \quad (5.13)$$

where $n=1,2, \dots$ is the iteration number, K_{n-1} and Y_{n-1} are the matrix of the weighting functions and reflectance vector calculated using the state vector X_{n-1} . The iteration process is finished if the difference between X_n and X_{n-1} is smaller than a pre-selected criterion. The calculation of the weighting functions and reflectance at flight altitude is performed at each iteration step, using SCIATRAN.

In SCIATRAN, weighting functions are calculated employing an efficient forward–adjoint technique, which is based on the joint solution of the linearised forward and adjoint radiative transfer equations (Rozanov and Rozanov, 2007; Rozanov, 2006). This enables the TOA reflectance and required weighting function to be calculated simultaneously.

5 Improved assessment of BRF and snow surface reflectance for Aerosol Optical Thickness retrieval

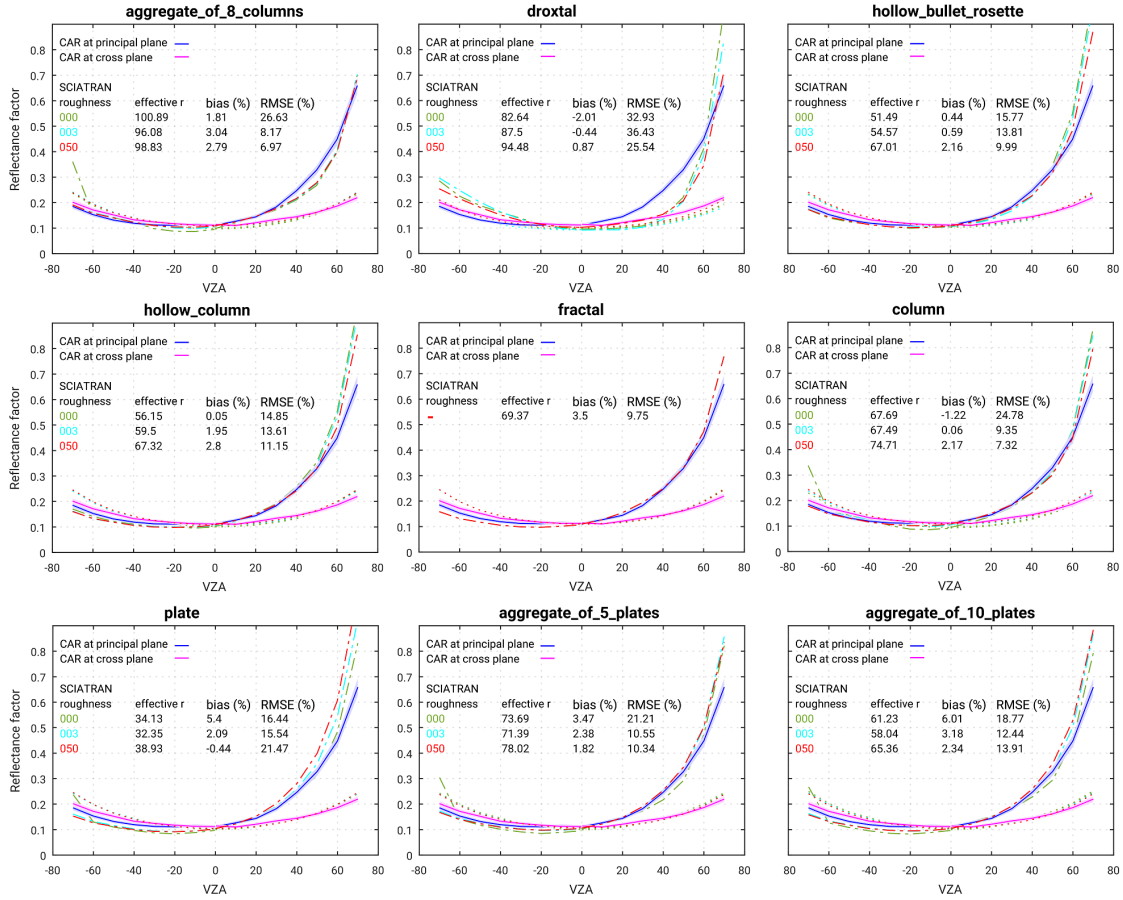


Figure 55: Comparison of measured and simulated reflectance factors. Measurements were performed by the CAR instrument over old snow at 647 m flight altitude on 7th April 2008 at 1.649 μm . The uncertainty in CAR measurements is indicated by the envelope (shading). SCIATTRAN simulations in the principal and cross plane given by the dashed-dotted and dotted lines, respectively, and by different colors (green, blue, and red) present smooth, moderately roughened, and severely roughened crystal surfaces. Positive and negative VZA (viewing zenith angles) correspond to azimuthal angles $\Phi = 0^\circ$ and $\Phi = 180^\circ$ for the principal plane and $\Phi = 90^\circ$ and $\Phi = 270^\circ$ for the perpendicular plane, respectively.

The retrieval algorithm is applied to measurements at principal and cross planes at 1.649 μm , assuming different shape and crystal surface roughness. To find the best representative shape and size, the bias and root mean square error (RMSE) between the measured and simulated reflectance factor were determined for each case study.

Figures 55 and 56 show the comparison between RMSE and bias values for different shapes in case of aged and fresh snow, respectively. Each panel indicates CAR measurement with its corresponding accuracy within 5% and the simulated BRF values using SCIATTRAN with the accuracy of 1%.

Old snow case

In general, as can be seen in Fig 55, for the case of old snow, the angular pattern of reflectance observation is reproduced by SCIATRAN successfully. The highest accuracy is achieved using the aggregate of eight columns with a maximum size of 650 μm . Using the severely roughened habit, the RMSE is 6.97% and bias is 2.79%, which is the smallest compared to those of other habits. These results make the aggregate of eight columns habit the best representative shape for the simulation of reflectance over a snow layer covered with old snow particles.

In all cases, the largest difference between measurement and simulation occurs in the forward direction at which reflectance of snow has a strong peak, while the smallest difference is observed at nadir. After the aggregate of eight columns, the second and third best results are achieved using column (RMSE of 7.32% and bias of 2.17%) and fractal (RMSE of 9.75% and bias of 3.50%) shape. Among different habits, the largest RMSE is observed for the case of droxtal, which is 25.5%. A summary of statistics for the snow grain size and shape retrieval is provided in Table 7.

Ice crystal habit	Asymmetry parameter		Retrieved effective radius (μm)		Old snow		Fresh snow	
	Old snow	Fresh snow	Old snow	Fresh snow	Bias (%)	RMSE (%)	Bias (%)	RMSE (%)
Fractal	0.825	0.827	69.37	76.06	3.50	9.75	13.16	14.69
Droxtal	0.856	0.863	94.48	106.95	0.87	25.54	10.10	34.14
Column	0.873	0.877	74.71	80.49	2.17	7.32	12.36	15.72
Hollow column	0.884	0.888	67.32	72.85	2.80	11.15	13.66	15.14
Aggregate of eight columns	0.844	0.849	98.83	107.62	2.79	6.97	11.85	18.27
Plate	0.923	0.942	38.93	61.44	-0.44	21.47	11.68	16.99
Aggregate of five plates	0.874	0.877	78.02	83.41	1.82	10.34	11.23	12.85
Aggregate of 10 plates	0.893	0.893	65.36	69.28	2.34	13.91	11.52	13.16
Hollow bullet rosette	0.887	0.889	67.01	73.28	2.16	9.99	12.71	15.16

Table 7: Retrieval of the physical characteristics of ice crystals with different shapes in the case of most roughened habits. Numbers in italics indicate minimum root mean square error (RMSE).

Fresh snow case

For the case study of fresh fallen snow on 15th April, the retrieved snow shape and size is presented in Fig. 56. For this case, the effect of surface inhomogeneity is larger because the measurement is only available at a lower altitude compared to aged snow, and therefore the RMSE and bias values are in general larger compared to the previous case of old snow. The best representative shape for fresh fallen snow is the aggregate of five plates with the corresponding RMSE value of 12.85% and bias of 11.23%. The second and third best ice crystal morphology is the aggregate of ten plates (RMSE of 13.16% and bias of 11.52%) and the fractal (RMSE of 14.69% and bias of 13.16%), respectively.

Although, there is no snow grain morphology measurement available for the time

and location of CAR measurements in Barrow, Alaska in April 2008, there are a number of studies indicating the relationship between temperature, wind, humidity and snow grain morphology (Slater and Michaelides, 2019; Shultz, 2018; Libbrecht, 2007; Bailey and Hallett, 2004). Based on the relationship between temperature and snow grain morphology, the column-based shapes are the dominant ice crystal morphology in environments with temperatures higher than -10°C , whereas plates are dominant if the temperature is less than -10°C . The results are in line with this argument.

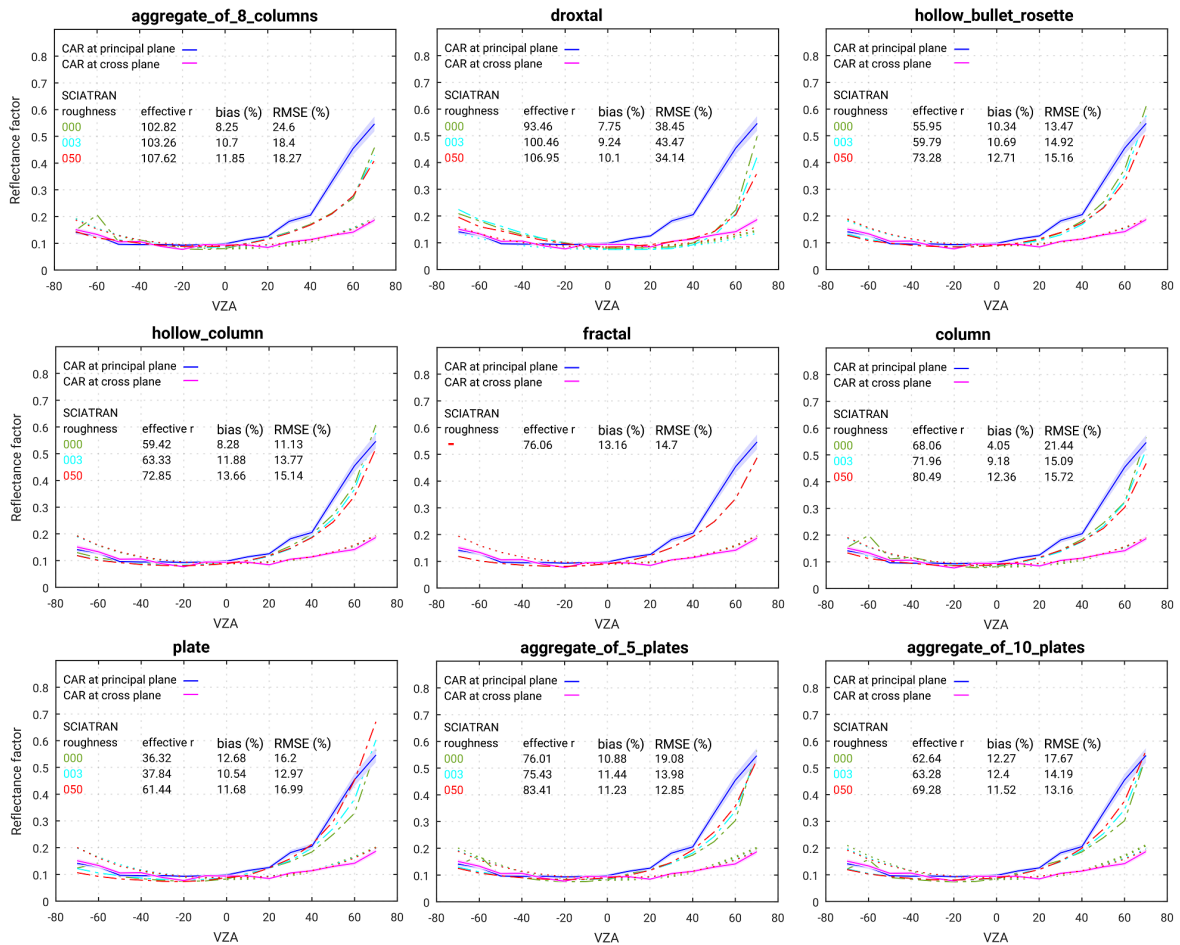


Figure 56: The same as Fig. 55 but the measurements by the CAR instrument were performed on 15th April at 181 m flight altitude over fresh snow.

Effect of selected shape on the size retrieval

The selected ice crystal shape plays a key role in the final size retrieval. Here, this effect is investigated and Fig. 57 and 58 show the results. For this purpose, the measurements at $1.649 \mu\text{m}$ at principal plane are used to retrieve the effective radius per ice crystal shape. Measurements are selected from the old snow case in which the effect of surface inhomogeneity is less significant compared to fresh snow. To calculate the reflectance factor at 0.677 and $0.873 \mu\text{m}$, we use the effective radius obtained by using measurements at $1.649 \mu\text{m}$. The uncertainty of the effective radius

retrieval is estimated to be 10%, based on the optimal estimation technique. The RMSE and bias is presented for each retrieved size and selected shape.

The variation of the retrieved effective radius value as a function of ice crystal shape can be seen in Fig. 57 and 58. The difference in retrieved effective radius generally does not exceed 40%, but in the case of the plate ice crystals, the retrieved effective radius is about 70% smaller than the other shapes, e.g. the aggregate of eight columns. This is a large difference. However, these results are presented for the principal plane in which the maximum differences between simulation and measurement are expected. Therefore, the overall bias and RMSE value for all azimuth directions are smaller than what is presented here.

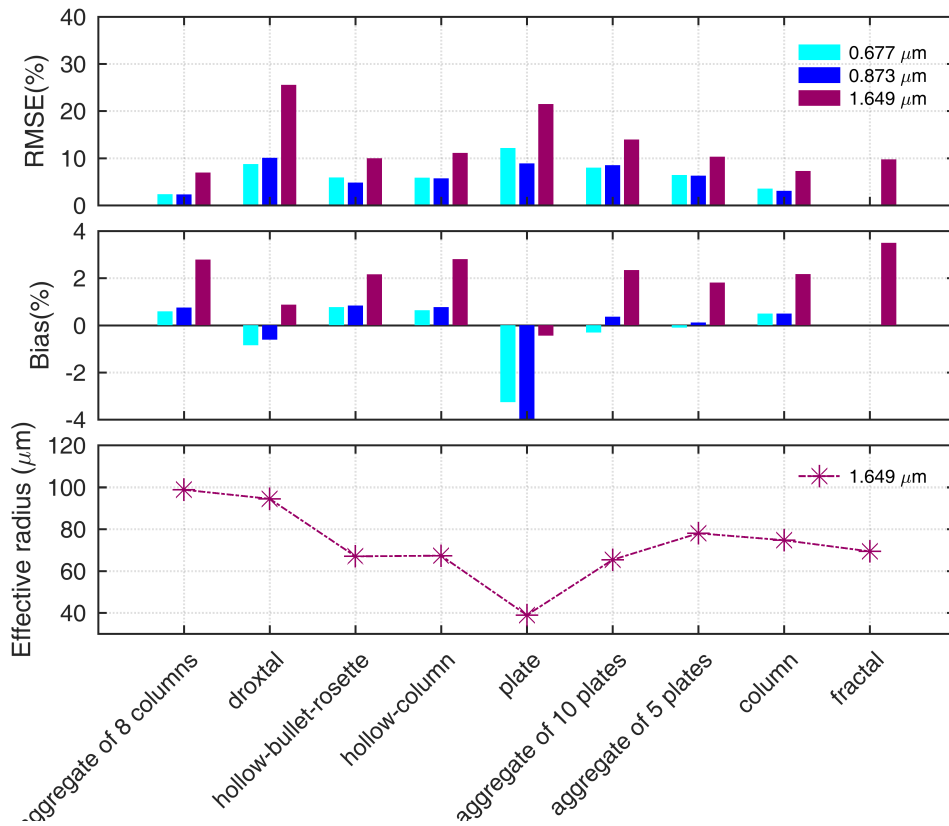


Figure 57: Comparison of snow grain size retrieval and best fit of reflectance at three wavelengths of 0.677, 0.873, and 1.649 μm . Old snow case. Effective radius is retrieved at 1.649 μm .

It can be seen that the RMSE values at 0.677 and 0.873 μm are significantly smaller than that at 1.649 μm . This can be explained by the high reflectance values at these wavelengths, and therefore the larger denominator in the RMSE formula, in which the difference of measured and simulated reflectance factor is divided by the measured reflectance.

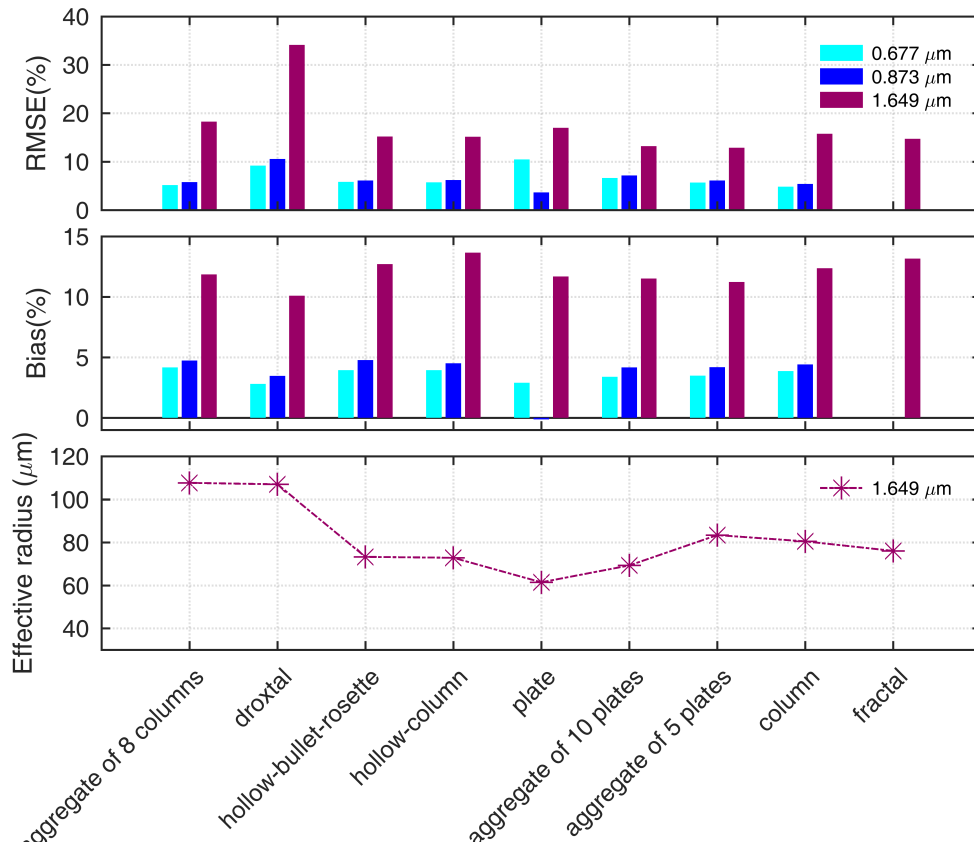


Figure 58: Comparison of snow grain size retrieval and best fit of reflectance at three wavelengths of 0.677, 0.873, and 1.649 μm . for fresh snow case. Effective radius is retrieved at 1.649 μm .

5.3.2 Atmospheric effect

The atmosphere varies spatially and temporally and therefore plays a role in the variation of reflectance in a snow-atmosphere system. In this section, the sensitivity of the reflectance to the changes in aerosol load and gases absorption is calculated. For this purpose, three different scenarios are assumed for the atmospheric condition over a snow layer:

- Rayleigh scattering (scattering by the air molecules);
- gases absorption; and
- absorption and scattering by aerosols.

The variability due to atmospheric effects is dependent on wavelength since aerosol load increases the diffuse component in solar flux and the dependence of BRF on incident zenith angle also varies with wavelength (Aoki et al., 1999). The difference is largest at absorption bands for the same reason. For the sensitivity study, reflectance is calculated at 0.65 μm .

To evaluate the effect of atmospheric scattering and absorption, the reflectance in

the snow-atmosphere system is calculated and compared in different conditions: first with an atmosphere above snow layer containing only a Rayleigh scattering; then Rayleigh plus absorption by Ozone (O_3) and Nitrogen-dioxide (NO_2). The radiative transfer calculation of water vapour (H_2O) absorption is time consuming and is not considered in current analysis. To quantify absorption effects by the other gases, SCIATRAN incorporates a comprehensive database containing monthly and zonally vertical distribution of trace gases e.g. O_3 , NO_2 , SO_2 etc., spectral characteristics of gases absorbers, vertical profiles of pressure and temperature and molecular scattering characteristics (for more information, see Rozanov et al. (2014)).

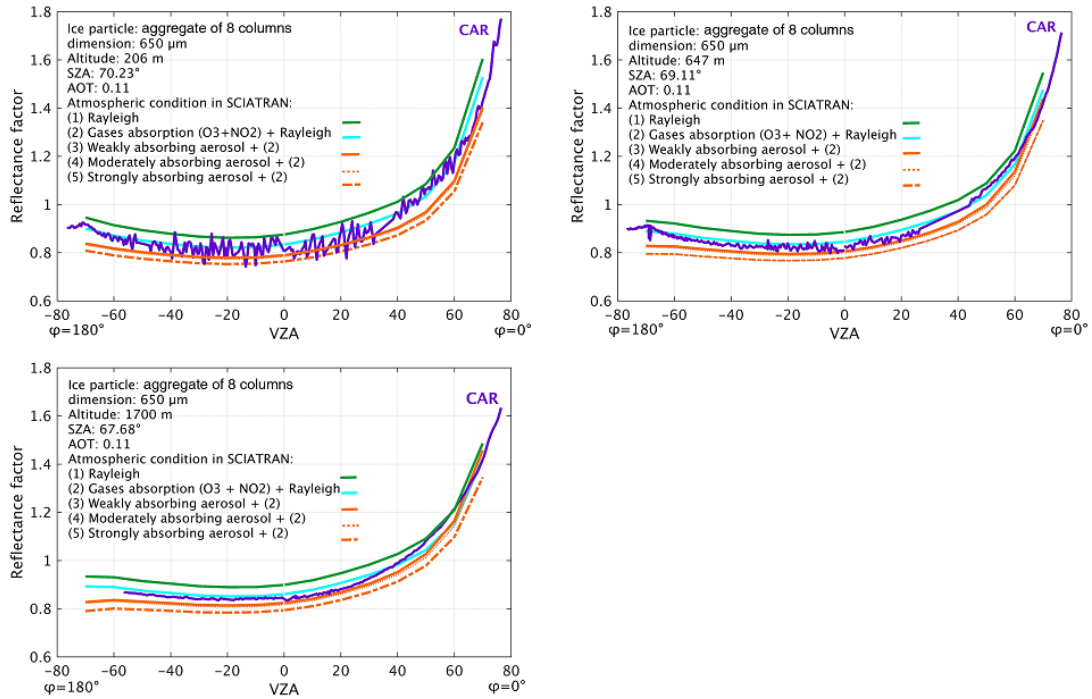


Figure 59: Measured and simulated reflectance factor at ($0.67 \mu\text{m}$) versus the viewing zenith angle (VZA) in the principal plane ($\Phi=0^\circ$ and 180°) at three different flight altitudes. Panels represent results at 206, 647, and 1700 m flight altitudes, respectively. The green lines indicate simulated reflectance assuming Rayleigh scattering (case i). The blue line shows reflectance for case ii (as in case i, including absorption of O_3 and NO_2). The orange lines show the reflectance for case iii (as in case ii but adding aerosol with an aerosol optical thickness (AOT) of 0.11 for three types of aerosol, namely (i) weakly absorbing, (ii) moderately absorbing, and (iii) strongly absorbing)

To calculate the aerosol effect on reflectance in a snow-atmosphere system in the framework of SCIATRAN, the optical characteristics (extinction, scattering cross-section and scattering matrix) and vertical distribution of number density of aerosols are defined within aerosol layers with a defined bottom at top altitude (Aoki et al., 1999). In this study, the internal database of MODIS aerosol model is used (Levy

et al., 2007a). In this database, a spherical shape for aerosol particles is assumed. By defining the aerosol type as i) weakly absorbing, ii) moderately absorbing and iii) strongly absorbing, the refractive index and particle size distribution are also specified (for more information, see Levy et al. (2007a)). To calculate AOT, the ground-based measurement of AERONET is used, which is located at Barrow, Alaska. These measurements are provided at different wavelengths. The Angstrom exponent is used to calculate AOT values at the reference wavelength ($0.55 \mu\text{m}$) needed for SCIATRAN simulation.

Figure 59 shows the difference between BRF values for an atmosphere above snow layer containing 1) only Rayleigh scattering, 2) with gas absorption and 3) aerosol scattering and absorption. The snow surface is assumed to contain aggregates composed of eight columns particles with a maximum dimension of $650 \mu\text{m}$. The BRF reduction at 647 m flight altitude due to gas absorption is smallest at the nadir region 5% and becomes larger in the forward scattering direction 10%, which decreases to 8% at 1700 m altitude. The results in the Fig. 59 also show the BRF values with an atmosphere containing aerosol and without aerosol (only Rayleigh and gases absorption). The changes in BRFs due to weakly absorbing aerosol with AOT of 0.11 at 206 m flight altitude are 5% at nadir and increases in forward scattering direction to 13%.

The strongly absorbing aerosol reduces the BRFs by 7% at the nadir and 20% in the forward scattering direction, which decreases 6% at the nadir and 7% in the forward scattering direction at 1700 m altitude. In general, differentiating between three aerosol types does not bring a BRF change larger than 5% in close to nadir areas.

5.4 Comparison of results: CAR measurements vs. SCIATRAN modelling

Figure 60 shows the scatter plot and the correlation coefficient between CAR and SCIATRAN BRF reproduced by the aggregate of eight columns ice crystals with a dimension of $650 \mu\text{m}$., an atmosphere containing O_3 and NO_2 and weakly absorbing aerosol with AOT of 0.11. The correlation coefficient is high at about 0.98 and the RMS error is 0.03 and 0.05 at $0.67 \mu\text{m}$ and $0.87 \mu\text{m}$, respectively. The deviation of SCIATRAN simulation values from those of measurements is largest in the forward scattering region where $|\Delta\Phi| < 40^\circ$ reaching 0.06 but in close to nadir areas it is 0.04. These values are larger at $0.87 \mu\text{m}$, and the maximum difference is around 0.08 in the glint region (where $|\Delta\Phi| < 40^\circ$ and SZA is almost equal to VZA) but 0.05 in smaller VZA. The results in the principal plane indicate that the general snow BRF pattern of CAR measurement is reproduced by SCIATRAN successfully with the highest accuracy assuming ice crystals with an aggregate of eight columns shape. The lesser degree of agreement between modelling and measurements compared to the aggregate of eight columns shape is provided by Koch fractals.

Going from Koch fractals to the aggregate of eight columns shape provides a no-

ticeable reduction 10% in forward peak and helps to obtain better agreement with CAR airborne measurements. However, the results obtained by using the droxtal ice crystals exhibit large discrepancies, reaching to 20% in the forward or backward scattering direction.

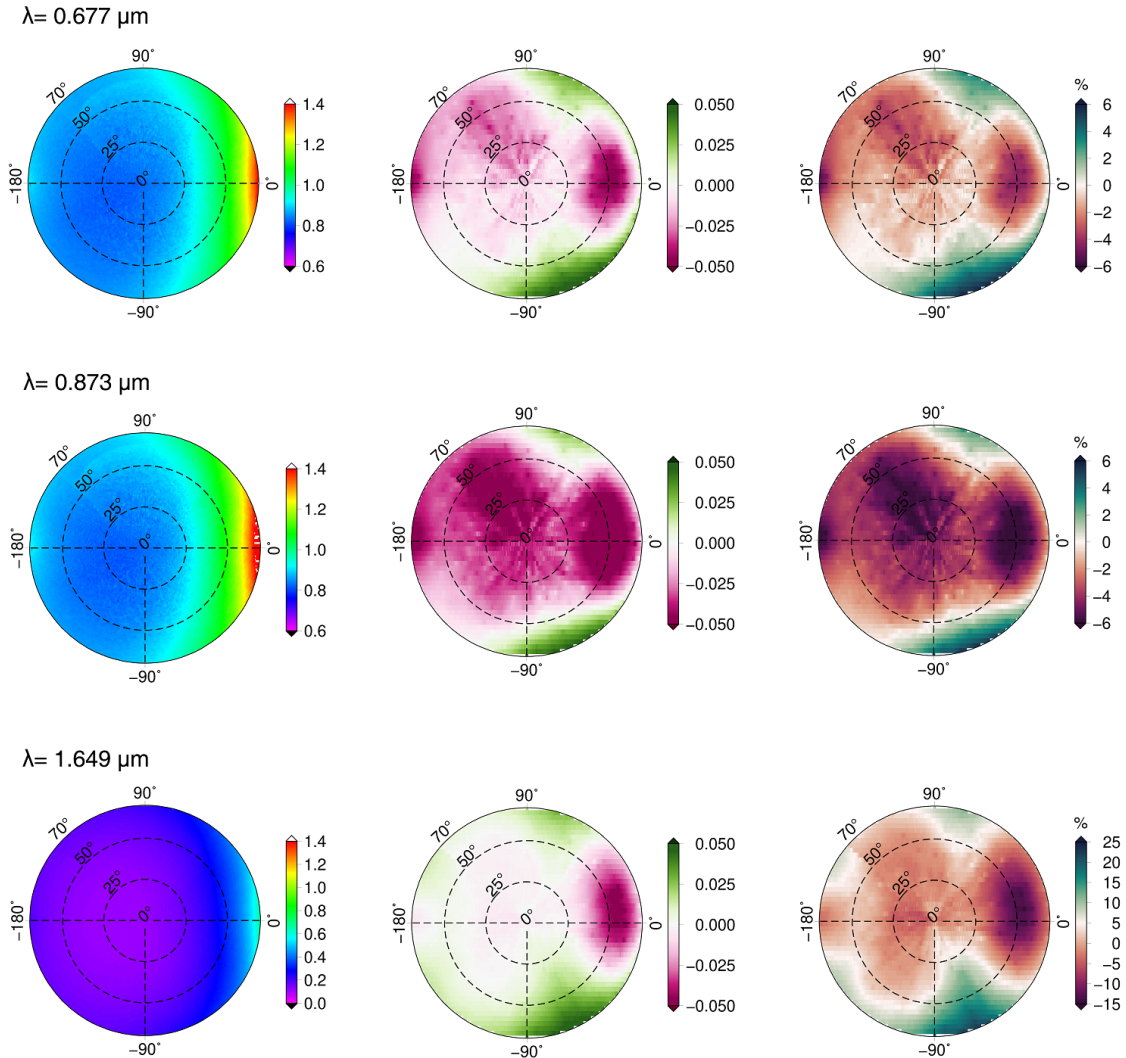


Figure 60: Left column: the reflectance factor at three wavelengths, namely 0.677, 0.873, and 1.649 μm , from the CAR measurements acquired on 7th April 2008 at Barrow, Alaska, at an altitude of 647 m. middle column: the absolute difference between reflectance of simulation(RSCIATRAN) and that of measurement (RCAR): $(RSCIATRAN - RCAR)$; right column depicts the relative difference in percent (%).

Although the real nature of ice crystal shape at the time of measurement is not known, the existence of droxtal ice particles in the measurement field is of less probability, since, previous studies have shown that the extremely low temperature

(-50°) is needed to form droxtal or quasi-spherical shape of ice crystals (Yang et al., 2003), whereas the temperature during CAR measurements was about -14 to -21° .

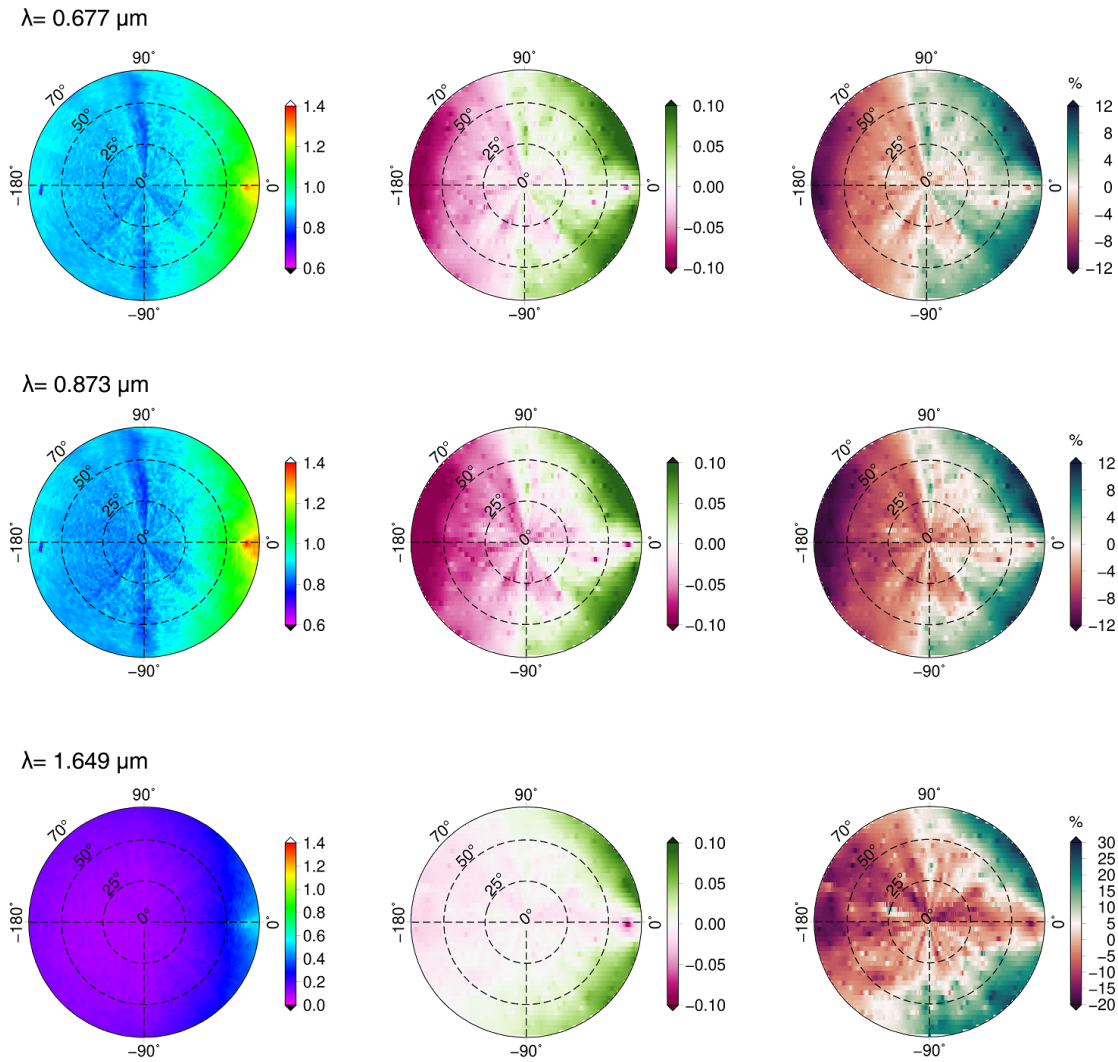


Figure 61: The same as Fig. 60 but the measurements by the CAR instrument were performed on 15th April 2008 at 181 m flight altitude over fresh snow.

This partly explains why the aggregate of eight columns shape ice crystals better capture the derived snow BRF values from CAR measurements as compared to droxtals. In general, the comparison between SCIATRAN and CAR measurements show that SCIATRAN reproduces the BRF measurements at the $1.649 \mu\text{m}$ channel with a high accuracy in the principal plane. By using the aggregate of eight columns shape with the maximum dimension of $650 \mu\text{m}$, the overall difference between the

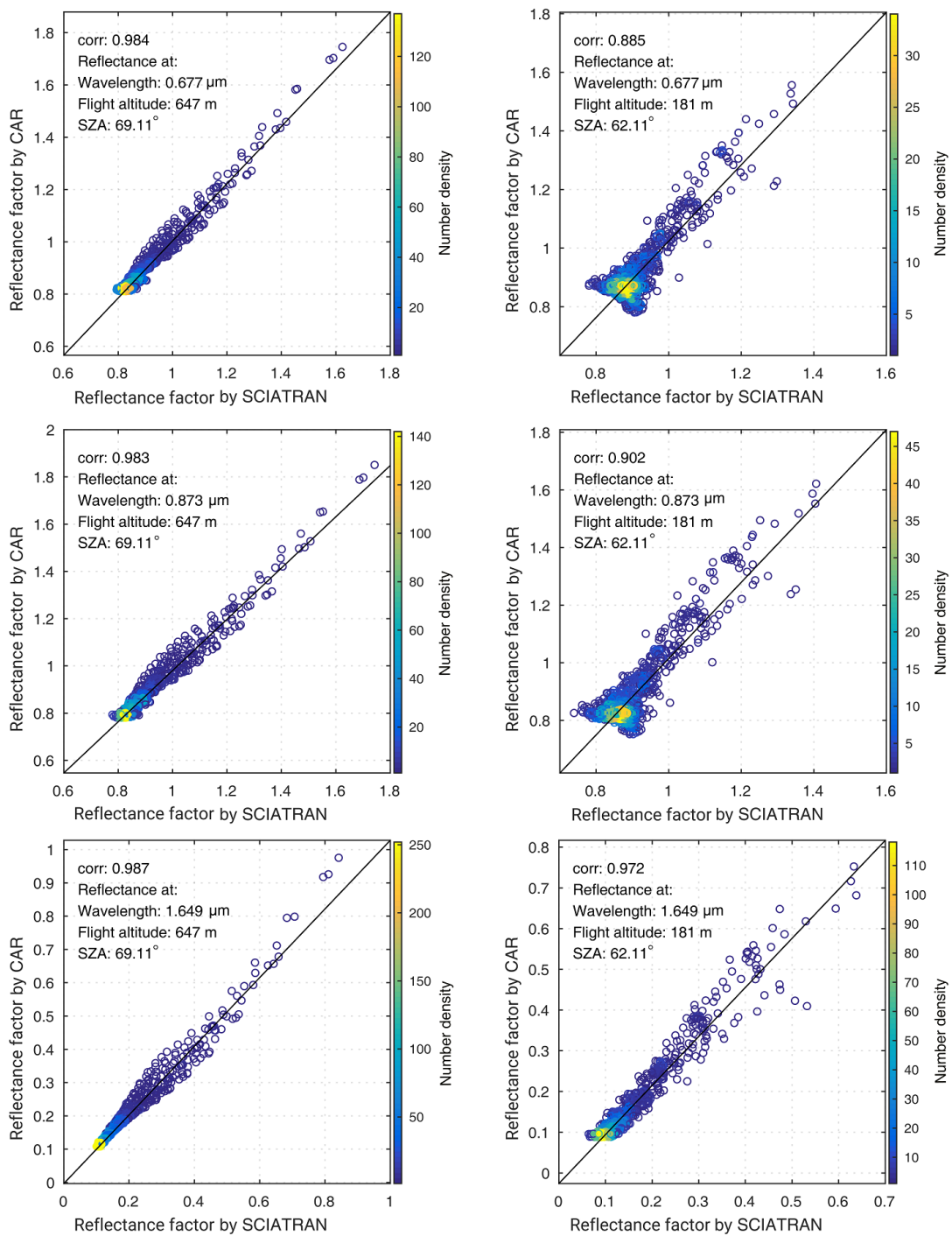


Figure 62: The scatterplot with corresponding Pearson correlation coefficient of reflectance factor measured by CAR and simulated by SCIATRAN. Left column: the results for old snow and right column: fresh snow. Here the color bar represents the number density of the pixels.

CAR and SCIATRAN BRF is small. The largest discrepancy is in the backward scattering direction with high VZA. The minimal difference is about 3%, which is observed in the close to nadir area where $|VZA| < 25^\circ$. To have an analysis of the

SCIATRAN accuracy for all azimuth angles, the correlation plot and the correlation coefficient between CAR and SCIATRAN BRF reproduced by an aggregate of eight column ice crystals with the dimension of $650 \mu\text{m}$ are shown in Fig 62. The correlation coefficient is high at about 0.98 and the RMS error is 0.04. The deviation of SCIATRAN simulation values from those of measurements is small on average and about 0.04 in regions of $\text{VZA} < 50^\circ$ and does not exceed 0.07 for larger VZA.

The results show the high accuracy of the SCIATRAN RTM in simulating the radiation field in the snow-atmosphere scenes for off-glint observations. For the glint condition, one way to mitigate the relatively large differences between measurements and simulation is the use of a vertically inhomogeneous snow layer comprising different ice crystal shapes and sizes in future works. The outcome of this work will help to improve the calculation of snow-atmosphere reflectance and relevant assumptions in future works for the inversion of snow and atmospheric data products from the satellite or airborne passive remote sensing measurements above snow.

6 Retrieval of Aerosol Optical Thickness in the Arctic using satellite measurements

As discussed in Section 2, aerosols in the Arctic have origins from both anthropogenic sources (with a high concentration of sulphate, organic matter and BC) and natural ones (mainly containing sea salt with more than 50% mass fraction, mineral dust with 35% mass fraction, and a lesser amount of NSS sulphate and biomass burning combustion products) (Quinn et al., 2007; Tomasi et al., 2015). The variability of microphysical, chemical and optical characteristics of aerosol particles in space and time and its direct and indirect RF effects in the surface-atmosphere system highlight the importance of aerosols in climate change studies. In the last two decades, several ground-based and airborne measurements have been conducted to determine the aerosol characteristics observed in polar regions. A review of these measurements can be found in Tomasi et al. (2015) and Willis et al. (2018). Nevertheless, the remoteness and special environmental conditions in the Arctic makes satellite-based observation a valuable tool for retrieving Arctic aerosol on a large scale.

Although, the spatial and temporal change of aerosols in the Arctic region - as the sentinel of climate change - holds strong importance, quantification of these changes using space-borne measurements remains uncertain due to the difficulties in retrieving aerosol over highly reflecting surface covered with snow/ice. The small values of AOT in the Arctic lead to the strong contribution of surface reflectance to the measured TOA signal and therefore to the challenge of decoupling the surface signal from that of the atmosphere. The study of snow surface properties in Section 5 indicated the importance of having a priori information about surface properties for accurate estimation of reflectance in snow-atmosphere system. Nevertheless, this information is not available for the Arctic circle.

One solution to minimise the assumptions about the surface and overcome this challenge is using multi-angle measurements from which more information about surface can be obtained to ease the removal of surface signal. The multi-angle imaging spectroradiometer (MISR) on-board the Terra satellite -launched by NASA in 1999- and the AATSR on-board ENVISAT satellite - launched by ESA in 2002 - are the two instruments used for a number of Arctic applications. The common feature making these two instruments favourable for remote sensing of the Arctic is the enhanced capability of acquiring multi-angle measurements nearly simultaneously.

The current operational products for MISR (Diner et al., 2005; Kahn et al., 2010) and AATSR (Holzer-Popp et al., 2013) can determine AOT over the Arctic ocean (Ice-free). Glantz et al. (2014) validated nine years of MODIS/Aqua AOT product against AERONET measurements over Svalbard and found accuracy of $\pm 0.03 \pm 0.05$ AOT. The maps from Holzer-Popp et al. (2013) shows over-estimation of AOT in the Arctic ocean compared to mean AOT values provided by Glantz et al. (2014). The analysis of the operational MISR product over the Arctic ocean shows similar results to that of MODIS (Tomasi et al., 2015). The mentioned satellite-based operational AOT products can be utilised for studying aerosol climatology associated with the sources, transport and sinks of specific aerosol types. Nevertheless, AOT retrieval over land covered by snow/ice and sea ice is an unresolved problem due to the high reflectance of the surface encountered for large solar zenith angles in the Arctic.

Examples of AOT algorithms applied to AATSR data include the AATSR Dual-View algorithm (ADV) which was initially proposed by Veefkind et al. (1999) and AATSR single-view algorithm (ASV) by Veefkind and de Leeuw (1998), the SU algorithm (North et al., 1999) and Oxford RAL Aerosol and Cloud retrieval (ORAC) algorithm (Thomas et al., 2009). These algorithms typically are not optimised for the retrieval of AOT at high latitudes. Istomina et al. (2011) developed a method to retrieve AOT over snow/ice-covered surface using AATSR measurements. The central idea in this approach is the usage of the dual view capability of AATSR and determining the ratio between observations in the forward and nadir directions by calculating the difference between TOA reflectance and atmospheric path reflectance in both directions and taking features of the total atmospheric transmission into account (Istomina et al., 2011). In order to reduce the role of the unknown snow spectral albedo in the retrieval, the ratio of observations in different views is used and account for the asymmetry of the TOA reflectance and not for its magnitude. The retrieval method is a look-up table (LUT) based approach developed for a single aerosol type "Arctic haze" that appears regularly in late winter and early spring in the Arctic region. In this work, the algorithm developed by Istomina (2012) is improved and used.

In the following, a summary of the approach developed by Istomina (2012) called AEROSNOW is briefly presented with the theoretical background, uncertainty and limitations, for which a complete description can be found in Istomina (2012). In this work, the AEROSNOW algorithm is improved using the cloud identification algorithm presented in Section 4. The improved algorithm is applied to a long-term data record of AATSR and the results are validated against AERONET measurements. Details of validation, the conclusion and outlook are presented in the following sub-sections.

6.1 Theoretical background

The measured TOA reflectance comprises the effects from both surface and atmosphere and their interaction, which vary with the geometry of observation. Re-

flectance is defined as follows:

$$R = \frac{\pi I}{\mu_0 F_0} \quad (6.1)$$

where I is the measured radiance, μ_0 is the cosine of solar zenith angle and F_0 is solar irradiance at TOA.

Aerosols scatter light in different directions (dependent on aerosol size, shape and chemical composition) and this information is provided by the scattering phase function (for more details see Section 2). To retrieve aerosol properties under cloud-free condition, an adequate cloud screening is needed as a prerequisite for the retrieval (for more details see Section 4). After cloud screening, the next step is to account for surface contribution to the TOA signal (more details in Section 5). In development of dual-view algorithms (Veefkind et al., 1999), surface is assumed to be isotropic over water in single view. With this assumption, the difference between the two views is associated with the atmospheric effect. However, over land and the cryosphere, surface BRDF affects the interactions between surface and atmosphere. For this reason, a more complex model is needed to retrieve atmospheric contribution.

For a surface-atmosphere system with a Lambertian surface, the TOA reflectance can be re-written as follows:

$$R_{TOA}(\lambda, \mu_0, \mu, \phi) = R_{atm}(\lambda, \mu_0, \mu, \phi) + \frac{R_{Sur}(\lambda)T(\lambda, \mu_0, \mu)}{1 - R_{Sur}(\lambda).s(\lambda)} \quad (6.2)$$

where R_{TOA} is the total reflectance of the surface-atmosphere system, R_{atm} is the atmospheric reflectance (the reflectance of the aerosol, Rayleigh scattering, ozone gas), s is the atmospheric hemispherical albedo, and R_{Sur} is the Lambertian reflectance of the surface. All parameters except the surface reflectance R_{Sur} , are dependent on AOT. The value of R_{Sur} must be either retrieved during the inversion process or removed in the retrieval process. Another solution can be the usage of an independent spectral surface reflectance database (dependent on a given location) in the retrieval process. T is the total atmospheric transmittance defined as the product of the downward and upward transmissions: $T_1(\lambda, \mu_0)$ and $T_2(\lambda, \mu)$. Each transmission is the sum of a diffuse and direct component as follows:

For the atmospheric transmittance from the TOA to the surface:

$$T_1(\mu, \phi_0) = E(\mu_0) + exp(-\tau/\mu_0) \quad (6.3)$$

where $E(\mu_0)$ is the diffuse transmittance from TOA to surface, and $exp(-\tau/\mu_0)$ is the direct component respectively. The total atmospheric transmittance from the surface to satellite is:

$$T_2(\mu, \phi) = E(\mu) + exp(-\tau/\mu) \quad (6.4)$$

where $E(\mu)$ is the diffuse transmittance from surface to TOA, and $exp(-\tau/\mu)$ is the direct component respectively.

6.2 AOT retrieval algorithm: AEROSNOW

In the sensitivity study reported in Section 5, variation of the range of snow reflectance with temperature, humidity, age, pollution and snow morphology is shown. A priori knowledge about snow surface properties is necessary to have an accurate reflectance model of the surface. In this work, the goal is to retrieve AOT in the Arctic circle for which the required a priori information is not available at a large scale. Therefore, reducing the role of snow surface reflectance in the aerosol retrieval method holds strong importance. Istomina (2012) applied the same idea for development of AEROSNOW, which we briefly explain in this section (for more information about AEROSNOW, see Istomina (2012)).

Assuming that $R_{Sur.s} \ll 1$, the LTE solution can be written for the surface and atmosphere for the nadir and forward view as follows:

$$R_{TOA}^f(\lambda, \mu_0, \mu, \phi) = R_{atm}^f(\lambda, \mu_0, \mu, \phi) + R_{Sur}^f(\lambda, \mu_0, \mu, \phi)T^f(\lambda, \mu_0, \mu) \quad (6.5)$$

$$R_{TOA}^n(\lambda, \mu_0, \mu, \phi) = R_{atm}^n(\lambda, \mu_0, \mu, \phi) + R_{Sur}^n(\lambda, \mu_0, \mu, \phi)T^n(\lambda, \mu_0, \mu) \quad (6.6)$$

where the superscripts f and n stand for forward and nadir, respectively. To reduce the role of surface reflectance, the ratio of surface reflectance at nadir to forward view is calculated:

$$R_{Sur}^f(\lambda, \mu_0, \mu, \phi) = \frac{R_{TOA}^f(\lambda, \mu_0, \mu, \phi) - R_{atm}^f(\lambda, \mu_0, \mu, \phi)}{T^f(\lambda, \mu_0, \mu)} \quad (6.7)$$

$$R_{Sur}^n(\lambda, \mu_0, \mu, \phi) = \frac{R_{TOA}^n(\lambda, \mu_0, \mu, \phi) - R_{atm}^n(\lambda, \mu_0, \mu, \phi)}{T^n(\lambda, \mu_0, \mu)} \quad (6.8)$$

By taking the ratio of surface reflectance:

$$\frac{R_{Sur}^f(\lambda, \mu_0, \mu, \phi)}{R_{Sur}^n(\lambda, \mu_0, \mu, \phi)} = \frac{R_{TOA}^f(\lambda, \mu_0, \mu, \phi) - R_{atm}^f(\lambda, \mu_0, \mu, \phi)}{R_{TOA}^n(\lambda, \mu_0, \mu, \phi) - R_{atm}^n(\lambda, \mu_0, \mu, \phi)} \cdot \frac{T^n(\lambda, \mu_0, \mu)}{T^f(\lambda, \mu_0, \mu)} \quad (6.9)$$

This ratio is sensitive to the shape of snow BRDF rather to the value of BRDF. In Section 5, several points about the shape of snow BRDF and its dependency on several factors have been highlighted:

- The anisotropy of reflectance increases with wavelength. This means that the value of surface reflectance ratio has greater values at longer wavelengths.
- The change of reflectance and therefore the surface reflectance ratio at principal plane is much larger than for the perpendicular plane.
- The study of fresh and old snow in Section 5 indicated that BRDF shape and its anisotropy is more pronounced for old snow compared to the fresh case.

In addition, the reflectance ratio cannot be defined in a way that meets all snow surface conditions. Istomina et al. (2009) mentioned the effect of surface inhomogeneities and proposed to weight the pre-assumed snow surface reflectance model by the measured TOA reflectance. Following this idea, the surface reflectance equation

can be written as:

$$\frac{R_{Sur}^f(\lambda, \mu_0, \mu, \phi)}{R_{Sur}^n(\lambda, \mu_0, \mu, \phi)} = \frac{R_{Sur,sim}^f(\lambda)}{R_{Sur,sim}^n(\lambda)} \cdot \frac{R_{TOA,sim}^n(\lambda, \mu_0, \mu, \phi)}{R_{TOA,sim}^f(\lambda, \mu_0, \mu, \phi)} \frac{R_{TOA}^f(\lambda, \mu_0, \mu, \phi)}{R_{TOA}^n(\lambda, \mu_0, \mu, \phi)} \quad (6.10)$$

where $R_{Sur,sim}(\lambda, \mu_0, \mu, \phi)$ is the simulated snow surface reflectance, $R_{TOA,sim}(\lambda, \mu_0, \mu, \phi)$ is the simulated TOA reflectance for a given AOT, and $R_{TOA}(\lambda, \mu_0, \mu, \phi)$ observed top-of-atmosphere reflectance. The optical thickness and type of aerosol is contained in the observed and simulated TOA reflectance. Assuming that the aerosol type is chosen appropriately and the AOT is retrieved correctly, the two terms of TOA reflectance from simulated and observed data will cancel out each other. For the simulated surface reflectance of snow, a semi-analytical model of a medium comprising fractal grains (Kokhanovsky et al., 2005) is used. To retrieve AOT, we replace Eq. 6.10 in 6.9, and minimise the difference until we find the appropriate AOT from the LUT.

Weighting the snow surface reflectance with reflectance of TOA will reduce the impact of not having sufficient knowledge of surface, e.g. by accounting for surface inhomogeneities in real snow surfaces, being adjusted to the variations originating from snow grain size and shape for which data in full scale is not available, and finally the difference in scale and resolution of observation from satellite compared to models or field measurements. Nevertheless, using the ratio of TOA reflectance measured by satellite measurement instead of the ratio of true snow surface reflectance introduces an error due to the atmospheric contribution included in TOA reflectance, e.g. caused by aerosols. To estimate this error, Istomina (2012) performed radiative transfer simulations using SCIATRAN, for two different scenarios:

- reflectance above surface covered with clean snow;
- TOA reflectance over clean snow (containing Rayleigh scattering, aerosol scattering and absorption and gases absorption e.g., by Ozone).

The two different ratios calculated for the two mentioned scenarios indicate the strong dependence of relative error on the relative azimuth angle and AOT Istomina (2012):

- for a relative azimuth angle around 90° , the error is within 0.02%, with no dependence on AOT;
- for larger/smaller relative azimuth angles, the error is larger and changes with AOT; in the forward scattering direction ($\Delta\phi = 0^\circ$), the relative error varies between 0.02% to 0.04% for AOT of 0 to 1, while in the backward scattering direction ($\Delta\phi = 180^\circ$), the range of relative error can be 0.02% to -12% for AOT of 0 to 1, respectively.

The difference in relative error for various angles can be interpreted using the shape of the aerosol phase function. When the relative azimuth angle is about 90° , the amplitude of the phase function is similar for nadir and forward direction. This means the effect of aerosol reflectance is similar in the forward and nadir direction. Therefore, the aerosol effect is mostly cancelled when we calculate the ratio of TOA

reflectance. For this reason, the relative error is minimal (0.02%) for this azimuth angle (for more details, see Istomina (2012)). The independence of relative error from AOT means that this error is not caused by aerosols but rather the atmospheric contribution. The extreme relative azimuth angles in which the relative error is larger are less likely to occur. To compensate for the residual (0.02%), we account for simulated TOA reflectance in Eq. 6.10.

The above-mentioned equations are written for a surface-atmosphere system assuming a Lambertian surface. In Section 5 we indicated that the effect of taking directional surface reflectance into account is not negligible. Istomina (2012) conducted a sensitivity study on introducing surface BRDF effects on Eq. 6.9. Istomina (2012) applied the assumption from Tanre et al. (1979) to have an approximate analytical expression for TOA reflectance in case of non-Lambertian non-homogeneous surface, which accounts for light scattering between the observed point M, its neighbour surface areas, and an atmosphere with optical thickness of τ . The sensitivity study shows that:

- for relatively high sun elevation $\theta_e = 45^\circ$ and observation angles close to the nadir, the accuracy of TOA reflectance calculated using assumptions from Tanre et al. (1979) is around 5%, which is much better than that of Eq. 6.2 formulated assuming a Lambertian surface.
- for lower sun elevations, TOA reflectance - calculated by Tanre et al. (1979) - is underestimated by around 30%. For larger observation angles, $\theta_e = 65^\circ - 85^\circ$ the error is decreasing and in some cases becomes close to zero. For $\theta_e = 45^\circ$, the error is increasing to 20% for viewing angles of 50° .

Although accounting for a non-Lambertian surface leads to achieving higher accuracy when the sun elevation is high (e.g. 45°), it does not indicate an improvement in accuracy when the sun elevation is low (e.g. $5^\circ - 25^\circ$). In addition, equations based on a non-Lambertian surface assumption show different accuracies for nadir and forward observation angles, which will cause stray asymmetry between forward and nadir views during the retrieval (Istomina, 2012). This effect is less pronounced in Eq. 6.2. Therefore, for further AOT retrieval in this study we will use the mentioned equations with the assumption of a Lambertian surface.

Istomina (2012) estimated the uncertainty in aerosol retrieval method and indicated that for the AOTs smaller than 0.3 and a difference of 5% between the surface assumptions in the retrieval and the real surface, the AOT retrieval error can be assumed to be constant, giving the value of approximately ± 0.1 .

6.3 Look-up table calculation

For the retrieval of AOT from space-borne AATSR data, using the explained algorithm, a LUT is constructed that describes the relation between AOT, atmospheric reflectance, TOA reflectance and surface reflectance for channel $0.55 \mu\text{m}$). For this purpose, the SCIATRAN RTM has been used. The atmospheric reflectance includes

Rayleigh scattering, aerosol scattering and absorption and gas absorption. In the following, the specific implementation in AEROSNOW is described.

6.3.1 Rayleigh scattering

The phase function of Rayleigh scattering is well known and considered based on the study by Bucholtz (1995). For elevated areas, the dependency of Rayleigh scattering on temperature and pressure is taken into account and can be written as follows:

$$\tau_{Ray}(\lambda, z) = \frac{P(z)}{P_0} \cdot \frac{T_0}{T(Z)} \cdot \tau_{Ray}(\lambda, 0) \quad (6.11)$$

for which the altitude is taken from the gtopo30 elevation model (Danielson and Gesch, 2011) and temperature from AATSR measurements at the 12 μm channel. The pressure at altitude z can be calculated using the barometric equation as follows:

$$P(z) = P_0 e^{\frac{-M \cdot g_0 \cdot z}{R \cdot T(z)}} \quad (6.12)$$

where M is the molar mass of Earth's air, g_0 is the gravitational constant, R is the universal gas constant, and $T(z)$ is the temperature at the surface. Rayleigh reflectance is simulated using RTM at sea level, and scaling it with the above-mentioned formulation:

$$\rho_{Ray}(\lambda, z) = \rho_{Ray}(\lambda, 0) \cdot \frac{T_0}{T(Z)} \cdot e^{\frac{-M \cdot g_0 \cdot z}{R \cdot T(z)}} \quad (6.13)$$

For the low sun case when the solar zenith angle is greater than 60° , the curvature of the atmosphere has to be considered. To account for air mass correction, in RTM the pseudospherical model of the atmosphere is assumed, and the AATSR measurements using the method explained in Section 2.5.2 are corrected. (Kasten and Young, 1989).

6.3.2 Aerosol scattering and absorption

The aerosol phase function varies with particle size distribution, particle shape and chemical composition and this affects the aerosol single SSA and extinction. Since the resultant atmospheric reflectance depends on aerosol type and observation geometry, the aerosol retrieval methods utilises several LUTs to account for different types and models of aerosols.

The aerosol retrieval over snow/ice surface is challenging and the goal of this work is not to find the best representative aerosol type and model, but rather to overcome the challenge of decoupling atmospheric reflectance from that of TOA in presence of a highly reflecting snow/ice surface. For this reason, the aerosol phase function of Arctic haze (see Fig. 63) is used, which is representative of frequently occurring haze episodes in the Arctic. This phase function is measured during one of regular

Arctic haze events occurred 23rd March 2000 at Ny Ålesund, Svalbard, 78°55′00″N, 11°56′00″E, by the Alfred Wegener Institute of Polar and Marine Research.

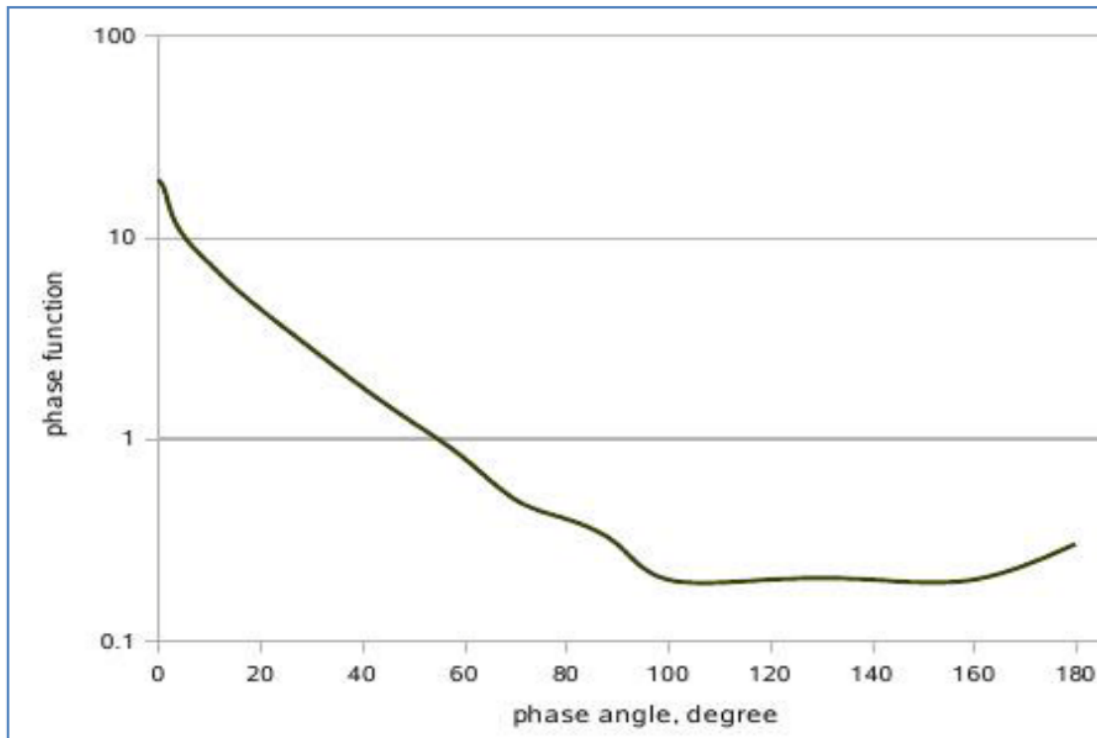


Figure 63: Measured aerosol phase function of Arctic haze, on 23rd March 2000, and Spitsbergen, Ny Ålesund, Svalbard (Istomina, 2012).

6.4 Application limits of the algorithm

Despite the advantages of the dual-view algorithm in reducing the role of surface in retrieving aerosol over snow/ice-covered surfaces, there are inherent sources of errors that limit the application of the described algorithm under specific conditions:

1) Effect of observation geometry

The low sun elevation in the Arctic leads to a small signal to noise ratio in the measured reflectance at the satellite level. In addition, as explained in Section 5, at extreme scattering angles, surface and aerosol properties significantly vary with aerosol type, i.e. in the presence of an unknown aerosol type or surface, the assumptions about the directional properties might be inadequate and lead to incorrect AOT. One solution for the two mentioned problems is limiting the retrieval to solar zenith angles smaller than 75°.

2) Surface properties

The principle assumption behind the design of the AOT retrieval algorithm is that the snow/ice surface reflectance contributes significantly to the TOA reflectance, unlike the aerosol reflectance. Otherwise, Eq. 6.9 will not be valid. Nevertheless, there are situations that contradict this assumption, e.g. a darker surface covered by melting snow. Another assumption is the sufficiently accurate simulation of snow reflectance. As indicated in Section 5, the largest differences between measured and simulated reflectance in the snow-atmosphere system occur in the principal plane. It has been shown that the effect of snow morphology (shape and size) is much smaller in the perpendicular plane at which the relative azimuth angle is 90° . Therefore, at relative azimuth angles around 90° , the simulated reflectance over the snow surface is sufficiently close to a real one unlike extreme relative azimuth angles.

3) Aerosol type and amount

It is important to note that the LUT in this work was created using the phase function measured during an Arctic haze event. This potentially limits the application of retrieval algorithm to regularly occurring Arctic haze in late winter and early spring. Istomina et al. (2009) conducted a sensitivity study and showed that the retrieved AOT significantly varies if the assumed aerosol type and therefore phase function changes in calculation of LUT. In addition, Eq. 6.10 is only valid if the TOA reflectance is mostly affected by surface reflectance. As discussed, for $AOT < 0.3$ and the case of 5% between the surface assumptions in the retrieval and the real surface, the uncertainty of the retrieved AOT is about ± 0.1 . This means that, if the surface reflectance in reality differs from the simulated reflectance by more than 5% (e.g. in the case of old snow), larger error will contribute to the retrieved AOT.

6.5 Brief highlights of anomaly fixes and improvements in the updated version of AEROSNOW

In this section, the main anomalies in the application of AEROSNOW algorithm to the AATSR measurements are briefly explained. There is a list of technical and scientific issues addressed in this work before applying AEROSNOW to the long-term data record of AATSR from 2002-2012:

Technical issues

- The required libraries and tools for running AEROSNOW were out of date, which is expected if we take the date of development in 2012 into account. For this reason, the necessary updates were applied.
- The run time of AEROSNOW algorithm was significantly long, e.g. several hours per orbit over the Arctic circle. This issue limits the application of AEROSNOW to process ten years of AATSR data, which was solved by applying parallel processing with a significant speed-up.

Scientific issues

1) Error in the programming of AEROSNOW processor

In this work, the initial AOT retrieved in the Arctic comprised invalid values (e.g. zero or AOT significantly larger than 1) over most observed scenes. For instance, the left panel of Fig. 64 indicates the result of using AEROSNOW to retrieve AOT for the case study of a well-known haze event occurred in May 2006 over Svalbard during which, smoke from agricultural fires burning in Eastern Europe was transported to Svalbard (for more details about this event, see Law and Stohl (2007)). The AERONET measurements made at Zeppelin observatory indicate a large AOT - up to 0.6 - on this day. As can be seen, the AOT result from AEROSNOW indicates incorrect values. This example highlights the necessity of reviewing the entire source code of AEROSNOW and comparing it with the scientific background to understand the cause of unsuccessful AOT retrieval.

We found that a programming error in the formulation of the scattering angle in the AEROSNOW processor resulted in ineffective performance of AEROSNOW. The invalid scattering angle used in AEROSNOW was corrected using the relevant theoretical background. The right panel of Fig. 64, presents AOT after applying the correction of scattering angle to the AEROSNOW processor. As can be seen, AOT

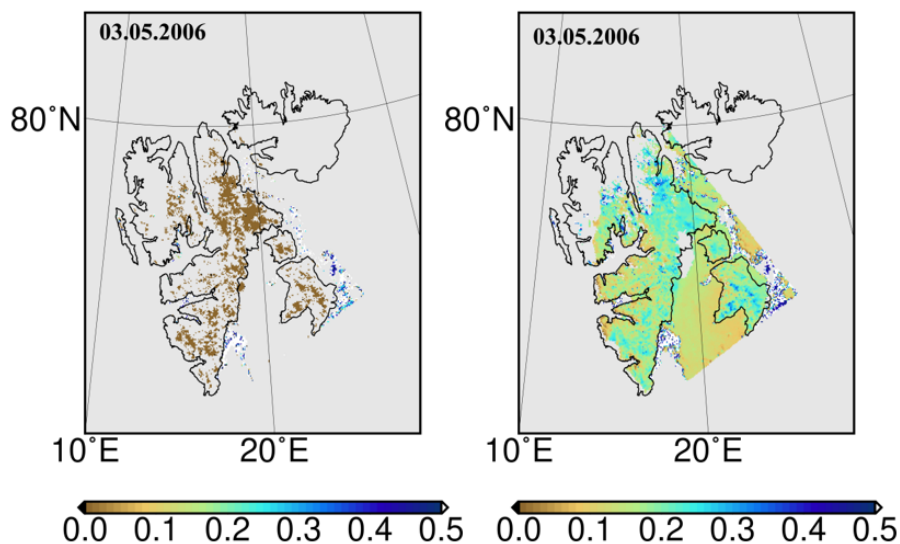


Figure 64: Haze event, 3rd May 2006, Svalbard, left panel: output of AEROSNOW with the incorrect formulation of the scattering angle, right panel: the output of AEROSNOW after solving the issue.

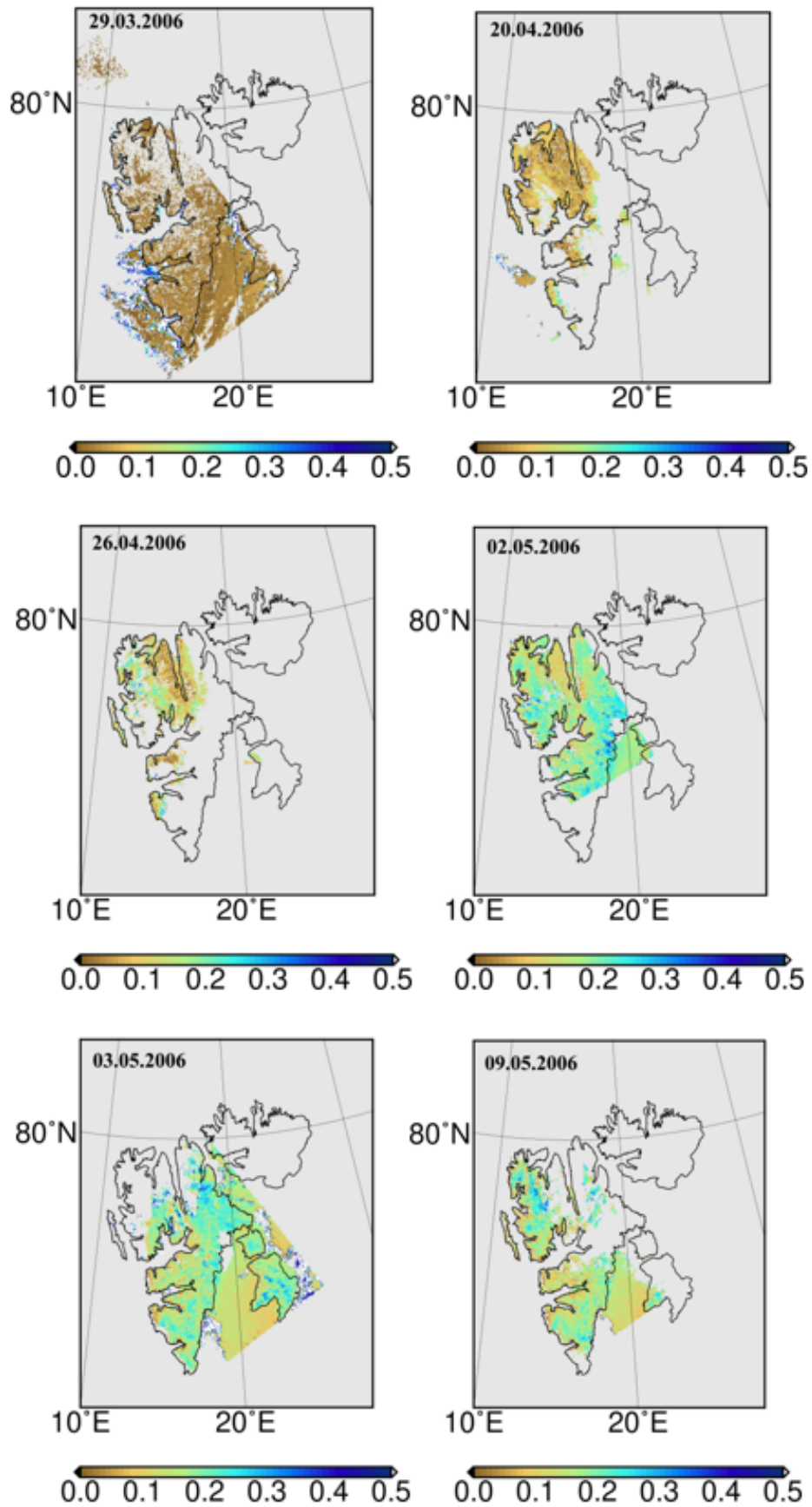


Figure 65: Time series of AOT maps before and during the Haze event, May 2006, Svalbard.

values become larger than zero and remain in the range expected for this particular haze event.

Fig. 65 shows a short time series of AOT maps before and during a haze event in May 2006 over Svalbard, retrieved using AEROSNOW and the AATSR data. The general pattern seems to be consistent with the existing information about the haze event in this particular period. Nevertheless, the impact of cloud residuals can be seen in the retrieved AOT. In the following sub-sections, we will focus on this issue and present the solution applied to fix it.

2) Artificial glint condition and large AOT

In the global map of AOT over the Arctic circle, a halo-like pattern around the central Arctic has been found (see Fig. 66 upper panel). This pattern is constructed from smaller stripe-like patterns (see Fig. 66 bottom panel). The pixels forming the artificial patterns all show large AOT values. Several parameters have been tested and finally the source of this issue was found to be "an artificial glint condition" created due to an error in the libraries used to read AATSR L1B data within the processing chain of AEROSNOW. The cause of issue originates from an interpolation method used in the reading libraries to fill the gaps between the azimuth angles of tie points. However, in this particular area the azimuth angle has different signs on the two sides of stripe pattern, which leads to the creation of incorrect azimuth angles - with values around 0° - in the output.

To better represent the issue, Fig. 67 shows the stripe-like pattern over a small region with the corresponding AOT and reflectance values together with all relevant geometry parameters (VZA, SZA and RAA). One can see that the very large AOT in the stripe-like pattern corresponds to a RAA value of 0° , while VZA and SZA are almost equal and both close to 50° . This geometry is close to the glint condition at which the snow surface reflectance is significantly high and the performance of AEROSNOW is limited (for further details, see Section 5 and 6.2).

Nevertheless, the observed glint condition is not real, and it has been created artificially. To solve this issue, the relative azimuth angles of these pixels are replaced with those of the closest neighbours. The updated result after excluding the artificial glint condition is presented in Fig. 68.

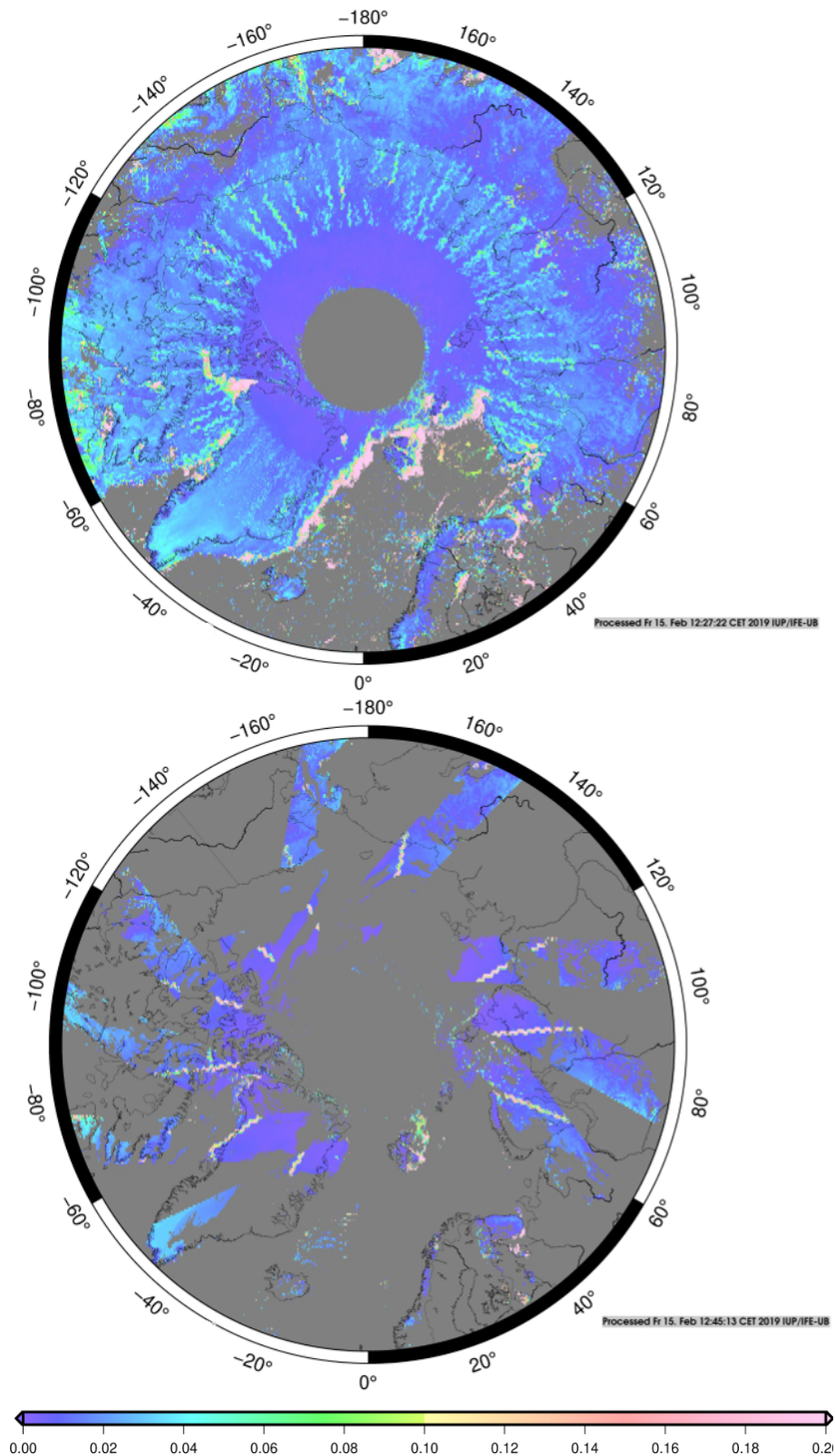


Figure 66: The impact of creating artificial glint conditions using the AEROSNOW algorithm, shown for May 2006 over the Arctic circle, upper panel: the average AOT for the whole of May, bottom panel: one selected day to highlight the stripe pattern in the AOT records for all of orbits.

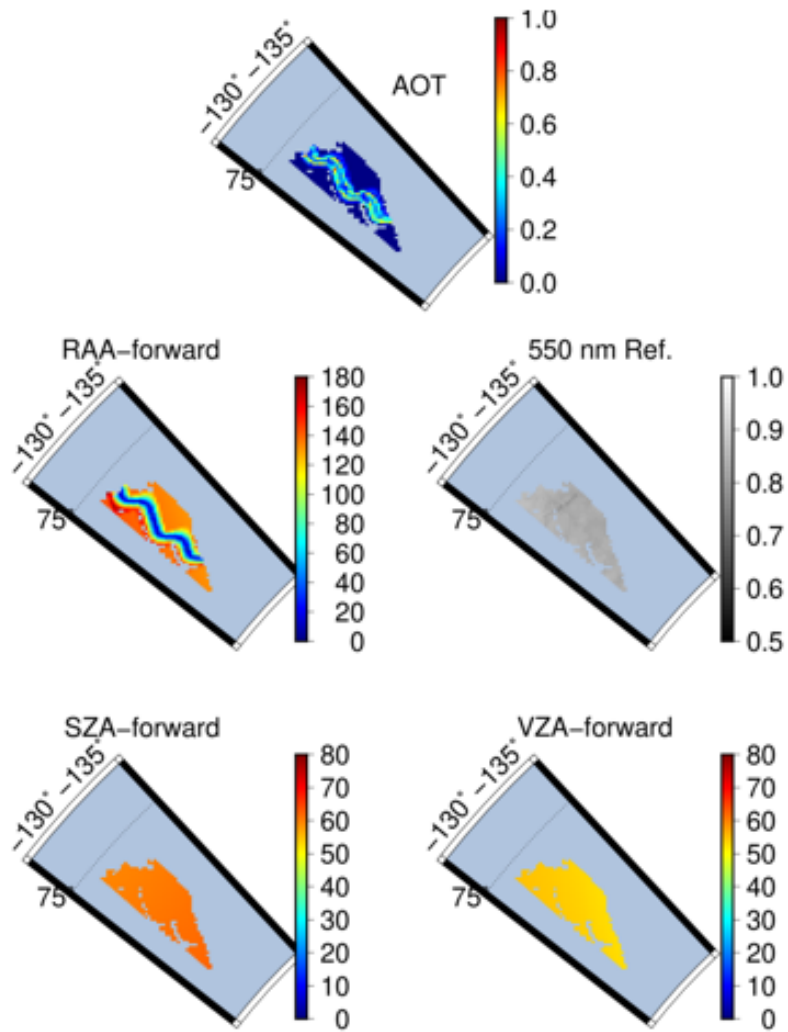


Figure 67: Zoom into one region where the pattern could be detected to study all parameters related to AOT on the sample pixels: reflectance, AOT and corresponding VZA, SZA and RAA.

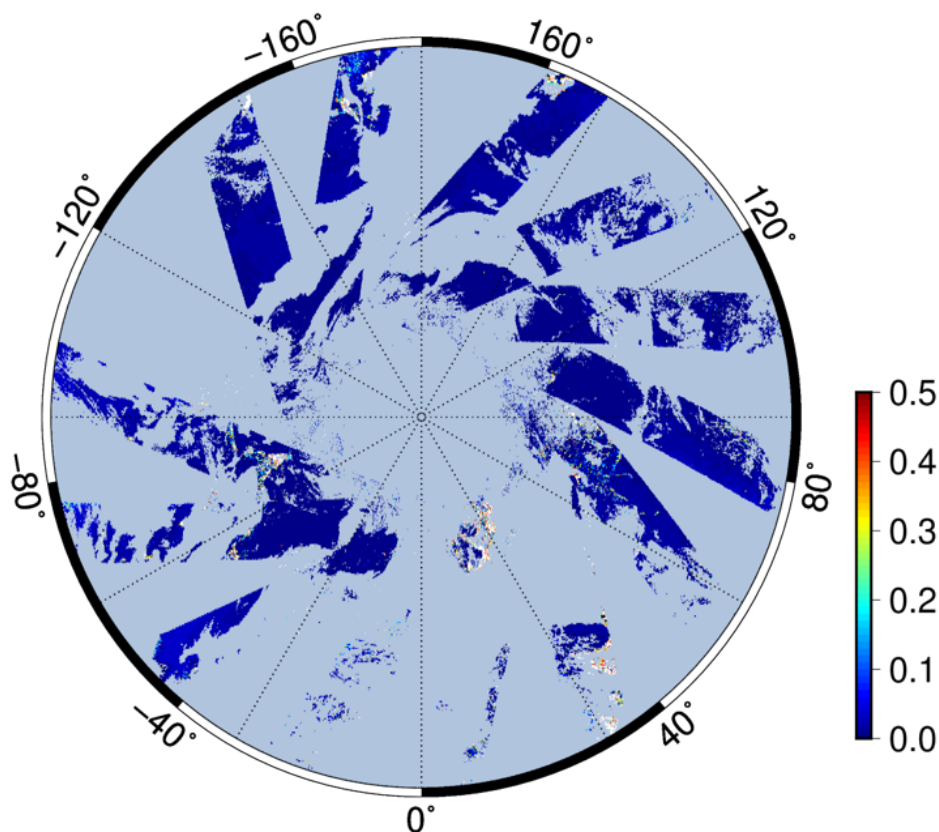


Figure 68: The impact of solving the artificial glint condition, for one day selected in May 2006, over the Arctic circle.

3) Residual clouds

Unresolved residual clouds were a known limitation of AEROSNOW algorithm as reported by Istomina (2012). The cause was presence of thin clouds and inadequate cloud masking for detecting them.

In this work, a simplified version of the ASCIA algorithm is applied to improve the cloud mask of AEROSNOW (Istomina et al., 2010). The simple version contains only tests on the reflectance of ($3.7 \mu\text{m}$) (for details see, Section 4.4.1.2). The reason for not implementing the full version of ASCIA in AEROSNOW is the high processing time of ASCIA, which is not optimal for the application to long data record.

Figure 69 shows two examples of the improvement made in cloud detection: the left column shows the retrieved AOT from AEROSNOW with the original cloud detection method (based on spectral shape of snow/ice, for further details, see Istomina et al. (2010)) and the right column shows the same dates and scenes but after improving cloud masking in AEROSNOW using ASCIA. One can easily see the high AOT values indicated by blue colour in the left panel, which are all excluded in the right one. This is a promising confirmation for the successful performance of ASCIA and improvements made in the cloud detection scheme.

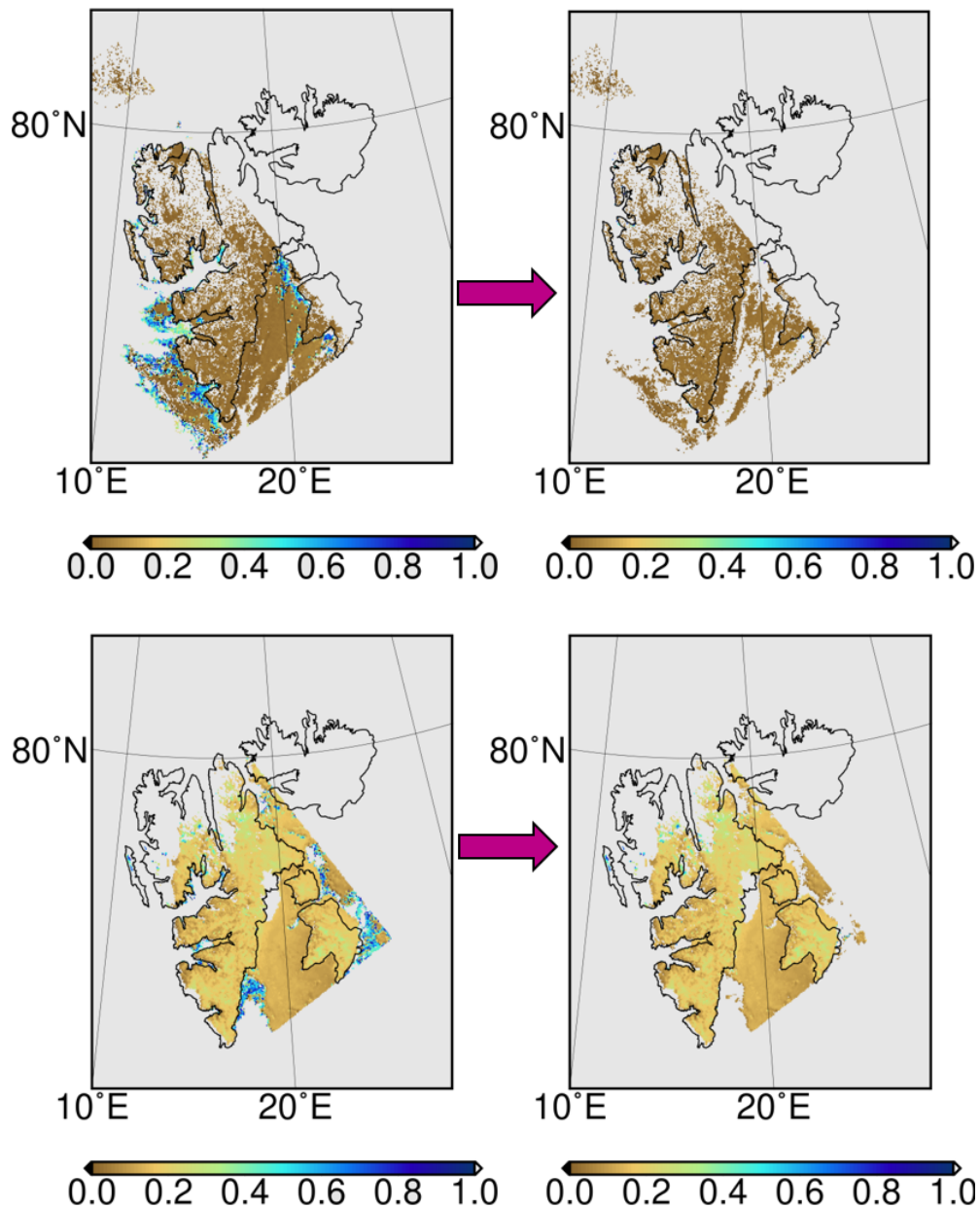


Figure 69: The effect of improving cloud detection in AEROSNOW AOT retrieval algorithm for two days. Left column: AEROSNOW with original cloud detection method (see details in Istomina et al. (2010)). Right column: AOT after improving cloud detection in AEROSNOW algorithm using ASCIA (see Sect. 4). Upper row: 29th March 2006, bottom panel: During Haze event, 3rd May 2006, Svalbard.

6.6 Processing of a long-term AOT data record

After finding and solving several technical and scientific issues in the application of AEROSNOW over the Arctic circle, the algorithm is applied to the whole time

series of data from AATSR delivered during its operation from 2002-2012 comprising 51,100 orbits. For the spatial coverage, the whole Arctic circle is selected and created a AOT data record with the spatial resolution of $1 \times 1 \text{ km}^2$.

Figure 70 shows one example of monthly mean AOT in 2006 over the Arctic. In the following sub-section, the retrieved long-term AOT data record is validated using AERONET measurements.

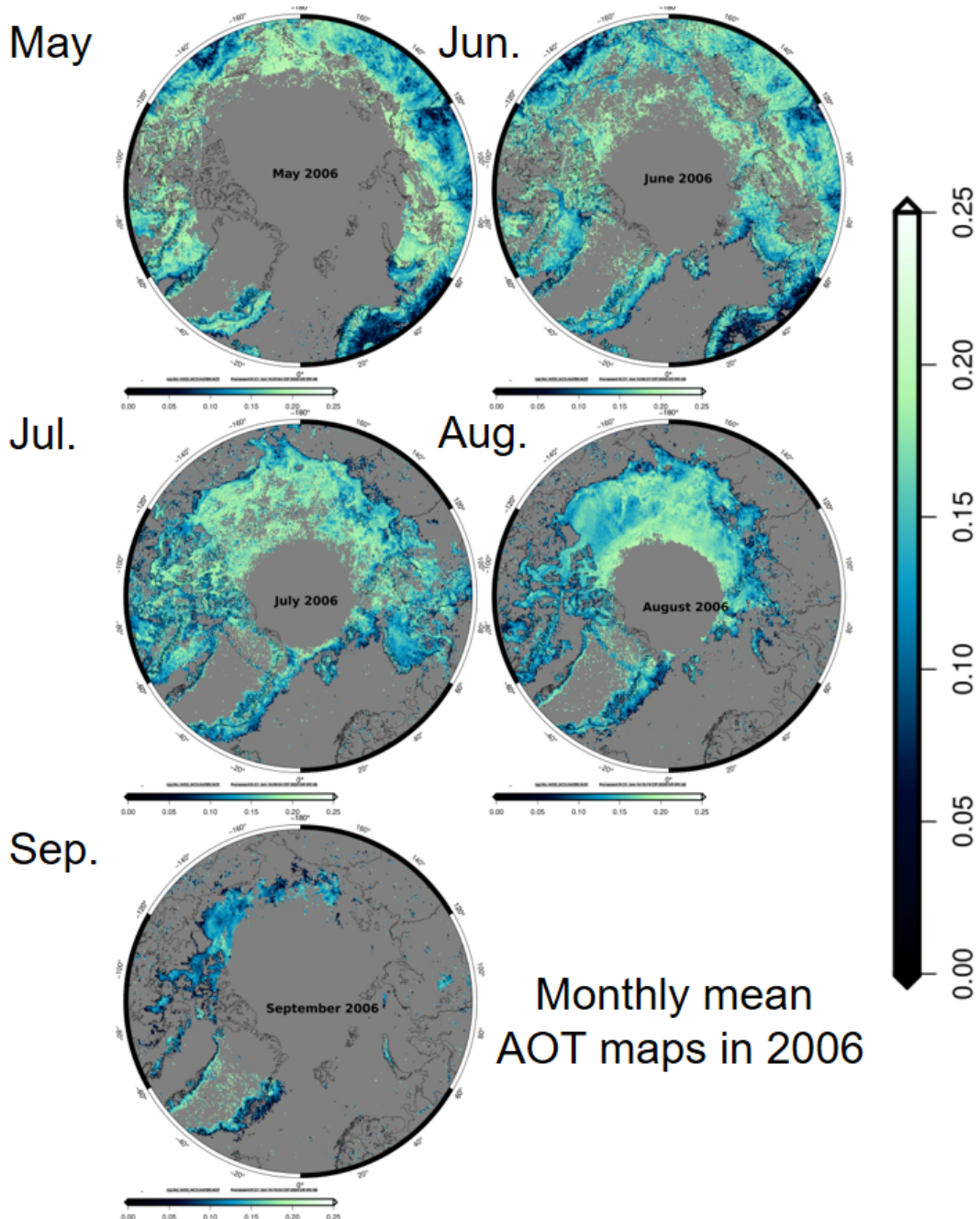


Figure 70: Monthly mean AOT over the Arctic circle in 2006, reprocessed using the new version of AEROSNOW algorithm.

6.7 Validation vs. AERONET

For the validation of the newly-created AOT data record, the ground-based AERONET data is used. In Section 3.3.2, the AERONET global network and its data content is explained. Despite the extensive use of AERONET data for AOT validation in several studies, the validation of AOT over the Arctic region using AERONET is limited due to the lack of adequate spatial and temporal coverage. Figure 71 shows the distribution of available AERONET stations in the polar region. As it can be seen, there are twenty AERONET stations in this area, of which only eight stations provide data for the period of interest in 2002-2012. Additionally, most of the available AERONET stations are located at the coastal areas with open water at which AOT retrieval is challenging because AEROSNOW has been designed for retrieval over snow and ice-covered surfaces and AOT retrieval over melting snow is a known limitation of AEROSNOW. Table 8 shows the list of stations used, their location and the temporal coverage of the measured data.

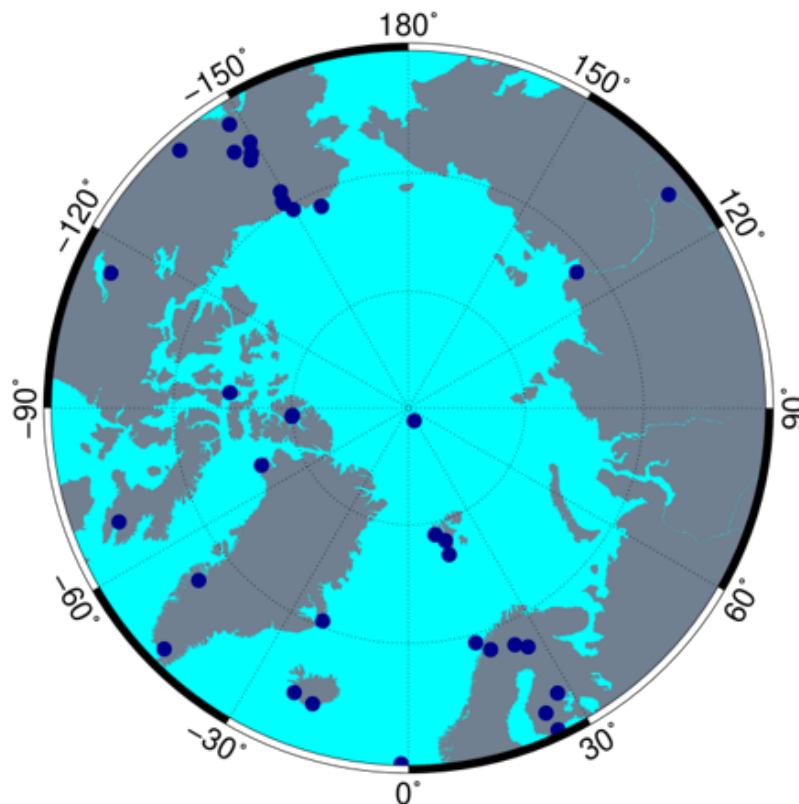


Figure 71: AERONET stations in the Arctic region.

The validation method is based on defining a suitable spatial distance and temporal interval between AERONET data and retrieved AOT from AATSR. In this work, the spatial distance is about 25 km and temporal interval of 1h around the time of measurement acquisition by AATSR.

Station name	Geographical coordinate	available data period
Resolute Bay	74.705N, 94.969W	2006-2011
Pearl	80.054N, 86.417W	2007-2011
Kangerlussuaq	66.996N, 50.621W	2008-2011
Barrow	71.312N, 156.665W	2005-2011
Opal	79.990N, 85.939W	2007-2010
Thule	76.516N, 68.769W	2007-2011
Hornsund	77.001N, 15.540E	2005-2011
Ny Alesund AWI	78.923N, 11.923E	2006

Table 8: Available AERONET stations and corresponding coordinates and temporal coverage.

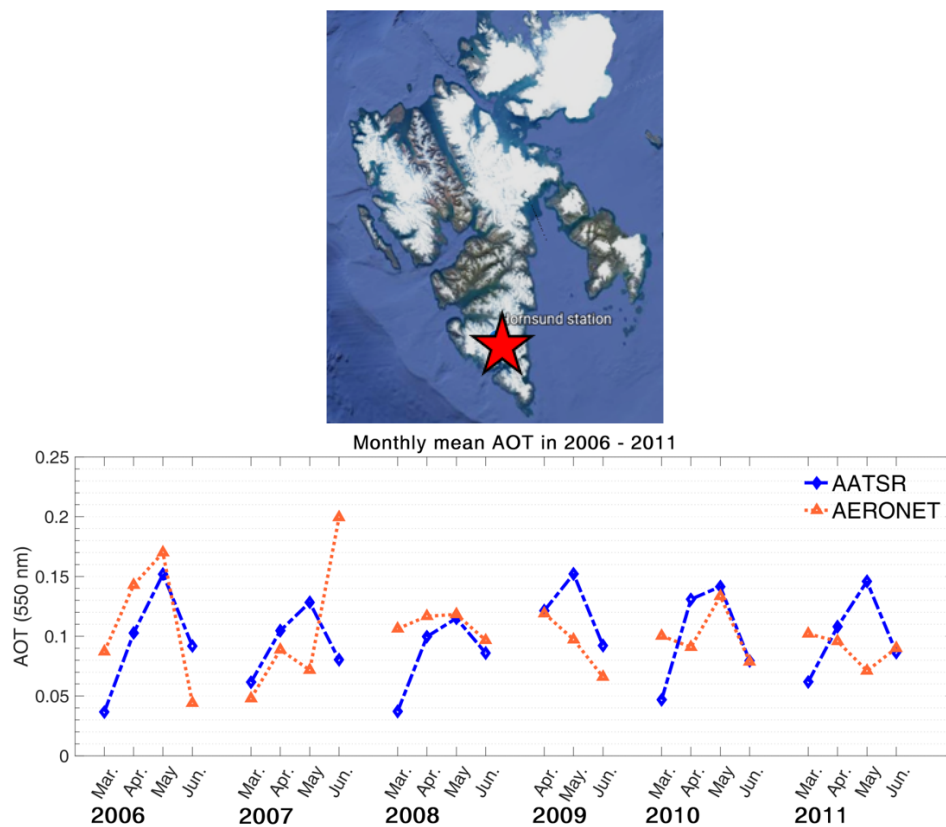


Figure 72: Top panel: Hornsund station, the red star shows the location of station at Svalbard, bottom panel: Monthly mean AOT in 2006-2011. AATSR data are shown with blue lines and symbols, AERONET measurements are shown in orange.

The results of two representative stations providing a sufficiently long temporal record are presented in Fig. 72 and 73. Here, the monthly mean AOT retrieved with the new version of AEROSNOW and that of AERONET measurements at $0.55 \mu\text{m}$ is presented. The temporal coverage is mostly limited to the spring-time (March-

May) in which Arctic haze frequently occurs. AEROSNOW is optimised for haze events (see Section 6.3.2). The results shown here indicate a peak per year in the retrieved AOT occurring every April-May, which is in line with our expectations and understanding of Arctic haze.

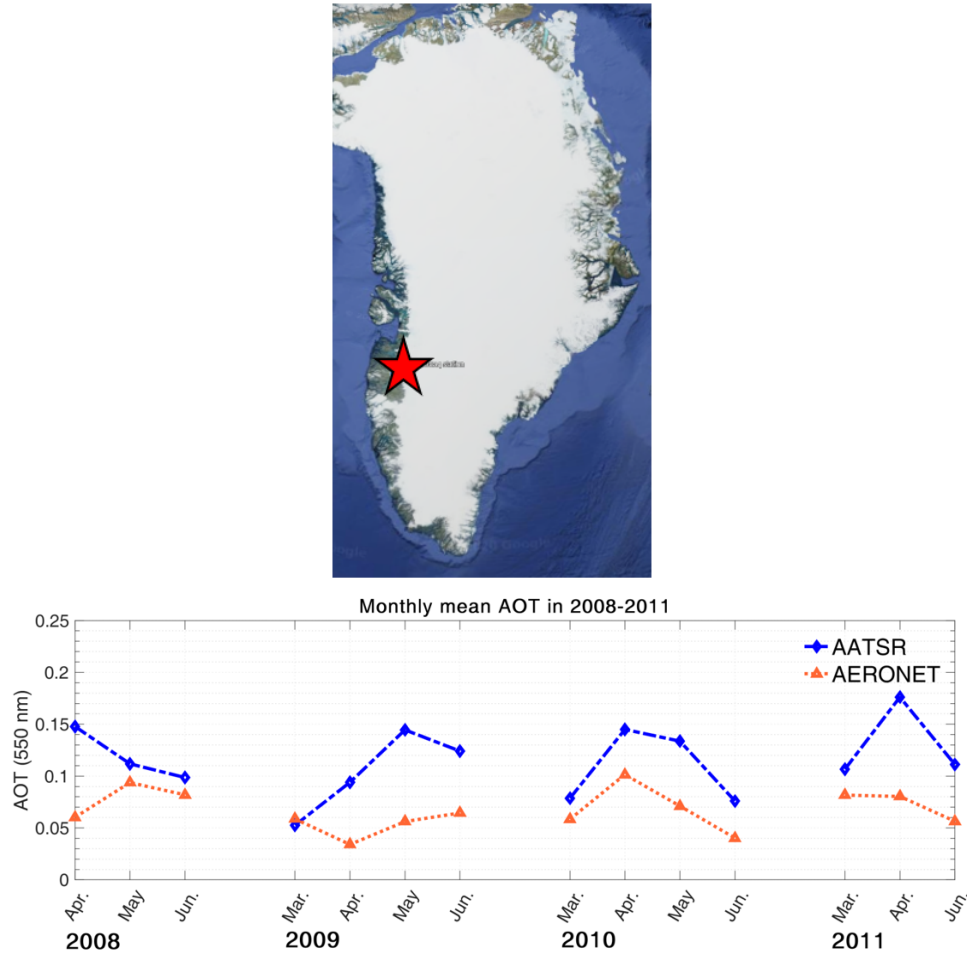


Figure 73: Monthly mean AOT at Kangerlussuaq station, Greenland, 2008-2011. AATSR data are shown with blue lines and symbols, AERONET measurements are shown in orange.

To take a closer look at the comparison of AOT retrieved from AATSR and that of AERONET, here the daily time series are presented from the mentioned two stations. The AOT time series of other stations indicate more or less similar features. For example, at some temporal points a very good agreement exists between AEROSNOW result and AERONET, while large discrepancies occur with some other cases. Despite discrepancies, a general agreement pattern exists between AATSR and AERONET, as can be seen in Fig. 74. In addition, a seasonality pattern that corresponds to haze episodes (late winter-early spring) can be distinguished in the time series. Nevertheless, more analysis is needed to better understand the reason behind having less accurate retrievals. For this purpose, we divided the whole times series in two categories:

- Cases in which retrieved AOT is very close to measurement from AERONET, whereby the difference is smaller than 0.05;
- Cases in which the difference between AOT of AATSR and AERONET is larger than 0.05.

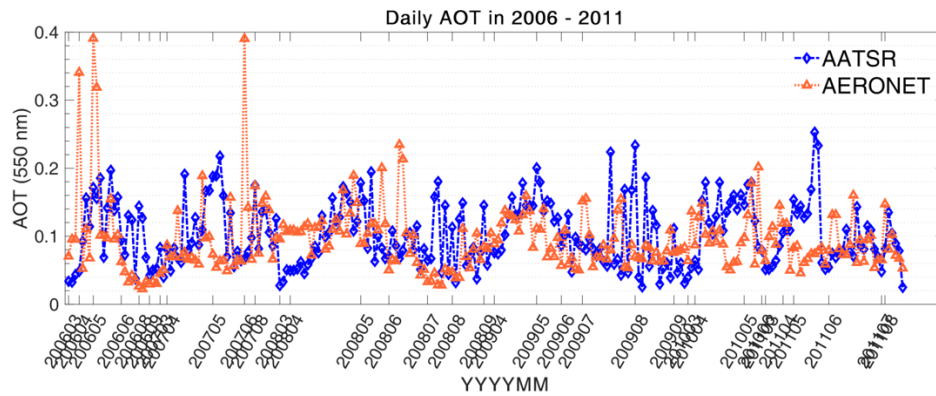


Figure 74: Daily AOT at Hornsund station, Svalbard, 2006-2011. AATSR data are shown with blue line and symbols, AERONET measurements are shown in orange.

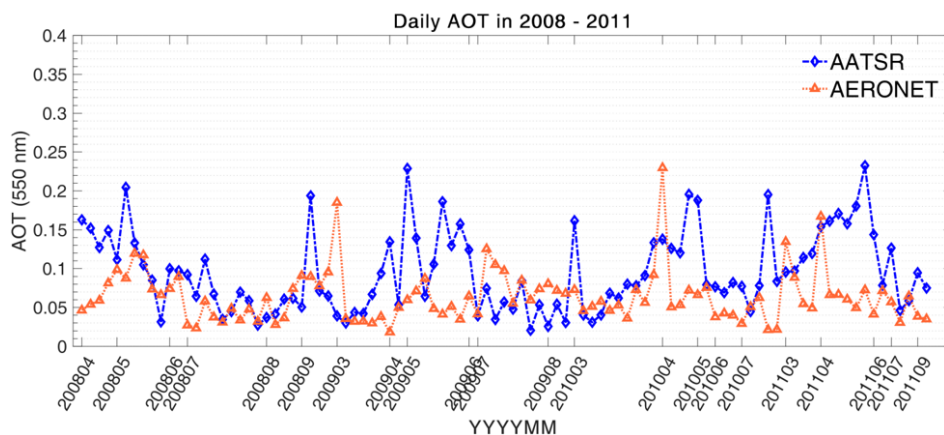


Figure 75: Daily AOT at Kangerlussuaq station, Greenland, 2008-2011. AATSR data are shown with blue line and symbols, AERONET measurements are shown in orange.

Before focusing on the less accurate retrievals, here measurements from category 1 are shown, and it can be seen that AEROSNOW captures the signature of Arctic haze successfully. Despite having well representative cases as shown in Fig. 76 and 77, there are several issues occurring repeatedly in all stations:

- In case of having several satellite orbit overpasses over a station in one day, we usually observe significantly different values for morning and afternoon orbits.
- For extreme observation geometries (e.g. close to glint), the retrieved AOT is much higher than the AOT from AERONET.

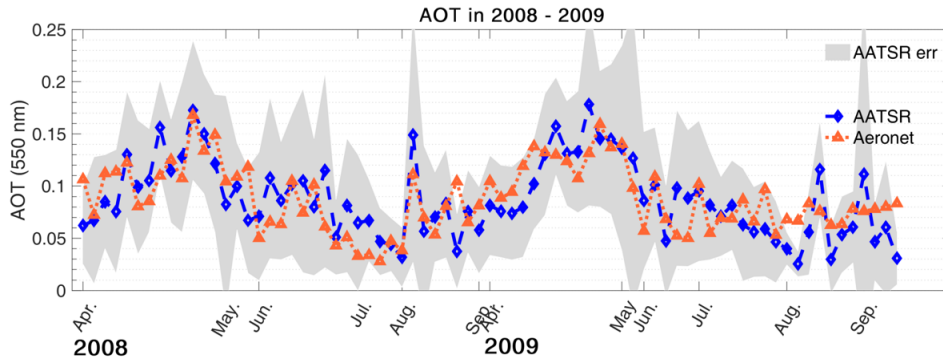


Figure 76: Daily AOT at Hornsund station, Svalbard, 2008-2009. AATSR data are shown with blue line and symbols, AERONET measurements are shown in orange.

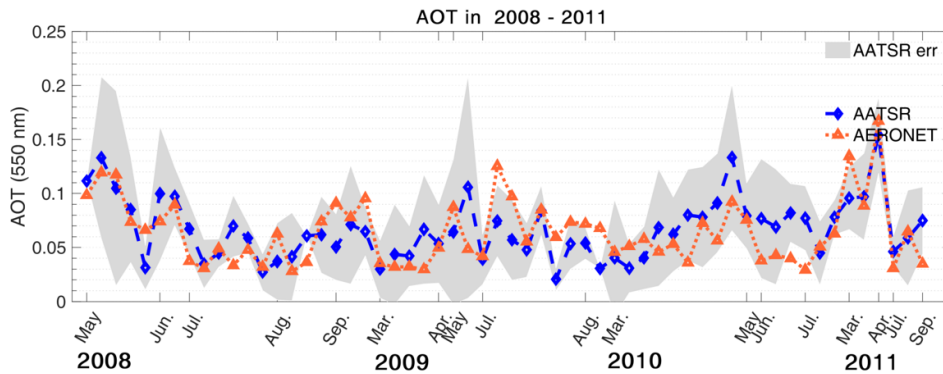


Figure 77: Daily AOT at Kangerlussuaq station, Greenland, 2008-2011. AATSR data are shown with blue line and symbols, AERONET measurements are shown in orange.

The latter is in line with the discussion about the application limits of AEROS-NOW in Section 6.4. Therefore, the AOT retrieval cases, which are processed under extreme observation geometry can be excluded from the validation routine. One example of such cases is shown in Fig. 78. The upper panel shows all of retrieved cases including pixels in glint condition, and the bottom panel shows the same time series but excluding the glint geometry from the retrieval cases.

As mentioned before, another issue is having different AOT values for various satellite orbits during different time of one day. Over some stations (e.g. OPAL station in the Canadian Arctic), this issue is more highlighted due to having more satellite overpasses compared to other AERONET stations. As can be seen in Fig. 79, there is a strong oscillation of AOT. It can be seen in the bottom panel of Fig. 79 that four different values of AOT are retrieved in one day (highlighted with the green oval). However, this change of AOT with time of day, is not observed in AERONET measurements. Several points have been checked to understand the reason behind the variation of AOT across day-time, e.g. the geometry of observation and having different values for azimuth angle in ascending/descending orbits of satellites.

Another reason could be having a different contribution of surface BRDF to the retrieved AOT, since observation geometry changes for different orbits during day. Nevertheless, the current tests are not adequate to confirm the cause of this issue and further investigation is necessary.

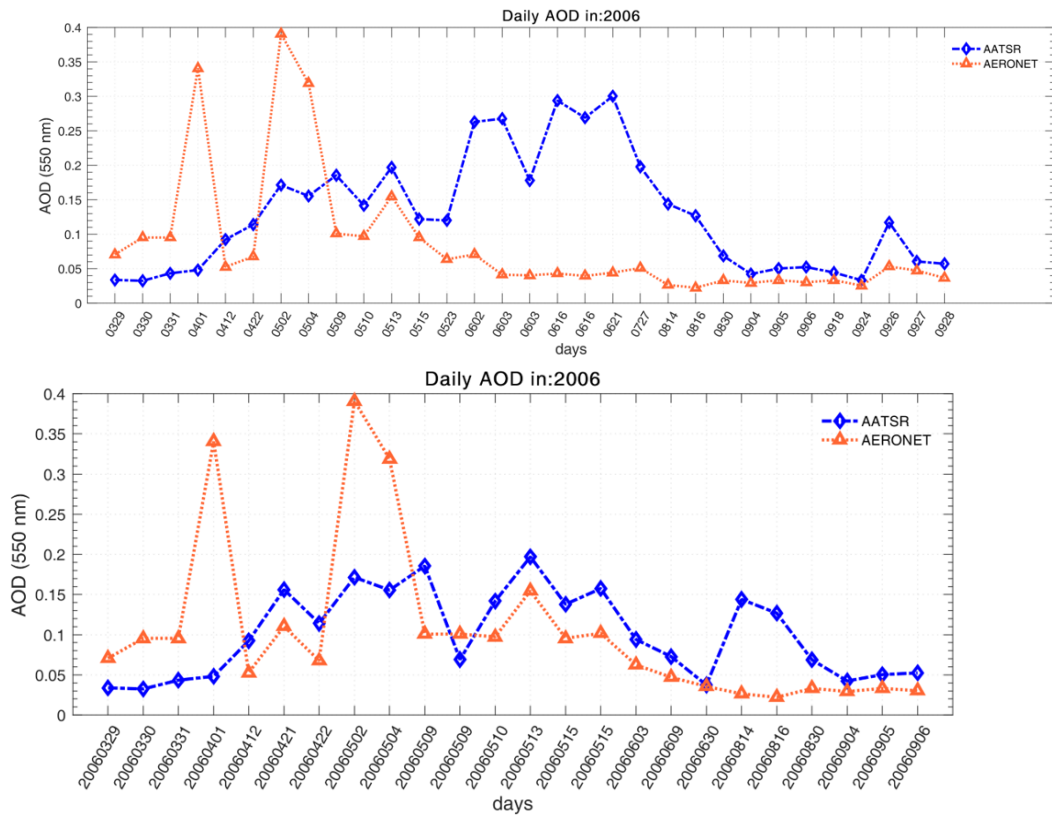


Figure 78: Daily AOT at Hornsund station, Svalbard, 2006. AATSR data are shown with blue line and symbols, AERONET measurements are shown in orange.

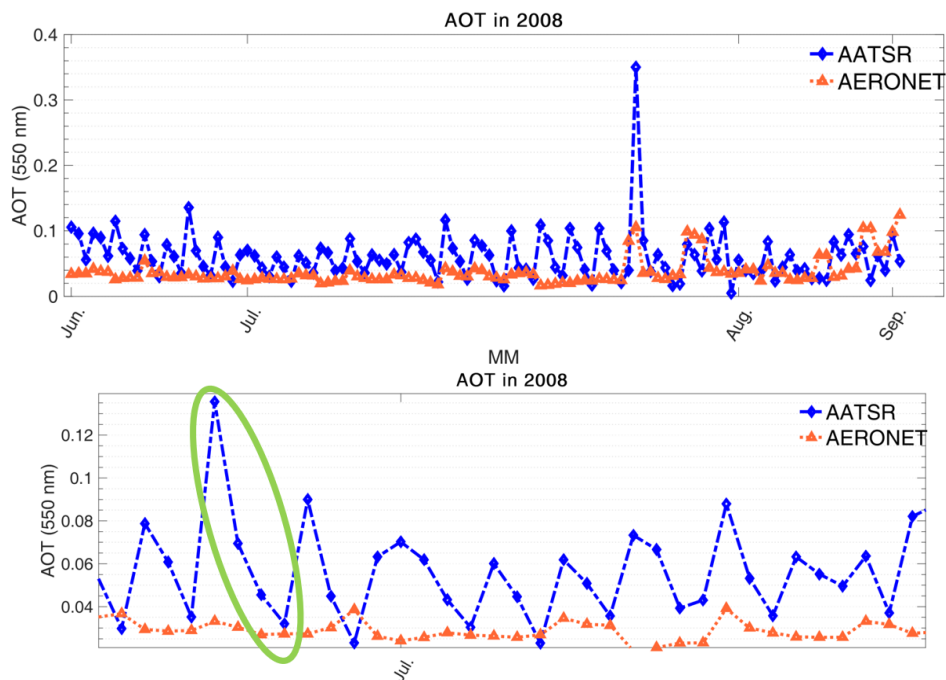


Figure 79: Daily AOT at OPAL station, Ellesmere Island, Nunavut, Canada, 2008. AATSR data are shown with blue line and symbols, AERONET measurements are shown in orange, upper panel shows daily AOT, bottom panel: zoom in upper panel, the green ellipse highlights the 4 different AOT value in one day.

7 Summary and outlook

The main motivation behind this doctoral work is to retrieve AOT over the Arctic circle using space-borne data and for the first time to create a long-term data record. This AOT dataset holds immense importance because it can be used to study the change of aerosol load and properties during the period of AA. Furthermore, based on the statistical analysis - e.g. trend analysis - the role and impact of aerosols in AA can be determined.

The challenging task of aerosol retrieval over highly reflecting snow/ice surface and the resultant gap in the global AOT products over the Arctic circle is well known to the aerosol community. In this work, to overcome the difficulties and extend our understanding, first we focus on two main obstacles of cloud detection and snow surface properties to improve the AOT retrieval in the Arctic. The outcome of this step was partly used to improve the previously-developed AEROSNOW algorithm (for AOT retrieval) (Istomina, 2012). After the creation of long-term AOT data, the product is validated using ground-based AERONET measurements.

This work is defined in the framework of (AC)³ project (Wendisch et al., 2017).

Improved Cloud detection for Aerosol Optical Thickness retrieval

In this work, a new cloud detection algorithm has been developed called ASCIA as a prerequisite for aerosol retrieval over the Arctic using AATSR and SLSTR measurements. ASCIA is based on using time series of data, exploiting the stability of reflectance in cloud-free scenes throughout time. The central component of algorithm is PCC analysis as an indicator of the stability of reflectance. As a complementary step, the extracted reflectance part of thermal infrared channel of AATSR/SLSTR at $3.7 \mu\text{m}$ is used.

One of the main issues in Arctic applications is the failure of threshold-based methods due to the lack of sufficient contrast between clouds and the underlying surface. In ASCIA, this problem is solved by applying the concept of PCC statistical analysis as the key parameter in the cloud detection algorithm. The PCC parameter mainly controls the procedure, whereby the algorithm is independent from many problems originated by various threshold sets and therefore the cloud detection algorithm is unlikely to misclassify cloud and snow. Additionally, we use the BT measurements

from the 3.7 μm channel as complementary data to provide extra information and compensate the shortcomings of the PCC analysis and convert a block-level ($25 \times 25 \text{ km}^2$) cloud mask resulted from PCC analysis to a pixel-level ($1 \times 1 \text{ km}^2$) one. It is important to note that we need to exclude the emission part of the 3.7 μm channel and create a substantial contrast in the remaining reflectance part between snow/ice and cloud at 3.7 μm .

The cloud detection algorithm is applied to AATSR and SLSTR data and the results have been validated against four existing cloud products over the Arctic: 1) surface synoptic observations (SYNOP), 2) one existing method based on spectral shape of clear snow (Istomina et al., 2010), 3) AATSR L2 nadir cloud flag, and 4) The MODIS cloud product. The validation indicates 90.19% and 92.86% agreement between SYNOP and ASCIA in May and March, respectively. The comparison between the new algorithm and the previous method has revealed the beneficial aspect of the used method particularly in the case of detecting thin clouds and its sufficient performance in extreme situations such as having a large solar zenith angle. According to the validation results, the AATSR L2 nadir cloud flag often falsely identifies clouds over snow/ice, except during summer time.

The comparison between the AATSR L2 cloud product and the SYNOP measurements resulted in 60% and 48.27% agreement in May and March, respectively. The overall better performance of the newly-developed time series algorithm over snow and ice has proven its capability to be applied to SLSTR data. However, according to the results, more investigation and modification is needed to detect cloud over land (soil, vegetation, etc.) specifically for blocks with small PCC values, since the strict performance of the algorithm in cloudy blocks result in labelling clear land as cloud due to the high reflectance of land pixels at 3.7 μm . Additionally, sub-pixel water clouds detection is not carried out yet in the current version of ASCIA.

The outcome of this study has been published in Jafariserajehlou et al. (2019).

Improved assessment of BR_F and snow surface reflectance for Aerosol Optical Thickness retrieval

In this study, the objective was to extend our knowledge about snow surface properties and assess the accuracy of the simulation of the reflectance in a snow–atmosphere system, taking different snow morphology and atmospheric absorption and scattering into account. For this purpose, we used a state-of-the-art RTM, SCIATRAN (Rozanov et al., 2002, 2014), and the airborne CAR measurements (Gatebe and King, 2016).

The airborne CAR data were acquired by NASA over Elson Lagoon at Barrow/Utqiagvik, Alaska, during the Arctic Research of the Composition of the Troposphere from Aircraft and Satellites (ARCTAS) campaign in spring 2008 (Lyapustin et al., 2010). The spectral coverage of the airborne measurements is wide (0.3–2.30 μm), comprising important wavelengths relevant for remote-sensing applications such as aerosol retrievals, in which the outcome of this study can be used. Measurements obtained at different flight altitudes (200, 600, and 1700m) provided an opportunity

to investigate the sensitivity of simulated reflectance to atmospheric parameters.

The SCIATRAN RTM was used to simulate the reflectance factor in the snow–atmosphere system and its changes related to different snow morphologies (i.e. snow grain size and shape). These simulations explicitly take atmospheric scattering and absorption into account. The sensitivity of reflectance in the snow–atmosphere system to snow grain size and shape has been investigated. It has been shown that the selection of the most representative shape and size of the nine ice crystals used in SCIATRAN to describe the snow surface is essential to minimise the difference between simulations and measurements.

To obtain a priori knowledge of snow morphology, the snow grain size and shape retrieval algorithm is used and applied to CAR data. In the case study at Barrow/Utqiagvik, the simulated reflectance factor assuming the ice crystals with an aggregate composed of eight column shape agreed well with measurements for the old snow case. The results show an RMSE of 6.9% and an average bias of 2.7% for the measured CAR reflectance in the principal plane where the largest discrepancies are expected. For the case of freshly fallen snow, an aggregate of five plates shape was the most representative ice crystal, with an RMSE value of 12.8% and a bias of 11.23% with respect to the measured CAR reflectance. The data for the freshly fallen snow case were acquired at altitude of 181 m. Larger differences compared to the older snow case at 647 m are attributed to surface inhomogeneity. The surface inhomogeneity most likely originates from sastrugi. Simulations in which the snow layer was comprised of ice crystals with a droxtal shape (being semispherical particles) did not yield accurate reflectance for the snow–atmosphere system in any of our case studies. The knowledge from studies of the temperature dependence of ice crystal morphologies agrees with our findings about the most representative ice crystal size and shape for our case studies.

In our study, the simulated reflectance agrees well with the measurements with respect to spectral and directional signatures. This is evidenced by the high correlation coefficients in the range from 0.88 to 0.98 between measurements (old and fresh snow) and simulations at the selected wavelengths of 0.677, 0.873, and 1.649 μm . In the off-glint regions $|\Delta\Phi| > 40^\circ$ and $VZA < 50^\circ$, the overall absolute difference between the modelled reflectance factor from SCIATRAN and CAR measurements is below 0.05. This absolute difference in the off-glint area is smaller in the shortwave infrared region compared to the visible one. It should be noted here that the reflectance of the snow is lower in the shortwave infrared compared to the visible one.

In summary, the approach shows the high accuracy of SCIATRAN in simulating the radiation field in the snow–atmosphere scenes for off-glint observations. The results are applicable for the inversion of snow and atmospheric data products from satellite or airborne passive remote-sensing measurements above snow. To mitigate the relatively large differences between measurements and simulation for the glint condition compared to the off-glint region, the use of a vertically inhomogeneous snow layer comprising different ice crystal shapes and sizes is proposed.

The outcome of this study has been published in Jafariserajehlou et al. (2021).

Retrieval of Aerosol Optical Thickness in the Arctic using satellite measurements

To retrieve AOT over a highly reflective surface, a previously-developed dual-view algorithm called AEROSNOW (Istomina, 2012) is improved and used. The main motivation to use AATSR and dual view in this method is to reduce the role of surface reflectance in the retrieval approach because highly reflecting surfaces are a known obstacle in the retrieval of aerosol above snow/ice. The principle idea behind the algorithm is using the ratio of reflectance measured at the forward and nadir view and weighting it by TOA reflectance to account for unique surface features besides including surface reflectance simulations to account for modelled surface directionality.

The AEROSNOW algorithm is applied in the visible spectrum using the LUT set up to retrieve AOT during Arctic haze. When applying the algorithm to long-term data of AATSR (2002-2012), several technical and scientific issues were found and solved:

- The required libraries were out of date and needed to be checked, updated or changed if needed.
- Sanity check and bug fixes were required for AEROSNOW source code.
- The run time was quite high (several hours per orbit over the Arctic circle), which was not optimal for the creation of ten years of AOT data (51,100 orbits).
- Artificial glint geometry that was found and understood by the knowledge gained from snow surface properties study (details in Section 5).
- Residual clouds are minimised by applying cloud detection criteria from ASCIA (details in Section 4).

After solving technical and scientific issues, the new version of the AEROSNOW algorithm is applied to AATSR data from 2002-2012 and created ten years of AOT data. The retrieved AOT is validated using AERONET measurements during spring-time in which an adequate performance of algorithm is expected due the LUT, which is set up using aerosol phase function measured during a haze event.

In general, the results of validation show promising agreement between AERONET and AATSR based AOT, especially during haze events. Nevertheless, there are also degraded validation results, some of which are common for all AERONET stations. For example, having different AOT value for different satellite overpasses and corresponding orbits during different times of day, e.g. morning and afternoon. Current analyses are not adequate to explain this issue yet. In addition, there are cases for which we did not expect to have accurate retrievals due to the known limitations of AEROSNOW such as retrieval at extreme relative azimuth angles and retrieval over surfaces covered with melting snow/ice (this was the case for some of coastal

stations).

Open questions and future work

The application of AEROSNOW to the AATSR data is the first step for the creation of a long-term AOT product over the Arctic. This product can be used to study the change of AOT and aerosol properties during AA. Nevertheless, to cover the whole period of AA, it is necessary to apply AEROSNOW on SLSTR data (the successor of AATSR after the failure of ENVISAT). To fill the four-year gap between AATSR and SLSTR, one can use another instrument such as AVHRR. The statistical approaches can be used to exclude outliers and apply trend analysis.

To improve the AEROSNOW algorithm, one can introduce new/more LUTs to account for different aerosol types. Although the current version of AEROSNOW is able to retrieve AOT during haze episodes in late winter and early spring, a new additional aerosol type will also enable AEROSNOW to retrieve AOT in summertime.

The snow grain morphology retrieval study presented in this work can be applied to space-borne data to create a database of snow properties in the Arctic circle by which a better estimation of surface directional properties can be obtained.

8 Bibliography

References

- J. P. D. Abbatt, W. R. Leaitch, A. A. Aliabadi, A. K. Bertram, J.-P. Blanchet, A. Boivin-Rioux, H. Bozem, J. Burkart, R. Y. W. Chang, J. Charette, J. P. Chaubey, R. J. Christensen, A. Cirisan, D. B. Collins, B. Croft, J. Dionne, G. J. Evans, C. G. Fletcher, M. Galí, R. Ghahremaninezhad, E. Girard, W. Gong, M. Gosselin, M. Gourdal, S. J. Hanna, A. B. Hayashida, H. and Herber, S. Hesaraki, P. Hoor, L. Huang, R. Hussherr, V. E. Irish, S. A. Keita, J. K. Kodros, F. Köllner, F. Kolonjari, D. Kunkel, L. A. Ladino, K. Law, M. Levasseur, Q. Li-bois, J. Liggio, M. Lizotte, K. M. Macdonald, R. Mahmood, R. V. Martin, R. H. Mason, L. A. Miller, A. Moravek, E. Mortenson, E. L. Mungall, J. G. Murphy, M. Namazi, A.-L. Norman, N. T. O'Neill, J. R. Pierce, L. M. Russell, J. Schneider, H. Schulz, S. Sharma, M. Si, R. M. Staebler, N. S. Steiner, J. L. Thomas, K. von Salzen, J. J. B. Wentzell, M. D. Willis, G. R. Wentworth, J.-W. Xu, and J. D. Yakobi-Hancock. New insights into aerosol and climate in the Arctic. *Atmos. Chem. Phys.*, 19:2527–2560, 2019.
- N. J. Abram, E. W. Wolff, and M. A. J. Curran. A review of sea ice proxy information from polar ice cores. *Quaternary Science Reviews*, 79:168–183, 2013.
- A.S. Ackerman, O.B. Toon, D.E. Stevens, A.J. Heymsfield, V. Ramanathan, and E.J. Welton. Reduction of tropical cloudiness by soot. *Science*, 288(5468):1042, 2000.
- B.A. Albrecht. Aerosols, cloud microphysics, and fractional cloudiness. *Science*, 245(4923):1227–1230, 1989.
- R. C. Allen, P. A. Durkee, and C. H. Wash. Snow/cloud discrimination with multi-spectral satellite measurements. *J. Appl. Meteor.*, 29:994–1004, 1990a.
- R. C. Allen, P. A. Durkee, and C. H. Wash. Snow/cloud discrimination with multi-spectral satellite measurements. *J. Appl. Meteor.*, 29:994–1004, 1990b.
- E. Andrews, J. Sheridan, P., M. Fiebig, A. McComiskey, A. Ogren, J., P. Arnott, D. Covert, R. Elleman, R. Gasparini, D. Collins, H. Jonsson, B. Schmid, and J. Wang. Comparison of methods for deriving aerosol asymmetry parameter. *J. Geophys. Res.*, 111:D05S04, 2006.
- A. Angstrom. On the atmospheric transmission of sun radiation and on dust in the air. *Geograf. Ann. Deut.*, 11:156–166, 1929.
- T. Aoki, T. Aoki, M. Fukabori, and A. Uchiyama. Numerical simulation of the atmospheric effects on snow albedo with a multiple scattering radiative transfer model for the atmosphere-snow system. *J. Meteorol. Soc. Jpn.*, 77:595–614, 1999.
- T. Aoki, T. Aoki, M. Fukabori, A. Hachikubo, Y. Tachibana, and F. Nishio. Effects of snow physical parameters on spectral albedo and bidirectional reflectance of snow surface. *J. Geophys. Res.*, 105(D8):10219–36, 2000.

- A. Arking and J. D. Childs. Retrieval of cloud cover parameters from multispectral satellites images. *J. Clim. Appl. Meteorol.*, 24:322–333, 1985.
- G. T. Arnold, S.-C. Tsay, M. D. King, J. Y. Li, and P. F. Soulen. Airborne spectral measurements of surface-atmosphere anisotropy for arctic sea ice and tundra. *Int. J. Remote Sens.*, 23:3763–3781, 2002.
- A. Arola, T. F. Eck, H. Kokkola, M. R. A. Pitkänen, and S. Romakkaniemi. Assessment of cloud-related fine-mode aod enhancements based on aeronet sda product. *Atmos. Chem. Phys.*, 17:5991–6001, 2017.
- S. Arrhenius. On the influence of carbonic acid in the air upon the temperature of the ground. *Mag. J. Sci., London, Edinburgh, Dublin Phil.*, 41:237–276, 1896.
- E. Asmi, V. Kondratyev, D. Brus, T. Laurila, H. Lihavainen, J. Backman, and et al. Aerosol size distribution seasonal characteristics measured in tiksi, russian arctic. *Atmos. Chem. Phys.*, 16(3):1271–1287, 2016.
- M. Bailey and J. Hallett. Growth rates and habits of ice crystals between 20 c and 70c. *J. Atmos. Sci.*, 61:514–544, 2004.
- B. Barkstrom. Some effects of multiple scattering on the distribution of solar radiation in snow and ice. *J. Glaciol.*, 11:357–368, 1972.
- L. A. Barrie. Arctic air pollution – an overview of current knowledge. *Atmos. Environ.*, 20:643–663, 1986.
- J. Benesty, J. Chen, Y. Huang, and I. Cohen. Noise reduction in speech processing. Springer Topics in Signal Processing 2, Springer-Verlag Berlin Heidelberg, 2009.
- U.S. Bhatt, D.A. Walker, M.K. Reynolds, J.C. Comiso, H.E. Epstein, G.-S. Gia, R. Gens, J.E. Pinzon, C.J. Tucker, C.E. Tweediw, and P.J. Webber. Circumpolar Arctic tundra vegetative change is linked to sea ice decline. *Earth Interact.*, 14: 1–20, 2010.
- A. R. Birks. Improvements to the aatsr ipf relating to land surface temperature retrieval and cloud clearing over land. AATSR Technical Note, Rutherford Appleton Laboratory, Chilton, UK, 2007.
- R. Boers, M.J. de Haij, W. M. F. Wauben, H. K. Baltink, L. H. van Uft, M. Savenije, and C. N. Long. Optimized fractional cloudiness determination from five ground-based remote sensing techniques. *J. Geophys. Res.*, 115:D24116, 2010.
- J. Bojanowski, R. Stöckli, A. Tetzlaff, and H.: Kunz. The impact of time difference between satellite overpass and ground observation on cloud cover performance statistics. *Remote Sens.*, 6:12866–12884, 2014.
- T.C. Bond and R.W. Bergstrom. Light absorption by carbonaceous particles: an investigative review. *Aerosol Science and Technology*, 40(1):27–67, 2006.
- A. F. Bouwman, D. S. Lee, W. A. H. Asman, F. J. Dentener, K. W. Van Der Hoek, and J. G. J. Olivier. A global high-resolution emission inventory for ammonia. *Global Biogeochemical Cycles*, 11(4):561–597, 1997.

- R. S. Bradley, F. T. Keimig, and H. F. Diaz. Climatology of surface-based inversions in the North American Arctic. *J. Geophys. Res.*, 97:699–712, 1992.
- J. Browse, K. S. Carslaw, G. W. Mann, C. E. Birch, S. R. Arnold, and C. Leck. The complex response of arctic aerosol to sea-ice retreat. *Atmos. Chem. Phys.*, 14(14):7543–7557, 2014.
- F.M. Breon and S. Colzy. Cloud detection from the spaceborne polder instrument and validation against surface synoptic observations. *J. Appl. Meteor.*, 38:777–785, 1999.
- A. Bucholtz. Rayleigh-scattering calculations for the terrestrial atmosphere. *Appl. Opt.*, 34:2765–2773, 1995.
- MI Budyko. The effect of solar radiation variations on the climate of the earth. *Tellus*, 21:611–619, 1969.
- C. E. Bulgin, S. Eastwood, O. Embury, C. J. Merchant, and C. Donlon. Sea surface temperature climate change initiative: alternative image classification algorithms for sea-ice affected oceans. *Remote Sens. Environ.*, 162:396–407, 2015.
- J. P. Burrows, P. Borrell, and U. Platt. The remote sensing of tropospheric composition from space. 2011.
- T. N. Carlson. Speculations on the movement of polluted air to the Arctic. *Atmos. Environ.*, 15:1473–1477, 1981.
- Siewert C.E. A concise and accurate solution to Chandrasekhar’s basic problem in radiative transfer. *J. Quant. Spectrosc. Radiat. Transfer*, 54:109–130, 2000.
- S. Chandrasekhar. *Radiative Transfer*. Dover Publications, New York, 1960. ISBN 0486605906 9780486605906.
- M. W. Christensen, D. Neubauer, C. A. Poulsen, G. E. Thomas, G. R. McGarragh, A. C. Povey, S. R. Proud, and R. G. Grainger. Unveiling aerosol–cloud interactions – part 1: Cloud contamination in satellite products enhances the aerosol indirect forcing estimate. *Atmos. Chem. Phys.*, 17:13151–13164, 2017.
- J. A. Coakley, Jr. Francis, and P. Bretherton. Cloud cover from high-resolution scanner data: Detecting and allowing for partially filled fields of view. *J. Geophys. Res.*, 87:4917–4932, 1982.
- J. Cohen, J. A. Screen, C. Furtado, J., M. Barlow, D. Whittleston, D. Coumou, J. Francis, K. Dethloff, D. Entekhabi, J. Overland, and J. Jones. Recent Arctic amplification and extreme mid latitude weather. *Nat. Geosci.*, 7:627–637, 2014.
- J. Cohen, X. Zhang, and J. et al. Francis. Divergent consensus on Arctic amplification influence on midlatitude severe winter weather. *Nat. Clim. Chang.*, 10: 20–29, 2020.
- P. Coppo, B. Ricciarelli, F. Brandani, J. Delderfield, M. Ferlet, C. Mutlow, G. Munro, T. Nightingale, D. Smith, S. Bianchi, P. Nicol, S. Kirschstein, T. Hennig, W. Engel, J. Frerick, and J. Nieke. Slstr: a high accuracy dual scan temperature radiometer for sea and land surface monitoring from space. *J. Mod. Optic.*,

- 57:1815–1830, 2010a.
- P. Coppo, B. Ricciarelli, F. Brandani, J. Delderfield, M. Ferlet, C. Mutlow, G. Munro, T. Nightingale, D. Smith, S. Bianchi, S. Nicol, P. and Kirschstein, T. Hennig, W. Engel, J. Frerick, and J. Nieke. Slstr: a high accuracy dual scan temperature radiometer for sea and land surface monitoring from space. *Mod. Optic. J.*, 57(18):1815–1830, 2010b.
- D. S. Covert, A. P. Waggoner, R. E. Weiss, N. C. Ahlquist, and R. J. Charlson. Atmospheric aerosols, humidity, and visibility. *Adv. Environ. Sci. Technol.; (United States)*, 9, 1 1980.
- B. Croft, R. V. Martin, W. R. Leitch, P. Tunved, T. J. Breider, S. D. Andrea, and J. R. Pierce. Processes controlling the annual cycle of arctic aerosol number and size distributions. *Atmos. Chem. Phys.*, 16(6):3665–3682, 2016.
- J. A. Curry, J. L. Schramm, and E. E. Ebert. Sea ice-albedo climate feedback mechanism. *J. Climate*, 8:240–247, 1995.
- J. A. Curry, W. B. Rossow, D. Randall, and J. L. Schramm. Overview of arctic cloud and radiation characteristics. *J. Climate*, 9:1731–1764, 1996.
- M. Dall’Osto, D. C. S. Beddows, P. Tunved, R. Krejci, J. Ström, H. C. Hansson, and et al. Arctic sea ice melt leads to atmospheric new particle formation. *Scientific Reports*, 7(1):3318, 2017.
- Jeffrey J. Danielson and Dean B. Gesch. Global multi-resolution terrain elevation data 2010 (gmted2010). OFR, 2011-1073, 2011.
- M. Degünther and R. Meerkötter. Influence of inhomogeneous surface albedo on uv irradiance: effect of a stratus cloud. *J Geophys Res.*, 105(D18):22755–61, 2000.
- M. Derrien, B. Farki, L. Harang, D. Pochic, A. Sairouni, H. LeGldau, and A Noyalet. Automatic cloud detection applied to noaa-11/avhrr imagery,. *Remote Sens. Environ.*, 46:246–267, 1993.
- C. G. Deshpande and A. K. Kamra. Physical properties of the arctic summer aerosol particles in relation to sources at ny-Ålesund, svalbard. *Journal of Earth System Science*, 123(1):201–212, 2014.
- JL. Deuze, Goloub P. Tanre D. Herman, M., and A. Marchand. Characterization of aerosols over ocean from polder/adeos-1. *Geophys. Res. Lett.*, 26(10):1421–1424, 1999.
- D.J. Diner, J.V. Martonchik, R.A. Kahn, B. Pinty, N. Gobron, D.L. Nelson, and B.N. Holben. Using angular and spectral shape similarity constraints to improve misr aerosol and surface retrievals over land. *Remote Sens. Environ.*, 94 (2): 155–171, 2005.
- R. Doscher, T. Vihma, and E. Maksimovich. Recent advances in understanding the arctic climate system state and change from a sea ice perspective: A review. *Atmos. Chem. Phys.*, 14(24):13571–13600, 2014.
- O. Dubovik, M. Herman, A. Holdak, T. Lapyonok, D. Tanre, J.L. Deuze, F. Ducos,

- A. Sinyuk, and A. Lopatin. Statistically optimized inversion algorithm for enhanced retrieval of aerosol properties from spectral multi-angle polarimetric satellite observations. *Atmos. Meas. Tech.*, 4:975–1018, 2011.
- R.V. Dunkle and J.T. Bevens. An approximate analysis of the solar reflectance and transmittance of a snow cover. *J. Meteorol.*, 13:212–216, 1956.
- A. Dybbroe, K.-G. Karlsson, and A. Thoss. Nwcsaf avhrr cloud detection and analysis using dynamic thresholds and radiative transfer modeling part ii: Tuning and validation. *J. Appl. Meteorol.*, 44:55–71, 2005.
- R. Döscher, T. Vihma, and E. Maksimovich. Recent advances in understanding the Arctic climate system state and change from a sea ice perspective: a review. *Atmos. Chem. Phys.*, 14:13571–13600, 2014.
- A. C. Engvall, J. Ström, P. Tunved, R. Krejci, H. Schlager, and A. Minikin. The radiative effect of an aged, internally mixed arctic aerosol originating from lower-latitude biomass burning. *Tellus Series B-Chemical and Physical Meteorology*, 61(4):677–684, 2009.
- M. G. Flanner. Arctic climate sensitivity to local black carbon. *J. Geophys. Res.: Atmospheres*, 118:1840–1851, 2013.
- P. Q. Fu, K. Kawamura, and L. A. Barrie. Photochemical and other sources of organic compounds in the canadian high arctic aerosol pollution during winter-spring. *Environmental Science Technology*, 43(2):286–292, 2009.
- V. Galindo, M. Levasseur, C. J. Mundy, M. Gosselin, J. E. Tremblay, and et al. Scarratt, M. Biological and physical processes influencing sea ice, under-ice algae, and dimethylsulfoniopropionate during spring in the canadian arctic archipelago. *J. Geophys. Res.: Oceans*, 119:3746–3766, 2014.
- C. Gatebe and M. King. Airborne spectral brdf of various surface types (ocean, vegetation, snow, desert, wetlands, cloud decks, smoke layers) for remote sensing applications. *Remote Sens. Environ.*, 179:131–148, 2016.
- D. J. Ghent, G. K. Corlett, F.-M. Göttsche, and J. J. Remedios. Globalland surface temperature from the along-track scanning radiometers. *J. Geophys. Res.*, 122: 12167–12193, 2017.
- A. Gilgen, W. T. K. Huang, L. Ickes, D. Neubauer, and U. . Lohmann. How important are future marine and shipping aerosol emissions in a warming arctic summer and autumn? *Atmos. Chem. Phys.*, 18(14):10,521–10,555, 2018.
- P. Ginoux, D. Garbuzov, and H. C. Hsu. Identification of anthropogenic and natural dust sources using moderate resolution imaging spectroradiometer (modis) deep blue level 2 data. *J. Geophys. Res., Atmospheres*, 115:D05204, 2010.
- P. Glantz, A. Bourassa, A. Herber, T. Iversen, J. Karlsson, A. Kirkevåg, M. Maturilli, Ø. Seland, K. Stebel, H. Struthers, M. Tesche, and L. Thomason. Remote sensing of aerosols in the arctic for an evaluation of global climate model simulations. *J. Geophys. Res.*, 119 (13):8169–8188, 2014.

- R.G. Grainger. Some useful formulae for aerosol size distributions and optical properties. Available online: <http://eodg.atm.ox.ac.uk/user/granger/research/aerosols.pdf> (accessed on 15 September 2021), 2015.
- B. S. Grandey, P. Stier, and T. M. Wagner. Investigating relationships between aerosol optical depth and cloud fraction using satellite, aerosol reanalysis and general circulation model data. *Atmos. Chem. Phys.*, 13:3177–3184, 2013.
- R. G. Graversen. Do changes in the midlatitude circulation have any impact on the Arctic surface air temperature trend? *J. Clim.*, 19:5422–5438, 2006.
- R.G. Graversen and M. Wang. Polar amplification in a coupled climate model with locked albedo. *Climate Dyn.*, 33:629–643, 2009.
- R.G. Graversen, T. Mauritsen, M. Tjernstrom, E. Kallen, and G. Svensson. Vertical structure of recent Arctic warming. *Nature*, 451:53–56, 2008.
- RO. Green, J. Dozier, D. Roberts, and T. Painter. Spectral snow reflectance models for grain-size and liquid-water fraction in melted snow for the solar-reflected spectrum. *J. Geophys. Res.*, 34:71–3, 2002.
- K. R. Greenaway. Experiences with Arctic flying weather. Royal Meteorological Society Canadian Branch, 1950.
- TC. Grenfell, SG Warren, and PC. Mullen. Reflection of solar radiation by the antarctic snow surface at ultraviolet, visible, and near-infrared wavelengths. *J. Geophys. Res.*, 99(D9):18669–84, 1994.
- G. Gutman, D. Tarpley, and Ohring G. Cloud screening for determination of land surface characteristics in a reduced resolution satellite data set. *Int. J. Remote Sens.*, 8:859–870, 1987.
- L. Gómez-Chova, J. Amorós-López, Muñoz-Marí J. Mateo-García, G., and G. Camps-Valls. Cloud masking and removal in remote sensing image time series. *J. Appl. Remote Sens.*, 11:015005, 2017.
- O. Hagolle, S. Sylvander, M. Huc, M. Claverie, D. Clesse, C. Dechoz, V. Lonjou, and V. Poulain. Spot4 (take5): A simulation of sentinel-2 time series on 45 large sites. *Remote Sens.*, 7:12242–12264, 2015.
- D. K. Hall, G. Riggs, and V. V Salomonson. Algorithm theoretical basis document (atbd) for the modis snow and sea-ice mapping algorithms. NASA GSFC, available at: https://modis.gsfc.nasa.gov/data/atbd/atbd_mod10.pdf (*lastac - cess* : *May2018*), 2001.
- J. Haywood and O. Boucher. Estimates of the direct and indirect radiative forcing due to tropospheric aerosols: A review. *Reviews of Geophysics*, 38(4):513–543, 2000.
- J. Heintzenberg. Particle size distribution and optical properties of Arctic haze. *Tellus*, 32B:251–260, 1980.
- M. Herman, JL. Deuze, C. Devaux, PH. Goloub, FM. Breon, and D. Tanre. Remote

- sensing of aerosols over land surfaces, including polarization measurements; application to some airborne polder measurements. *J. Geophys. Res.*, 102:17039–17049, 1997.
- L. D. Hinzman, C. J. Deal, A. D. McGuire, S. H. Mernild, I. V. Polyakov, and J. E. Walsh. Trajectory of the Arctic as an integrated system. *Ecological Applications*, 23(8):1837–1868, 2013.
- J.S. Hobgood. Fundamentals of weather and climate. *Int. J. Climatol.*, Robin McIlveen, Chapman and Hall (London), 1993.
- B. N. Holben, T. F. Eck, I. Slutsker, D. Tanre, J. P. Buis, A. Setzer, E. Vermote, J. A. Reagan, Y. J. Kaufman, T. Nakajima, F. Lavenu, I. Jankowiak, and A. Smirnov. Aeronet - a federated instrument network and data archive for aerosol characterization. *Remote Sens. Environ.*, 66:1–16, 1998.
- R. Hollmann, C. J. Merchant, R. Saunders, C. Downy, M. Buchwitz, A. Cazenave, E. Chuvieco, P. Defourny, G. de Leeuw, R. Forsberg, T. Holzer-Popp, F. Paul, S. Sandven, S. Sathyen-dranath, M. van Roozendaal, and W. Wagner. The esa climate change initiative satellite data records for essential climate variables. *B. Am. Meteorol. Soc.*, 94:1541–1552, 2013.
- T. Holzer-Popp, G. de Leeuw, J. Griesfeller, D. Martynenko, L. Klüser, S. Bevan, W. Davies, F. Ducos, J.L. Deuzé, R.G. Graigner, A. Heckel, W. von Hoyningen-Hüne, P. Kolmonen, P. Litvinov, P. North, C.A. Poulsen, D. Ramon, R. Siddans, L. Sogacheva, D. Tanré, G.E. Thomas, M. Vountas, J. Descloitres, J. Griesfeller, S. Kinne, M. Schulz, and S. Pinnock. Aerosol retrieval experiments in the esa aerosol_cproject. *Atmos. Meas. Tech.*, 6(8) : 1919–1957, 2013.
- NC. Hsu, SC. Tsay, MD. King, and JR Herman. Aerosol properties over bright-reflecting source regions. *IEEE Trans. Geosci. Remote Sens.*, 42(3):557–569, 2004.
- J. Huang and L. Jaeglé. Wintertime enhancements of sea salt aerosol in polar regions consistent with a sea ice source from blowing snow. *Atmos. Chem. Phys.*, 17(5): 3699–3712, 2017.
- S. R. Hudson and S. G. Warren. An explanation for the effect of clouds over snow on the top-of atmosphere bidirectional reflectance. *J. Geophys. Res.*, 112:D19202, 2007.
- S. R. Hudson, S. G. Warren, R. E. Brandt, T. C. Grenfell, and D. Six. Spectral bidirectional reflectance of antarctic snow: measurements and parameterization. *J. Geophys. Res.*, 111:D18106, 2006.
- J.-P Huot, H. Tait, M. Rast, Delwart Steven, Jean-Loup Bezy, and Guido Levrini. The optical imaging instruments and their applications: Aatsr and meris. *Esa Bulletin-European Space Agency*, 106:56–66, 06 2001.
- T. Inoue. A cloud type classification with noaa 7 split-window measurements. *J. Geophysic. Res.*, 92:991–4000, 1987.
- L. Istomina. Retrieval of aerosol optical thickness over snow and ice surfaces in the

- arctic using advanced along track scanning radiometer. PhD thesis, University of Bremen, Bremen, Germany, 2012.
- L. Istomina, W. Hoyningen-Huene, A.A. Kokhanovsky, and J.P. Burrows. The detection of cloud-free snow-covered areas using aatsr measurements. *Atmos. Chem. Phys.*, 9:1279–1288, 2010.
- L.G. Istomina, W. von Hoyningen-Huene, A.A. Kokhanovsky, V.V. Rozanov, K. Schreier, M. Dethloff, M. Stock, R. Treffeisen, A. Herber, and J. P. Burrows. Sensitivity study of the dual-view algorithm for aerosol optical thickness retrieval over snow and ice. Proceedings of the 2nd MERIS/(A)ATSR user workshop, ESRIN, Frascati, Italy, 22-26 Sept, 2009.
- L.G. Istomina, W. von Hoyningen-Huene, A.A. Kokhanovsky, E. Schultz, and J.P. Burrows. Remote sensing of aerosols over snow using infrared aatsr observations. *Atmos. Meas. Tech.*, 4:1133–1145, 2011.
- T. Iversen. On the atmospheric transport of pollution to the Arctic. *Geophys. Res. Lett.*, 11:457–460, 1984.
- T. Iversen. Simulation of the atmospheric transport of sulphur dioxide and particulate sulphate to the Arctic. NILU Rpt. OR 83/86. NILU, N-2001 Lillestrem, Norway, 1986.
- S. Jafariserajehlou, L. Mei, M. Vountas, V. Rozanov, J. P. Burrows, and R. Hollmann. A cloud identification algorithm over the arctic for use with aatsr–slstr measurements. *Atmos. Meas. Tech.*, 12:1059–1076, 2019.
- S. Jafariserajehlou, V. V. Rozanov, M. Vountas, C. K. Gatebe, and J.P. Burrows. Simulated reflectance above snow constrained by airborne measurements of solar radiation: implications for the snow grain morphology in the arctic. *Atmos. Meas. Tech.*, 14:369–389, 2021.
- Z. Jin, T. P. Charlock, P. Yang, Y. Xie, , and W. Miller. Snow optical properties for different particle shapes with application to snow grain size retrieval and modis/ceres radiance comparison over antarctica. *Remote Sens. Environ.*, 112:3563–3581, 2008.
- R.A. Kahn, B.J. Gaitley, M.J. Garay, D.J. Diner, T.F. Eck, A. Smirnov, and B.N. Holben. Multiangle imaging spectro radiometer global aerosol product assessment by comparison with the aerosol robotic network. *J. Geophys. Res.*, 115:D23209, 2010.
- F. Kasten and A.T. Young. Revised optical air mass tables and approximation formula. *Appl. Optics*, 28:4735–4738, 1989.
- Y.J. Kaufman, D. Tanre, LA. Remer, EF. Vermote, A Chu, and BN. Holben. Operational remote sensing of tropospheric aerosol over land from eos moderate resolution imaging spectroradiometer. *J. Geophys. Res.*, 102(D14):17051–17067, 1997.
- K. Kawamura and S. Bikkina. A review of dicarboxylic acids and related compounds in atmospheric aerosols: Molecular distributions, sources and transformation. *Atmospheric Research*, 170(15):140–160, 2016.

- K. Kawamura, H. Kasukabe, and L. A. Barrie. Secondary formation of water-soluble organic acids and alpha-dicarbonyls and their contributions to total carbon and water-soluble organic carbon: Photochemical aging of organic aerosols in the arctic spring. *J. Geophys. Res.*, 115:D21306, 2010.
- W. W. Kellogg. *Aerosols and climate*. W. BACH, J. PANKRATH and J. WILLIAMS (Editors), Interactions of Energy and Climate. Reidel, Dordrecht, pages 281–296, 1980.
- J. Key and R. G. Barry. Cloud cover analysis with arctic avhrr data. 1. cloud detection. *J. Geophys. Res.*, 94:18521–18535, 1989.
- B.-M. Kim, J.-Y. Hong, .-Y. Jun, X. Zhang, H. Kwon, Kim. S.-J, J.-H. Kim, S.-W. Kim, and H.-K. Kim. Major cause of unprecedented Arctic warming in January 2016: critical role of an Atlantic windstorm. *Sci. Rep.*, 7(40051), 2017.
- R. M. Kirpes, A. L. Bondy, D. Bonanno, R. C. Moffet, B. Wang, A. Laskin, and et al. Secondary sulfate is internally mixed with sea spray aerosol and organic aerosol in the winter arctic. *Atmos. Chem. Phys.*, 18(6):3937–3949, 2018.
- A. Klonecki, P. Hess, L. Emmons, L. Smith, J. Orlando, and D. Blake. Seasonal changes in the transport of pollutants into the Arctic troposphere – model study. *J. Geophys. Res.*, 108:8367, 2003.
- L. Klüser, N. Killius, and G. Gesell. Apollo ng a probabilistic interpretation of the apollo legacy for avhrr heritage channels. *Atmos. Meas. Tech.*, 8:4155–4170, 2015.
- KR Knapp, R. Froulin, S. Kondragunta, and AI Prados. Towards aerosol optical depth retrievals over land from goes visible radiances: Determining surface reflectance. *Int. J. Remote Sens.*, 26(18):4097–4116, 2005.
- R. Koffler, A.G. De COTIIS, and P. Krishna RAO. A procedure for estimating cloud amount and height from satellite infrared radiation data. *Mon. Wea. Rev.*, 101: 240–243, 1973.
- H. Kohler. *Meteorologische zeitschrift*. 38:168, 1921.
- A. Kokhanovsky. *Cloud Optics*, volume 34. 01 2006. ISBN 978-1-4020-3955-3. doi: 10.1007/1-4020-4020-2.
- A. Kokhanovsky and V. V. Rozanov. Droplet vertical sizing in warm clouds using passive optical measurements from a satellite. *Atmos. Meas. Tech.*, 5:517–528, 2012.
- A. Kokhanovsky and C. Tomasi. *Physics and chemistry of the arctic atmosphere*. Springer Polar Sciences. Springer, Cham. https://doi.org/10.1007/978-3-030-33566-3_4, 2020.
- A. Kokhanovsky, T. Aoki, A. Hachikubo, M. Hori, and E. Zege. Reflective properties of natural snow: approximate asymptotic theory versus in situ measurements. *IEEE Transactions on Geoscience and Remote Sensing*, 43:1529–1535, 2005.
- A. Kokhanovsky, V.V. Rozanov, T. Aoki, D. Odermatt, C. Brockmann, O. Krüger, M. Bouvet, and M. Drusch, M. Hori. Sizing snow grains using backscattered solar light. *Int. J. Remote Sens.*, 32:22:6975–7008, 2011.

- A. Kokhanovsky, M. Lamare, B. Di Mauro, and Arnaud L. Dumont M. et al. Picard, G. On the reflectance spectroscopy of snow. *Cryosphere*, 12(7):2371–82, 2018.
- A. A. Kokhanovsky and F. Breon. Validation of an analytical snow brdf model using parasol multi-angular and multispectral observations. *IEEE T. Geosci. Remote*, 9: 928–932, 2012.
- A. A. Kokhanovsky and G. de Leeuw. Introduction, in: *Satellite aerosol remote sensing over land*, edited by: Kokhanovsky a. a., de leeuw, g. Springer Praxis Publ, Chichester, pages 1–15, 2009.
- A. A. Kokhanovsky and E. P. Zege. Scattering optics of snow. *Appl. Optics*, 43: 1589–1602, 2004.
- A. A. Kokhanovsky, W. von Hoyningen-Huene, and J. P. Burrows. Determination of the cloud fraction in the sciamachy ground scene using meris spectral measurements. *Int. J. Remote Sens.*, 30:6151–6167, 2009.
- P. Kolmonen, A.-M. Sundström, L. Sogacheva, E. Rodriguez, T. Virtanen, and G. de Leeuw. Uncertainty characterization of aod for the aatsr dual and single view retrieval algorithms. *Atmos. Meas. Tech.*, 6:4039–4075, 2013a.
- P. Kolmonen, A.-M. Sundström, L. Sogacheva, E. Rodriguez, T. Virtanen, and G. de Leeuw. Uncertainty characterization of aod for the aatsr dual and single view retrieval algorithms. *Atmos. Meas. Tech.*, 6:4039–4075, 2013b.
- A. Z. Kotarba. A comparison of modis-derived cloud amount with visual surface observations. *J. Atmos. Res.*, 92:522–530, 2009.
- A. Z. Kotarba. Inconsistency of surface-based (synop) and satellite-based (modis) cloud amount estimations due to the interpretation of cloud detection results. *Int. J. Climatol.*, 37:4092–4104, 2017.
- P. L. Langen and V. A. Alexeev. Polar amplification as a preferred response in an idealized aquaplanet GCM. *Clim. Dynam.*, 29:305–317, 2007.
- K. S. Law and A Stohl. Arctic Air Pollution: Origins and Impacts. *Science*, 315: 1537–1540, 2007.
- W. R. Leaitch, R. M. Hoff, S. Melnichuk, and A. Hogan. Some physical and chemical properties of the Arctic winter aerosol in northeastern Canada. *J. Clim. Appl. Met.*, 23:916–928, 1984.
- W. R. Leaitch, S. Sharma, L. Huang, D. Toom-Sauntry, A. Chivulescu, A. M. Macdonald, and et al. Dimethyl sulfide control of the clean summertime arctic aerosol and cloud. *Elemental Science of the Anthropocene*, 1(17):000017, 2013.
- C. Leck and E. Svensson. Importance of aerosol composition and mixing state for cloud droplet activation over the arctic pack ice in summer. *Atmos. Chem. Phys.*, 15(5):2545–2568, 2015.
- K.H. Lee, Z. Li, Y.J. Kim, and A.A. Kokhanovsky. Aerosol monitoring from satellite observations: a history of three decades. In Y.J. Kim, U. Platt, M. B. Gu, and H. Iwahashi, editors, *Atmospheric and Biological Environmental Monitoring*. Berlin:

- Springer (in press), 2009.
- J. A. Leese, C. S. Novak, and V. R. Taylor. The determination of cloud pattern motions from geosynchronous satellite image data. *J. Pattern Recognition*, 2:279–292, 1970.
- C. Leroux, J-L. Deuzé, P. Goloub, C. Sergent, and M. Fily. Ground measurements of the polarized bidirectional reflectance of snow in the near-infrared spectral domain: comparisons with model results. *J. Geophys. Res.*, 1031:19721–32, 1998.
- M. Leroy, J. Deuzé, F. Bréon, O. Hautecoeur, M. Herman, J. Buriez, D. Tanré, S. Bouffières, P. Chazette, and J. Roujean. Retrieval of atmospheric properties and surface bidirectional reflectances over land from polder/adeos. *J. Geophys. Res.*, 102(D14):17023–17037, 1997.
- M. Lévassieur. Impact of arctic meltdown on the microbial cycling of sulphur. *Nat. Geosci.*, 6(9):691–700, 2013.
- R. C. Levy. The dark-land modis collection 5 aerosol retrieval: algorithm development and product evaluation. In A. A. Kokhanovsky and G. de Leeuw, editors, *Satellite Aerosol Remote Sensing Over Land*, page 193–225. Springer, Berlin, Germany, 2009.
- R. C. Levy, L. A. Remer, S. Mattoo, E. F. Vermte, and Y. J. Kaufman. Second-generation operational algorithm: Retrieval of aerosol properties over land from inversion of moderate resolution imaging spectroradiometer spectral reflectance. *J. Geophys. Res.*, 112:D13211, 2007a.
- RC. Levy, Mattoo S. Remer, LA., EF Vermote, and YJ. Kaufman. A second-generation algorithm for retrieving aerosol properties over land from modis spectral reflectance. *J. Geophys. Res.*, 112(D13211), 2007b.
- S. Li and X. Zhou. Modelling and measuring the spectral bidirectional reflectance factor of snow-covered sea ice: An intercomparison study. *Hydrol. Process.*, 18: 3559–3581, 2004.
- K. G. Libbrecht. The formation of snow crystal. *Am. Sci.*, 95:52–59, 2007.
- K. Liou. Radiation and cloud processes in the atmosphere. 20, 1992.
- W.A. Lotz, M. Vountas, T. Dinter, and J.P. Burrows. Cloud and surface classification using sciamachy polarization measurement devices. *Atmos. Chem. Phys.*, 9:1279–1288, 2009.
- A. Lyapustin and Y. Wang. The time series technique for aerosol retrievals over land from modis, in: *Satellite aerosol remote sensing over land*, edited by: Kokhanovsky a. a., de leeuw, g. Springer Praxis Publ, Chichester, pages 69–99, 2009.
- A. Lyapustin, Y. Wang, and R. Frey. An automated cloud mask algorithm based on time series of modis measurements. *J. Geophys. Res.*, 113:D16207, 2008.
- A. Lyapustin, C. K. Gatebe, R. Kahn, R. Brandt, J. Redemann, P. Russell, M. D. King, C. A. Pedersen, S. Gerland, R. Poudyal, A. Marshak, Y. Wang, C. Schaaf, D. Hall, and A. A. Kokhanovsky. Analysis of snow bidirectional reflectance from arctas spring-2008 campaign. *Atmos. Chem. Phys.*, 10:4359–75, 2010.

- A. Lyapustin, S. Korin, Y. Wang, B. Quayle, and I. Laszlo. Discrimination of biomass burning smoke and clouds in maiaac algorithm. *Atmos. Chem. Phys.*, 12(20):9679–9686, 2012.
- A. Macke, J. Mueller, and E. Raschke. Scattering properties of atmospheric ice crystals. *J. Atmos. Sci.*, 53:2813–25, 1996.
- J. V. Martins, D. Tanre, L. Remer, Y. J. Kaufman, S. Mattoo, and R. Levy. Modis cloud screening for remote sensing of aerosol over oceans using spatial variability. *Geophys. Res. Lett.*, 29:1619, 2002.
- Diner DJ. Kahn RA Ackerman TP. Verstraete MM Pinty B. Martonchik, JV. and HR Gordon. Techniques for the retrieval of aerosol properties over land and ocean using multiangle imaging. *IEEE Trans. Geosci. Remote Sens.*, 36:1212–1227, 1998.
- JV. Martonchik and DJ Diner. Retrieval of aerosol and land surface optical properties from multi-angle satellite imagery. *IEEE Trans. Geosci. Remote Sens.*, 30:223–230, 1992.
- N. W. May, P. K. Quinn, S. M. McNamara, and K. A. Pratt. Multiyear study of the dependence of sea salt aerosol on wind speed and sea ice conditions in the coastal arctic. *J. Geophys. Res.: Atmospheres*, 121:9208–9219, 2016.
- R. Meerkötter, C. König, P. Bissolli, G. Gesell, and H. Mannstein. A 14-year european cloud climatology from noaa/avhrr data in comparison to surface observations. *Geophys. Res. Lett.*, 31:L15103, 2004.
- J. F. Meirink and G. J van Zadelhoff. Algorithm theoretical basis document sevir cloud physical products claa edition 2. EUMETSAT CM SAF, available at: <https://www.cmsaf.eu/SharedDocs/Literatur/document/2016/>, 2016.
- E. Mészáros. *Atmospheric Chemistry: Fundamental Aspects*. Elsevier Scientific publishing company, 1981. ISBN 0444997539.
- K. Meyer and S. Platnick. Utilizing the modis 1.38 m channel for cirrus cloud optical thickness retrievals: Algorithm and retrieval uncertainties. *J. Geophys. Res.*, 115: D24209, 2010.
- W. Middleton and A. Mungal. The luminous directional reflectance of snow. *Journal of the Optical Society of America*, 42(8), 1952.
- G. Mie. A contribution to the optics of turbid media, especially colloidal metallic suspensions. *Annals of Physics*, 25(4):377–445, 1908.
- Q.-L. Min and M. Duan. A successive order of scattering model for solving vector radiative transfer in the atmosphere. *J. Quant. Spectrosc. Radiat. Transfer*, 87:243–259, 2004.
- P. Minnis and E. F. Harrison. Diurnal variability of regional cloud and clear-sky radiative parameters derived from goes data. part i: Analysis method. *Journal of Applied Meteorology and Climatology*, 23(7):993–1011, 1984.
- P. Minnis, V. Chakrapani, D. R. Doelling, L. Nguyen, R. Palikonda, D. A. Spangenberg, T. Uttal, R. F. Arduini, and M. Shupe. Cloud coverage and height during fire

- ace derived from avhrr data. *J. Geophys. Res.*, 106:15215–15232, 2001.
- P. Minnis, D. A. Spangenberg, and V. Chakrapani. Distribution and validation of cloud cover derived from avhrr data over the arctic ocean during the sheba year. Proc. 13th ARM Science Team Meeting, 31 March–4 April 2003,, Broomfield, Colorado, USA,, 2003.
- M. I. Mishchenko. Light scattering by size-shape distributions of randomly oriented axially symmetric particles of size comparable to a wavelength. *Appl. Opt.*, 32: 4652–4666, 1993.
- M. I. Mishchenko, J. M. Dlugach, E. G. and Yanovitskij, and N. T. Zakharova. Bidirectional reflectance of flat, optically thick particulate layers: an efficient radiative transfer solution and applications to snow and soil surfaces. *J. Quant. Spectrosc. Ra.*, 63:409–432, 1999a.
- M. I. Mishchenko, I. V. Geogdzhayev, B. Cairns, W. B. Rossow, and A. A. Lacis. Aerosol retrievals over the ocean by use of channels 1 and 2 avhrr data: Sensitivity analysis and preliminary results. *Appl. Opt.*, 38:7325–7341, 1999b.
- M. Mitchell. Visual range in the polar regions with particular reference to the Alaskan Arctic. *J. Atmos. Terrestrial Phys., Special Suppl.*, pages 195–211, 1956.
- E. C. Monahan, D. E. Spiel, and K. L. Davidson. A model of marine aerosol generation via whitecaps and wave disruption. in e. c. monahan g. mac niocail (eds.), *oceanic whitecaps*. Norwell: D. Reidel, pages 167–174, 1986.
- J. P. Musial, F. Husler, M. Sutterlin, C. Neuhaus, and S. Wunderle. Daytime low strati form cloud detection on avhrr imagery. *Remote Sens.*, 6:5124–5150, 2014.
- M. R. Najafi, F. W. Zwiers, and N. P. Gillett. Attribution of arctic temperature change to greenhouse-gas and aerosol influences. *Nat. Clim. Chang.*, 5(3):246–249, 2015.
- F. Nansen. *Blandt Sel og Bjorn*. Dybwad, Oslo, 1924.
- J. C. A. Navarro, I. Varma, V. and Riipinen, O. Seland, A. Kirkevåg, H. Struthers, and et al. Amplification of arctic warming by past air pollution reductions in europe. *Nat. Geosci.*, 9(4):277–281, 2016.
- F. E. Nicodemus. Directional reflectance and emissivity of an opaque surface. *Appl. Optics*, 4:767–773, 1965.
- F. E. Nicodemus, J. C. Richmond, J. J. Hsia, I. W. Ginsberg, and T. Limperis. Geometrical considerations and nomenclature for reflectance. In L. B. Wolff, S. A. Shafer, and G. Healey, editors, *Radiometry*, page 94–145. Jones and Bartlett Publishers, Sudbury, 1977.
- A. E. Nordenskiöld. Nordenskiöld on the inland ice of Greenland. *Science*, 2(44): 732–738, 1883.
- P. R. J. North, S. A. Briggs, S. E. Plummer, and J. J. Settle. Retrieval of land surface bidirectional reflectance and aerosol opacity from atsr-2 multi-angle imagery. *IEEE Trans. Geosci. Remote Sens.*, 37:526–537, 1999.

- P.R.J. North. Estimation of aerosol opacity and land surface bidirectional reflectance from atsr-2 dual-angle imagery: operational method and validation. *J. Geophys. Res.*, 107 (D12):1–11, 2002.
- B. Ottar, Y. Gotaas, O. Hov, T. Iversen, E. Joranger, and co authors. Air pollutants in the Arctic. Final report of a research programme conducted on the behalf of British Petroleum, Ltd. The Norwegian Institute of Air Research, Kjeller, Norway, NILU OR 30/86. 80p. 1986.
- J.E. Overland and M. Wang. Large-scale atmospheric circulation changes are associated with the recent loss of Arctic sea ice. *Tellus*, 62A:1–9, 2010.
- T. H. Painter, J. Dozier, D. A. Roberts, R. E. Davis, and R. O. Greene. Retrieval of subpixel snow-covered area and grain size from imaging spectrometer data. *Remote Sens. Environ.*, 85:64–77, 2003.
- J. Pavelsky, T. M. and Boe and E. J. Hall, A. nd Fetzer. Atmospheric inversion strength over polar oceans in winter regulated by sea ice. *Climate Dyn.*, 36(5-6):945–955.
- M. J. Pavolonis, A. K. Heidinger, and T. Uttal. Daytime global cloud typing from avhrr and viirs: Algorithm description, validation, and comparison. *J. Appl. Meteorol.*, 44: 804–826, 2005.
- K. Pearson. Vii. mathematical contributions to the theory of evolution. – iii. regression, heredity, and panmixia. *Philos. T. Roy.Soc. A.*, 187:253–318, 1896.
- DK Perovich. Theoretical estimates of light reflection and transmission by spatially complex and temporally varying sea ice covers. *J. Geophys. Res.*, 95(C6):9557–67, 1990.
- F. Pithan and T. Mauritsen. Arctic amplification dominated by temperature feedbacks in contemporary climate models. *Nat. Geosci.*, 7:181–184, 2014.
- S. Platnick and J. M. Fontenla. Model calculations of so-lar spectral irradiance in the 3.7 band for earth re-mote sensing application. *Am. Meteorol. Soc.*, 47:124–134, 2008.
- P. Quinn, G. Shaw, E. Andrews, E. Dutton, T. Ruoho-Airola, and S. Gong. Arctic haze: current trends and knowledge gaps. *Tellus*, 59B:99–114, 2007.
- K. Rahn, R. Borys, and G. Shaw. The Asian source of Arctic haze bands. *Nature*, 268:713–715, 1977.
- C. A. Randles, L. M. Russell, and V. Ramaswamy. Hygroscopic and optical properties of organic sea salt aerosol and consequences for climate forcing. *Geophys. Res. Lett.*, 31:L16 108, 2004.
- CRN. Rao, EP. McClain, and LL. Stowe. Remote sensing of aerosols over the oceans using avhrr data theory, practice, and applications. *Int. J. Remote Sens.*, 10(4–5): 743–749, 1989.
- E. Raschke, W. Rossow, and R. Schiffer. The international satellite cloud climatology project- preliminary results and its potential aspects. *Advances in Space Research*, 7:137–145, 1987.

- L. Remer, D. Tanre, and YJ. Kaufman. Algorithm for remote sensing of tropospheric aerosols from modis, collection 5, algorithm theoretical basis document. <http://modis.gsfc.nasa.>, 2006.
- L. A. Remer, Y. J. Kaufman, D. Tanre, S. Mattoo, D. A. Chu, J. V. Martins, R. R. Li, C. Ichoku, R. C. Levy, R. G. Kleidman, T. F. Eck, E. Vermote, and B. N. Holben. The modis aerosol algorithm, products and validation. *J. Atmos. Sci.*, 62:947–973, 2005a.
- L. A. Remer, S. Mattoo, R. C. Levy, A. Heidinger, R.B. Pierce, , and M. Chin. Retrieving aerosol in a cloudy environment:aerosol product availability as a function of spatial resolution. *Atmos. Meas. Tech.*, 5:1823–1840, 2012.
- LA Remer, YJ. Kaufman, D. Tanre, S. Mattoo, DA. Chu, JV. Martins, RR. Li, C. Ichoku, RC. Levy, RG. Kleidman, TF. Eck, E. Vermote, and BN Holben. The modis aerosol algorithm, products and validation. *J. Atmos. Sci.*, 62:947–973, 2005b.
- D. W. Reynolds and T. H. Vonder Haar. A bispectral method for cloud parameter determination. *Monthly Weather Review*, 105(4):446–457, 1977.
- R. H. Rhodes, X. Yang, and E. W. Wolff. Sea ice versus storms: What controls sea salt in arctic ice cores? *Geophys. Res. Lett.*, 45:5572–5580, 2018.
- M. Rinaldi, S. Decesari, C. Carbone, E. Finessi, S. Fuzzi, and D C. O’Dowd J. Sciare J. P. Burrows M. Vrekoussis B. Ervens K. T. Facchini M. C. Ceburnis, D. Evidence of a natural marine source of oxalic acid and a possible link to glyoxal. *J. Geophys. Res.*, 116:D16204, 2011.
- A. Rinke, K. Dethloff, and M. Fortmann. Regional climate effects of arctic haze. *Geophys. Res. Lett.*, 31:L16202, 2004.
- J. L. Rodgers and W. A Nicewander. Thirteen ways to look at the correlation coefficient. *Am. Stat.*, 42:59–66, 1988.
- D. Rosenfeld, E. Cattani, S. Melani, and V. Levizzani. Considerations on daylight operation of 1.6 versus 3.7 μm channel on noaa and metop satellites. *Am. Meteorol. Soc.*, 85:873–881, 2004.
- W. B. Rossow. Measuring cloud properties from space: A review. *J. Climate*, 2: 201–213, 1998.
- W. B. Rossow and L. C Garder. Validation of isccp cloud detection. *J. Climate*, 6: 2370–2393, 1993.
- W.B. Rossow, Kinsella E. Mosher, F., A. Arking, M. Desbois, E. Harrison, P. Minnis, E. Ruprecht, G. Seze, C. Simmer, and E. Smith. Isccp cloud algorithm intercomparison. *J. Clim. Appl. Meteorol.*, 24:877–903, 1985.
- V. V. Rozanov. Adjoint radiative transfer equation and inverse problems, in: *Light scattering reviews: Single and multiple lightscattering*, edited by: Kokhanovsky, a. a. Springer, Berlin and Heidelberg, Germany:339–392, 2006.
- V. V. Rozanov and A. V. Rozanov. Relationship between different approaches to derive weighting functions related to atmospheric remote sensing problems,. *J. Quant.*

- Spectrosc. Ra., 105:217–242, 2007.
- V. V. Rozanov, M. Buchwitz, K. U. Eichmann, R. de Beek, and J. P. Burrows. Sciatran – a new radiative transfer model for geophysical applications in the 240–2400 nm spectral region:the pseudo-spherical version. *Adv. Space. Res.*, 29:1831–1835, 2002.
- V. V. Rozanov, A. V. Rozanov, and A. A. Kokhanovsky. Derivatives of the radiation field and their application to the solution of inverse problems. In A. A. Kokhanovsky, editor, *Light Scattering Reviews 2: Remote Sensing and Inverse Problems*, page 205–265. Springer, Berlin and Heidelberg, Germany, 2007.
- V. V. Rozanov, A. V. Rozanov, A. A. Kokhanovsky, and J. P. Burrows. Radiative transfer through terrestrial atmosphere and ocean: Software package sciatran. *J. Quant. Spectrosc. Ra.*, 133:13–71, 2014.
- M. L. Salby. *Fundamentals of Atmospheric Physics*. International Geophysics Series. Academic Press, USA, 1996. ISBN 9780126151602.
- M. Sand, T. K. Berntsen, J. E. Kay, J. F. Lamarque, O. Seland, and A. Kirkevåg. The arctic response to remote and local forcing of black carbon. *Atmos. Chem. Phys.*, 13(1):211–224, 2013a.
- M. Sand, T. K. Berntsen, O. Seland, and J. E. Kristjansson. Arctic surface temperature change to emissions of black carbon within arctic or mid-latitudes. *J. Geophys. Res.: Atmospheres*, 118:7788–7798, 2013b.
- A. M. Sayer, G. E. Thomas, and R.G. Grainger. A sea surface reflectance model for (a)atsr, and application to aerosol retrievals. *Atmos. Meas. Tech.*, 3:813–838, 2010.
- G. Schaepman-Strub, M. E. Schaepman, T. H. Painter, S. Dangel, and J. V. Martonchik. Reflectance quantities in optical remote sensing – definitions and case studies. *Remote Sens. Environ.*, 103:27–42, 2006.
- C. Schlundt, A. A. Kokhanovsky, W. Hoyningen-Huene, T. Dinter, L. Istomina, and J. P. Burrows. Synergetic cloud fraction determination for sciamachy using meris. *Atmos. Meas. Tech.*, 4:319–337, 2011.
- S.H. Schneider and R.E. Dickinson. Climate modeling. *Reviews of Geophysics and space physics*, 12(3):447–493, 1974.
- J.H. Seinfeld and S.N. Pandis. *Atmospheric Chemistry and Physics: From air pollution to climate change*. Wiley, 1998. ISBN 0471178160, 9780471178163.
- W.D. Sellers. A global climate model based on the energy balance of the earth-atmosphere system. *J. Appl. Meteorol.*, 8:392–400, 1969.
- M. C. Serreze and R. G. Barry. Processes and impacts of Arctic amplification: a research synthesis. *Global Planet. Change*, 77:85–96, 2011.
- M. C. Serreze and J. A. Francis. The arctic amplification debate. *Climatic Change*, 76:241–264, 2006.
- G. E. Shaw. Microparticle size spectrum of Arctic haze. *Geophys. Res. Lett.*, 11: 409–412, 1984.

- G. E. Shaw. Aerosols as climate regulators: a climate-biosphere linkage? *Atmos. Environ.*, 21:985–986, 1987.
- G.E. Shaw. The arctic haze phenomenon. *Bull. Am. Meteorol. Soc.*, 76 (12):2403–2413, 1995.
- W. E. Shenk and R. J. Holub. A multispectral cloud type identification method using nimbus 3 mrir measurements. *Mon. Wea. Rev.*, 104:284–291, 1976.
- Y. Shi, J. Zhang, J. S. Reid, B. Liu, and E. J. Hyer. Critical evaluation of cloud contamination in the misr aerosol products using modis cloud mask products. *Atmos. Meas. Tech.*, 7:1791–1801, 2014a.
- Y. Shi, J. Zhang, J. S. Reid, B. Liu, and E. J. Hyer. Critical evaluation of cloud contamination in the misr aerosol products using modis cloud mask products. *Atmos. Meas. Tech.*, 7:1791–1801, 2014b.
- D. Shindell and G. Faluvegi. Climate response to regional radiative forcing during the twentieth century. *Nat. Geosci.*, 2:294–300, 2009.
- M. J. Shultz. Crystal growth in ice and snow. *Phys. Today.*, 71:35–39, 2018.
- B. M. Sinnhuber. *Fernerkundung atmosparischer*. 2015.
- B. Slater and A. Michaelides. Surface pre-melting of water ice. *Nat. Rev. Chem.*, 3: 172–188, 2019.
- J. A. Sobrino, J. C. Jiménez-Muñoz, G. Sòria, A. B. Ruescas, O. Danne, C. Brockmann, D. Ghent, J. Reme-dios, P. North, C. Merchant, M. Berger, P.P. Mathieu, and F. M. Göttsche. Synergistic use of meris and aatsr as a proxy for estimating land surface temperature from sentinel-3 data. *Remote Sens. Environ.*, 179:149–161, 2016.
- L. Sogacheva, P. Kolmonen, T. H. Virtanen, E. Rodriguez, G. Saponaro, and G. de Leeuw. Post-processing to remove residual clouds from aerosol optical depth retrieved using the advanced along track scanning radiometer. *Atmos. Meas. Tech.*, 10:491–505, 2017.
- A. Soliman, C. Duguay, W. Saunders, and S Hachem. Pan-arctic land surface temperature from modis and aatsr: Product development and intercomparison. *Remote Sens. Base*, 4:3833–3856, 2012.
- D. A. Spangenberg, V. Chakrapani, D. R. Doelling, P. Minnis, and R. F. Arduini. Development of an automated arctic cloud mask using clear-sky satellite observations taken over the sheba and arm nsa sites. *Proc. 6th Conf. on Polar Meteor. and Oceanography*, San Diego, CA, page 246–249, 2001.
- K. Stamnes, S. Tsay, W. Wiscombe, and K. Jayaweera. Numerically stable algorithm for discrete-ordinate-method radiative transfer in multiple scattering and emitting layered media. *Appl. Opt.*, 27:2502–2509, 1988.
- S. M. Steinberg and J. L. Bada. Oxalic, glyoxalic and pyruvic acids in eastern pacific-ocean waters. *Journal of Marine Research*, 42(3):697–708, 1984.
- LL. Stowe. Cloud and aerosol products at noaa/ nesdis. *Paleogeogr. Paleoclimatol.*

- Paleoecol, 90:25–32, 1991.
- LL. Stowe, AM Ignatov, and RR. Singh. Development, validation, and potential enhancements to the second-generation operational aerosol product at the national environmental satellite, data, and information service of the national oceanic and atmospheric administration. *J. Geophys. Res.*, 102:16923–16934., 1997.
- J. C. Stroeve, V. Kattsov, A. Barrett, M. Serreze, T. Pavlova, M. Holland, and W. N. Meier. Trends in Arctic sea ice extent from CMIP5, CMIP3 and observations. *Geophys. Research letter*, 39:L16502, 2012.
- G. SÈZE and W. Rossow. Time-cumulated visible and infrared radiance histograms used as descriptors of surface and cloud variations. *Int. J. Remote Sens.*, 12:5: 877–920, 1991.
- I.N. Tang, A.C. Tridico, and Fung. K.H. Thermodynamic and optical properties of sea salt aerosols. *J. Geophys. Res.*, 102(23):269–299, 1997.
- D. Tanre, YJ. Kaufman, M. Herman, and S. Mattoo. Remote sensing of aerosol properties over oceans using the modis/eos spectral radiances. *J. Geophys. Res.*, 102(D14): 16971–16988, 1997.
- D. Tanre, L.A. Remer, Y.J. Kaufman, Hobbs PV. Mattoo, S., J Livingston, PB Russell, and A. Smirnov. Retrieval of aerosol optical thickness and size distribution over ocean from the modis airborne simulator during tarfox. *J. Geophys. Res.*, 104(D2): 2261–2278, 1999.
- D. Tanre, M. Herman, PY Deschamps, and A. De Lefte. Atmospheric modeling for space measurements of ground reflectances including bidirectional properties. *Appl. Opt.*, 18(21):3587–3594, 1979.
- P. C. Taylor, et al., and jet al. A decomposition of feedback contributions to polar warming amplification. *J. Clim.*, 26:70237043, 2013.
- G. E. Thomas, E. Carboni, A. M. Sayer, C. A. Poulsen, R. Siddans, and R. G. Grainger. Oxford-ral aerosol and cloud (orac): aerosol retrievals from satellite radiometers. In A. A. Kokhanovsky and G. de Leeuw, editors, *Satellite Aerosol Remote Sensing Over Land*, page 193–225. Springer, Berlin, Germany, 2009.
- Jeffery A. Thompson, David. J. Paull, and G. L. Brian. An improved liberal cloud-mask for addressing snow/cloud confusion with modis. *Photogrammetric Engineering and Remote Sensing*, 2015:23–33, 2015.
- C. Tomasi, A. A. Kokhanovsky, A. Lupi, C. Ritter, A. Smirnov, N. T. O’Neill, R. S. Stone, B. N. Holben, and S. Nyeki. Aerosol remote sensing in polar regions. *Earth-Science Reviews*, 140:108–157, 2015.
- O. Torres, P.K. Bhartia, J.R. Herman, A. Sinyuk, P. Ginoux, and Holben. B. A long-term record of aerosol optical depth from toms observations and comparison to aeronet measurements. *Journal of the Atmospheric Sciences*, 59(3):398–413, 2002.
- Q. Trepte, R. F. Arduini, Y. Chen, S. Sun-Mack, P. Minnis, D. A. Spangenberg, and D. R. Doelling. Development of a daytime polar cloud mask using theoretical models

- of near-infrared bidirectional reflectance for arm and ceres. Proc. AMS 6th Conf. Polar Meteorology and Oceanography, San Diego, CA, 4–18 May, page 242–245, 2001.
- S.A. Twomey, M. Piepgrass, and T.L. Wolfe. An assessment of the impact of pollution of global cloud albedo. *Tellus B*, 36:356, 1984.
- R. Udisti, R. Traversi, S. Becagli, C. Tomasi, M. Mazzola, A. Lupi, and P. K. Quinn. Arctic aerosols. In A. A. Kokhanovsky and C. Tomasi, editors, *Physics and Chemistry of the Arctic Atmosphere*. Springer Nature Switzerland AG, Cham, Switzerland, 2020. ISBN 978-3-030-33566-3.
- J. P. Veefkind and G. de Leeuw. A new algorithm to determine the spectral aerosol optical depth from satellite radiometer measurements. *J. Aerosol Sci.*, 29:1237–1248, 1998.
- J. P. Veefkind, G. de Leeuw, and P. A. Durkee. Retrieval of aerosol optical depth over land using two-angle view satellite radiometry during tarfox. *Geophys. Res. Lett.*, 25:3135–3138, 1999.
- E.F. Vermote, C.O. N. El Saleous, Y.J. Justice, Kaufman J.L., L. Privette, J.C. Remer, D. Roger, and Tanré. Atmospheric correction of visible to middle-infrared eos-modis data over land surfaces : Background, operational algorithm and validation. *J. Geophys. Res.*, 102 (D14):17131–1714, 1977.
- W. von Hoyningen-Huene, M. Freitag, and JP. Burrows. Retrieval of aerosol optical thickness over land surfaces from top-of-atmosphere radiance. *J. Geophys. Res.*, 108: 4260, 2003.
- W. von Hoyningen-Huene, AA. Kokhanovsky, JP. Burrows, V. Bruniquel-Pinel, P. Renger, and F. Baret. Simultaneous determination of aerosol and surface characteristics from meris top-of-atmosphere reflectance. *Adv. Space Res.*, 37:2172–2177, 2006.
- W. von Hoyningen-Huene, J. Yoon, M. Vountas, L. G. Istomina, G. Rohen, T. Dinter, A. A. Kokhanovsky, and J. P. Burrows. Retrieval of spectral aerosol optical thickness over land using ocean color sensors meris and seawifs. *Atmos. Meas. Tech.*, 4:151–171, 2011.
- M. Vountas, K. Belinska, Lelli Luca Mei L. Jafariserajehlou S. Rozanov, V.V., and J.P. Burrows. Retrieval of aerosol optical thickness and surface parameters based on multi-spectral and multi-viewing space-borne measurements. *J. Quant. Spectrosc. Radiat. Transfer*, 56:107311, 2020.
- T. Várnai and A. Marshak. Effect of cloud fraction on near-cloud aerosol behavior in the modis atmospheric correction ocean color product. *Remote Sens.*, 7:5283–5299, 2015.
- J. M. Wallace and P. V. Hobbs. *Atmospheric Science, An introductory survey*. Amsterdam; Boston : Elsevier Academic Press, 2 edition, 2006.
- S. G. Warren. Optical properties of snow. *Rev. Geophys. Space Ge.*, 20:67–89, 1982.
- S. G. Warren, R. E. Brandt, and Hinton P. O. R. Effect of surface roughness on

- bidirectional reflectance of antarctic snow. *J. Geophys. Res.*, 103:25789–807, 1998.
- M. Wendisch, A. Macke, A. Ehrlich, Mech M. Chechin D. Dethloff K. Barientos C. Bozem H. Brückner M. Clemen H. C. Crewell S. Donth T. Dupuy R. Ebell K. Egerer U. Engelmann R. Engler C. Eppers O. Gehrman M. Gong X. Gottschalk M. Goubeyre C. Griesche H. Hartmann J. Hartmann M. Heinold B. Herber A. Herrmann H. Heygster G. Hoor P. Jafariserajehlou S. Jäkel E. Järvinen E. Jourdan O. Kästner U. Kecorius S. Knudsen E. M. Köllner F. Kretzschmar J. Lelli L. Delphine L. Maturilli M. Mei L. Mertens S. Mioche G. Neuber R. Nicolaus M. Nomokonova T. Notholt J. Palm M. van Pinxteren M. Quaas J. Richter P. Ruiz-Donoso E. Schäfer M. Schmieder K. Schnaiter M. Schneider J. Schwarzenböck A. Seifert P. Shupe M. D. Siebert H. Spreen G. Stapf J. Stratmann F. Vogl T. Welti A. Wex H. Wiedensohler A. Zanatta M. Lüpkes, C., and S. Zeppenfeld. The arctic cloud puzzle: using acloud/pascal multiplatform observations to unravel the role of clouds and aerosol particles in arctic amplification. *Bulletin of the American Meteorological*, 100 (15): 841–871, 2019.
- M. Wendisch, M. and Brückner, J. P. Burrows, S. Crewell, K. Dethloff, K. Ebell, C. Lüpkes, J. Macke, A. and Notholt, J. Quaas, A. Rinke, and I. Tegen. Understanding causes and effects of rapid warming in the Arctic. *Eos*, 98:22–26, 2017.
- A. Werkmeister, M. Lockhoff, M. Schrempf, K. Tohsing, B. Liley, and G. Seckmeyer. Comparing satellite to ground-based automated and manual cloud coverage observations – a case study. *Atmos. Meas. Tech.*, 8:2001–2015, 2015.
- F. Werner, G. Wind, Z. Zhang, S. Platnick, L. Girolamo, G. Zhao, Amarasinghe N., , and K. Meyer. Marine boundary layer cloud property retrievals from high-resolution aster observations: Case studies and comparison with terra-modis. *Atmos. Meas. Tech.*, 9:5869–5894, 2016.
- M. D. Willis, W. R. Leaitch, and J. P. Abbatt. Processes controlling the composition and abundance of arctic aerosol. *Reviews of Geophysics*, 56:621–671, 2018.
- G. Wind, A. M. da Silva, P. M. Norris, S. Platnick, S. Mattoo, and R. C. Levy. Multi-sensor cloud and aerosol retrieval simulator and remote sensing from model parameters – part 2: Aerosols. *Geosci. Model Dev.*, 9:2377–2389, 2016.
- M. Winton. Amplified Arctic climate change: what does surface albedo feedback have to do with it? *Geophys. Res. Lett.*, 33:L03701, 2006.
- W. J. Wiscombe and S. G. Warren. A model for the spectral albedo of snow, i. pure snow. *J. Atmos. Sci.*, 37:2712–2733, 1980.
- Y. Xie, P. Yang, B-C. Gao, GW. Kattawar, and MI. Mishchenko. Effect of ice crystal shape and effective size on snow bidirectional reflectance. *J Quant Spectrosc Radiat Transfer*, 100:457–69, 2006.
- Y. Xue, J. Guo, and X Zhang. Aerosol optical thickness retrieval over nonlambertian land surface with synergistic use of aatsr radiance measurements and modis derived albedo model parameters. *Atmos. Res.*, 93:736–746, 2009.
- P. Yang and K. N. Liou. Single-scattering properties of complex ice crystals in terres-

- trial atmosphere. *Contr. Atmos. Phys.*, 71:223–248, 1998.
- P. Yang, L. Bi, B. A. Baum, K. Liou, G. W. Kattawar, M. I. Mishchenko, and B. Cole. Spectrally consistent scattering, absorption, and polarization properties of atmospheric ice crystals at wavelengths from 0.2 to 100 μ m. *J. Atmos. Sci.*, 70:330–347, 2013.
- A. M. Zavody, C. T. Mutlow, and D. T. Llewellyn-Jones. Cloud clearing over the ocean in the processing of data from the along-track scanning radiometer (atsr). *J. Atmos. Ocean. Tech.*, 17:595–615, 2000.
- T. B. Zhuravleva and A. A. Kokhanovsky. Influence of surface roughness on the reflective properties of snow. *J. Quant. Spectrosc. Ra.*, 112:1353–1368, 2011.

Acknowledgment

This is the last page of my dissertation, and it means that I am close to the end of a long extraordinary journey I had at IUP, University of Bremen. I gained a lot of experience and skills, for which I am deeply grateful. Indeed, being part of IUP was a turning point in my life, without which it would be impossible for me to stand where I am today.

I am extremely thankful to Prof. John P. Burrows FRS, for his invaluable advice and supervision throughout this project. His overall insight was really influential in shaping my work. I was always inspired by his impressive dedication on his work and this project.

I would like to thank Dr. Marco Vountas for his incredible supervision, continuous support and encouragement. His level of patience is something I will always keep aspiring to.

I would like to express my sincere thanks to Dr. Vladimir V. Rozanov for his support and guidance, without which this work would have not been the same. His immense knowledge and experience have motivated me all the time, especially when working with SCIATRAN. I'm proud of the time working with him.

Thanks to my committee members, Prof. Andreas Macke and Prof. Annette Ladstätter-Weißenmayer. Their encouraging words and thoughtful, detailed feedback in several PhD committee meetings have been very important to improve my work.

I gratefully acknowledge the funding by the German Research Foundation (DFG, Deutsche Forschungsgemeinschaft) of the Transregional Collaborative Research Centre SFB/TRR 172 (Project-ID 268020496).

I would like to thank Prof. Manfred Wendisch and all (AC)³ community members. It was a unique chance to be part of this project and take a step to better understand and explain Arctic Amplification. Prof. Wendisch, thanks for keeping us motivated by your encouraging feedbacks.

I thank all my friends and colleagues not only in IUP, but also in the (AC)³ project, especially Ilias Bougoudis, Christine Pohl, Arantxa Triana Gómez, Luca Lelli, Sebastian Zeppenfeld, Ana Radovan, Rosa Gierens, Elena Ruiz Donoso, Carola Barrientos Velasco, and Vasileios Pefanis. I am grateful for all the nice moments we shared.

I would like to express my deepest gratitude to my parents for their endless and unconditional support. Thanks for believing in me, you have always stood behind me, and this was no exception.

Finally, I would like thank my husband, Hamoun. Thanks for always being there for me. Without your understanding and encouragement in the past few years, it would be impossible for me to complete this work. We came a long way from our first day in Germany, when we learned to say "Tschüss".

Soheila Jafariserajehlou

September 2021
Darmstadt